

# A Simulation Study of the JEM–EUSO Mission for the Detection of Ultra–High Energy Cosmic Rays

**Dissertation**

der Mathematisch–Naturwissenschaftlichen Fakultät  
der Eberhard Karls Universität Tübingen  
zur Erlangung des Grades eines  
Doktors der Naturwissenschaften  
(Dr. rer. nat.)

vorgelegt von  
Francesco Fenu  
aus Villafranca di Verona (Italien)

Tübingen  
2013

---

Tag der mündlichen Qualifikation: 10. September 2013

Dekan: Prof. Dr. Wolfgang Rosenstiel

1. Berichterstatter: Prof. Dr. Andrea Santangelo

2. Berichterstatter: Prof. Dr. Toshikazu Ebisuzaki

# Zusammenfassung

Im Rahmen dieser Dissertation ist eine Simulationsstudie über die JEM–EUSO Weltraummission für den Nachweis Kosmischer Strahlung durchgeführt worden. Das "Extreme Universe Space Observatory on-board the JEM experimental module" (JEM–EUSO) beschäftigt sich mit dem extremsten Teil des Spektrums der kosmischen Strahlung ( $E > 10^{20}$  eV) und zielt auf deren Nachweis aus dem Weltall. Die JEM–EUSO Mission ist für die Jahre 2017–2022 geplant und wird von der internationale Weltraumstation aus die Atmosphäre nachtsüber überwachen um das Fluoreszenzlicht der Luftschauer nachzuweisen.

In dieser Doktorarbeit wird die wissenschaftliche Performance des JEM–EUSO Observatoriums evaluiert. Insbesondere die Trigger und die Rekonstruktion werden präsentiert. Die Trigger Algorithmen für die Hintergrundunterdrückung wurden in die Euso Simulation & Analysis Framework (ESAF) Software implementiert. Eine systematische Studie über die Triggereffizienzen, die Exposition, die getriggerten Spektren und die Datenmenge ist durchgeführt worden. Außerdem wurden Energie und  $X_{max}$  Algorithmen entwickelt, unter verschiedenen Bedingungen getestet und ihre systematischen Fehler bestimmt. Mit ihnen könnte eine weitreichende Studie über die Energie und  $X_{max}$  Auflösung durchgeführt werden.

Im ersten Kapitel dieser Dissertation wird, nach einer historischen Einleitung, die JEM–EUSO Mission und der Kontext in dem sie stattfinden wird beschrieben. Im zweiten Kapitel wird die Luftschauer Fluoreszenztechnik vorgestellt und eine kurze Einführung in die Technologie des JEM–EUSO Detektors gegeben. Das Kapitel 3 beschäftigt sich mit der Beschreibung der ESAF Software, mit ihrer Struktur und mit den physikalischen Grundlagen. Kapitel 4 enthält eine Beschreibung der Triggerkette und eine Studie über ihre Performance. Im Kapitel 5 und 6 werden Energie und  $X_{max}$  Rekonstruktion beschrieben. Die Algorithmen werden charakterisiert und ihre Performances unter verschiedenen Bedingungen getestet. In dieser Dissertation wird gezeigt dass die wissenschaftlichen Anforderungen an die JEM–EUSO Mission erfüllt sind.

---

# Abstract

In this thesis I present a simulation study on the JEM–EUSO mission performances. The “Extreme Universe Space Observatory on–board the JEM experimental module” (JEM–EUSO) is a space mission which aims at the detection of extreme–high energy cosmic rays. Target of this mission is the detection of cosmic rays above  $10^{20}$  eV by means of the air fluorescence technique from space. This mission, planned to fly between 2017 and 2022, aims at the detection night–time of the fluorescence light produced by extensive air showers in the atmosphere. Such a technique aims at the maximization of the exposure at the extremes of the spectrum.

In this thesis the scientific performances of the JEM–EUSO mission have been assessed. More in detail I studied the trigger and reconstruction performances. I therefore introduced in the Euso Simulation & Analysis Framework (ESAF) the trigger algorithms for the background rejection. A systematic study on the trigger efficiency, on the exposure, on the triggered spectra and on the triggered event size has been performed both in nadir and in tilt mode. I furthermore developed and tested the algorithms for the energy and  $X_{max}$  reconstruction. A wide characterization work has been performed together with an estimation of the systematics affecting the procedure. At last, a comprehensive study on the energy and  $X_{max}$  performances under several conditions has been also performed.

More in detail, the first chapter is devoted to the description of the JEM–EUSO scientific case and of the context within which such a mission will operate. The open questions in the extremely high energetic cosmic rays field will be therefore presented as well as the scientific requirements to be satisfied by JEM–EUSO. The space based fluorescence technique will be then presented in Chapter 2 together with an overview of the JEM–EUSO mission. A brief description of the JEM–EUSO instrument will be also given. Chapter 3 will be devoted to the description of the ESAF software, to its structure and to the physical modelization assumed in it. Chapter 4 is related to the trigger chain description and performances assessment. Eventually, chapters 5 and 6 are devoted to the energy and  $X_{max}$  reconstruction algorithms. Such algorithms have been therefore characterized and their limits clearly recognized and quantified. The performances within a broad spectrum of conditions have been assessed. The performances have been found to be compliant with the JEM–EUSO requirements.

# Contents

<b>Introduction</b>	<b>7</b>
<b>1 Cosmic Ray Science</b>	<b>9</b>
1.1 Historical background . . . . .	10
1.2 Phenomenology of Cosmic Rays . . . . .	18
1.3 Theories on the origin . . . . .	24
1.3.1 The second order Fermi mechanism . . . . .	24
1.3.2 The first order Fermi mechanism . . . . .	26
1.3.3 Supernova remnants as sources . . . . .	27
1.3.4 Toward higher energies . . . . .	29
1.3.5 Alternative theories . . . . .	45
1.4 Propagation . . . . .	46
1.5 The end of the spectrum: the role of JEM–EUSO . . . . .	51
<b>2 Observational Techniques</b>	<b>61</b>
2.1 Shower physics . . . . .	62
2.2 Fluorescence and Cherenkov emission . . . . .	66
2.2.1 Photon propagation in atmosphere . . . . .	69
2.3 Background in atmosphere . . . . .	69
2.4 Detectors . . . . .	71
2.5 JEM–EUSO . . . . .	73
<b>3 ESAF</b>	<b>81</b>
3.1 The EUSO Simulation and Analysis Framework (ESAF) . . . . .	81
3.2 Shower development . . . . .	86
3.3 Photon production . . . . .	93
3.4 Atmosphere . . . . .	99
3.5 Photons propagation . . . . .	99
3.6 Optics . . . . .	106
3.7 Electronics . . . . .	114
3.8 Reconstruction: pattern recognition . . . . .	117

3.9	Reconstruction: angular reconstruction . . . . .	120
<b>4</b>	<b>The JEM–EUSO Trigger Performances</b>	<b>125</b>
4.1	The Persistent Tracking Trigger . . . . .	126
4.2	The CCB–Linear Tracking Trigger . . . . .	128
4.3	Average background and fake trigger rates . . . . .	130
4.4	Trigger performances . . . . .	133
4.5	Exposure . . . . .	137
4.6	Triggered events energy distribution . . . . .	142
4.7	Tilt mode . . . . .	146
4.8	Data rate studies . . . . .	152
<b>5</b>	<b>The Energy and <math>X_{max}</math> Reconstruction Algorithms</b>	<b>165</b>
5.1	The PmtToShowerReco algorithm . . . . .	166
5.2	Procedure systematics . . . . .	174
5.3	Iterative procedure . . . . .	187
5.4	Conclusions . . . . .	192
<b>6</b>	<b>JEM–EUSO Reconstruction Performances</b>	<b>197</b>
6.1	The reconstructed event . . . . .	197
6.2	Energy reconstruction . . . . .	200
6.2.1	Fixed condition . . . . .	200
6.2.2	Full field of view . . . . .	202
6.2.3	Full sample . . . . .	206
6.3	$X_{max}$ reconstruction . . . . .	207
6.3.1	Fixed condition . . . . .	207
6.3.2	Full field of view . . . . .	211
6.4	The quality of the event reconstruction . . . . .	214
6.5	Reconstruction quality cuts . . . . .	220
6.6	The $\chi^2$ at the highest energies . . . . .	226
6.7	The reconstructed Cosmic Ray spectrum . . . . .	229
6.8	Parameter variation . . . . .	231
	<b>Conclusions: the JEM–EUSO Performances</b>	<b>235</b>
	<b>Acronyms</b>	<b>241</b>
	<b>Bibliography</b>	<b>243</b>

# Introduction - UHECR: toward the solution?

This thesis deals with one of the topics considered of highest importance in modern Astronomy: the origin of Ultra High Energy Cosmic Rays (UHECR). Since their discovery, 100 years ago, cosmic rays (CR) have been one of the most intriguing mysteries of physics. In fact, neither cosmic ray astrophysical origin, nor the mechanisms responsible for their production, as well as their interaction with the interstellar and intergalactic medium are still fully understood. Furthermore the degree of uncertainty regarding the above mentioned questions increases with energy. In fact, at the most extreme energies ( $E > 10^{20}$  eV or  $\sim 10$  J) just few astrophysical objects can (in principle) accelerate particles up to such macroscopic energies. The puzzle is even more complicated by the extremely low fluxes at such energies implying the need of extremely large exposures for detecting a significant amount of events. This led to the increase in the dimension of the detector arrays and to explore the possibility of building a UHECR observatory in space. JEM-EUSO, the Extreme Universe Space Observatory on board the JEM exposure facility, is the last and most advanced evolution of several UHECR space-based detector concepts. It aims at becoming the pathfinder for a new generation of detectors which will hopefully be able to solve the longstanding questions about UHECR's origin. In this work we will present the results of a simulation study to assess the performances of the JEM-EUSO mission. All the important details of the software ESAF (Euso Simulation Analysis Framework), which has been used for this study, will be presented as well as the work done to improve its algorithms. Not to forget is the presence in the community of alternative ideas, proposed in the course of the years, in order to explain the presence of UHECR as product of non standard physics.

The thesis has been organized as it follows: In the first chapter we resume the present status of cosmic ray science focusing on the most extreme part of the energy spectrum. The questions in the scope of JEM-EUSO are identified and discussed. Essentially we will explain the role which JEM-EUSO

intends to assume in the present research on cosmic rays. Chapter 2 will be related to the detection techniques through the entire CR spectrum. As in the first chapter, we describe more carefully the giant detectors for  $E > 10^{19}$  eV and we go into detail just for JEM–EUSO. Chapter 3 is devoted to the description of the simulation software we used, the models and assumptions we make and the way it has been structured. Chapter 4 focuses on the JEM–EUSO trigger algorithms, whose purpose is to reject the highest amount of background still keeping the real events. In this chapter the performances of such algorithms are extensively assessed. Results on trigger efficiency, data transfer rate, trigger exposure for several species and for different tilting conditions are presented. Chapter 5 is devoted to another major part of our contributions to ESAF, namely to the description of the energy reconstruction algorithms that we developed and implemented. An extensive description of the energy and  $X_{max}$  algorithms is given together with a detailed estimation of the systematics of the algorithm. The statistical error of the parameters is also assessed. In Chapter 6 we instead present the results of the reconstruction studies. Results on the energy,  $X_{max}$  reconstruction are presented and discussed. In the Conclusions we summarize the entire discussion starting from the questions posed in Chapter 1 and confronting them with the results presented in chapter 4 and 6.



# Chapter 1

## Cosmic Ray Science

In the hundredth anniversary of V. Hess flights, CRs science can be still considered a very young field. Although lots of progresses have been made, many of CRs fundamental questions remain still unanswered. The reason of this apparent slow progress is to be searched in the very difficult conditions under which CRs experiments are usually performed. In fact, the limited knowledge on the systematics makes extremely challenging a proper reconstruction of the detected events. Moreover neither the hadronic interaction at very high energy nor the strength and structure of the magnetic fields in the galaxy is known. For these reasons it is not surprising that many of the questions relative to CRs origin and phenomenology remain still open. Where are cosmic rays coming from? Which mechanisms are responsible for their production? Which are the processes involved in their propagation? How are galactic and extragalactic magnetic fields affecting CRs propagation? Can we use CRs as probes to assess galactic and extragalactic magnetic fields structure? Can we use CRs to explore particle physics in an energy range which is by far out of the reach of the present particle accelerators? Is there physics beyond the standard model responsible for this particle's production? Can CRs be used as messengers to observe the universe? Can UHE-Neutrinos be used as well for astronomical purposes? To solve these questions a number of CRs missions have been proposed or recently started operation. All of them aim at a significant increase in the exposure or at minimizing the impact of the systematics through the cross calibration of different techniques in order to improve the quality of the information carried by the events. Worth to mention is also the so called multi-messenger approach which aims at gathering informations on the sources of cosmic rays through other channels like photons or (in the future) neutrinos.

This chapter will therefore present to the reader this fascinating field starting with an historical excursus along the 100 years of CRs history. An

introduction on the phenomenology, the physical nature and on the most evident observational aspects will be given. Some review on the theories about CRs origin will be presented. The list of potential candidate sources and most likely physical production mechanisms will be also explained. However just the most extreme part of the spectrum will be considered in more detail. The special interest in the extreme high energy part of the spectrum will be clearly stressed and the scientific case for space based UHECR detection will be stated. The scientific requirements of a mission for the investigation of the most extreme part of the energy spectrum are also presented.

## 1.1 Historical background

Traditionally CRs science birth is set to coincide with Hess balloon flights in 1912. At that time, shortly after the discovery of radioactivity, the ionizing effects of radiation had been already observed. Electroscopes were known to discharge near radioactive sources as well in absence of sources implying the presence in nature of a background radiation source. Still the origin of this background radiation was thought to be related to geological sources and therefore the discharge rate of an electroscope was expected to decrease with the altitude.

However at the end of the first decade of the twentieth century a series of observations led by Wulf [1] and Pacini [2] casted doubt on the generally accepted theory. Both of them found evidence that the known geological sources were not enough to account for the overall amount of ionizing particles.

The final breakthrough however came with Hess flights campaign of the years 1911–1913 [3]. The Austrian scientist carried electroscopes up to an altitude of about 5000 m in order to measure the radiation rate at different altitudes. He discovered that the amount of radiation after a decrease up to a limited altitude was increasing again with increasing altitude. His results were unexpected given the current accepted theory on the geological origin of natural radiation. In fact radiation should have been attenuated along the path from the ground to the balloon and therefore the rate should have decreased for an increasing altitude. The explanation which Hess gave to this phenomenon was that the radiation was coming from space instead. For this discovery Hess was awarded of the Nobel Prize in 1936. Few years later his results were confirmed by Kolhörster who flew to 9 km height also measuring the same feature as Hess. We report here his results in Fig. 1.1 (right panel) from the book of Longair [4].

However more than 10 years would have been necessary for this evidence

## 1.1. HISTORICAL BACKGROUND



Altitude (km)	$\Delta\text{Ion}$ ( $10^8$ ions/ $m^3$ )
0	0
1	-1.5
2	+1.2
3	+4.2
4	+8.8
5	+16.9
6	+28.7
7	+44.2
8	+61.3
9	+80.4

Figure 1.1: **Left panel:** Hess pioneering flight. **Right panel:** Variation of ionization from Kolhörster flight. Difference from observed ionization and that at the sea level ( $10^8$  ions/ $m^3$ ). Data taken from Longair book [4]

to became widely accepted. Still in the early 1920s a debate was open on the origin of CRs. Robert Millikan, the inventor of the term "Cosmic Ray", was in fact at a first moment still skeptical on the cosmic origin of the background radiation. In some early work he published measurements from unmanned balloon experiments sent up to 15 km, and from mountains peaks, arguing against the Kolhörster findings [5]. In 1925 however, performing measurements on the attenuation of the radiation inside two different mountain lakes, Millikan found the difference of radiation rate to be equal to the attenuation of a water-equivalent of 6 feet [5]. This difference was due exactly to the difference in altitude of the two lakes namely 6700 feet, at that altitude 6 feet in water. This implied that the radiation was in fact coming from a source higher than the highest of the two lakes. Eventually Millikan was forced by experimental evidences to conclude on the extra atmospheric origin of what he called Cosmic Rays<sup>1</sup>.

Another very important step in Cosmic Ray science was made in 1929 by Dmitri Skobeltsyn, who by using a Wilson Chamber [11], managed to take an image of CRs tracks [12]. He immediately associated these tracks with CRs. An example of how his tracks could have looked like is given in Fig.

---

<sup>1</sup>The name "Cosmic Ray" was extrapolated from the fact that the most penetrant radiation known at that time were  $\gamma$ -Rays. CRs were thought to be some very penetrant and energetic form of  $\gamma$ -Rays. The same Millikan believed CRs to be produced in some ultra energetic nuclear process in Space. From these considerations came the conclusion, later proven erroneous, of the electromagnetic nature of cosmic radiation. The name "Cosmic Ray" is therefore originated by a misconception but still entered the scientific language resisting till our days.

1.2 (right panel).

In those years a revolution was happening in particle physics. Till that moment, in fact, radiation measurements in CR science were performed by electrometers and ionization chambers allowing basically an integral measurement of the radiation dose over time. But in summer 1928 Geiger and Müller presented a new device later called Geiger–Müller counter [6], advancement of an older instrument built by Geiger in 1908 [7]. The principle of such a detector is similar to that of a ionization chamber in the sense that the charged particle produces ionization of the noble gas in a tube. The charge is then collected by a potential difference between two electrodes and measured. Changes in the current indicate the passage of charged particles through the tube. The most important innovation of the Geiger–Müller was the ability to count single charged particles. Moreover this detector combined high sensitivity, portability and large volumes. Although incapable of telling anything about type, energy and arrival direction of the particle the Geiger–Müller made possible the beginning of coincidence and timing studies on CRs a very necessary step to determine their nature<sup>2</sup>.

Not surprisingly, also the Geiger–Müller was subject to the so called "high altitude radiation". More in detail it was believed that  $\gamma$ s traversing the detectors were generating secondary electrons in their walls which then triggered the avalanche in the gas chamber. As an attempt to better understand the nature of the cosmic radiation Bothe and Kolhöster initiated a series of experiment based on the coincident trigger of a couple of Geiger counters. After putting the detectors in different positions, exposing them to artificial sources and putting shielding between them they came to the conclusion that the so called "*Altitude radiation*" is:

*"...not  $\gamma$  radiation but rather Corpuscular radiation."*

Also conscious of the potential of this technique, in 1930 B. Rossi presented an improved version of the coincidence electronics invented by Bothe [13]. The great advantage of his circuit design was essentially the possibility of detection of  $n^{th}$ -fold coincidence instead of just two coincidence counts. From one side this allowed both the reduction of chance coincidences and on the other an enormous leap forward in CR science. In fact, much more advanced direction and timing studies were made possible. The same Rossi proposed in that year that due to Earth magnetic field an asymmetry in the arrival direction of charged CRs should have been observed[14]. The observation of the so called east–west asymmetry by L. Alvarez and A. Compton [15] was the final proof of the charged nature of primaries. In their measurements in Mexico City they found an overabundance of CRs coming from the

---

<sup>2</sup>A very good historical review on such a technique can be found in [8] of Bonolis.

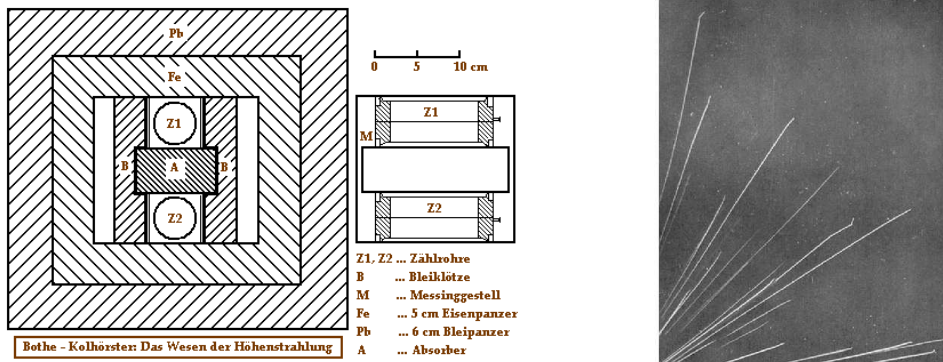


Figure 1.2: **Left panel:** a sketch of the Bothe–Kohörster apparatus. With Z1 and Z2 we can identify the counters and with A the shielding. Taken from Kollhörster and Bothe[10]. **Right panel:** an example of tracks in a cloud chamber. Picture from[11] by C. T. R. Wilson.

west up to 12% indicating the preponderance of positively charged particles.

Another product of the coincidence method was the finding of a lower hardness of secondary particles generated by CRs with atmosphere [16]. The same Rossi in 1931 proved that, contrary to what he expected, the penetrating power of CRs decreases with a higher inclination angle of a shielded coincidence detector. This can be explained just by the presence of a softer secondary component which became more evident at high tilting angles.

The thirties can be with good reasons considered the golden age of particle physics by means of CRs. In those years, just to cite some example, muons, pions, positrons were discovered by studying the interaction of CRs with matter. Of the same years is also the discovery of the pair–production mechanism which confirmed the Dirac theory over antiparticles and gave a powerful tool to explain the large amount of particles observed in the more and more refined detectors developed in those years. In fact H. Bahba, W. Heitler [17] and independently F. Carlson and J. R. Oppenheimer [18] published a new theory on electromagnetic cascades giving a first detailed explanation on the formation of CR generated showers. This model by making use of the quantum theory was moreover able to establish a rough relation between shower size and primary energy. It was however still non capable of explaining the harder and most penetrant part detected in the cascade and able of penetrating enormous thicknesses ( $\sim 1$  m) of lead.

In the same period, on the experimental front, P. Auger managed to measure coincident events over a distance of more than 300 m. In his paper published in 1939 [19] he estimated by multiplying number of detected secondaries and energy of each of them a primary energy of more than  $10^{15}$  eV. Confronting his estimate with the model of Bahba and Heitler he could

find a good agreement knowing the number of radiative units traversed in atmosphere and number of electrons produced.

As we mentioned above, already since 1932 the harder component of CRs showers had been observed. No clear explanation was available for that till 1937 when Anderson and Neddermeyer [20] proposed the existence of a particle much heavier than the electron but of the same charge. This particle was detected in cloud chambers [21] and its decay time was later measured to be of the order of  $\sim 2\mu s$ . However it was erroneously identified with the Yukawa particle and called mesotron. It will be necessary to wait the discovery of the  $\pi$  meson in 1947 [22] in high altitude measurements to identify clearly that the old mesotron was not the one predicted by Yukawa. In fact after this discovery the highly penetrating mesotron was renamed to what we know today as muon ( $\mu$ ) and identified to be a lepton like the electron.

Another very important contribution was made in 1948 by Freier et al. [23]. By sending cloud chambers up to 30000 m on a balloon they could prove the presence of heavy nuclei in the primary spectrum of CR.

At the end of the fifties therefore CR science had made significant improvement on the phenomenological description of CR. It was known the charged particle nature of the primaries, the existence of a electromagnetic, and hadronic component of the showers as well the presence of nuclei in the primary spectrum. Furthermore, models to estimate the energy of those cascades and the detectors to analyze data had been also developed. But still it was totally unknown which was the origin of the high energy of the primaries. A first contribution in that direction came from E. Fermi in 1949 [24] who proposed a new acceleration model based on the interaction of cosmic charged particles with moving irregularities in interstellar magnetic field. According to his theory particles interacting with such clouds of matter and the attached magnetic field have more probability to gain than to lose energy. A more refined version of his theory would have been given years later by Blandford and Ostriker and several other groups independently [25]. In their theory of 1977 they proposed astrophysical shocks as source of magnetic scatterings to enhance the energy of the particle. The highest efficiency of this model and the presence of potential sources candidates made it up to now the most credible of the acceleration mechanisms of CRs.

The decade between 1950 and 1960 saw the introduction of plastic scintillator detectors in CRs field. With a plastic scintillation material surveyed by a photomultiplier was in fact possible to record the arrival of charged particles on the detector with extremely good time resolution. An advantage of these detector was also the proportional signal to the amount of charge entering the detector.

The experimental effort in the fifties was concentrated on reconstructing the properties of the primaries starting from the air shower structure with special attention to the highest part of the spectrum. Very important in this sense are the studies carried out by Rossi in the US and Zatsepin in the USSR at the Agassiz and Pamir detectors respectively. Rossi, developed a technique aiming at the reconstruction of arrival direction and energy of the primary starting from the timing and signal intensity information from an array of plastic scintillators [26]. In this way the spectrum was reconstructed up to very high energies ( $10^{18}$  eV) and the direction of arrival could be determined to be isotropic. This technique would have been used later in the sixties for the construction of the Volcano Ranch array, a very large extension scintillator array, where for the first time particles with an energy of  $10^{20}$  eV were detected by J. Linsley [27][28]. A picture of a single detector element can be seen in Fig. 1.3 (left panel) together with J. Linsley at work.

The fifties saw also the onset of space exploration. In fact the launch of the Sputnik satellite in 1957 started a race between USA and USSR for the supremacy in this field. Cosmic Ray science benefited greatly from this effort since a new window could be opened to the experimenter of that time: the direct measurement of CRs at the top of the atmosphere. In fact in 1959 the Luna 2 satellite could for the first time perform a space based measurement of charged particle in space by using a ion trap [29].

Continuing our excursus in the sixties, the introduction of another very important technique must be mentioned: the air fluorescence technique. This method, proposed independently by Chudakov [30], Greisen [31] and others, was put in practice by the same Greisen from 1965 at Cornell University. However neither himself nor anyone else would have been able to measure fluorescence signal till end of the seventies when this task was accomplished by Mason et al. [32]. A very detailed study can be found in the PhD thesis of Bunner [33]. In this kind of detectors, the basic principle consists to detect the emitted UV fluorescence light generated by extended air showers in atmosphere. This method allows finally to follow directly the entire longitudinal development of the shower through the atmosphere. Such a kind of detector is structured usually like an array of wide angle UV telescopes monitoring the sky during clear dark nights. An example of a single element taken from [33] can be seen in Fig. 1.3 (right panel).

From the theoretical point of view of very great importance is the theoretical prediction made in 1967 by Greisen[34], Zatsepin and Kuzmin about the interaction of CRs with the CMB. According to their studies CRs with energies higher than  $3-4 \cdot 10^{19}$  eV should have a limited propagation length in space due to their interaction with the CMB.

Always in 1967 the Haverah Park array started operation and it would

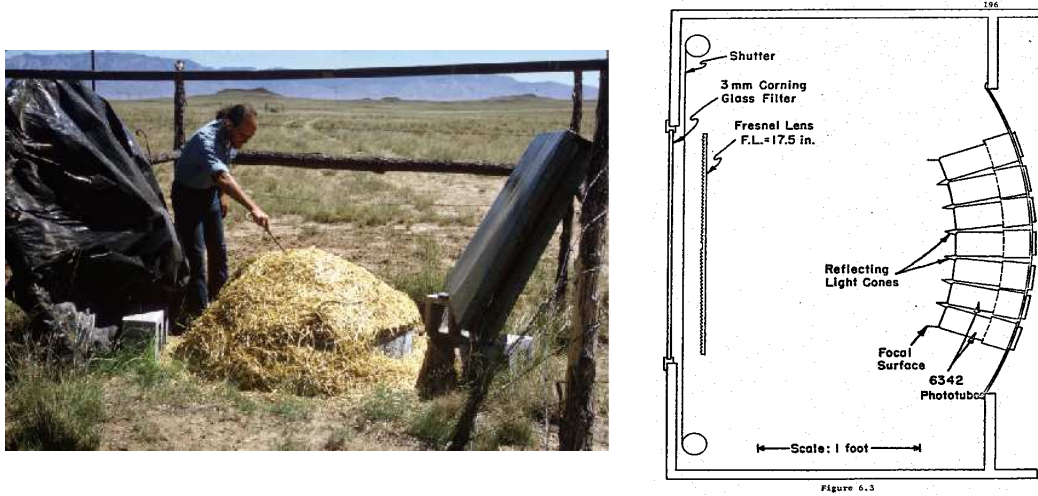


Figure 1.3: **Left panel:** a picture of J.Linsley at work in the Volcano Ranch array <http://www.auger.org/>. **Right panel:** single element of a UV multiple air fluorescence telescope. Taken from Bunner's work [33].

remain in operation till 1987 detecting several CRs over  $10^{20}$  eV [41]. This innovative technique aims at the detection of Cherenkov induced by secondaries in water tanks through photomultipliers and would be used later thanks to the low cost of the detector material (namely water) in the construction of extremely large arrays.

After the first detection of air shower fluorescence in 1977, the technique was soon applied on large scale. In 1981 became operative the Fly's Eye detector [42]. It consisted of several UV telescopes monitoring the sky. The detector was updated in 1986 to a stereoscopic configuration allowing a much better spatial resolution of air shower events. Worth to mention is the fact that thanks to this detector in 1991 the highest energy particle ever recorded was detected. The particle with an enormous energy of  $3.1 \cdot 10^{20}$  eV, recorded by Fly's Eye on the night of October 15, was later named the: "Oh my god Particle" [43]. This experiment took data till 1993 where it was replaced by the HiRes Fly's Eye, an improved version of the Fly's Eye [44]. This experiment could rely on larger mirrors and finer pixels allowing a higher exposure, lower threshold and better event reconstruction.

Another historically extremely important detector is the AGASA detector which started operation in 1990 [45]. The plastic scintillators array was deployed over a surface of over  $100 \text{ km}^2$  in Yamanashi prefecture, Japan in order to study the most extreme part of the CRs spectrum.



Fundamental to understand the future developments is the debate originated by a discrepancy between AGASA and HiRes over the presence of the GZK cutoff. This fact had, as side effect in the following developments, to bring ground detectors toward a more and more integrated detection technique. Following this concept the Pierre Auger observatory was developed in Argentina and started operation in 2005 [46]. It is the currently largest detector array ever built reaching over 3000 km<sup>2</sup>. It merges on the same location fluorescence detectors and water Cherenkov particle detectors on ground. The discrepancy was then solved with the introduction of a systematic in the energy scale between the two techniques.

At the present time due to the power law decline in the spectrum a general tendency toward larger and larger detectors for the most extreme part of the spectrum can be observed. Furthermore a general tendency of merging different techniques by integrating several detector concepts on the same site to reduce systematics is presently ongoing. For that reason fluorescence detectors, water Cherenkov tanks, radio detectors deep muon detectors and many more have been integrated and are now taking data.

Nowadays the increasing size of the ground array is clearly approaching the limit. The proposed, but never funded, Auger North Array was supposed to have an extension of 21000 km<sup>2</sup>. To increase further the size is clearly impossible since the surface would be of the same order of a middle size nation.

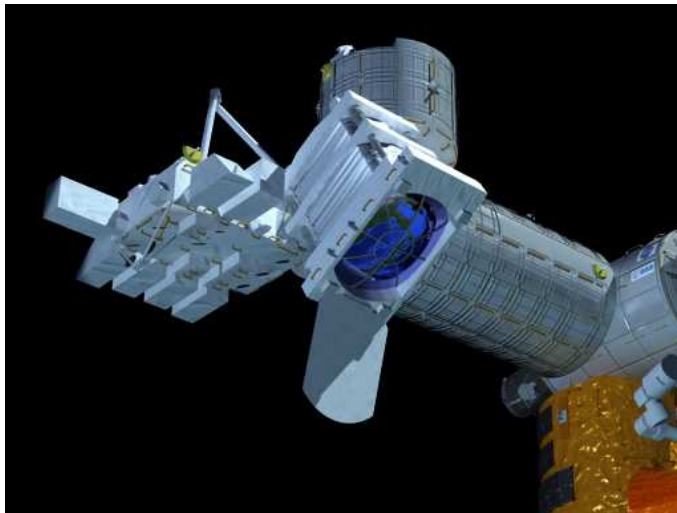


Figure 1.4: Artistic representation of the JEM-EUSO telescope.

An attracting opportunity comes from a technique proposed in 1981 by

J. Linsley [48]. This technique aims at the detection of fluorescence light from CRs showers from a space based detector. Basically a UV telescope monitoring the atmosphere from above will detect the light emitted by air showers exactly as already done today by fluorescence detectors on ground. In this way the spatial limitation is removed by simply monitoring from space a huge amount of atmosphere. Several experiments have been proposed in the course of the years but the most advanced mission currently ongoing is the JEM–EUSO mission [49]. The telescope is planned to fly in 2017 on-board the JEM exposure facility of the ISS. It aims at the far most extreme part of the spectrum above  $10^{20}$  eV.

## 1.2 Phenomenology of Cosmic Rays

CRs are highly energetic particles propagating through space. As can be seen in Fig. 1.5 by Swordy [50], their spectrum spans through many orders of magnitude both in energy and in flux. CRs start from energies of  $10^8$  eV or even lower and continue with a power-law distribution till over  $10^{20}$  eV. At energies of  $\sim 10^9$  eV fluxes of the order of hundreds or thousands of particles per  $\text{m}^2$  per second can be measured. On the other extreme of the spectrum over,  $10^{20}$  eV, measured fluxes are of the order of less than one particle per square kilometer per millennium. Between  $10^8$  and  $10^{10}$  eV their composition is the one shown in Tab. 1.1 (from [4]).

Particle type	Percentage
Protons	86%
Alpha particles	11%
Electrons	2%
Heavier elements	1%

Table 1.1: Cosmic Ray population composition at the top of the atmosphere in the energy range from  $10^8$  to  $10^{10}$  eV. Data taken from Longair book[4].

Starting from the lowest part of the spectrum few distinctive features can be observed. At first the spectrum tends to decline toward lower energies. This is caused by the solar activity. In fact solar wind and solar magnetic fields can shield particles incoming from out of the solar system. This effect is explained by the fact that lower energy particles have lower magnetic rigidity.

At even lower energies ( $\sim 50$  MeV, which cannot be seen in Fig. 1.5) the spectrum tends to recover. This component is called anomalous CRs and is due to the interaction of solar wind with the interstellar medium and is

believed to be generated at the edge of the solar system in the termination shock between solar wind and interstellar matter (see Fisk [51]).

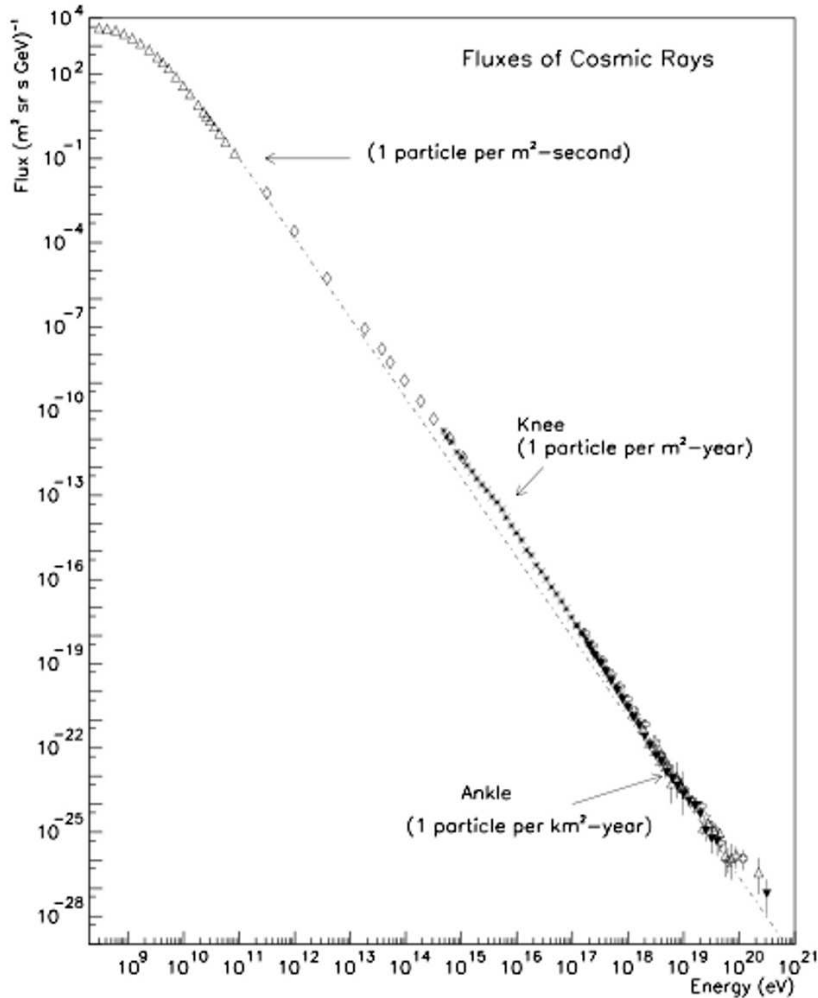


Figure 1.5: Cosmic Ray Spectrum as published by Swordy in 2001 [50]

Furthermore, at energies below  $10^{10}$  eV, the spectrum exhibits time dependent features which are anti-correlated with the solar cycle. Obviously a stronger solar activity prevents more and more extra-solar particles from reaching Earth. This effect, the so called solar modulation, makes possible a different shape of the spectrum depending on the Sun's cycle for low energy particles (see Longair [4] and Stanev [52] books).

However CRs with an increasing primary energy start to be undisturbed

by Sun's activity. Above some GeV in fact the spectrum assumes a power-law decline which remains rather uniform till  $\sim 10^{15}$  eV. The steepness of the spectrum, which can be expressed by the index of the power law, is (in this region) approximately 2.7.

Around  $10^{15}$  eV a feature traditionally called the knee represents a transition toward a softer spectrum. Therefore above the knee the spectrum assumes a steeper profile with an index approximately around 3. Discovered for the first time in 1958 by Kulikov and Khristiansen [53], it has been associated for the first time with a magnetic rigidity cutoff in the source in 1961 by Peters [54]. In Hörandel's work [55] a review of the most important proposed models for the Knee has been given. The author here identifies four great families of theories for explaining this feature: a loss in the production efficiency of protons, leakage of CRs from our galaxy, interaction of CRs with interstellar medium or a drastic change of interaction properties between CRs and atmosphere around  $10^{15}$  eV. At the moment however the most widely accepted theories belong to the first two families who explain this feature with the increase in magnetic rigidity of CRs. In this view, the limiting factor would be the capability of either the source or the galaxy to contain the particles. Several studies have related this feature with the lightest component of the CRs spectrum.

This steepness is observed till an energy of about  $10^{17}$  eV after that spectrum softens again to reach an index of 3.2 or 3.3. The feature is called The second knee and has been observed in several experiments like the Akeno [56], Fly's Eye [57] and Haverah Park detectors [58]. There is up to now no clear explanation for this feature. A possible explanation has associated it with a loss of efficiency of acceleration mechanisms of heavier nuclei. In analogy with what happens for the first knee this kink in the spectrum is related to the magnetic rigidity of heavier nuclei. Recently Cascade Grande [59] claimed the first possible detection of a knee in a separate analysis on CRs heavier component. This if confirmed would strengthen the association of the second knee with heavy nuclei magnetic rigidity.

Around  $4 \cdot 10^{18}$  eV then, the spectrum hardens considerably taking an index of 2.7–2.8. The first observation of this feature was made in 1963 by J. Linsley [60]. Several theories have been developed to explain this feature. Traditionally the ankle is viewed as the onset of the extragalactic CRs spectrum since galactic CR couldn't be confined in the galaxy at such energies and since no clustering toward the galactic plane has been observed. A common problem related to these models is the gap between the maximum energy achievable by galactic sources and the onset of extragalactic flux.

To overcome this problem several models have been developed all aiming at the extension of Galactic sources range up to higher energies. Between

them we cite Hillas [61], Hörandel [62], Wibig and Wolfendale [63].

Recently some possible explanation associated the presence of this flattening with the interaction of CRs with CMB through pair-production has been proposed by Berezhinsky [65]. Under this interpretation the extragalactic flux would be starting already at the second knee. A great advantage of this model is to allow a little bit more relaxed requirements on the galactic sources although postulating some almost proton-pure extragalactic component.

Also to mention is another model proposed by Globus et al. [64] which fits the observed spectrum by assuming a mixed composition for extragalactic sources and propagation effects to explain all the relevant features above  $10^{17}$  eV. In this view the original source composition and spectrum would be changed along the propagation to the Earth allowing a good fit with the observations.

More generally the problem of where does the galactic to extragalactic transition takes place remains still object of debate. However there is a general consensus on the fact that this transition most likely happens between  $10^{17}$ – $10^{18}$  eV.

At energies  $\sim 2$ – $3 \cdot 10^{19}$  eV, then, a sharp cutoff seems to be observable. Detected by the Pierre Auger observatory [144] and HiRes [67] arrays there seem to be convergence toward the confirmation of this feature. Both measurements see good agreement within 20% systematic uncertainty. However, it is still not clear whether this drop is due to the already mentioned GZK effect or to an intrinsic loss in the production mechanisms efficiency.

A possible explanation avoiding the effect of the GZK effect sees this flux collapse as a rigidity dependent cutoff as explained by Aloisio [68] [146]. In this view the cutoff observed at  $2$ – $3 \cdot 10^{19}$  eV is associated with the loss of containment of heavy nuclei in the acceleration sites. This model developed to match the Auger spectrum and composition results has some "disappointing" consequences for CRs science like the guaranteed end of the spectrum, the absence of Cosmogenic Neutrinos and the increased difficulty in identifying sources.

A very important feature of CRs is the isotropy in arrival direction at least till energies  $E \sim 5 \cdot 10^{19}$  eV. This energy dependent feature is due to the presence of galactic and extragalactic magnetic fields along the propagation path of CRs and to the higher magnetic rigidity of the particles at the extreme of the spectrum. Therefore if present at all this anisotropy would be confined just at the very end of the spectrum. However, even at the highest energies no clear agreement has been found yet on whether an anisotropy is present or not. For more informations Auger [69] and Telescope Array [70] works should be read.

To conclude our review it is necessary to talk about CRs composition.

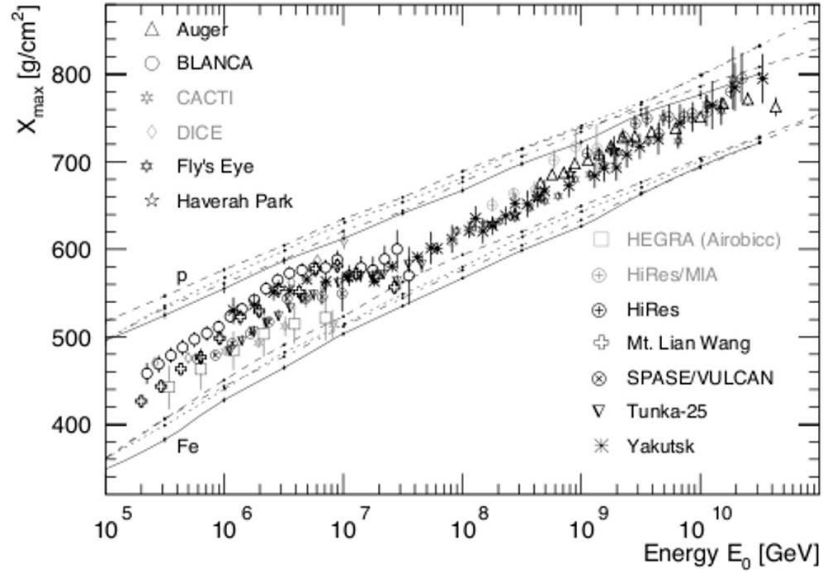


Figure 1.6: A review taken from Blümer [71] plotting the average slant depth at maximum from different experiments as a function of primary energy. This parameter is used as an estimator for the average primary composition. We see plotted together with the experimental data also the model corresponding to proton (higher line) and iron (lower line).

Essentially can be said that the composition till the knee ( $10^{15}$  eV) is more or less compatible with the one shown in Tab. 1.1. A predominance of protons is almost constant through the lowest part of the spectrum and reflects the composition of the environments where CRs are thought to be accelerated. In this energy range direct measurements can be performed directly in space allowing a much more reliable measurement.

The first big change happens immediately after the knee as can be seen in Fig. 1.6. In this plot taken from Blümer's work [71] the average slant depth of the maximum ( $\langle X_{max} \rangle$ ) of an Air Shower population is plotted as function of energy. Since over  $10^{14}$ – $10^{15}$  eV direct measurements are not possible anymore the  $\langle X_{max} \rangle$  parameter is used as an estimator of the average primary mass (see Sect. 2.1). Plotted together with the experimental data from different detectors are also various theoretical models. As can be seen, the highest curve represents proton rich while the lower iron rich composi-

tions. What can be clearly observed is that in the region immediately after the knee data tend to drift toward Iron parameterizations. As can be seen in Fig. 1.6 this trend toward higher mass has been observed by many CRs air Cherenkov detectors.<sup>3</sup> We cite among them Yakutsk [72] [73] BLANCA [75] and Tunka [77]. Moreover also experiments which in principle cannot directly access to the longitudinal development could confirm by other means the higher mass of the populations. One example is Kascade which by modeling the muon fraction of the showers, divided the detected population in two families according to the muon to electron ratio. The first sub-population is associated to light component and has less muons, the second is more muon rich and is associated to a higher mass. In [78] the Kascade collaboration could observe a kink in the spectrum of the light component above the knee. Such a feature could not be observed in the heavy component at that energy implying an increase of the average mass.

This feature can be explained if we consider the knee as a rigidity dependent feature associated with acceleration of hydrogen in the sources. Since heavier elements have a lower magnetic rigidity they can be accelerated toward higher energies in the same environment as hydrogen. For that reason in the interval between the knees the composition gets heavier.

This trend seems to be reversed around  $10^{17}$  eV where the spectrum starts getting lighter again as seen by the Fly's Eye and HiRes collaborations [79] [80]. However, although some agreement has been found about the first decade in energy ( $10^{17} - 10^{18}$  eV) for the most extreme energies the composition still remains an unsolved problem. In fact the Pierre Auger collaboration [81] claims the detection of a progressively heavier composition starting from  $10^{18}$  eV while HiRes [80] and Telescope Array [82] do not confirm this trend showing instead a very light composition till the most extreme energies.

One additional remark has to be however done regarding composition studies at such energies. Since the hadronic interaction models at these energies are not known but rather extrapolated from lower energies an additional source of uncertainty should be taken into account making the overall picture even more complicated.

To conclude, while for the part of the spectrum under  $\sim 10^{17}$ – $10^{18}$  eV there seem to be some kind of convergence toward a general model, no satisfactory explanation for the highest part of the spectrum has been delivered yet. Models attempting to describe observed spectra, compositions and arrival distributions are very often in contrast between each other. Questions

---

<sup>3</sup>In these detectors the information of the Cherenkov timing can be used to reconstruct the longitudinal profile of the shower. In [74] [76] an overview of respectively the Yakutsk and BLANCA instruments is given.

like where does the extragalactic component starts, which mechanisms are responsible for CRs acceleration to the highest energies, which sources are active, whether GZK is present or not and many other remain unanswered.

### 1.3 Theories on the origin

The first consideration that can be done about CRs origin is about the total amount of energy contained in our galaxy. From that argument comes the first hint of a possible relation between CRs and supernovae. By considering the the mean CRs energy density contained in the Milky Way to be approximately equal to  $0.5 \text{ eV/cm}^3$  and the total volume of the galaxy to be  $\sim 10^{67} \text{ cm}^3$  the total amount of energy contained in it can be estimated. As calculated in [52] by Stanev, knowing also the leakage time  $\sim 10^7 \text{ years}^4$ , the total necessary power to replace the leaking cosmic rays can be estimated to be of the order of

$$L_{CR} \sim 3 \cdot 10^{40} \text{ erg/s} \quad (1.1)$$

This can be compared with the estimated power of a supernova namely  $\sim 10^{42} \text{ erg/s}$ . Even one single SNR can therefore provide nearly 100 times more energy than needed for sustaining CRs flux. Obviously this argument becomes even more convincing by adding several SNR within the Milky Way as is reasonable to expect. Thus, even a relatively low efficiency acceleration process could justify the measured energy densities.

This is by far not enough to accept SNRs as CRs sources but it is at least a necessary condition before starting any discussion about the production mechanisms and the potential sources.

#### 1.3.1 The second order Fermi mechanism

As already mentioned in the previous sections, in 1949 Fermi proposed a new mechanism for explaining the acceleration of CRs [24]. In his view charged particles can gain energy through multiple encounters with moving interstellar clouds. Following the principles of magnetohydrodynamics, who had been formulated in the preceeding years, Fermi could postulate a moving plasma cloud carrying with it turbulent and unstable magnetic fields. The charged particles after the encounter with these instabilities would be scattered randomly several times. To roughly understand the principles of this models,

---

<sup>4</sup>The containment time is calculated with aid of elemental ratios in CRs and atomic clocks. In fact Spallation is responsible for changing the ratios between different elements in a way which is proportional to the amount of matter traversed or in other terms to the flight time. See Longair book [4] for a first introduction to the topic.



as done in Stanev's book[52], let's consider the energy of the particle in the cloud reference system to be equal to:

$$E_0^* = \gamma_{cl}(E_0 + \beta_{cl}p_0) \quad (1.2)$$

whereas  $E_0$  and  $p_0$  are the energy and momentum of a ultra-relativistic particle and  $\gamma_{cl}$  and  $\beta_{cl}$  are the known relativistic  $\gamma$  and  $\beta$  factors of the cloud motion. In the system of the cloud the scattering is perfectly elastic i.e. the particle doesn't gain neither energy nor momentum. However after a certain amount of scatterings in the cloud the particle will eventually leave it. The energy of the particle as it leaves the cloud, supposed it will leave in the opposite direction as it entered, is:

$$E_1 = \gamma_{cl}(E_0^* + \beta_{cl}p_0^*) = E_0\gamma_{cl}^2(1 + \beta_{cl})^2 \quad (1.3)$$

where  $p_0^*$  is the momentum in the reference system of the cloud. Now, the energy fraction the particle gained is equal to:

$$\frac{\Delta E}{E} = \frac{E_1 - E_0}{E_0} = \gamma_{cl}^2(1 + \beta_{cl})^2 - 1 \equiv \xi \quad (1.4)$$

For extending this study to a more general case in which both entrance and exit angle are varying, an average over different angles is necessary. Once this is done the factor  $\xi$  assumes a form

$$\xi \sim \beta_{cl}^2 \quad (1.5)$$

We see here that the gain in energy for each encounter  $\xi$  is proportional to the square of  $\beta_{cl}$ . From this consideration comes the name "second order Fermi mechanism". The basic idea of Fermi was that thanks to multiple impacts of this kind a particle can in principle manage to gain enormous energies.

This model would be working just if several clouds are in a relatively compact region of space. By considerations on the total amount of encounters necessary to reach a certain energy and on the probability of escaping the region where all the clouds are concentrated we can calculate the form of the spectrum to be:

$$N(> E_n) \sim \left(\frac{E_n}{E_0}\right)^{-\frac{P_{esc}}{\xi}} \quad (1.6)$$

whereas  $E_n$  is the energy reached after n encounters,  $E_0$  the initial energy,  $P_{esc}$  the probability of the particle to escape the acceleration region and  $\xi$  the average energy gain per encounter. It can be clearly seen that the spectrum would be of the desired power law shape.

Despite that, more careful calculations on the efficiency of the model, the required times and the steepness of the resulting spectrum prove the model to be not adequate. In fact, the very small  $\beta_{cl}^2$  factor ( $10^{-7}$ ) and the huge distance between clouds in interstellar matter make the process extremely slow. This makes extremely difficult to justify the observed CR densities and spectra. As a result, the second order Fermi mechanism can be used as a good basis for further more refined modelizations but is not applicable to more realistic astrophysical situations.

### 1.3.2 The first order Fermi mechanism

Shocks are a very common phenomena in astrophysics. They represent a very sharp transition in temperature, pressure and velocity of a gas. They can be usually observed in contexts where a fast plasma interacts with interplanetary or interstellar gas having lower speed of sound compared to the plasma itself. This causes the slow gas not to be able to react to the fast plasma in a standard way since the "information" in the gas cannot travel faster than sound. In this situation therefore a sharp transition occurs. Examples can be found in the solar system between the transition from solar wind dominated and interstellar regions, in supernovae and at the boundaries between relativistic jets and intergalactic medium. A first introduction on the physics of shocks can be found in Longair [4] and Schlickeiser books [83].

More in detail, shocks form in supernovae because of the very high expansion speeds of the ejecta ( $\sim 5000\text{km/s}$ ). The interaction with the interstellar medium causes the formation of a shock which proceeds the ejecta with a velocity larger than the ejecta themselves. From fluidodynamical calculations the speed of the shock can be set to be equal to  $\frac{4}{3}v_r$  whereas  $v_r$  is the speed of the SN ejecta.

The basic idea is very similar to the one presented in the previous section. A charged particle in the ISM will "see" the shocked material approaching with a velocity  $v_r - v_{ISM}$  (being  $v_{ISM}$  the speed of interstellar medium). After crossing the shock the particle will interact with the magnetic turbulences in the shocked material and will be scattered randomly. Seen in the reference system of the shocked material those scattering are perfectly elastic as in the case of second order mechanism. After a certain amount of scatterings the particle will thermalize with the shocked material. When the particle crosses again the shock in the opposite direction it will therefore "see" the unshocked material as approaching with an opposite speed  $-v_r + v_{ISM}$ .

The substantial difference of the shock model with the magnetized cloud model lies essentially in the geometry of the encounters between particle and magnetized material. In the first case the particle will always "see" the

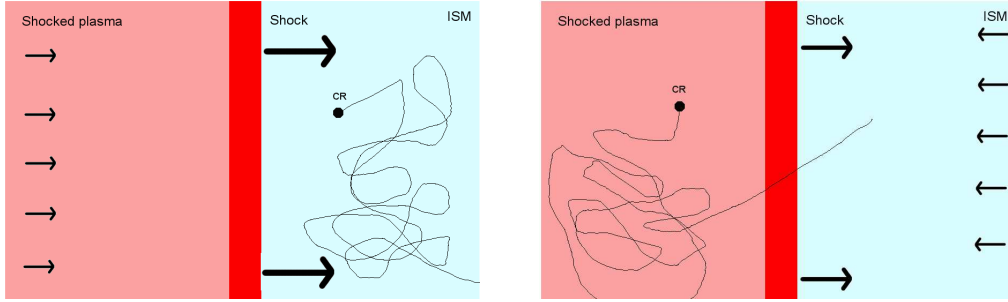


Figure 1.7: A representation of the first order Fermi mechanism. **In the Left panel** the situation before the first crossing is depicted. The CR "sees" the ejecta as approaching with a certain speed since it can be considered on average as bound to the ISM. However in the **right panel** the particle, after a certain amount of scatterings, "sees" the ISM as approaching. Here after many elastic scatterings the particle can be considered bound with the ejecta. After the particle goes back to the ISM its energy will result to be enhanced by a small amount.

other side of the shock as approaching and therefore the impact will always be head-on. In the case of the cloud, on the other hand, the particle by entering and exiting the magnetized plasma can both gain or lose energy depending on the outgoing direction. This makes possible the increase of the particle energy on every crossing of the Shock. Moreover the high speed of the ejecta and the relative compactness of the system makes the process extremely efficient. After some calculations taking also into account the direction distribution of the particles, the energy gain for each encounter can be assumed to be of the order of

$$\xi \sim \frac{4}{3}\beta_S \quad (1.7)$$

whereas  $\beta_S$  is the  $\beta$  relativistic factor for the relative speed of ejecta and ISM ( $v_r - v_{ISM}$ ). We see here the dependence of the energy gain from  $\beta_S$  factor. As can be easily imagined, from this fact derives the name "first order Fermi mechanism". This dependence on  $\beta_S$  is therefore the deciding factor for the higher efficiency of this mechanism compared to the second order mechanism.

### 1.3.3 Supernova remnants as sources

Knowing the basic acceleration mechanism is however of no use if no credible sources theory is developed. The first step toward the source identification would be to check if at least the model developed in Sect. 1.3.2 can account for the observed spectra and maximum energies.

As in Sect. 1.3.1 from considerations on the escape probability and on the gain for each single encounter, the spectral shape can be calculated at least

approximately. As in the second order mechanism the spectrum is without any doubt also power law like. However the fundamental difference with the previous section is the fact that in SN shocks the produced spectrum can be much harder thanks to the higher efficiency of this mechanism. Calculations for strong shocks bring in fact to spectral index of the order of  $\sim 1-2$ . To match the exact form of the spectrum is not a trivial task, but this result allows already a certain room to tune the parameters in order to reproduce all the relevant spectral features. More detailed calculations can be found in the book of Greisen [84].

Another point in favor of the Fermi theory is the maximum energy achievable by this model. A first estimate of the maximum energy can be given by considering the energy increase in time to be proportional to the energy gain  $\xi$ , to the energy to be reached  $E$  and to the inverse of the interaction time  $T_C$ .

$$\frac{dE}{dt} \sim \frac{\xi E}{T_C} \quad (1.8)$$

As shown in [84], after some consideration on the diffusion of the high energy particles in the ionized medium, a limit on the highest reachable energy can be set to be:

$$E_{max} \leq \frac{3}{20} \frac{u_1}{c} ZeB(u_1 T_A) \quad (1.9)$$

Whereas  $u_1$  is the speed of the shock,  $Z$  the atomic number of the particle,  $B$  the magnetic field and  $T_A$  the lifetime of the accelerator. It can be seen from Eq. 1.9, how heavier elements can achieve higher energies. This is somehow not surprising since the higher the charge, the lower the magnetic rigidity and the lower the interaction time  $T_C$  is. Also to mention is the dependence of the energy from the speed of the shock: a faster shock can give a higher energy. Another limiting factor for the maximum energy is the life-time of the accelerator. In fact, it has been shown that the acceleration process is continued till the shock has swept up a mass equal to the mass of the ejecta. Therefore modeling the average amount of mass in the remnant and the velocity of the remnant-shock, the life time of the accelerator can be estimated to be of the order of  $10^3$  years. Therefore, assigning to the mass of the remnant a value of  $10 M_{\odot}$  and  $u_1 = 10^9$  cm/s as done in [83] brings to a maximum energy estimate of the order of:

$$E_{max} = 2.4 \cdot Z \cdot 10^5 GeV \sim 10^{14} - 10^{15} eV^{(Protons)} \quad (1.10)$$

This is clearly a further argument to justify the choice of SNRs as sources even just for a part of the spectrum. Till the knee in fact the first order Fermi mechanism in SNRs can serve for a valid accelerator theory.

Recently a lot of effort on the source identification has been put to study potential CR sources through other messengers. In fact, Drury et al. [85] proposed in 1994 to look for  $\gamma$ -ray emission in SNRs as a proof of acceleration. In their view, hadrons up to  $10^{15}$  eV would be interacting with local matter generating  $\pi^0$  particles which by decaying should on their own generate a detectable  $\gamma$ -ray flux between 100 MeV and the TeV. Recently such a signature might have been found by the Fermi-LAT collaboration [86] confirming previous results from the HESS and MAGIC collaborations. The inverse Compton scenario seems not to be a valid option anymore.<sup>5</sup>

To conclude, we have to stress that for higher energies SNRs are not capable of containing CRs any more. Moreover, limits on the lifetime of the accelerator put other strong constraints on the maximum energy. We also saw how the acceleration theory allows CR protons from SNRs to reach at maximum  $10^{15}$  eV. On top of that, protons of higher energies cannot even be contained in the galaxy. It is clear that sources of higher energy CRs have to be searched somewhere else than in SNRs and most likely outside of the Milky Way.

### 1.3.4 Toward higher energies

As it has been said in the previous section, the most obvious problem for the acceleration processes involving SNRs is related to the capability of those accelerators to confine particles of increasing energy. As a result of that,  $10^{15}$  eV for protons and probably  $10^{17}$  eV for heavier elements represent a limit for SNRs. For that reason, in extending the existing models to higher energy the first thing which can be done is to make a review of all the known astronomical objects to check if at least the minimum requirement of confinement is satisfied. Intuitively an accelerator can work till the gyroradius of a particle is smaller than the size of the accelerator itself. This idea has been proposed by Hillas in 1984 [87].

Similarly to what has been shown previously for SNR (see Eq. 1.9), the confinement capability of a source can be used to give an estimate of the maximum energy achievable (see Letessier-Selvon and Stanev [89])

$$E_{max} = \beta Z e \frac{B}{\mu G} \frac{R}{kpc} [EeV] \quad (1.11)$$

whereas  $Z$  is the atomic number,  $B$  the magnetic field,  $R$  the size of the accelerator and  $\beta$  the velocity of the shock or the efficiency of the accelerator.

---

<sup>5</sup>In this alternative view seed photons produced from synchrotron emission (X-ray) of accelerated electrons would be scattered by the same population of electrons to reach high energy ( $\gamma$ -ray).

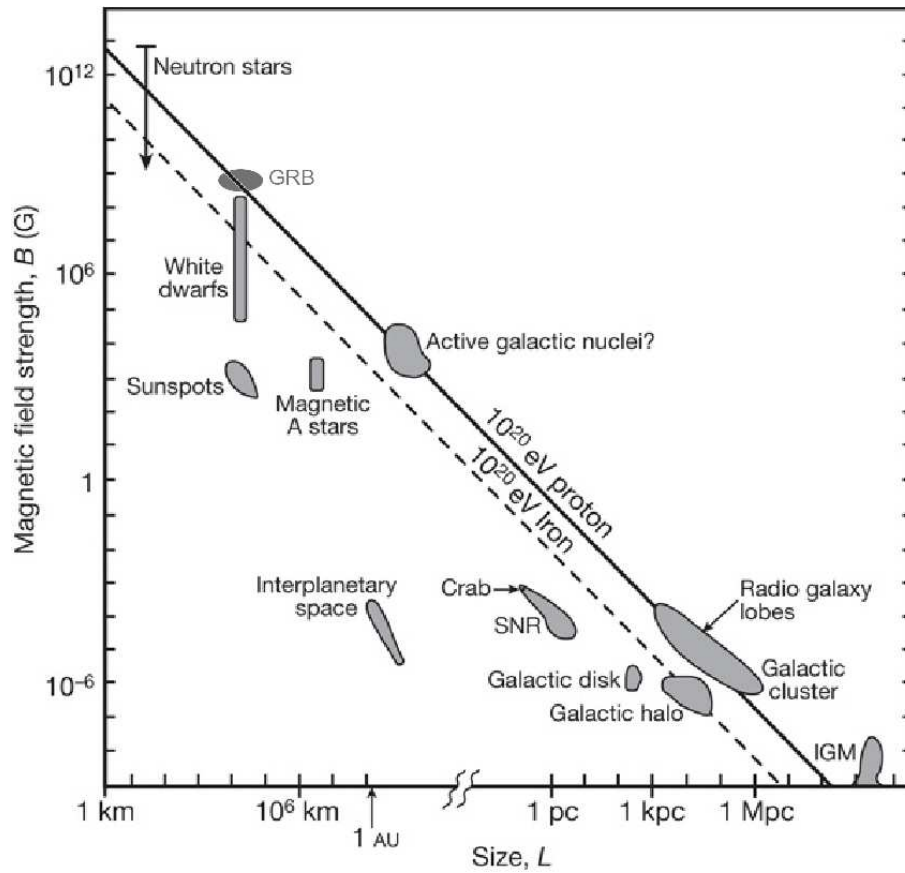


Figure 1.8: Hillas plot taken from Bauleo's work [88]. A review of the sources according to the magnetic field strength and size of the accelerator is plotted. GRBs sources have been added by the author of this thesis.

By choosing a certain value of energy and of atomic number, is therefore possible to define a region on the  $L$ - $B$  plane which represents the combination of size and magnetic field strength to achieve this energy. We can see in Fig. 1.8 two lines: one for protons and the other for iron. As can be seen iron allows a little bit more relaxed requirements. All the astronomical objects can be added to the plot according to previous knowledge. In order for an object to assume status of potential candidate for  $10^{20}$  eV CR it must lie on the upper-right part side of the curves. If this criterion fails it becomes much more difficult to build an acceleration theory based on a particular object. As it clearly appears from the plot most astronomical objects do not manage to satisfy the basic condition for  $10^{20}$  eV containment. The only sources which could be of potential interest are therefore: neutron stars (or

even better magnetars), GRB, AGN or possibly their jets and intergalactic shocks in galaxy clusters.

This picture however, does not take into account neither energy losses of the particles nor the finite lifetime of the source. In fact as shown in [90] by Kotera and Olinto, in order to be able to accelerate particles to such energies acceleration has to prevail over energy loss, and the source has to remain effective for long enough time. More generally, can be said that the acceleration time  $t_{acc}$  must be shorter than  $t_{esc}$ , the escape time,  $t_{loss}$  the characteristic energy loss time and  $t_{age}$  the life time of the accelerator.<sup>6</sup>

Another essential point to verify, in order to build a valid accelerator theory, is the emitted luminosity of the source. In one word it has also to be evaluated whether or not the population of candidate sources is able of maintaining the CR energy density observed at Earth. The emitted power per unit volume has been estimated to be of the order of  $\sim 10^{44}-10^{45}$  erg  $\cdot$  Mpc $^{-3}$   $\cdot$  yr $^{-1}$  above  $10^{19}$  eV as calculated by Waxman [91].

Keeping in mind all the previous considerations a review of the most popular UHECR accelerator candidates will be given in the following part of this section.

**Gravitational accretion shocks.** On the Hillas plot the most extended sources to be considered are shocks in extragalactic medium and in galaxy clusters. It is widely believed that smaller cosmological structures are forming at earlier times. As the universe evolves then, a process of mergers and accretion drives to the formation of larger and larger structures as explained by Press and Scheckter [92]. By modeling the cosmic evolution, it is possible to give an estimate of the number of mergers at each time in the history of the universe. Furthermore thanks to cosmological studies it is also possible to give an estimate of the parameters of mergers. The relative speed and the density of the clusters are fundamental parameters to understand the extension and strength of the shocks (Gabici and Blasi [93]) which are believed to form in this merger process. Such shocks, having an extension up to  $\sim 10$  Mpc have been taken into consideration as potential stochastic accelerators. More in detail, thanks to first order Fermi acceleration particles could be accelerated in these environments as suggested by Kang et al. in 1996 [94] and 1997 [95]. In fact, as explained in these studies, the presence of those accelerators could in principle account for the observed spectrum at least till

---

<sup>6</sup>The escape time is a factor quantifying the time needed for the particle to leave the accelerator. It is function of the size of the accelerator  $L$  and of the inverse of the diffusion coefficient  $D$ . It takes into account not just the size of the object but also the structure and turbulence features of the magnetic field. The parameter  $t_{loss}$  expresses basically the typical time scale of energy loss through synchrotron and pion production.

the GZK cutoff provided a sufficient magnetic fields strength.

However, one of the most evident problems of this model is the extreme size of the accelerator. In this context particles would be suffering from pair-production and photo-pion production with CMB. This will severely limit the maximum energy achievable by those accelerators. The second main problem lies in the very low magnetic field present in the intergalactic medium which causes extremely long acceleration times.

We can cite as an example the calculation of Vannoni et al. [97] who, assuming a realistic shock speed of  $\sim 1000$  km/s and magnetic fields of the order of  $\mu$  G, estimated the highest energy achievable by these accelerator to be few times to  $10^{19}$  eV. The integrated CR spectrum obtained in this study foresee a cutoff starting from  $\sim 5 \cdot 10^{18}$  eV. Furthermore a clear bump is observed at  $\sim 10^{18}$  eV. This is due to a pile-up effect of secondary particles from higher energy interaction and to the relatively unaffected spectrum at lower energies. Worth to note is also that those calculations have been performed on very long times  $\sim 10^{10}$  years taking into account the modeled merger history of the cluster. This is another effect of the extreme sizes of these accelerators: the acceleration times have to be considered of the order of the cluster lives.

Also here the multi-messenger approach is an important element in the study of the acceleration. The observation of a tenuous non-thermal emission in clusters, gave strong hints of the presence of an electron acceleration in these environments. In fact, radio (Feretti [98]) and X-ray (Fusco [99]) observations have been interpreted respectively as synchrotron and inverse Compton emission of a non-thermal electron population. This radio and X-ray emission is thought to be result of the acceleration of electrons in shocks. However the presence in these contexts of hadrons has not been confirmed yet. Gammas observation might also give important informations on the environment where the acceleration is taking place (Blasi [100]).

As conclusion, although probably powerful enough to account for the generated CR power<sup>7</sup>, cluster mergers have serious problems to explain the most extreme part of the spectrum over  $10^{20}$  eV. They can be nonetheless mentioned as potential contributors for the flux from the ankle region at least till the GZK cutoff.

**Active Galactic Nuclei (AGN).** AGNs are among the most powerful emitters in the universe. According to the standard AGN theory they are galactic nuclei which exhibit an exceptional high luminosity. The standard theory describes them as sources powered by accretion on a super-massive

---

<sup>7</sup>As explained by Blasi [100] the energy of the impact of two clusters of  $10^{14} \odot$  is of the order of  $10^{63}$  erg.



black hole placed in the galactic center. In the unified theory by Urry and Padovani [101] a large variety of astronomical observations is explained with the aid of these objects. The very high complexity of these structures is reflected in a direct way in their spectrum, which can cover the entire range from radio to  $\gamma$ s. A very important factor is also the relative inclination with respect to Earth giving explanation of a wide variety of behaviors under which these objects are observed. In Fig. 1.9 a schematic view of an AGN source is given.

An extremely important factor is also the presence or lack of a strong radio signal. Therefore sources divide themselves in radio-quiet and radio-loud. The most widely accepted theory explains this feature respectively with presence or lack of extended jets. In this model the radio signal would be generated by synchrotron emission of accelerated electrons in the jet. As observed, radio-loud sources represent just 10% of the total AGN population while the remaining 90% is made up by radio-quiet. We invite the reader to check Urry's and Padovani's work [101] for more detailed information.

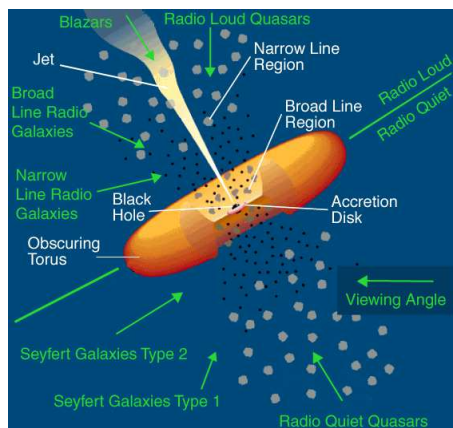


Figure 1.9: A schematic view of the unified theory on active galactic nuclei taken from <http://www.auger.org/>. The distinction between radio-loud and radio-quiet is made according to the presence or not of strong radio signal which implies the presence of jets. For the different source definitions present in the plot the reader is invited to read references.

Different acceleration mechanisms have been taken into consideration. Many of them consider again simply a scaled version of the popular Fermi mechanism while other propose alternative ways to achieve  $10^{20}$  eV. As a matter of fact, both radio-loud or radio-quiet sources have been presented as possible acceleration sites.

In the radio-quiet family we find all those models which mainly try to explain the observed spectrum without the need of extensive jets. To look

at these objects is somehow natural since they represent by far the most common AGN type. In the model of Boldt and Gosh [102] for example, particles are accelerated near the event horizon of rotating black holes similarly to what had been proposed by Blandford and Znajek in 1977 [103]. In this context, externally supplied magnetic fields lines (probably from currents in the accreting disc) threading the horizon of the super-massive Kerr black hole would generate an extremely strong electric potential. Despite Blandford-Znajek model was developed as a mechanism to extract energy and momentum from the black hole through electron-positron acceleration, Boldt and Gosh proposed this method to be also somehow applicable for protons. In this way the black hole would act basically like a dynamo capable of pushing protons till an energy of  $\sim 10^{21}$  eV. As a matter of fact, whether it is possible to reach these energies or not is disputed. Some study (like the one of Norman et al.[104]) showed this value to be totally out of the reach of these accelerators. In fact the central volume of the AGN is a radiation and matter-dense environment. Energy losses would be limiting the maximal energy of particles from the central AGN regions by several orders of magnitude.

For that reason, also Ptitsyna and Troitsky [105] excluded the generation of UHECR protons from the inner part of AGN but still leaving open possibility for single-shot nuclei acceleration.

Another possibility concerning radio-quiet sources reported by Pe'er et al. [106], sees the presence of very small jets in the proximity of the black hole. Unlike radio-loud sources, where the jets have extensions up to  $\sim$  Mpc, here jets would be just of the order of  $\sim$  pc, being not so evident in the radio emission <sup>8</sup>. Provided a heavy composition, magnetic fields of  $\sim 0.1$  G and accelerator size  $\sim pc$ , such accelerators can in principle account for the most extreme part of the spectrum. Such a scenario would be of course realistic just in case the composition at Earth results to be heavy. In other terms this model would not be successful if HiRes-TA compositions turn out to be true.

Also very similar to the last one is the model proposed by Alvarez-Muñiz and Mészáros [107]. In this view a radio-quiet source with an abortive jet would produce colliding blobs of matter. Thanks to the Fermi mechanism then, this would lead to the acceleration of particles. Although the authors concentrate mainly on neutrino production their model requires acceleration

---

<sup>8</sup>Various hypothesis have been proposed to explain the smaller size of these Jets. Generally it is believed that for some reason the ejected material doesn't have enough speed to escape the enormous gravitational attraction near the black hole. Therefore the jet remains confined near the central region of the AGN not managing to extend over its entire elongation and to produce massive radio emission

of hadrons up to extreme energies. After the interaction with ambient matter, the production of charged pions and the following decay chain neutrino would emerge. This study of course doesn't take directly into account the capability of hadrons to escape being the target of the study about neutrinos.

In the radio-loud family jets are the dominating feature. The classification of these sources can be done according the power of the jets and again depending on the orientation of the source. In fact, according to the orientation the classification between radio galaxy, radio-loud quasar and Blazar is made. At the same time within the radio galaxy group a distinction between FR-I and FR-II was developed according to the source morphology. In fact FR-I display a higher radio luminosity toward the center of the source while FR-II toward the edges. This is interpreted to be a feature dependent on the speed of the jet. In fact the faster FR-II jets are believed to be able to reach extreme distances from the source before encountering the intergalactic medium (IGM) where shocks are expected to occur and where the predominant part of the emission is also expected. On the other hand FR-I are believed to exhibit subsonic jets and therefore the main part of jet's energy is emitted near the center. Stronger jets are believed to have a more linear development while weaker tend to be more irregular. Therefore while FR-I exhibit beside a centered emission also bending plumes, FR-II show straight jets terminating in what has been named hot spots. Also very important for FR's morphology and for the acceleration models are radio lobes and cocoons forming in the FR-II galaxies. After the strong jet has impacted against the IGM the remaining plasma is expected to expand sideways in a region visible in the radio and to inflate a bubble called cocoon. The regions near the impact location are hotter and therefore more visible in the radio emission.

Jets, hot spots and cocoons are very interesting environments where acceleration could take place. Several models including both classical stochastic processes and other single-shot acceleration mechanisms are invoked to model an hypothetical CR acceleration. A possible hint in favor of this theory is the possible correlation between AGNs and the arrival direction of UHE-CRs as claimed by the Pierre Auger Observatory [69][144]. In particular the claimed detection of an excess in the UHECRs with energies  $\geq 5.5 \cdot 10^{19}$  eV from the direction of Cen-A<sup>9</sup> gives hope of a possible future source identification. Although no definitive identification can be claimed and no agreement in the scientific community has been found, this result adds some more credibility to the identification of radio-loud galaxies with UHECR sources.

One of the most popular models is the one which sees the acceleration to

---

<sup>9</sup>Cen-A is considered to be a bright radio galaxy with such a luminosity to put this source at the limit between FR-I and FR-II class

occur in the shock wave between jets and IGM directly at the hot spots of FR-II. As explained by Rachen and Biermann[108] the shock between the jet and IGM could allow the onset of the first order Fermi mechanism and the stochastic acceleration of particles. As explained by the authors those sources could well account for the maximum CR energy since hot spots are less dense regions compared to the inner part of the AGN. Thanks to that energy losses are going to be smaller compared to mechanisms taking place in the center of the AGN. Furthermore the modeled spectrum would have a power-law shape with a steepness not too different from the observed one. Last but not least, the extreme luminosities of those objects make their choice as potential sources very appealing.

Another study supporting the hot spot origin is the one proposed by Takami and Horiuchi [109]. In this case however a subclass of radio galaxy is considered: the so called CSO. These objects also display jets and associated hot spots however with a significantly smaller extension. For that reason they have been interpreted as early epoch radio-loud sources. In the above cited study they have been interpreted to be efficient accelerators capable of accelerating protons up to the most extreme energies. However those candidates show some problem to allow the escape of heavier nuclei due to photodisintegration in the cocoon. Furthermore the authors acknowledge how the extremely low density of sources of this kind could represent a serious limit on the required energy output for the sources. In fact the estimation of the authors accounts for an emitted energy budget which is 1/30 of the required emitted power.

As explained before, FR-II also present supersonically expanding cocoons. As proposed by Berezhko [110] and Ohira et al. [112] in shock waves between expanding Plasmas and IGM again particle acceleration is thought to occur thanks to first order Fermi acceleration mechanism. As shown in their studies both groups developed models which can reproduce quite reasonable spectra. As a result of their studies above  $10^{18}$  eV the spectral shape would be in both cases power-like. The spectral index would be respectively  $\sim 2.6$  and  $2.4-2.7$ . Both these results fulfill the requirements for extragalactic sources who take into account also propagation effects. Furthermore Berezhko [110] gives clear indication of the maximum to be around  $10^{20}$  eV adding to this scenario more plausibility.

Another area of intense research is the acceleration of CRs directly in the jets. Also here the Fermi mechanism in shocks is the most popular mechanism. As an example we can cite the calculations performed by Honda [113] on Cen-A. It is known from radio and X-ray observations that several AGN sources display irregular jets structures. As a matter of fact clumpy structures called knots are visible in Chandra's observational data [114]. The most

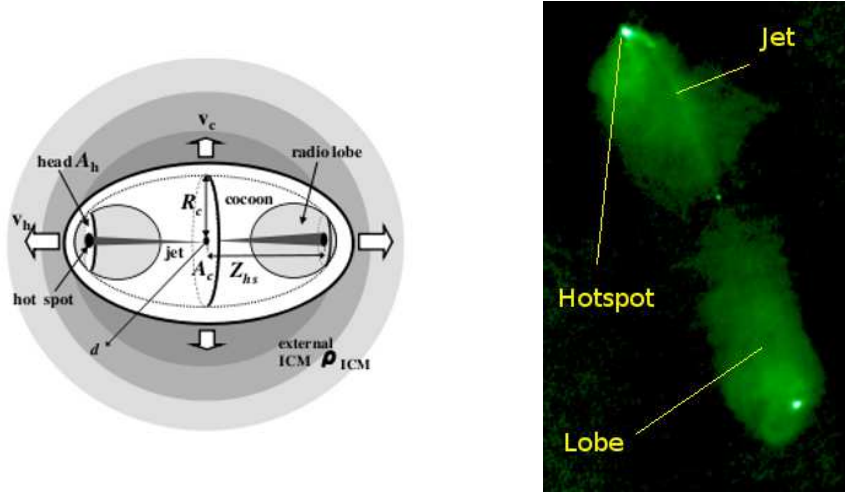


Figure 1.10: **Left Panel:** cocoon's schematic view. After the jets impacted against the IGM the plasma diffuses through the radio lobes and inflates a bubble delimited by shocks called the cocoon. Picture taken from Kino et al. [111]. **Left Panel:** a FR-II Galaxy. The jets are impacting against the IGM generating the very well visible hot spots. Image taken from <http://en.wikipedia.org/>

accepted explanation for these features is the presence of shocks in the jet flow. As concluded in the aforementioned study the maximum energy achievable in these environments by protons could (although with some problem) reach the maximum observed energy. The author sets the maximum energy limits for protons, depending on the distance from the center of Cen-A, between  $10^{19}$  and  $10^{20}$  eV. Worth to mention is the maximum energy achievable by nuclei which is calculated at least to be one order of magnitude higher than protons.

Another possibility involving jets is the one proposed by Gouveia Dal Pino et al. [115]. The authors, proposed shocks in the magnetic reconnection region as acceleration site. It is believed that in the interplay between the magnetic field generated by the accreting disc and the black hole in AGN's centers magnetic reconnection can occur<sup>10</sup>. As a result of the produced plasma outflow shocks in the vicinity of the black hole can occur. In this context first order Fermi acceleration may take place.

The jet has been also proposed to be the environment for other kinds of acceleration. As an example we can recall the shear acceleration model.

<sup>10</sup>Magnetic reconnection is a phenomenon which occurs when magnetic fields of opposite orientation encounter each other. After some threshold value has been reached a rearrangement of the line structure is performed. In this context charged particles can be accelerated. Phenomena like jets might form in a similar way as result of this particle acceleration.

From fluidodynamical studies it is to expect that jets are characterized by shear rather than uniform motion. As proposed by Berezhko and Krymskii in 1981 [116], the scattering of charged particles through plasma layers with different speeds, might lead to an increase of the energy of the particles. As in the case of the Fermi mechanism it is to expect that scattering of particles in a plasma on average do not lead to any change in the particle's energy. This is due to the fact that the bulk of particles share the same reference system as the ambient plasma. Therefore as a result of the elastic scatterings the average energy of the particles will not change. The situation changes however if the particle crosses the shear of the fluid encountering plasma flows with different speeds. As a result a particle scattering with the magnetic irregularities might increase its energy. As explained by Rieger and Duffy [117] the final spectrum is expected to be power-law like. Moreover as calculated by Ostrowski [118] the maximum energy achievable in this environment might exceed  $10^{18}$  eV. Problematic in this theory is however the limited knowledge of jets structure.

Another possibility to be mentioned is the one shown in [119] by Berezhko but originally proposed by Vlasov [120]. In this case a compression of a flow tube in the AGN jets called pinch instability causes particle acceleration. It is to expect that the plasma flow in the jet will cause a toroidal magnetic field along the jet. If a compression of the flow tube occurs (as observed experimentally in plasma physics experiments) the longitudinal current density increases leading to an increase of the magnetic field itself. This process therefore can develop a self growing tendency where the tube further shrinks and the current density further grows. As a result of this unstable process the longitudinal electric field is expected to reach enormous values which potentially could allow particles to reach high energies. As mentioned in the above mentioned study the resulting spectrum has been estimated to be power-like. Moreover according to the authors the steepness of the spectrum would be  $\sim 2.73$ . An estimate of the energy would be also capable of accounting for the maximum observed energy.

Other important source candidates are FR-I sources and Blazars. In fact as explained by Murase et al. [121] those radio galaxies could well explain the observed overall UHECR flux. Since the power emitted by them in the non-thermal  $\gamma$  is of the order of  $10^{45}$ – $10^{46}$  erg  $\cdot$  Mpc $^{-3}$  yr $^{-1}$  it could well account for the required power for the Cosmic Ray component. The authors made therefore a study on the morphology of several FR-I radio galaxy and Blazars and draw some limits on the maximum energy achievable by those objects. As pointed out in the cited publication the maximum energy achievable by those accelerators seem to be in the best case just  $\sim 5 \cdot 10^{19}$  eV even without considering detailed acceleration models which would be

limiting this value. However higher energies seem to be accessible for heavier nuclei. Following these consideration the study concludes the necessity of a heavier CR composition at higher energies to maintain the plausibility of this kind of accelerators. The conclusions drawn from the cited study are therefore compliant just with the detected Auger heavy spectrum.

**Gamma Ray Bursts (GRB).** In our excursus through the Hillas plot the next candidates are Gamma Ray Bursts (GRB). GRBs are the most violent events in the universe. With energies  $\gg 10^{51}$  ergs they can outshine even the most luminous supernovae. Their discovery was done accidentally thanks to the detection of very bright  $\gamma$ -ray flashes by military satellites in the 60s. After further investigation was soon clear that those powerful events were of extragalactic origin since no correlation with the galactic plane was observed. Moreover due to the extreme distances which had been inferred from redshift measurements the non isotropic emission pattern of those sources could be determined. In fact, if the emission would have been isotropic no known physical mechanism would have been able to explain such an energy output. As a matter of fact it is widely believed that those sources emit mainly along jets. Those objects get therefore detectable if the jet is pointed directly toward the observer.

Another fundamental element in GRB theory is the classification according to their duration. In fact GRBs have been subdivided in two categories: short and long duration GRB<sup>11</sup>. In the current interpretation the first group seems to be associated with a rare kind of star core-collapse event called hypernova. It has been proposed, similarly to what occurs for SNs, that the most extreme and unstable stars ( $\sim 100\odot$ ) can undergo a process of gravitational collapse leading to the formation of a black hole instead of a neutron star. On the other hand the origin of the short duration GRB is not fully understood. The most popular theory explains them as merger between two NSs or of a NS and a black hole. The extreme compact nature of these objects would also account for the extremely fast burst events which are typical for those objects.

The special interest that those objects stimulated in the cosmic ray community lies not surprisingly in the very high luminosities and of course in the very powerful jets emitted during the burst. GRBs were proposed as UHE-CRs sources for the first time in the 90ties by Waxman [122] and Vietri [123]. The first consideration made by [122] was about the frequency of the GRB events observable by CRs experiments. In fact knowing an estimate of the occurrence of bursts per unit of time and volume and the total volume sur-

---

<sup>11</sup>The dividing threshold between the two groups is set to be equal to 2 s.

veyed by CR detectors <sup>12</sup> it was possible to estimate the number of GRB in the fiducial volume of UHECR detectors per unit time. The result obtained was apparently discouraging since the estimate of GRBs visible by observatories currently operating was of the order of less than one in a decade. However, after more careful considerations, it was noted how the intervening intergalactic magnetic field traversed by the charged CRs are known to cause a spread in the arrival time of the particles on Earth. As estimated by the author this smearing effect can reach the order of  $\geq 100$  yr. For that reason direct time coincidence between CR arrival time and GRB is not required to postulate GRB as sources. furthermore by making some realistic assumption like the uniform distribution of GRB and by assuming the delay time much bigger than 100 yr the timing information is completely lost.

Several models attempt to calculate the maximum energy achievable by those accelerators. The most popular approach to this problem is the so called Fire Ball model. As widely accepted in the GRB models, the outburst results in an extremely narrowly beamed jet which lasts for relatively short times. In this context the GRB ejecta assume the form of an expanding plasma cloud moving along the jet axis. According to the present description, during the propagation of the FB CR acceleration can occur in several scenarios at different FB evolution phases.

As an example the FB is thought to be initially optically thick to  $\gamma$ s. In this phase, called "prompt phase", during which the FB expands relativistically, internal shocks are thought to form. This is probably due to the different speeds at which different parts of the ejecta are moving. The FB will eventually collide with the IGM generating further shock waves both forward and backward. Therefore all those environments can be considered to be potential locations where the Fermi mechanism can accelerate particles.

In Murase et al. [125] an estimate on the maximum energy achievable in all those environments has been done. Moreover a separate analysis on high or low luminosity GRBs has been performed. For the case of the internal shock model, for example, the authors calculate as possible the acceleration for both protons and nuclei for HL (High Luminosity) sources. Concerning the LL (Low Luminosity) counterpart then the acceleration of nuclei seem to be possible unlike for protons. For both classes of sources however the authors recognize how several problems might be arising in the acceleration process both for protons and nuclei. The best candidates for acceleration seem to be the shocks forming at the impact between ejecta and IGM. In the case of reverse shock the authors conclude on the possibility of protons and nuclei acceleration up to the maximum energies observed. The same

---

<sup>12</sup>Considering the GZK horizon  $\sim 100$  Mpc.



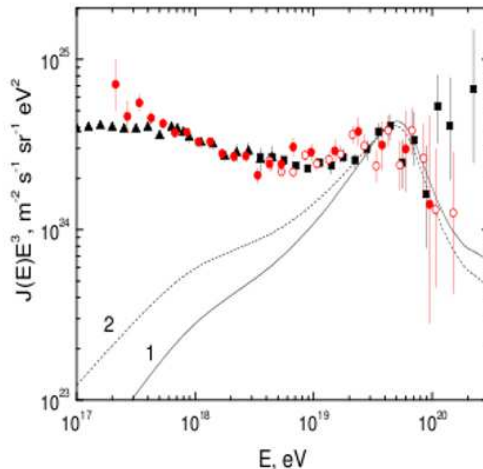


Figure 1.11: The spectra generated by internal and external shocks are marked respectively by 1 and 2. The modeled spectra are superposed with data from HiRes and AGASA. Note that the modeled curves are fitted to the data. The emissivity needed to match the data is therefore much bigger than a realistic one. Plot from Berezhinsky[119].

consideration is accepted also for the forward shock. Moreover also other studies confirm the maximal energy achievable by the sources confirming the potential interest of the GRB candidate (see Sigl [126] and Berezhinsky [119]).

However considerations on the required emitted power above  $10^{19}$  eV pose serious challenges to the GRB theory. As can be seen in Berezhinsky's work [119] no easy modeling can explain the observed UHECR production through GRB. Even though their power is exceptionally large they still represent a very rare event.

As a matter of fact, Berezhinsky [119] observed how the emitted power for GRB by means of  $\gamma$  photon emission is of the order of

$$W_{GRB} \sim 0.6 - 13 \cdot 10^{43} \text{ erg Mpc}^{-3} \text{ yr}^{-1} \quad (1.12)$$

depending on the approximation. This value is considered to be extremely important also for UHECR since this emission can be considered tightly related to the acceleration processes. Therefore it is reasonable to consider this value to be of the same order of magnitude as the produced power in the hadronic channel. However, as recognized by Berezhinsky [119] an identification GRB–cosmic ray source is possible just in case of a produced UHECR energy flux two orders of magnitude larger than the  $\gamma$  emission. Obviously this appears very difficult to be explained in the current modeling of GRB accelerators.

**Neutron Stars and Magnetars.** The last candidate to be taken into consideration are NSs. Those very exotic objects are formed during a core collapse event that leads to a SN explosion. While the external envelopes are blown away the core contracts violently under the enormous gravitational attraction. Eventually in the collapse process the only force capable of resisting to gravity is degeneracy pressure of neutrons. As result of the collapse process NS are characterized by extreme compact structures and enormous surface magnetic fields.

In fact the standard NS theory sees them as objects with masses of the order of some solar mass squeezed in just several kilometers radius. As a result of that the density reaches astonishing values even larger than the nuclear density. Thanks to magnetic flux conservation then, the magnetic field experiences a massive increase. For that reason NS display magnetic fields  $\sim 10^{12}$  G which can even be as high as  $10^{15}$  G in case of magnetars. Without any doubt those objects can be therefore considered the strongest magnetic dipoles of the Universe.

Another very important aspect is NS rotation. It is required by conservation of angular momentum that a contracting star simply increases its rotation frequency. For that reason NS can display very fast rotations which can even reach the physical limit beyond which the star would fall apart. It is known that NS can rotate as fast as kHz. It is also known that their speed is maximal at the beginning of their life. In fact, the rotational momentum which is maximum immediately after the SN explosion, tends to be dispersed thanks to electromagnetic drag of the NS magnetosphere.

In the past NS have been proposed as particle accelerators. For example, locations as polar caps and outer gaps have been taken into account as potential accelerators. However, as explained in Fang et al. [127] curvature radiation is most likely preventing acceleration up to extreme energies in these environments. Another possibility presented by Arons [128] is the one which sees the acceleration in the relativistic winds generated by young NS. In this model as result of magnetic fields rotation outside the so called light cylinder acceleration can occur. More in detail outside the light cylinder the magnetic field structure cannot maintain its dipolar structure due to loss of causality and assumes a spiral form. Under certain conditions at a certain distance from the NS particles can be accelerated in a radial direction. It is said that particles can "surf-ride" the field gaining energy like in the case of a linear accelerator. As shown by Arons [128] this kind of process applied to sub-millisecond magnetars can account for maximal energies exceeding even  $10^{21}$  eV.

A further possibility is the one studied by Fang et al. [127] where pulsars with magnetic fields of the order of  $10^{12}$ – $10^{13}$  G and millisecond period are

considered as accelerators. As mentioned by Fang et al. [127] a crucial issue is the capability of accelerated particles to escape SN envelopes. This is not by itself an easy and immediate issue since escaping particles will interact with the ejected materials. Most likely (if we follow Fang et al. [127] argument) protons with energies above  $10^{20}$  eV will not be able of escaping the ejecta. On the contrary nuclei will be allowed to escape making the average spectrum at the highest energies compliant with the Auger composition (see Fig. 1.12). Despite that a small room for a light composition remains open in case of dilute or pierced ejecta.

Considerations on the source density make this scenario also very plausible since this model requires not too large sources densities. In fact as stated always in Fang et al.[127] the observed spectrum could be justified just if 0.01% of NS would be in the favorable magnetic field and frequency conditions. As a matter of fact it appears that a much larger fraction of the NS population are in the desired condition ( $\sim 1-2\%$ ). This allows a much more relaxed efficiency requirements on the acceleration mechanisms.

However a problem for these models is represented by the generated spectrum. As they were developed in the "AGASA era" all the NS models were aiming at the theoretical justification of the absence of the GZK cutoff. In this view the presence of sources already in our galaxy was considered to be very appealing in order to avoid the GZK effect. Even for the case of extragalactic origin such sources were producing extremely hard spectra. As a matter of fact, this feature is not compliant with the state of the art knowledge which sees a strong cutoff at energies above some  $10^{19}$  eV. However, as proposed in Fang et al. [127], a proper choice of the source parameters could in principle account for the observed softening. In fact by choosing a proper distribution of parameters inside the NS population could in principle reproduce the observed energy spectrum softening.

Another issue is certainly the capability of injecting heavy nuclei in the accelerators. As said above, it is to expect that just heavy nuclei can survive the propagation through the ejected SN shells. This requires of course the presence of a heavy spectrum before traversing the ejecta. Fortunately NS seem to be quite favorable sources of heavy nuclei. In fact heavy nuclei could be stripped by the external NS layers. Another possibility is nucleosynthesis in the first epochs of the SNR evolution.

A last consideration can be done about the spatial and temporal distribution of the observed CR events. As explained above, NS periods are known to increase by time. In the same way magnetic fields are thought to decay. For that reason NS are thought to be valid UHECR accelerators just in their early epochs. As a result of that NS can be considered as transient sources. However coincidence detection would be extremely difficult both in

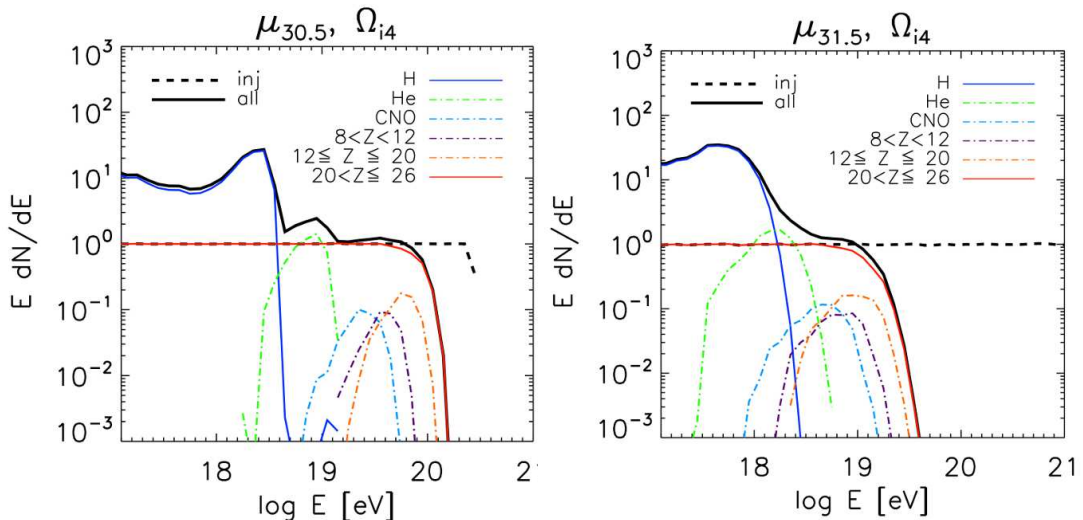


Figure 1.12: An example of calculated pulsar spectrum after the attenuation through the SNR. Pure iron injection is considered. The injected spectrum is represented by the thick black dashed line. As result of the propagation through the SNR several secondaries species are formed. Hydrogen and iron spectra escaping are represented as continuous lines. All the other elements are indicated in the legend. The thick continuous line represents the sum of all the escaping spectra. **Left Panel:** pulsar parameter  $\mu_{30.5} \equiv 10^{30.5} \text{cgs}$  (magnetic dipole moment) and  $\Omega_{i4} \equiv 10^4 \text{s}^{-1}$  (pulsar frequency). **Right Panel:** pulsar parameter  $\mu_{31.5} \equiv 10^{31.5} \text{cgs}$  (magnetic dipole moment) and  $\Omega_{i4} \equiv 10^4 \text{s}^{-1}$  (pulsar frequency). Taken from Fang et al. [127].

space and in time. In fact the identification of single NS in other galaxies by traditional means (radio, X-ray,  $\gamma$ s) is out of the reach of present techniques. Also direct pointing of charged particles toward the sources is out of question because of intergalactic magnetic fields and especially because of the very heavy composition. Also the time coincidence will be washed out by magnetic delays in the magnetic field. Most likely just some anisotropy coincident with luminous matter in the local universe can be observed. Moreover a burst event can be observed just in the rare case of an NS source inside our galaxy. This is also going to be affected with a significant magnetic delay but provided some favorable conditions the time coincidence of a CR burst with the SN could be kept.

As a conclusion of this section it can be stated without any doubt that to clearly identify the UHECR sources is still a very long way to go both experimentally and theoretically. Even though apparently AGNs seem to gain more credibility still a lot of issues must be solved. In particular a lot of uncertainty is still open on the detailed mechanisms at work on the accelerators and on the energy losses occurring at the accelerator location.

Future UHECR observations to reduce uncertainty on the spectrum, compositions and arrival directions will be mandatory to investigate those questions. A lot of help can be brought by other messengers like  $\gamma$  photons and neutrinos in order to confirm or reject the presence of hadrons at the accelerator locations.

Future tasks of a cosmic ray observatory would certainly be to maximize the exposures at the most extreme energies in order to reduce as much as possible the effects of magnetic field deflections and delays. This might help to find clustering around some source or to explore the possibility of some time modulation. In this view the most uniform exposure will also be valuable to reduce possible biases in the arrival distribution.

A detailed knowledge of the shape of the most extreme part of the spectrum well above the GZK cutoff will be fundamental in order to put further constraints on the acceleration models. The same remains of course valid also for the composition.

### 1.3.5 Alternative theories

For completeness it might be interesting to mention the so called top-down models. Historically the detection of CRs above the so called GZK cutoff has always been a challenge to the theoretical interpretation of the UHECR origin. If we assume that GZK is a real effect two possibilities remain: either some source is present in the local universe or UHECR are formed as decay of some super-heavy particle in some non standard physics scenario. Toward mid-end nineties, the experimental situation seemed to be heading toward the second option. The AGASA results in fact seemed to show no apparent decline in the flux above the GZK cutoff. Moreover no strong clustering around any source could be observed. Therefore the lack of a credible acceleration site candidate in the local universe pushed the community toward alternative explanations. In this view UHECR would be directly forming in the vicinity of the Earth as sub-product of non standard physics.

Such models can be essentially grouped in two families. The first one sees UHECR as products of a decay chain of super massive dark matter relics from the early Universe (see Berezhinsky et al. [129]). In this scenario cold dark matter particles with masses  $\geq 10^{13}$  GeV and long decay times would be at the origin of a decay chain that leads to a non GZK spectrum.

Another possibility would be the one proposed by Bhattacharjee et al. [130] in which the UHECR would be the result of annihilation of topological defects formed in the early universe. Under this theory many different options have been explored: superconducting cosmic strings, monopoles, and hybrid defects just to mention some of them.

Signatures for such scenarios are, beside the lack of the GZK cutoff, the presence of high UHE  $\gamma$  and UHE neutrino flux, the lack of point sources, the possible recovery of the spectrum at energies  $> 10^{20}$  eV and the possible clustering of events toward the milky way center (see Kachelrieß[131]).

Recently however several observations set strong limits on those models. First of all the most likely confirmation of a strong cut-off around GZK energies ( $3 \cdot 10^{19}$  eV) has been found. This observation had as first consequence the fall of the necessity of such models. Then, the energetic requirements for potential sources were massively relaxed making easier the search for an acceleration scenario.

Secondly no observation of UHE photons has been claimed by the recent generation detectors. Thanks to that, strong limits has been put on the photon flux. As a matter of fact, assuming top-down models, the expected photon flux at the most extreme energies would be several times larger than that of hadronic CR (see Kachelrieß[131]). However the Pierre Auger collaboration ruled out at all energies almost all theoretical scenarios [132][144] by putting strong limits on the observed flux. The same considerations can be done for neutrinos as well [132][144] adding more elements in favor of the acceleration models.

Furthermore, to mention is the lack of any clustering in the direction of the galactic center which would be required by all the cold dark matter scenarios.

At last, and to conclude, the question on whether some anisotropy is observed or not is still matter of debate. In fact, while HiRes and its TA [70] seem to be more in favor of an isotropic arrival direction, the Pierre Auger observatory [69][144] even claims some possible correlation between AGNs and UHECR arrival direction which obviously suggests the presence of some acceleration scenario.

As conclusion the present observational scenario seems to rule out most of the top-down models at least as main sources of super-GZK cosmic rays.

## 1.4 Propagation

Before entering the final part of this chapter some considerations about the propagation are mandatory. In fact, no modelization on the sources can be applied if the propagation from source to earth isn't taken into account.

The first concept to be introduced is the one of GZK. This effect has been postulated by Greisen [34] and independently Zatsepin and Kuz'min [133] in 1966. As explained in both studies the interaction of the hadrons with CMB during propagation would set a certain limit on the maximal

detectable CR energy. Thanks to blue-shift in the particle reference system the CMB photons permeating the entire universe would result to be of an energy of  $\sim$  GeV. At these energies as explained by Greisen [34] and Zatsepin and Kuz'min [133] photo-meson production is expected to take place. The reaction,

$$p + \gamma \rightarrow N + n\pi \quad (1.13)$$

whereas  $p$  is a proton,  $\gamma$  the blue-shifted photon,  $N$  a nucleon and  $n\pi$  a number  $n$  of pions, would take place in the propagation from the source to the detector. Here a proton interacting with CMB will produce a nucleon and a certain amount of pions. For the first term of the right-hand side of the equation we can basically assume that the final product will always be a proton since neutrons have a quite short decay time. On the other hand for the second term it must be stressed that both charged ( $\pi^\pm$ ) and neutral ( $\pi^0$ ) pions are produced. As a result of the  $\pi^0$  decay in almost all the cases two photons will be produced. As a result of the  $\pi^\pm$  decay, then, neutrinos and muons are produced. Muons would themselves decay producing more neutrinos and electrons. Thanks to that the nucleon  $N$  will have around 20% of the original proton energy and a background flux of UHE neutrinos and photons is to be expected.

In the above mentioned studies the authors drawn the conclusion that above  $3\text{--}4 \cdot 10^{19}$  eV CR proton spectrum would start to decline. Another consequence is that above this energy the universe should be opaque for protons. In fact, as also shown in Fig. 1.13 (left panel) after calculating the cross section as function of energy both the mean interaction path and the energy loss length can be calculated. As a result it is widely accepted that protons must be coming from the local universe otherwise their energy would be degraded. The GZK horizon is usually thought to be of the order of  $\sim$  100 Mpc.

Another very important effect to take into account especially for the energy slightly under the GZK cutoff ( $4 \cdot 10^{19}$  eV) is pair-production. In this reaction blue-shifted photons will be interacting with protons and generating electrons-positrons pairs.

$$p + \gamma \rightarrow N + e^+ + e^- \quad (1.14)$$

Two very important differences of this last reaction are the lower energy threshold and the lower cross section. As a result of that it can be observed in Fig. 1.13 (left panel) how the pair-production becomes relevant already at energies around  $\sim 10^{18}$  eV. On the other hand the much lower cross section is reflected in a much higher source horizon which never goes under 1000 Mpc.

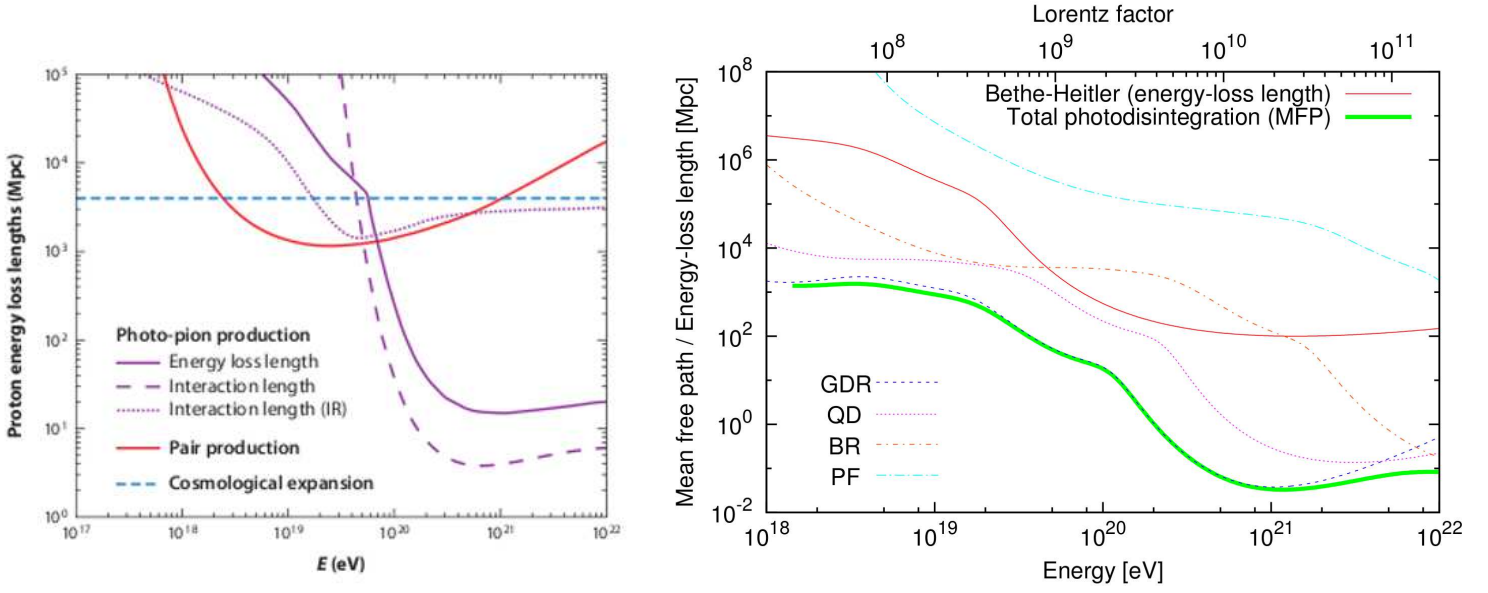


Figure 1.13: **Left Panel** : proton energy loss length as function of energy. The contribution of pair-production and photo-pion production are represented respectively in red and in violet. The different component of the photo-pion component are related to microwave photons and UV-IR photons. Taken from Kotera and Olinto [90]. All the curves have been calculated according to Stecker [134]. **Right Panel** : energy loss length for iron nuclei as plotted by Takami [135] following Rachen modelization [136]. Giant dipole resonance, the dominating process, is depicted in blue, quasi deuteron in violet, barionic resonance in red and photo fragmentation in cyan.

As a result of that pair-production spectral features are considered to be less model dependent than the photo-pion features. In fact the universe appears to be quite uniform at larger scales and so the modeling of source spatial distribution and source typology does not affect much the final spectrum unlike for the GZK feature effect.

An interesting consequence of the above mentioned models is the one outlined by Berezhinsky [65] and named dip model. In this interpretation, assuming a proton dominated composition, all the relevant spectral features above  $10^{18}$  eV can be explained by the combination of photo-pion and pair-production interactions. In few words in this study several spectral features can be identified: the GZK cutoff, the bump, the dip and the second dip. The GZK cutoff is due to the already explained photo-pion production. As a result of the energy loss of the highest part of the spectrum a kind of pile up around some  $10^{19}$  eV is formed in the spectrum of single sources (bump). This feature however is washed-away if we consider the superposition of several sources. Going down to lower energies a dip in the spectrum can be



observed. This hardening is interpreted to be as result of the pair-production process. In this model then, the so called ankle would not be any more a transition from galactic to extragalactic CR but rather a consequence of the pair-production losses. We should mention the fact that this model implies a transition from galactic to extragalactic component at energies lower than the ankle. The last feature to mention is the second dip which signalizes the transition between the pair-production and photo-pion regimes.

All the previous considerations have been done assuming just protons. However it is to expect that at least part (if not the main part) of the UHECR population is made by nuclei. A nucleus propagating will not be affected so much by photo-pion production since the GZK effect will be scaled to higher energies by a factor proportional to the mass number  $A$ . Despite that, nuclei suffer of substantial photodisintegration. In this process the interaction of nuclei with CMB will cause the ejection of nucleons from the nuclear potential well. Nucleons can be emitted singularly or bound in systems like deuteron nuclei or  $\alpha$  particles. As a result of this process the only group of nuclei which can survive for a reasonable astrophysical distance (more than some Mpc) are the one of the iron group. In fact lighter nuclei will be much more strongly dissociated with respect to iron.

Photodisintegration consists mainly of four processes: giant dipole resonance (GDR), quasi deuteron process (QD), barionic resonance (BR) and photofragmentation (PF). In Fig. 1.13 (right panel) the energy loss length for an iron nucleus propagating through the CMB as reported by Takami [135] (following Rachen [136] results) is plotted. The components associated with the processes mentioned above can be seen represented in different colors. It can be clearly seen that the dominating process is the GDR process. What can also be noticed is that nuclei are also limited in their propagation through space in similar magnitude as protons.

The last part of this section is devoted to magnetic fields. It is known that both galaxies and the IGM are filled with magnetic field. Both those components are responsible for a deflection of particles trajectories which prevented up to now the detection of any CR source. The studies on the magnetic fields structures and magnitudes are therefore fundamental to look for sources of any kind. However, while the galactic magnetic field is much more known both experimentally and theoretically, the extragalactic component remains uncertain.

More in detail galactic magnetic fields are believed to be of the order of  $\sim 1 \mu\text{G}$  while extragalactic are certainly smaller than  $\sim 1 \text{nG}$ . Moreover galactic magnetic fields are known to have a structure resembling the galactic spiral shape with in addition irregularity features.

As example we can cite Stanev [137] who estimated the deflection of CR

protons in the galactic magnetic field to be of the order of  $\leq 10$  degrees above  $4 \cdot 10^{19}$  eV. On the most extreme part of the spectrum, above  $10^{20}$  eV, the deflection has been calculated to be smaller than 5 degrees. Moreover being the magnetic field irregular some calculation of the effects of the random component must be performed. We cite Tinyakov [138] results where is explained how this additional deflection has to be considered always smaller than 30% of the overall deflection.

However, since UHECR are most likely of extragalactic origin, the deflection of extra galactic magnetic fields has also to be taken into account. As already said a lot of uncertainty is still associated on the structure and magnitude of the intergalactic magnetic fields. Generally it is believed that central regions of galaxy clusters have much higher magnetic fields than voids but a widely accepted model on the origin and evolution of such field is not fully developed. Nevertheless several estimates have been done to assess the deflection suffered by UHECR. Just as example we can report about Dolag et al. [139] who calculated the deflection associated with different cosmic regions for protons of an energy larger than  $4 \cdot 10^{19}$  eV and till a distance of 500 Mpc. The result cited in this study is somehow encouraging being the calculated deflection  $\leq 5$  degrees for directions associated with cosmic filaments and  $\sim 1$  degrees for cosmic voids. On the other hand, other studies by Sigl [140] show much bigger deflections which are  $> 10$  degrees for protons  $\geq 10^{20}$  eV.

On top of that, it must be mentioned how nuclei are going to be deflected at a much bigger extent than protons. In fact, in case of heavy composition all the deflections shown above have to be increased consistently thanks to the smaller magnetic rigidity of nuclei. In this case, it is to expect a strong deflection which would most likely preclude the possibility to detect coincidence with potential sources.

To conclude it must be stressed how challenging might be to identify UHECR sources. In fact even in the best cases at least a few degrees deflection are to be expected. However, no final word can be still said since, thanks to GZK and photodisintegration effects the number of sources within the observable horizon is very limited. For that reason in the UHECR sky, sources will be separated by large angles. Therefore, even in the case of very large deflections, unacceptable in other fields of astronomy, the possibility of doing UHECR astronomy remains still open.

## 1.5 The end of the spectrum: the role of JEM–EUSO

Several models have been proposed to explain in which astronomical environments and thanks to which mechanisms UHECR are produced. Up to now however, none of those models succeeded in answering UHECR fundamental questions. One of the reasons is the fact that no consensus on the most important observational features has been reached yet. The main goal of any future UHECR missions will necessarily be to try to solve these discrepancies in order to put further constraints on theoretical models. Therefore we will firstly try to identify the most crucial points in the scope of JEM–EUSO and then present the JEM–EUSO main scientific objectives.

One of the most intuitive approaches in the search for UHECR sources is to look for pointing toward some particular astrophysical object.

As of today no clear answer is given on whether CR arrival directions are isotropic or not. In fact the Pierre Auger observatory claims the detection of a correlation with AGN [69][144] and a very light autocorrelation of several events while the HiRes–TA confirms the compatibility of the UHECR sky with anisotropy [141][70].

More in detail the Auger collaboration claims the detection of a correlation of the UHECR arrival direction with the AGNs in the Veron Cetty Veron (VCV) catalog. This study has been performed checking the occurrence of coincidence of  $\sim 85$  CR's arrival directions with energies  $E > 5.5 \cdot 10^{19}$  eV within 3.1 degrees from the above mentioned AGN catalog. As a matter of fact compared with the expected 21% by–chance–coincidence the Auger collaboration claims the 38% coincidences as of 2011. The collaboration claims furthermore this excess to be significant at the order of 99 %. On the other hand however both HiRes [141] and Telescope Array [70] collaborations performed the same kind of analysis on the respective data sets not finding any statistically significant coincidence. As reported by the HiRes collaboration just 2 events were found to be coincident out of 13. Furthermore the TA collaboration claimed 6 events correlating out of 15. Both these results do not allow any confirmation of the Auger results and even more seem to be in favor of a non correlation with the VCV data set. In fact the claimed probability to get chance correlation of the same order as detected is 82% and 16% for HiRes and TA respectively.

Another very interesting result of the Auger collaboration is the observation of a significant excess in direction of the Cen–A AGN source. On a scale  $\sim 20$  degrees an excess with respect to isotropy well above 99.7% is claimed. Unfortunately this source is not in the FOV of the HiRes–TA detectors.

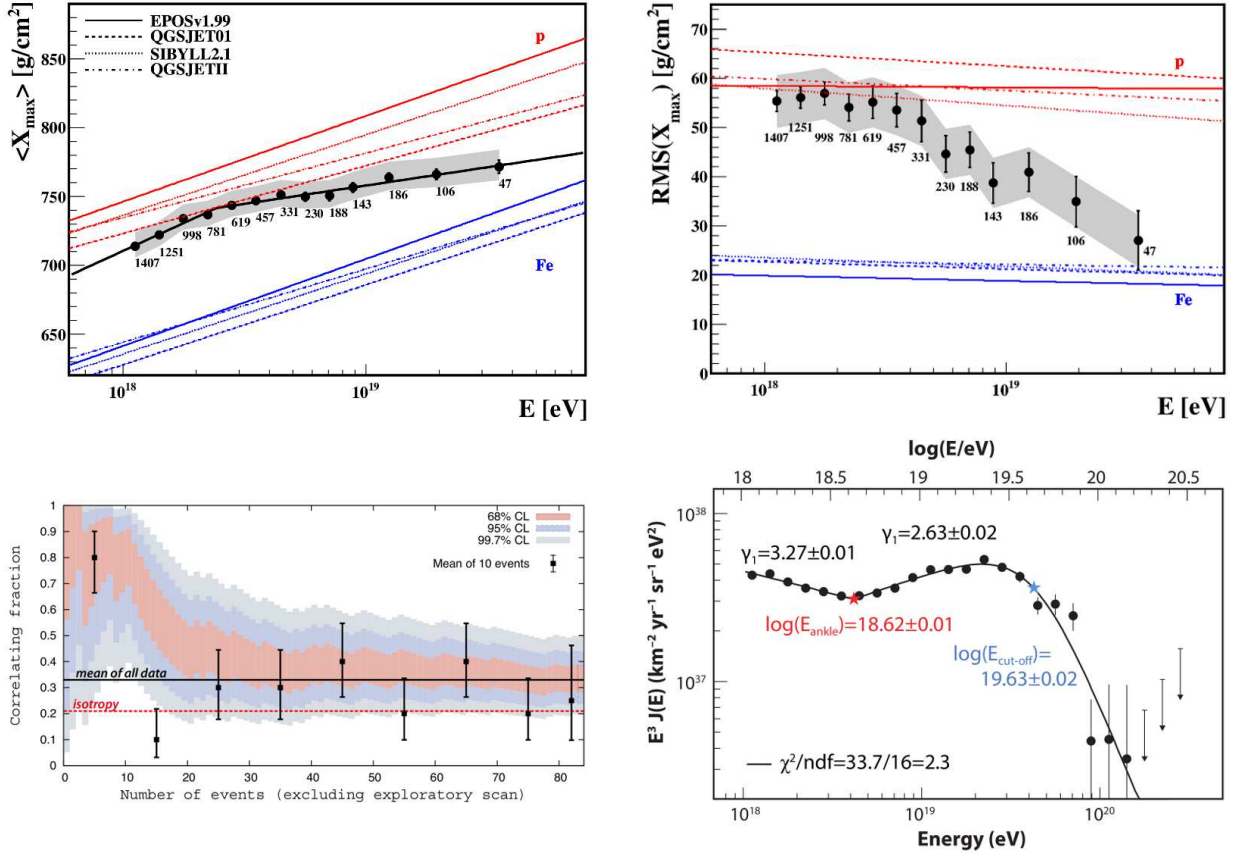


Figure 1.14: **Upper left plot:** the  $X_{max}$  parameter as function of energy as measured by the Pierre Auger observatory. Parameterizations for proton and iron according to different models are also depicted. **Upper Right plot:** mean oscillation in the  $X_{max}$  parameter as function of energy as measured by the Auger collaboration. Also here different parameterizations for irons and protons are depicted. In both the upper plots is clearly visible a tendency toward heavier composition. **Bottom left plot:** the correlating fraction of UHECR events ( $E > 5.5 \cdot 10^{19}$  eV) with VCV catalog AGNs. The fraction of events falling inside 3.1 degrees is divided by the total number of events and plotted in the y-axis. This parameter is depicted as function of the total number of detected events. Mean correlation for isotropy is plotted as a red line. The mean of all the correlations is plotted as black line. Different confidence levels on the correlating fraction are plotted with different colors. The average correlation every 10 events has been plotted as a black point. **Bottom right plot:** UHECR spectrum as detected by the Pierre Auger observatory. Together with the experimental points the fitted functions are plotted. The collaboration decided to fit the function with a broken power law and a cut-off function at higher energies. The relevant functions parameters are superposed with the plot together with the  $\chi^2$ . Taken from Auger publications [144][81].

## 1.5. THE END OF THE SPECTRUM: THE ROLE OF JEM-EUSO

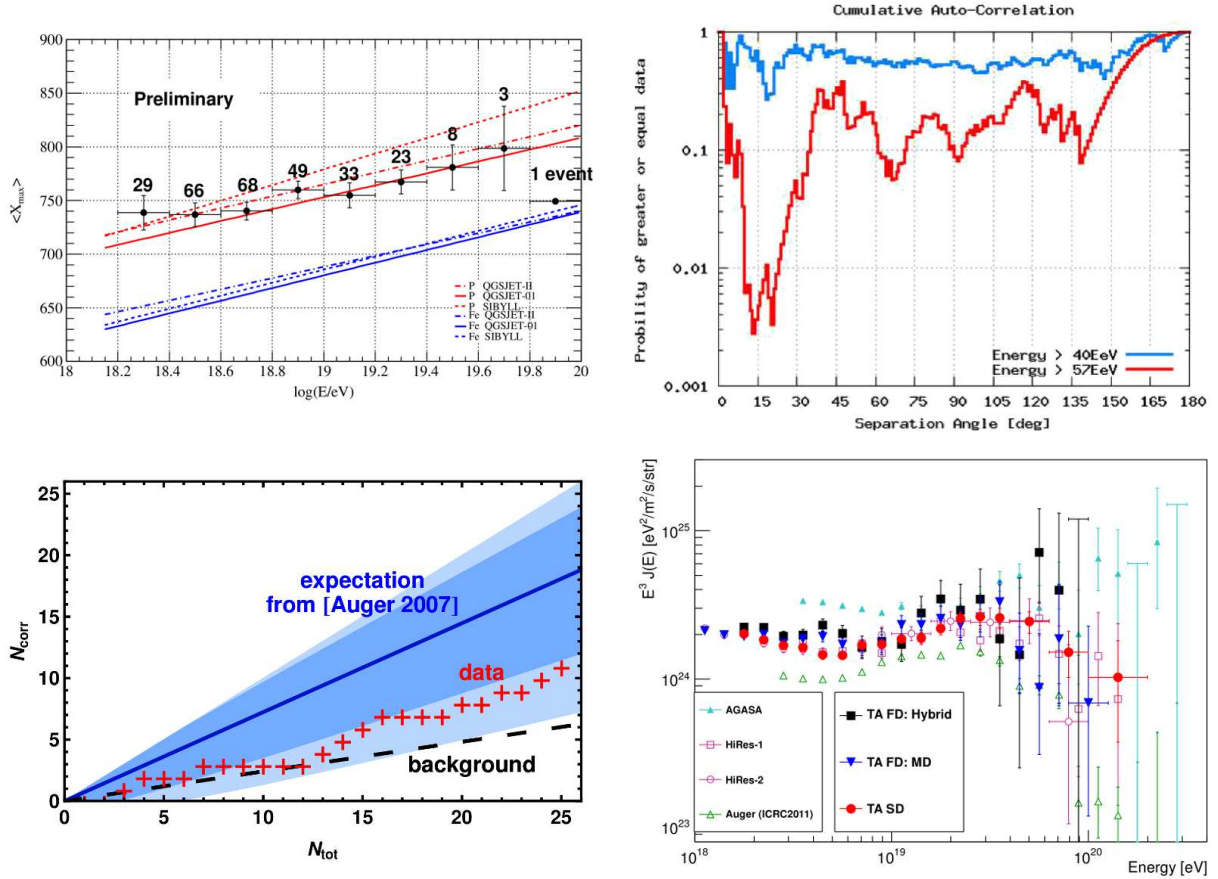


Figure 1.15: **Upper left plot:** the  $X_{max}$  parameter as function of energy as measured by the Telescope Array observatory. Parameterizations for protons and iron according to different models are also depicted. **Upper Right plot:** autocorrelation analysis. This study published by the Telescope Array collaboration searches for clustering of UHECR events. The autocorrelation between couples of events is first calculated. Secondly the probability of having equal or greater autocorrelation from random distribution is also calculated and plotted here. As can be seen around 10–20 degrees there seem to be some deviation from isotropy ( $p_{iso} < 1\%$ ). However the statistical significance of such a feature is not enough to claim anisotropy at such angular scale. **Bottom left plot:** correlation of UHECR events ( $E > 5.5 \cdot 10^{19}$  eV) with the VCV AGN catalog. The number of events falling inside a 3.1 degrees circle from the VCV sources is represented on the y-axis. TA data are marked as red crosses. The number of correlations expected from the first Auger correlation study [47] is reported. **Bottom right plot:** energy spectra of different experiments are shown in this plot. In particular we point out the TA SD (surface detector), TA FD:MD (FD–Monocular Mode), TA hybrid (FD–Stereoscopic Mode), AGASA, HiRes and Auger. All the experiments show good consistency within the systematic uncertainties. The cutoff above  $3 \cdot 10^{19}$  eV can be clearly seen in all the experiments apart in the AGASA case. Taken from TA publications [70] [82].

Always in the same context auto correlation studies have been performed to look for UHECR clustering. Essentially the correlation function of CR events pairs has been calculated and compared with the by-chance expectations. Here both Auger and TA seem to agree on the insufficient statistical significance of clustering at all the angular scales. However both of them show very modest excess which, must be stressed again, has not enough statistical significance to claim any anisotropy.

The Auger collaboration made also attempts to find anisotropy correlated with other catalogs. Always in the same study coincidence with the 2MRS and Swift-BAT AGN catalogs was searched. These are much more complete catalogs compared to the VCV and provide a much less biased set of data. Under these approximations coincidence incompatible with isotropy at a level  $> 95\%$  has been found for both models and at almost all angular scales.

As for HiRes collaboration on the contrary a study using the matter tracer catalog 2MRS found no apparent coincidence between the the catalog and the arrival direction of CRs [142]. Their results were therefore claimed to be compatible with isotropy up to a 95% confidence level.

The two experimental results appears therefore to be diverging on their conclusions even though some consideration is necessary. First of all the detectors work in two different hemispheres seeing different regions of sky. For that reason potential sources seen by one detector might not be seen by the other. Secondly both experiments work with a relatively small data set and therefore none of them can conclude with absolute reliability on whether the UHECR sky is isotropic or anisotropic or if any correlation is present or not. Third, biases on the energy scale or in the analysis procedures might be also possible.

Another extremely important open issue is the UHECR composition. Also on this topic strong disagreement is present in the community. In fact, the Auger observatory claims a composition getting heavier toward the highest energies [81]. On the other hand again both HiRes and TA claim a very light composition along the entire energy interval [80][82]. The Auger collaboration seem to confirm this tendency both in the  $X_{max}$  measurement and on the oscillation of this parameter<sup>13</sup>. For completeness it should be noticed however that these results might be in contrast with the one about anisotropy published by the same collaboration. In case the same heavy composition

---

<sup>13</sup>In fact, since hadronic interactions in nuclei are expected to have higher multiplicity than in single protons a larger number of secondaries is produced at the first interaction. For that reason showers from nuclei are expected to reach the critical energy and their maxima before. Moreover thanks to the bigger number of secondary particles involved, also statistical oscillations are reduced. Therefore nuclei are expected to display smaller oscillations on the  $X_{max}$  parameter.

is maintained above  $5.5 \cdot 10^{19}$  eV in fact most likely no anisotropy should be visible. The HiRes collaboration showed instead a very light composition through the entire range both for  $X_{max}$  and for  $\Delta X_{max}$ . As for TA collaboration it seems to confirm HiRes tendency although the statistics on the higher part of the spectrum is still limited (as of 2012). Reason for this difference are most likely due to the different reconstruction procedures both in energy and in  $X_{max}$ . Another limit in composition studies is the fact that all the present detectors cover the spectrum up to an energy of  $5\text{--}6 \cdot 10^{19}$  eV while no indication is present on how the spectrum continues well above the GZK cutoff which also covers the range used for anisotropy studies.

To conclude some consideration on the spectrum is necessary. As already explained at the beginning of this chapter, in the early 2000's a big discussion was open on the discrepancy between AGASA and HiRes spectra. In fact the second one claimed the detection of the expected GZK cutoff [67] while AGASA denied it [143]. With the onset of hybrid detector techniques this issue seems to be solved with the introduction of a systematic uncertainty on the energy scale. As a matter of fact the present generation of detectors seem to be heading toward a suppressed spectrum above  $4 \cdot 10^{19}$  eV. In fact in addition to the above mentioned HiRes data both the Pierre Auger [144] and the Telescope Array [145][82] collaborations seem to agree on this feature.

However on the scientific interpretation of this cutoff no clear explanation has been found. As explained in their publication the TA collaboration seem to favor a dip scenario in which the observed cut off is due to photo pion production effect. In this picture the collaboration claims also the detection of a dip feature. This result would be therefore perfectly compatible with the very light composition detected by the collaboration. In this scenario extragalactic protons would interact with CMB through pair production and photo pion production generating respectively dip and cutoff.

On the contrary, in the Auger case, a little more complicated scenario seems to arise. In fact, if the heavier composition remains for confirmed no dip scenario is realistic anymore. Several possibilities are therefore open in this case. The most likely sees the cutoff as the combined effect of accelerator limits and photodisintegration. In this scenario the heavier composition arises as a rigidity dependent effect in the accelerator. As a result of that while the maximum energy for protons would be of the order of  $\sim 3\text{--}4 \cdot 10^{18}$  eV the maximum for iron nuclei would be of the order of  $\sim 10^{20}$  eV. In this model defined as "disappointing" by Alosio et al. [68][146] the end of the spectrum would be guaranteed to be slightly above  $10^{20}$  eV. As direct consequence no GZK effect would be present and therefore neither GZK neutrinos nor photons are produced. It must be stressed again that in order this model to be true no anisotropy should be present since intergalactic magnetic fields

would completely erase any correlation with sources at least given the Auger statistics. Therefore it must be stressed how the confirmation or rejection of the Auger anisotropy is of extreme importance also from the point of view of composition studies.

Another possibility to reconcile the Auger spectrum–composition discrepancy is the possibility, given the present Auger results, of a sudden change in the hadronic interaction at the extreme energies. The composition might therefore be light and the current interpretation of the  $X_{max}$  observable would be wrong.

To resume, as explained by Kotera and Olinto [90], given the present status two possible scenarios are most likely. The first assumes light composition associated with dip–cutoff spectrum. In this case, possibly the rise of some anisotropy could be observed with higher statistics. Both cosmogenic neutrinos and photons would be observable in this case and the maximum energy could reach even higher values. In this scenario even a re–hardening (the GZK recovery) of the flux at the most extreme energies ( $> 3 \cdot 10^{20}$  eV) might be possible under certain conditions.

The second scenario sees a heavy spectrum and a rigidity dependent cutoff. No anisotropy should be present unless a sudden change in the hadronic interaction is present or the density source is very low (see Takami [135]). The spectral shape would be much harder till  $2\text{--}3 \cdot 10^{19}$  eV where an abrupt cutoff takes place thanks to photodisintegration and accelerator limits. No recovery is observable in this case. Obviously GZK–neutrinos and photons will not be produced.

The future mission candidates should therefore aim at the solution of the puzzle just described. The investigation of anisotropy, spectra and compositions with a much higher statistics is again the guideline to be followed in the quest for UHECR sources. The first (and probably easiest) task for a mission would be the detection or rejection of anisotropy at a  $> 5\sigma$  level. Most likely a detector collecting an order of magnitude more events above  $5.5 \cdot 10^{19}$  eV with respect to the present detectors would be capable of solving this issue. The possibility of performing scanning through the entire sky would also be a valuable tool to avoid observational biases. Moreover an extremely important possibility would be the search for anisotropies selecting higher thresholds reducing the magnetic deflections. Finally the search for excess near the Cen–A or other near AGNs must be considered a priority to confirm or reject the Auger large angle correlation.

As for the composition the up to now mainly unexplored range above  $5\text{--}6 \cdot 10^{19}$  eV should be covered. The importance of this range lies in the potential anisotropy of the CR sky above  $5.5 \cdot 10^{19}$  eV. The combined result anisotropy–composition will hopefully help to constrain the production



and propagation models. Also the continuation of the composition studies up to higher energies might help to solve the problem of the discrepancy between HiRes-TA and Auger. For this purpose some superposition with lower ranges is mandatory for the calibration with present detectors. On the other hand the confirmation of the Auger scenario, (anisotropy associated with apparent heavy composition) might imply the failure of the hadronic model extrapolations or some tight limit on the source distribution density.

The last topic to consider is the one related with the spectrum. In order to distinguish between the different models a detailed knowledge of the shape of the spectrum is needed. For example the decision on whether the spectrum is more compatible with a dip or a photodisintegration rigidity-dependent model requires necessarily the reduction of the statistical errors above the cutoff. The search of a possible GZK recovery (which would confirm the GZK scenario) requires also the possibility to explore energy ranges  $> 3 \cdot 10^{20}$  eV. An interesting way to confirm or reject the GZK cutoff might be the reconstruction of spectra from different known sources (provided they are detected). The effects of the photo-pion production might affect more distant sources than near sources. Therefore the typical distance dependent GZK feature could be identified if a sufficient number of known sources is identified. To remember is the fact that, in case of a GZK identification, a reliable energy scale calibration as well an important test for all the reconstruction models would be automatically provided. Not to forget is the association of the GZK cutoff with a light composition population which would be directly confirmed in case of a GZK detection. The detection of pre-GZK sources ( $D \ll 100$  Mpc) could even allow a GZK-free access to the produced spectrum.

The potential of a space based UHECR mission appears therefore immediately as these missions can provide much higher exposure and cover equally north and south hemisphere. As already explained, this idea, originally formulated by J. Linsley [48] in 1981, proposes the detection of air shower fluorescence light from space (see Fig. 1.16 left panel). In this kind of detectors a wide FOV angle, fast and high sensitivity telescope would detect the UV fluorescence light emitted by extensive air showers (EAS). As we will explain in the next chapter the interaction of a primary of high energy with the atmosphere would start a cascade process. This process can be imagined as a cloud of particles traveling through the atmosphere. During this propagation process the EAS, mainly consisting of electrons, would deposit part of its energy in the surrounding atmosphere. Then, part of this energy will be emitted by excited nitrogen atoms in form of fluorescence photons. This isotropic emission is already used by several ground based detectors and will

be used by the next generation space based detectors. Moreover it is known that charged particles traveling in a medium with a velocity larger than that of light in that medium will emit Cherenkov light. This highly beamed photons will travel ahead and after being partly scattered will be reflected on the ground. As a matter of fact, one of the advantages of space missions is the possibility of detecting the Cherenkov ground–reflected component. In fact, for ground based fluorescence telescopes the scattered (and direct) Cherenkov component represents just a contamination of the fluorescence signal. In space based detectors on the other hand unlike the backscattered contamination the reflected component can give valuable information on the timing of the shower and consequently on the shower geometry. By detecting direction, luminosity and profile of the light curve generated by these showers it is therefore possible to infer energy, arrival direction and type of the particle with an acceptable uncertainty.

A UV telescope pointing down toward earth would survey at night time huge masses of atmosphere. A telescope of this kind can achieve exposures of the order of 1 Mly<sup>14</sup> or even higher. This must be compared with the 10 times lower exposure achievable by ground–based detectors. With a proper choice of the mission parameters is therefore possible to reach the sufficient exposure up to above 10<sup>20</sup> eV but still allowing a low enough energy threshold to guarantee superposition between ground and space detectors. Moreover it will be shown how a mission of this kind can satisfy tight requirements in terms of energy, arrival direction and  $X_{max}$  resolution necessary to potentially achieve the above mentioned scientific goals.

More in detail we will present a specific mission concept namely the Extreme Universe Space Observatory on board the JEM exposure facility of the ISS, JEM–EUSO. This mission consists of a  $\sim 2.65$  m diameter telescope attached to the Japanese module on the ISS. From the altitude of  $\sim 400$  km and thanks to a field of view of  $\pm 30$  degrees this instrument can survey an area on ground of 500 km diameter managing so to gather the required exposure. Moreover this instrument allows the possibility of tilting allowing so to maximize the exposure. The increase of the exposure will however be compensated by an increase in the energy threshold of the mission. Therefore a trade-off must be found in order to maximize the scientific output of the mission.

The main advantage of the JEM–EUSO mission can be intuitively visualized by watching at Fig. 1.16 (right panel) where the area surveyed by this telescope can be seen in nadir mode.

---

<sup>14</sup>1 Ly  $\equiv$  1 Linsley has been proposed as the unit of measure of exposure in UHECR science. This corresponds to 1 km<sup>2</sup> · steradian · year.

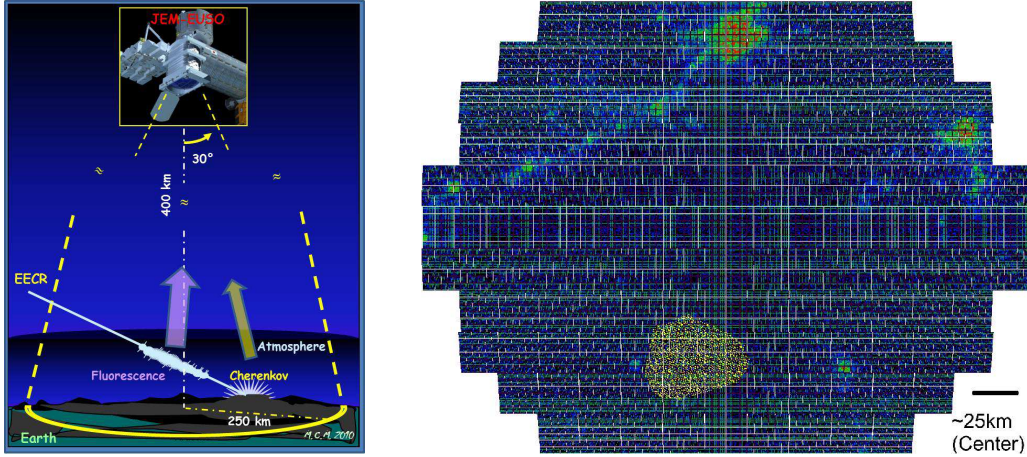


Figure 1.16: **Left Panel:** the observational principle of JEM-EUSO. The UHECR produces a cascade which by propagating through the atmosphere generates fluorescence and Cherenkov light. A UV telescope pointing downward can detect this light. **Right Panel:** a simulation of the background light detected by JEM-EUSO as would be above the Pierre Auger observatory. The Pierre Auger observatory is highlighted in yellow. The JEM-EUSO focal surface structure is also visible. Several cities are scattered around. On the right-low corner the scale is visible. Courtesy of K. Shinozaki.

As claimed by the JEM-EUSO collaboration [147] in order to achieve the above cited scientific results (anisotropy and possible source identification, determination of spectral shape, average composition as function of energy) several observational requirements have been defined. First the mission should be able of achieving an observational area of  $> 1.3 \cdot 10^5 \text{ km}^2$  over a period of at least 3 years with an observational duty cycle not smaller than 17%. The energy threshold should be low enough to guarantee a sufficient exposure under  $5.5 \cdot 10^{19} \text{ eV}$ . For a typical shower ( $10^{20} \text{ eV}$  60 degrees) then the angular resolution should be smaller than 2.5 degrees. The energy resolution is required to be smaller than 30%. Moreover in order to allow at least the capability of neutrino and photons discrimination from hadrons a minimal  $X_{max}$  reconstruction uncertainty of  $120 \text{ g/cm}^2$  is required. This is however a minimal requirement which should be certainly improved to give answer also about the mean mass of the hadronic component. A resume of the above mentioned requirements is given in Tab. 1.2.

Therefore, and to conclude, this thesis will be mainly devoted to the verification of these requirements. Some very basic conclusion on the scientific consequences of this study will be given. Nevertheless it must be noted that a full assessment of the scientific impact of JEM-EUSO requires more extended studies which are out of the scope of this thesis. This study will be therefore related to the capability of JEM-EUSO to extract energy and  $X_{max}$

Requirement	Value
Observational area	$\geq 1.3 \cdot 10^5 \text{ km}^2$
Mission duration	3–5 years
Observational DC	$\geq 0.17$
Full FOV 50% eff	$\leq 5.5 \cdot 10^{19} \text{ eV}$
Angular resolution	$\leq 2.5 \text{ deg}$
Energy resolution	$\leq 30\%$
$X_{max}$ resolution	$\leq 120 \text{ g/cm}^2$

Table 1.2: The JEM–EUSO requirements table is presented here. The collaboration assumes such values as needed to achieve mission success.

observables from the raw data. The angular reconstruction will be left for other studies. It will be checked if the detected statistics allows the achievement of the above mentioned targets. The detailed scientific interpretation of these results will be left for future work.

# Chapter 2

## Observational Techniques

The low flux of CRs above  $\sim 10^{15}$  eV makes their direct detection extremely problematic. In fact, just the use of large detector volumes can allow the measurement of such particles<sup>1</sup>. Given the extremely large detector areas ( $\sim 10^3$  km<sup>2</sup>) needed to observe particles above  $10^{20}$  eV, the only possibility to access such extreme energies is to use the Earth's atmosphere as a giant detector.

When high energy particles interacts with atmospheric nuclei a cascade process, usually defined extensive air shower (EAS) is started. The detection of the secondary particles and of the light emitted during the shower development, is used to reconstruct the energy, arrival direction and type of the primary particle. In fact, CR science above the knee energy is performed using large arrays of detectors, or systems of telescopes, measuring the development of such cascade events in the atmosphere.

In this context, JEM-EUSO aims at studying the most extreme region of the CR spectrum, above  $10^{20}$  eV, by detecting night-time the fluorescence light emitted by the EASs. With an area of  $\sim 10^5$  km<sup>2</sup> JEM-EUSO can monitor an instantaneous FOV about 2 orders of magnitude larger than any previously built detector.

The interaction processes, the most relevant shower features and the observational facts, for different types of primaries, are described in this Chapter. Furthermore, the fluorescence and Cherenkov emission mechanisms are described. The observables used to reconstruct the primary parameter will also be introduced. Eventually the detectors and the ground-based techniques will be briefly described before considering the JEM-EUSO mission.

---

<sup>1</sup>For example, in the range most relevant to JEM-EUSO (above  $10^{20}$  eV), fluxes are of the order of 1 particle per km<sup>2</sup> · sr · millennium.

## 2.1 Shower physics

Electromagnetic showers are triggered by a photon or an electron, and consist of a sequence of electromagnetic interactions. The two most important interaction processes involved in the electromagnetic cascade are bremsstrahlung and pair-production. Due to bremsstrahlung a charged particle interacting in the electromagnetic field of a nucleus, loses part of its energy emitting photons [52]. The energy loss is proportional to the particle energy. A concurrent process like ionization progresses on the other hand just logarithmically. Bremsstrahlung is therefore the dominant cooling process for electrons and positrons starting from a critical energy of  $\sim 10$  MeV. The radiation length for this process in air is approximately  $X_0 \sim 37$  g/cm<sup>2</sup> [52].

Pair-production applies for high energy photons: a photon interacting in the field of a nucleus can produce an electron-positron pair. The cross section for this process dominates above  $\sim 10$  MeV. Pair-production cross section increases moderately with energy above  $\sim 10$  MeV and translates to a mean free path of  $\frac{9}{7} \cdot X_0$  in air.

The combination of such processes shapes the EAS. As a result of the interaction of a high energy photon with the atmospheric nuclei, an electron-positron pair is generated. These particles radiate in turn via bremsstrahlung. The process continues iteratively with the number of involved particles growing like  $2^n$ , whereas  $n$  is the number of steps.

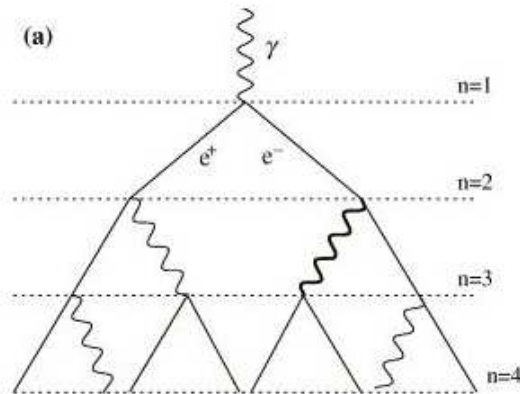


Figure 2.1: A schematic view of the initial steps of an electromagnetic shower. Every step either pair-production or bremsstrahlung is occurring. Picture from Matthews [148].

Since the energy must be conserved while the number of involved particles increases, their energy becomes lower until the electrons are not any more able to radiate via bremsstrahlung. In Fig. 2.1 a schematic and simplified view of the cascade process is shown. Ionization losses occur during the entire development of the EAS. Thanks to this interaction the charged particles of the shower deposit energy in the atmosphere. As already said this process leads to energy losses which are proportional to the logarithm of the energy. As the energy increases the fractional energy loss decreases until it becomes negligible compared to the energy. Provided the energy is high enough, pair-production and bremsstrahlung will therefore increase the size of the shower. Such a process can be therefore considered to be almost adiabatic till the critical energy ( $\epsilon_0 \sim 10$  MeV) is reached. After that, the only relevant process are ionization–excitation losses.

The electromagnetic cascade can be therefore visualized as a moving cloud of electrons, positron and photons. As long as the energy of the particles remains above the critical energy the cloud grows in size thanks to pair-production and bremsstrahlung. After this threshold has been reached the shower dies out. For this reason, the higher the energy of the primary is, the deeper the maximum of the shower occurs given the higher number of steps required to cool down the secondary population. The maximum of the shower results therefore to be proportional to the logarithm of the energy as shown as follows

$$X_{max} \propto \ln \frac{E}{\epsilon_0} \quad (2.1)$$

whereas  $\epsilon_0$  is the critical energy. Generally, the size of the shower is proportional to the energy of the primary. This is a direct consequence of energy conservation and of the predominance of bremsstrahlung at high energies, with respect to ionization losses.

Hadronic showers, generated by hadrons interacting with the atoms of the atmosphere, follow a different development. After the first interaction, several other types of particles like pions and other hadrons are produced [83]. Similarly to the electromagnetic processes described before, those particles are capable of generating several subsequent interactions. In the iterative process an increasing number of particles is produced.

More in detail neutral pions  $\pi^0$  will, thanks to their extremely short lifetime, decay immediately into photons.

$$\pi^0 \rightarrow 2\gamma \quad (2.2)$$

Through this channel, which accounts for  $\sim 1/3$  of the produced pions, basically at each step part of the shower's energy goes to electromagnetic sub-showers.

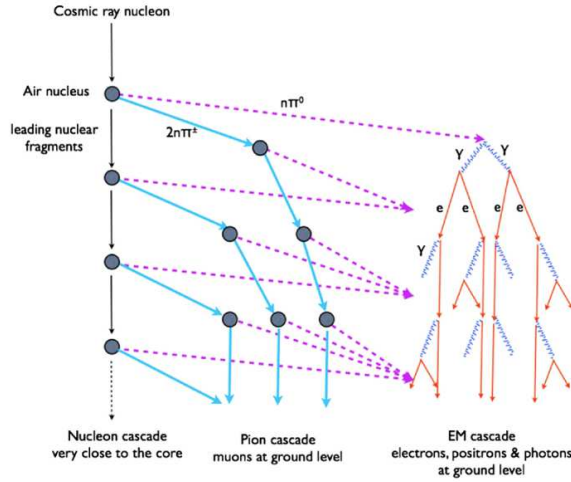


Figure 2.2: The schematic representation of an hadronic shower process. After the first interaction of the CR hadron with an atmospheric nucleus baryons, charged and neutral pions are produced. From the neutral pions, the electromagnetic sub–shower arises. The muonic component comes from the charged pion’s decay. Plot from [89].

In the interaction process also charged pions  $\pi^\pm$  are produced. Due to relativistic time dilation, the charged pions undergo several interactions before decaying. In these interaction processes several other generations of hadrons are produced. When the energy of the hadrons in the cascade is low enough, the  $\pi^\pm$  decay as it follows:

$$\pi^+ \rightarrow \mu^+ + \nu_\mu \text{ or } \pi^- \rightarrow \mu^- + \bar{\nu}_\mu \quad (2.3)$$

A non negligible part of the shower’s energy goes therefore into neutrinos and muons. Once the charged pions start decaying the hadronic component of the shower is completed and again the rest of the shower is electromagnetic. A schematic view of the hadronic shower development is given in Fig. 2.2 left panel. The total amount of energy that goes into muons and neutrinos can be easily estimated to be roughly 10% of the primary energy around  $10^{19}$  eV.

Due to the higher multiplicity of the hadronic interaction, the shower cools at much faster rate than in the electromagnetic case. The electromagnetic sub–showers will, therefore, reach the critical energy at an earlier stage than in the pure–electromagnetic case. In other words, hadronic showers reach their maximum earlier than in the pure–electromagnetic case. The previous qualitative considerations apply also in the case of a primary nucleus. In this case, all the nucleons share part of the primary energy and so the cooling



process is even more rapid than in the case of the proton. As a matter of fact, the depth of the maximum is used as an observable to discriminate different type of particles. To summarize, photons reach maxima deeper than protons, whose maxima are reached later than nuclei.

In addition we notice that the higher multiplicity of interactions involving nuclei makes statistical oscillations in the first steps less significant compared to the case of protons. Therefore, nuclear showers reach their maxima within a much more constrained depth range than protons. Clearly, these observables can be measured just by techniques where the longitudinal development of the EAS is reconstructed. Fluorescence detectors are able to observe the longitudinal development. This feature can be schematized in Figs. 1.14 and 1.15 of Chap. 1.

The statistical oscillations and measurement uncertainties make however impossible to determine the mass of the hadronic particle. Discrimination is just possible on a statistical basis over the largest possible sample of events. The only possible statement achievable is therefore how heavy on average the composition is.<sup>2</sup>

The last part of the section will be devoted to neutrinos. The high mass of the weak interaction mediating bosons causes the suppression of the neutrino cross section [52]. Neutrinos are therefore extremely penetrating particles. The cross section of neutrinos increases however as a function of the energy. For this reason, the probability of an interaction with the atmosphere is not negligible anymore at the ultra high energies. However, even at the most extreme energies neutrinos always have a considerably smaller cross section than protons. For this reason the depth of the maximum will certainly be a valid discriminator between neutrinos and hadrons. Extremely deep showers will therefore have to be interpreted as neutrinos.

As it has been shown, key information can be extrapolated from the shower structure. For example the measurement of the depth of the maximum is essential to identify both the mass and the energy of the particle. To determine the absolute size of the shower is also extremely important to reconstruct the primary energy. Moreover the shower develops collinearly with respect to the primary direction. For that reason a space–time fit can be used to reconstruct the trajectory of the particle.

---

<sup>2</sup>A very important exception is however represented by neutrinos and photons which are clearly separated from the hadrons. In this case statistical oscillations are significantly smaller than the separation between the species.

## 2.2 Fluorescence and Cherenkov emission

When a CR traverses the atmosphere generating an EAS, fluorescence and Cherenkov photons are produced. Charged particles, propagating relativistically through the atmosphere, deposit energy through ionization and excitation losses. As a result of these processes the molecules are left in excited state. Following the consequent de-excitation, a fraction of the energy is radiated as fluorescence photons.

As can be seen in the seminal PhD thesis of Bunner [33], the processes involved are essentially of two kinds. The first one is a simple one-step de-excitation process in which a photon is emitted, by a collisionally excited molecule. In the second type, excitation is induced by slow electrons emitted during ionization. Two different transitions between the energy levels of molecular nitrogen ( $N_2$ ) correspond to the two processes. In the first case the transition occurs between states of molecular nitrogen ( $N_2$ ), while in the second, it occurs between states of positively ionized molecular nitrogen ( $N_2^+$ ).

Several concurrent processes must be also taken into account. For example, collisional quenching removes energy from the excited atom by means of collisions with other molecules. Moreover, molecules can also de-excite through internal mechanisms by redistributing their excitational energy in different modes or to lower electronic shells. For this reason, pressure and temperature of the air are essential to estimate the amount of produced light. The composition of the atmosphere is also of deciding importance to quantify the emission. As explained in [33], oxygen ( $O_2$ ) molecules are excellent quenchers due to their particular electronic structure.

In Fig. 2.3 the fluorescence spectrum as published in [33] is shown. As can be seen the dominant lines are concentrated between 290–430nm. Shorter wavelengths are strongly suppressed by ozone absorption.

Several studies have been published to quantify the fluorescence yield<sup>3</sup> in air. Also the knowledge of the dependence of the yield on pressure, temperature and composition of the gas has been subject of deep experimental investigation. We refer to the study of Nagano et al.[149] and Kakimoto et al.[150] for details. Both studies measured the yield by detecting the light emitted by gases traversed by electron beams. Such beams, depending on the energy, have been produced by radioactive sources and synchrotron accelerators. The measurements were done in different condition of pressure, temperature and for different energies. The altitude and temperature depen-

---

<sup>3</sup>By fluorescence yield it is usually meant the amount of photons per unit length and per particle produced in some medium by the ionizing particles.

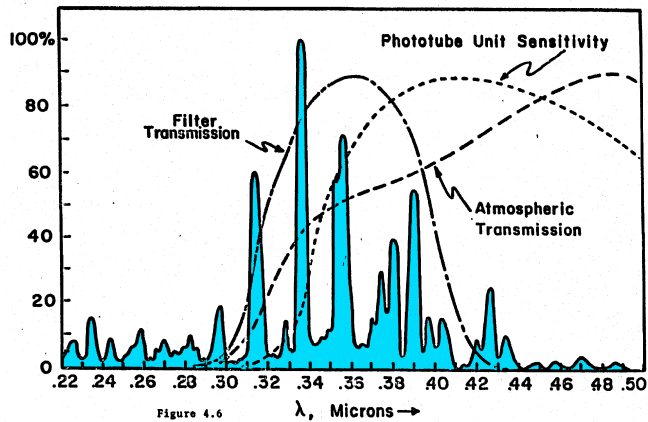


Figure 2.3: fluorescence spectrum as published by Bunner [33]. Superposed with the emission lines the atmospheric transmission curve can be observed together with the used phototube sensitivity. A filter is usually applied in air fluorescence observations in order to reduce contamination from other wavelengths.

dence have then been extrapolated by using standard atmospheric parameterizations. In [149], a separated study for different wavelengths (15 bands in the 290–430nm range) has been also performed. A fluorescence Yield of  $\sim 4$  ph/m/part detected at 1013 hPa and 20 C is reported in [149] More detailed results are shown in Fig. 2.4 (right panel) where the altitude dependence can be seen.

As it can be seen in Fig. 2.4 the fluorescence yield tends to increase up to  $\sim 10$  km before starting to decline again. At the highest altitudes a yield  $\sim 25\%$  of that at sea level is estimated. The Nagano's results refer to a wavelength range 300–406 nm while the above cited  $\sim 4$  ph/(m·part) is for 300–430 nm.

Another relevant feature is seen in Fig. 2.4 (right panel), in which the fluorescence yield as function of the electron beam energy is shown [150]. Superposed to the measured yield (left Y-axis), the energy deposit<sup>4</sup> curve (right Y-axis) is shown. The two vertical axis have been scaled to have optical superposition between the curve and the experimental point at  $\sim 1$ MeV. At higher energies both the energy loss and the yield tend to slightly

<sup>4</sup>By energy deposit is meant the energy deposited by a single electron in one slant depth by means of ionization–excitation. It is measured in  $\text{eV}/(\text{g}/\text{cm}^2)$ .

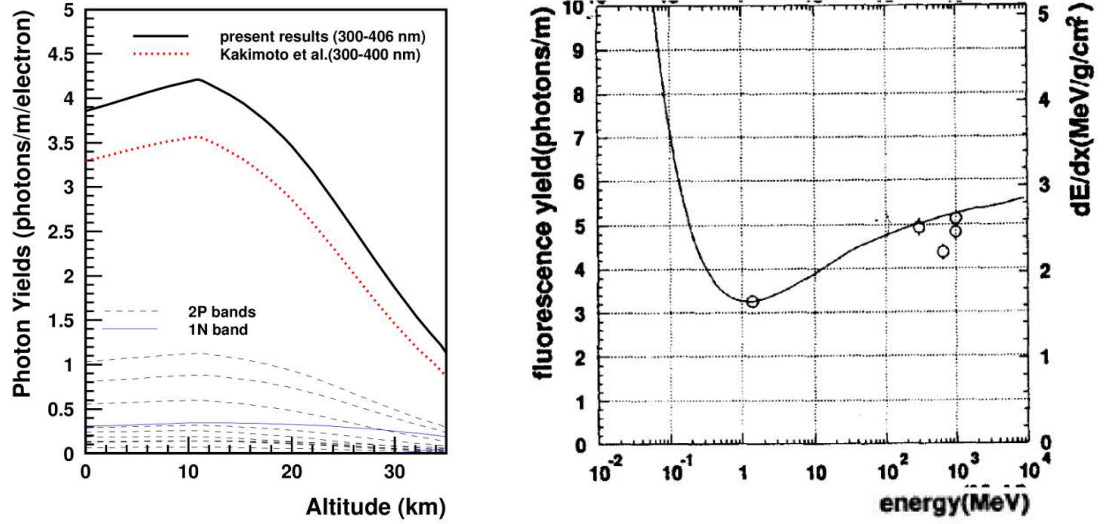


Figure 2.4: **Left panel:** Fluorescence yield as a function of the altitude assuming US standard 1976 atmosphere for 0.85 MeV electrons as published by Nagano et al.[149]. The range assumed here is 300–406 nm. For comparison the same curve for Kakimoto et al.[150] is also shown. Contributions from different bands are shown as thinner lines. Taken from Nagano et al. [149]. **Right panel:** fluorescence yield as a function of energy as measured by Kakimoto et al.[150]. Superposed with the experimental points the energy deposit in air can be observed on the right axis.

increase.

Fluorescence is not the only light component associated to the EAS. Charged particles passing through a medium emit Cherenkov light if their speed is larger than the speed of light in the medium [52]. Cherenkov light is emitted under a narrow angle in the direction of propagation of the particle, and therefore is collinear to the shower development. The emitted power per unit length and per unit frequency is described by the so called Frank–Tamm formula [4]:

$$I(\omega) = \frac{\omega e^2 v}{4\pi\epsilon_0 c^3} \left( 1 - \frac{c^2}{n^2 v^2} \right) \quad (2.4)$$

In Eq. 2.4  $\omega$  is the pulsation of the light wave,  $e$  and  $v$  the electron’s charge and speed and  $n$  the refractive index of the medium. Shorter wavelengths emission is more intense than longer. The total Cherenkov yield can be calculated by integrating Eq. 2.4 over the entire spectral range.

For air fluorescence detectors the Cherenkov component in general contaminates the fluorescence signal, introducing systematic effects. However, a very interesting possibility for space–based fluorescence detectors is the detection of the Cherenkov diffusively reflected component. When the Cherenkov beam reaches the Earth surface a reflection bump is produced and may be

detected in the light curve associated to the EAS. The timing of this bump adds precious information on the position and timing of the shower during its entire development. Showers for which the Cherenkov reflection is observed represent therefore a sub-sample of good quality events for space-based fluorescence observations.

As a conclusion, the application of the above mentioned knowledges on fluorescence and Cherenkov emission makes the shower development measurable by fluorescence detectors. However, still large uncertainties must be taken into account due to the limited knowledge over the complicated atmospheric structure. On these principles is based the air fluorescence technique which will be described later in this Chapter.

### 2.2.1 Photon propagation in atmosphere

Essentially three processes affect the propagation of UV photons in atmosphere. The first process is Rayleigh scattering, in which air molecules act as point-like scattering centers. The cross section of Rayleigh scattering follows  $\sim 1/\lambda^4$  [35].

The second relevant process is Mie scattering [36]. While Rayleigh assumes point-like scattering centers, in Mie scattering larger suspended particles act as scattering centers. Aerosols and dust particles interact with light and cause the partial loss of photons. The monitoring of the amount of clouds, aerosols and pollution is of extreme importance to quantify the effect of Mie scattering on the EAS signal light. This component is strongly variable. Also Mie scattering tends to decline at longer wavelengths although at a much slower rate than Rayleigh.

The third process, which however modifies mostly the Cherenkov spectrum is ozone absorption [37]. This gas is known to concentrate mainly in the high layers of the atmosphere. Ozone molecules  $O_3$  absorb UV photons, and dissociate in molecular and atomic oxygen (respectively  $O_2$  and  $O$ ). This process is relevant in the range between 200 and 330 nm. For this reason, air fluorescence observations are limited to the range above 300–330 nm.

## 2.3 Background in atmosphere

Several types of background affect space-based fluorescence detectors. Between them both natural and artificial sources must be taken into account. As natural sources a vast sample of phenomena like airglow, Earth albedo, zodiacal light, moon light, stars, aurora, transient luminous events, lightnings and meteors can be mentioned. In the second category we find all the light

sources related to anthropic activity like city light, planes, satellites and so on. In both natural and artificial sources a further distinction can be done according to the temporal evolution of such phenomena. Some of them are of transient nature while others are stable. Also of fundamental importance is the spatial distribution and strength of such sources.

Depending on the above mentioned features both ground and space based detectors have to develop techniques in order to reject these contamination sources by maintaining high acceptance of real events. In Chap. 4 the specific JEM–EUSO approach to the background rejection problem will be described in detail. In the following however we give a qualitative description of the physics of the most important background components.

A persistent source of background is airglow [38][39]. This phenomenon consists essentially in the production of UV light in the high layers of the atmosphere ( $\sim 100$  km altitude). At that altitude in fact, as a result of solar light exposure dissociation of molecular oxygen ( $O_2$ ) occurs. As a result of recombination then, during night time the newly formed  $O_2$  molecules, left in an excited state, will emit photons. Such background component constitutes the most important source of contamination for fluorescence detectors. Seasonal, geographical and daily variations are possible but a certain amount of such a background is always to be expected. Additionally to that, part of the sky background is caused by planets, stars and zodiacal light backscattered photons. This component is also relatively constant.

Another very deciding source is related to auroras [39]. Although geographically limited to polar regions, such a light–emitting phenomenon might have considerable impact on fluorescence observations. In fact, compared to airglow and star’s background such a source can reach intensities several orders of magnitude larger. Auroras can reduce the exposure of space–based detectors especially in the case of high latitude orbits.

Backscattered moonlight, limits the observational time of both ground– and space– based fluorescence observatories. In some conditions in fact, the Moon light can increase the background level by large factors. moonlight is however a predictable source, and its impact on the exposure can be precisely calculated.

The most unpredictable and tricky background sources are however all the transient luminous phenomena [40]. Such phenomena are more representative for space based detectors given the possibility of observing in cloudy conditions. In this vast class of events we find lightnings, meteors, sprites, elves, and many others. The frequency, luminosity and time duration range over several orders of magnitudes and typically represent a challenge for hardware and data analysis. Lightnings could even compromise the functionality of detectors due to their extreme intensity and unpredictable nature. Space–

based missions have to cope with such events with a dedicated trigger logic and solid protection functions. The peculiarity of each category must be therefore analyzed. Fortunately, the time scale of EAS events ( $\sim 100\mu\text{s}$ ) is much shorter compared to such transient events ( $\gtrsim 1\text{ ms}$ ). Another discriminating factor is in the linear development of showers. Furthermore, the much higher intensities produced by the above mentioned phenomena provides an additional selection criterion. Moreover such events are quite rare and have been estimated by the JEM–EUSO collaboration to imply  $\sim 2\%$  loss of observational time [177]. Also to mention is the quite limited geographical and seasonal distribution of such events.

Finally in the man-made sources like cities, ships, planes and others can be mentioned. Probably space based missions measurements will be limited in relatively small portions of the Earth’s surface. Most likely Europe, Japan, eastern China, US east and west coasts will be extremely challenging from the observational point of view. On the other hand, in the vast majority of the Earth’s surface a quite reduced light contamination can be expected. The detailed mapping of such sources and dedicated recognition algorithms for the unpredictable man-made component must be developed in the framework of Space based missions. An analysis of such a kind of sources can be found in [177].

## 2.4 Detectors

This section is devoted to the description of the current UHECR detection techniques. As we have seen, EAS produce detectable amounts of fluorescence and Cherenkov light. Systems of telescopes are currently operating to observe such an emission to reconstruct the shower profile. The arrival of the secondaries on ground will also offer a possibility for the shower detection. Both particle and fluorescence detectors are therefore presently in operation.

As examples of past and present ground particle detectors Haverah Park [41], Pierre Auger Observatory [46], Telescope Array (Surface), Volcano Ranch, Yakutsk, SUGAR and AGASA [45] can be mentioned. All the above cited observatories are characterized by arrays of detectors deployed on extended surfaces. These arrays have different extension and detector density. Typically arrays aiming at higher energies will require a less dense sampling due to the much higher number of secondary particles involved and to the much wider extension of UHECR Showers. On the other hand the steeply declining flux toward higher energies forces the increase in the dimension of such arrays at the extreme energies. For example the Pierre Auger surface detector covers a surface of  $\sim 3000\text{ km}^2$ . In this array each of the 1600 single units is



Figure 2.5: **Left panel:** the Pierre Auger fluorescence detector. Taken from [151]. **Right panel:** the Telescope Array fluorescence detector. Taken from [152].

separated by  $\sim 1500$  m allowing the achievement of an aperture of  $\sim 7000$   $\text{km}^2 \cdot \text{sr}$  above  $\sim 10^{18}$  eV.

Although similar, the above mentioned detectors show some significant difference in their basic principles. For example, some of them are based on plastic scintillators some other use water Cherenkov tanks. In the first group detectors like AGASA, Yakutsk, Volcano Ranch and Telescope Array (Surface Detector) can be mentioned. In the second group Haverah Park and Auger (Surface) are of significant importance. Another class of detectors in the UHECR field are presently water Cherenkov detectors. In this kind of detectors the charged secondary particles produce Cherenkov light directly in the tank's water which is detected by photomultipliers.

The other main family of detectors are the fluorescence telescopes. HiRes [44], Telescope Array and Auger (Fluorescence Detector) use this technique. Essentially these observatories consist of a system of several wide angle telescopes that, by monitoring the atmosphere night-time, aim at the detection of EAS. Usually each telescope consists of several mirrors focusing the UV light on a fast camera. Examples are shown in Fig. 2.5.

As a matter of fact, both Auger and TA have very similar structures basically consisting of a system of hexagonal mirrors and a PMT camera. Auger use a Schmidt optics which combines both mirrors and a corrector lens at the entrance pupil of the telescope. In both cases UV filters are deployed on the PMTs in order to reduce contamination from wavelengths outside the 300–400 nm range. In both telescopes the signal is digitized and after that the recognition algorithms are applied. Both detectors aim at the detection of fast moving tracks in the sky. For that reason, after trigger thresholds on the single pixels have been applied some clustering pattern is searched. At the end of this multiple stage selection a trigger signal might be issued. Following



the trigger, data are sent to the control center and further analyzed. Several fit procedures are applied to reconstruct the arrival direction of the CR. The correction of atmospheric absorption and Cherenkov contamination as well as the estimation of the fluorescence yield is done at this stage. As a result of the final reconstruction procedure, the arrival direction, energy and  $X_{max}$  of the particle are calculated.

Several calibration methods are applied in the mentioned UHECR observatories. In fact, both Auger and TA make use of laser facilities and IR cameras to sound the atmospheric conditions. In this way the presence of clouds and aerosols profiles is constantly monitored. Balloons offer the possibility of direct in situ measurements of the atmospheric conditions. At the Telescope Array site an electron accelerator is used to calibrate directly in atmosphere the value of fluorescence yield. At last, of great help is the presence of the surface detector which in both these observatories provides a valuable information for the arrival time and position on ground of the shower.

Although the size of the ground–arrays is already enormous, it is largely believed that next generation of UHE observatories requires at least an order of magnitude increase in the exposure, and especially at the highest energies. It appears clear how a complete change of strategy is necessary since the required exposure can be just achieved only if surfaces of the order of  $\sim 10^5$  km<sup>2</sup> are monitored. Such exposures are unlikely to be reached by ground–based detectors. The application of the now mature fluorescence technique from space is the next frontier in experimental studies of the UHECRs.

## 2.5 JEM–EUSO

The use from space of the fluorescence technique was proposed for the first time by Linsley in 1981 [48]. Basically an UV telescope monitoring the Earth’s atmosphere from above can detect the light emitted by the EAS propagating into the atmosphere. This idea is at the core of the JEM–EUSO mission. More in detail, the JEM–EUSO instrument consists of an UV telescope attached to the JEM exposure facility of the International Space Station<sup>5</sup>.

The JEM–EUSO mission is currently developed by an international collaboration gathering about 300 scientists from 13 countries (as of 2012). The mission is developed to meet a launch date in 2017, and to operate for at least 5 years. JEM–EUSO will detect the air fluorescence signal of the EASs from an altitude of 400 km. The JEM–EUSO telescope will monitor the

---

<sup>5</sup>This is the exposure facility of the Japanese module of the ISS.

atmosphere during night time. From the ISS altitude, with a FOV of  $\pm 30$  degrees, the monitored area of such a detector is  $\sim 10^5 \text{ km}^2$ , two orders of magnitude larger than ground based arrays. The instrument can be tilted increasing the monitored area by another order of magnitude (even though at the price of a higher energy threshold). For these reasons, JEM-EUSO is particularly suited for measurements on the most extreme part of the spectrum ( $\geq 10^{20} \text{ eV}$ ) where ground-based detectors would not detect enough statistics.

According to the current baseline, JEM-EUSO will observe for 3 years in Nadir mode, while the remaining 2 years it will be tilted. JEM-EUSO aims at covering a wide spectral range: from the trans-GZK ( $\sim 3 \cdot 10^{19} \text{ eV}$ ) region to the most extreme (and largely unexplored) parts of the spectrum ( $3 \cdot 10^{20} \text{ eV}$ ).

The fluorescence technique is relatively mature and do not pose a major challenge applied in space-based missions. Several differences between ground- and space-based detectors have however to be mentioned. Space detectors observe EAS from a larger distance than in the case of ground arrays. This makes the signal scale like  $1/d^2$  whereas  $d$  is defined as the distance of the shower from the detector. Tougher requirements must be satisfied and the background rejection algorithms must cope with a more severe environment. However, a significant advantage of such a concept is the limited uncertainty on the distance of the shower from the detector. This is because the shower develops in the lowest 10–20 km of the atmosphere, a negligible amount if compared with the 400 km altitude of the ISS. The reduced proximity effect doesn't eliminate the uncertainty on the atmospheric absorption but reduces the geometrical one to the minimum. In addition the much larger distance allows to monitor the entire development of the shower event from the first interaction till end. This is a great advantage compared to ground-based fluorescence telescope where just part of the shower is usually detected. In this way an important systematic effect on the profile of the event is removed. Space-based missions can observe in cloudy conditions, which is out of the range of the present arrays. In fact at least for low clouds, the highest part of the shower development can be observed from space. Another basic advantage of the space approach is in the almost uniform exposure which can be achieved by space-based missions, which in addition monitor the entire sky.

JEM-EUSO consists of a refractive optics based on Fresnel lenses[147]. Its diameter is 2.65 m with a cut side of  $\sim 1.9 \text{ m}$ . In order to manage the accommodation on the HTV transport vehicle [175], an extendable structure has been developed. In its extended configuration JEM-EUSO has therefore a length of  $\sim 3\text{--}3.5 \text{ m}$ . The Fresnel lens structure has been preferred in order

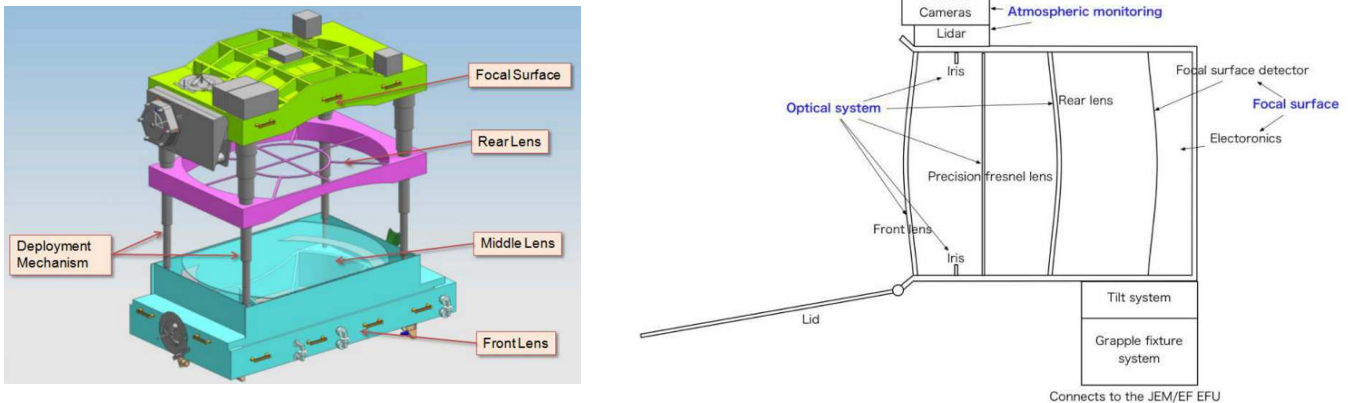


Figure 2.6: the JEM-EUSO optics structure. The triple lens structure is shown here. Behind the focal surface the data processing electronic is mounted. In the left panel the extendable structure and the lens supporting frame is visible. Attached to the external part of the detector both LIDAR and Infrared Camera are visible. Taken from [147].

to cope with the requirements of wide FOV and relatively compact structure.

As can be seen in Fig. 2.6, the JEM-EUSO optics consists of a system of three parallel Fresnel lenses. Essentially, a front and rear curved Fresnel lenses will focus the light while a central planar precision lens will correct vignetting and chromatic aberrations. The material of the lenses will most likely be PMMA<sup>6</sup> at least for the rear and middle lens. Alternatively a similar material called Cytop<sup>7</sup> might be used for the front lens given its better chemical properties. In fact, Cytop proved to be more resistant to the space environment and therefore might guarantee a longer lifetime. Cytop has also a better transparency. The use of Cytop is however still under investigation given its higher density, fragility and cost. Two different optics configurations are therefore under study: the PPP and CPP configurations. In the PPP baseline three PMMA lenses are used, while the CPP advanced option foresees a Cytop front lens. The lens structure is organized in several segments to ease the production, transport and to increase robustness. As shown in Fig. 2.6, an iris is present to suppress vignetting effects. To protect the photo-detection components from strong illumination, an openable lid is present on the top of the telescope. Band-pass filters will be glued directly on the PMTs photocathodes. This is necessary to cut photons outside the 300—

<sup>6</sup>This acronym means Poly-Methyl Methacrylate. It represents a plastic material particularly suited for such kind of applications.

<sup>7</sup>Amorphous Perfluoro-Polymer produced by the Asahi Glass co. ltd. Another plastic material similar properties compared to PMMA. See also <http://www.agc.com/english/chemicals/shinsei/cytop/about.html>

400 nm range. As baseline for JEM–EUSO the Schott BG3 absorption filter is selected<sup>8</sup>.

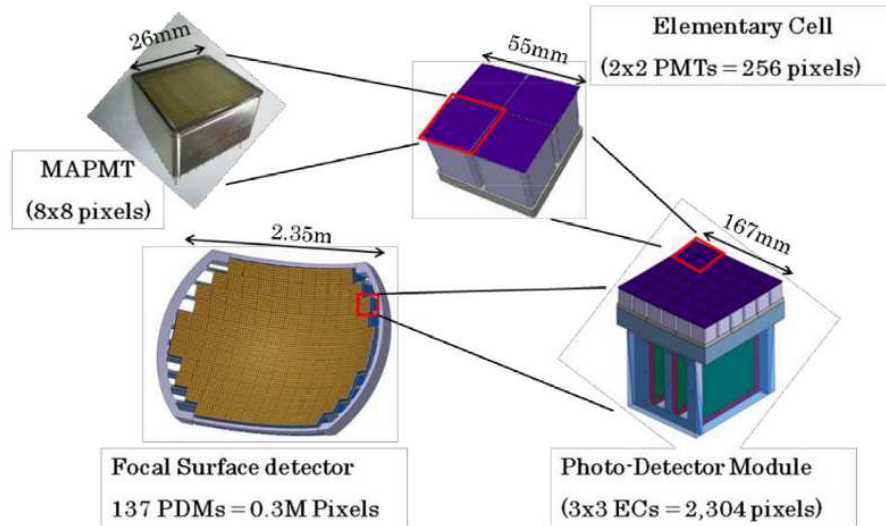


Figure 2.7: a sketch of the JEM–EUSO focal surface structure. The entire focal surface consists of  $\sim 3 \cdot 10^5$  pixels,  $\sim 5000$  PMTs,  $\sim 1200$  ECs and 137 PDMs. Taken from "Report on the phase A study 2010" of the JEM–EUSO collaboration[147].

Photons are focused onto a focal surface where the detection modules are deployed. The basic detector unit is the Multi–Anode Photomultiplier (MAPMT) R11265–M64 of Hamamatsu Photonics. An MAPMT consists of an ultra–bialcali photo–cathode and of a metal channeldynodestructure of 12 stages which provides high gain at a given high voltage of 0.9 kV. They have 64 pixels disposed in an 8X8 square layout. The typical size of a MAPMT is  $\sim 26 \times 26$  mm. Each pixel has a size of  $\sim 3 \times 3$  mm which allows a  $\sim 0.07$  degrees angular resolution. The quantum efficiency of the PMT is wavelength dependent and varies from a maximum of 42% and a minimum of 30% in the range 290–450 nm. Thanks to several improvements the cross talk<sup>9</sup> is negligible while a collection efficiency<sup>10</sup> of 80% has been achieved.

<sup>8</sup>See also [http://www.schott.com/advanced`optics/english/download/schott\\_bandpass\\_bg3\\_2008.e.pdf](http://www.schott.com/advanced`optics/english/download/schott_bandpass_bg3_2008.e.pdf)

<sup>9</sup>The cross talk identifies the fraction of events which are going to be misidentified as belonging to one pixel but which are in reality generated by photons hitting another one. As a matter of fact, a kind of matrix can be imagined where each number identifies the probability of one pixel to issue a count as a result of a photon landing somewhere else.

<sup>10</sup>The collection efficiency is the fraction of photoelectrons who eventually manage to generate a cascade reaching the anode.

The operation gain<sup>11</sup> is  $\sim 10^6$ .

On the entire focal surface about 5,000 PMTs, for a total of  $\sim 3 \times 10^5$  pixels, will be deployed. Such a huge number of sensitive elements and their geometrically large surface distribution requires the organization of several hierarchical modules. The lowest level of the modular structure is the elementary cell (EC). It consists of 4 PMTs arranged in  $2 \times 2$  squares. At the EC level the readout of the PMT outputs is performed. In this unit an ASIC [153][154] performs the digitation of the current pulses. The ASIC is operated normally (for low fluxes) in photon counting mode. For the higher fluxes, a charge-to-time conversion on the PMT output current is performed. Through measuring the time duration of the pulse is therefore possible to have information on the count rates. For the charge-to-time mode 8 channels of preamplifier output are integrated together. The count integration is performed for one gate time unit (GTU), a predefined time frame, nominally set to  $2.5 \mu\text{s}$ . This is the time frame in which both photon counting and charge-time mode will be integrating. In order to allow single counting to have a reasonable linearity a time resolution of  $\sim 10 \text{ ns}$  is achieved.

The next modular element is the Photo-Detector Module PDM [155]. This unit includes 36 PMTs, 9 ECs corresponding 2304 pixels arranged in a square layout of  $\sim 17 \text{ cm}$  side. At this level an FPGA is implemented to execute the first level trigger. The first level trigger search for persistency at EC level on the digitized data which have been sent by the ASICs. The algorithm has the duty to perform data selection to reject background.

The next logical unit is the Cluster Control Board (CCB) [156]. On the entire focal surface 18 such boards are implemented. Signals from 8 PDMs are redirected to the CCB where the second level trigger is performed. Here the presence of patterns resembling moving bright spots on the focal surface is searched.

The final logical stage is the on-board data processing system, the SCU [157]. The SCU manages the entire instrument: main processing via the on-board CPU, data storage, communication interfaces with the ISS, house-keeping and interfaces for event acquisition. The CPU has the task to perform the instrumental operation. The power-off and -on signals of all the subsystems, calibration, data acquisition, selection of trigger mode, house-keeping monitoring, contingency planning, data read-out and down-link will be controlled by this unit as well as the real-time management of the data to be sent to ground.

---

<sup>11</sup>By gain the ratio between the anode current and the generated photoelectrons is defined. It describes the amount of charge generated in the passage between dynodes as response to one single photoelectron.

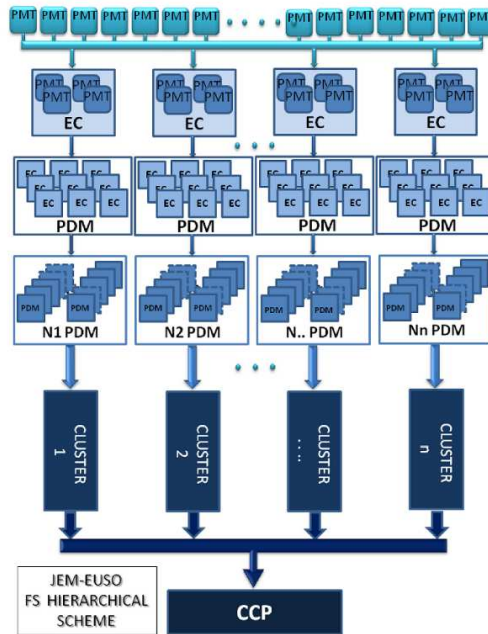


Figure 2.8: The JEM-EUSO electronics hierarchical structure. The most elementary components are PMTs. Output signals will be collected by ECs where single counting or charge–time integration is done. At the PDM level the first level trigger is performed. After the trigger signal is issued the cluster will perform the so called second level trigger. Once the signal satisfies also the conditions for the CCB trigger the processing unit decides about down–link and instrument functions. Taken from ”Report on the phase A study 2010” of the JEM–EUSO collaboration[147].

All the elements of both Focal Surface and lens must be arranged in a metallic–frame structure. Of fundamental importance will be the test on the stability under vibrations and temperature variations. In the same way the radiation hardness of all the components must be assessed together with the in–vacuum thermal stability.

The calibration of the instrument is performed at different stages during the entire mission life–time. A ground–based calibration of the instrument must be performed. The response of the instrument to known light sources will be measured as well as the optics efficiency and spot size measurement for various incident angles. Furthermore built–in LED sources will provide the possibility to perform some calibration during the flight time. Such elements with different proper wavelengths will be put on the internal face of the rear lens’s frame structure. During an operation in space, JEM–EUSO will be calibrated using ground light flashers and laser stations installed in various

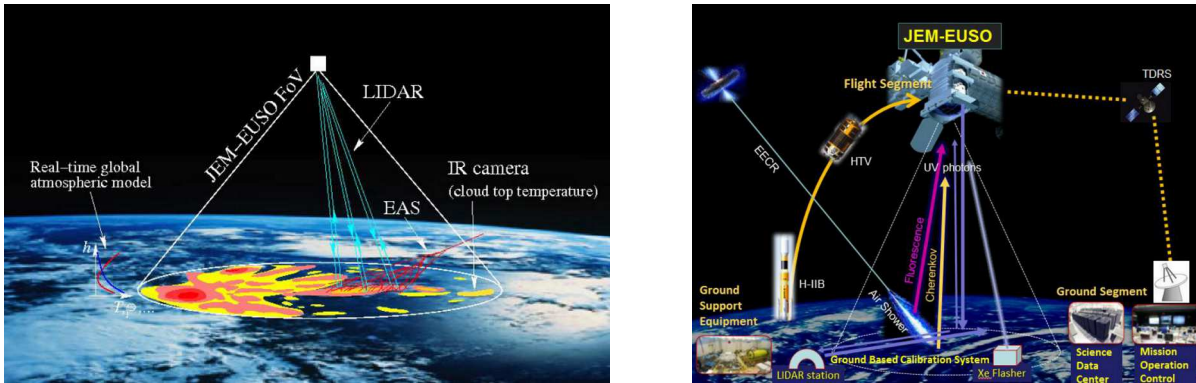


Figure 2.9: **Left panel:** A schematic view of the JEM-EUSO atmospheric monitoring system. Highlighted in red and yellow is the cloud's structure as seen by the IR camera. LIDAR pulses are sent in direction of an incoming shower to better assess systematics from scatterings. **Right panel:** a schematic view of the JEM-EUSO mission from launch to data collection. More in detail, the transport to the ISS will be performed by the HTV module and the H-IIIB rocket by JAXA. The launch will be performed by the JAXA launch site of Tanegashima island. Once on the ISS JEM-EUSO will perform measurement of fluorescence and Cherenkov light. Furthermore ground LIDARs and flashers will serve as standard candles for calibration. An array of antennas on ground and satellites will operate the communication of the detector with the control and data facility centers on Earth. Both figures are taken from "Report on the phase A study 2010" of the JEM-EUSO collaboration[147].

locations. Flashers of known intensity and millisecond period will be used to send a calibrated signal to JEM-EUSO while ground based laser sources, allow the measurement of the scattering profiles for different inclinations from ground to the top of the atmosphere.

The atmospheric monitoring of JEM-EUSO is performed with an on-board infra red camera and a LIDAR<sup>12</sup>. The infra red camera will assess the cloud coverage of the observed scene. The altitude of the cloud top is measured in case of thick clouds by using temperature informations. Therefore by modeling the atmospheric profiles and by measuring the surface temperature of clouds it may be possible to have a 3D mapping of the cloud coverage. A lot of important information can be also inferred by the on-board LIDAR, like the optical profile of aerosols .

The IR camera will take all-FOV images at fixed intervals of time. The LIDAR can operate both in scan or in targeting mode. In the first case, a shot will be sent to Earth at regular intervals in predefined directions while in the second several pulses will be sent just in direction of an occurring

<sup>12</sup>LIDAR: Light Detection and Ranging. Remote sensing device based on a laser beam and a receiver. In the JEM-EUSO case the laser pulse is used for the determination of the profile of the atmosphere.

trigger. The choice of such a mode must be a trade-off between high quality reconstruction and telemetry constraints.

Finally, it can be mentioned how the JEM-EUSO mission will also consist of a complex of ground-based facilities and organizations. Aim of the ground segment will be the management of the instrument during the flight time, the data formatting storage and distribution, mission operation and transmission of tele-commands to the detector. Data will be collected and organized in the science data center, and will be made available to the entire collaboration.



# Chapter 3

## ESAF

*This chapter is a review of the ESAF software as it is implemented at the end of 2012. A general overview about its structure is given together with a comprehensive description of all the relevant physical approximations and modelizations.*

### 3.1 The EUSO Simulation and Analysis Framework (ESAF)

The ESAF package is a simulation software specifically designed for the performance assessment of space based cosmic ray observatories. It has been developed in the framework of the EUSO mission [158] during the ESA phase A study. This software has been written mainly in C++ and makes use of the ROOT routines of CERN<sup>1</sup>. The entire software has been developed following an object oriented approach and is structured in a modular way. Worth to mention is the presence in ESAF of significant parts developed in fortran.

The compilation of the ESAF software produces two distinct executable files called respectively Simu and Reco. The first one performs the simulation of the entire physical process from shower to telemetry. In this context, several air shower generators like SLAST [159], CONEX [160][161], CORSIKA [162] and others are available for use. An atmospheric modelization according to the 1976 Standard US Atmosphere [163] is implemented as well as different parameterizations for Fluorescence and Cherenkov yield. Both the already described Nagano [149] and Kakimoto [150] studies have been implemented in the software. The standard Cherenkov theory is used in the ESAF modelizations. The Rayleigh scattering and ozone absorption processes are

---

<sup>1</sup>Check documentation on the web <http://root.cern.ch/>.

simulated in ESAF by means of the LOWTRAN 7 [164] atmosphere software. Several different versions of the optics Monte Carlo simulator, developed at RIKEN, (RIKEN ray trace code) have been interfaced with ESAF. Beside that, a GEANT 4 optics interface [165] and a parametrical optics simulator are implemented. Both the PMT and the EC electric signal treatment is performed in a parametrical way. The last part of the simulation chain consists of the trigger sequence. A multiple stage trigger scheme has been therefore developed in order to maximize the ratio of real events to background [157]. Once the trigger sequence has been applied the Simu executable stops producing an output *.root* file.

The Reco executable activates the entire reconstruction chain. If the event has been selected by the trigger algorithms, the first task is the recognition of pixel-GTUs with signal within the detector response table. Several algorithms have been implemented for this purpose. Currently the so called *PWISE* algorithm and the *LTTPreselection* trigger algorithms are in use. Once a clear shower-like pattern has been identified several time and space fits are performed for the arrival direction recognition [168]. Eventually, the profile reconstruction is performed in order to fit the  $X_{max}$  and energy parameters.

The simulation code is structured in several independent modules the higher of whom is the so called *SimuApplication*. An instance of such a class is created in the *simu.main.cc* file where the method *SimuApplication::DoAll()* is called. Such a method performs the iterative call of the *SimuApplication::DoEvent()* method which takes care of the entire physical process on a single event basis. Such a method will create an instance of the *LightToEuso* class which executes the entire process from primary particle to photons on pupil. Several choices are available on which simulator is to be used but the default option is the so called *StandardLightToEuso* class. By calling the *StandardLightToEuso::Get()*, the virtual *Get()* methods of the shower generator, of the light production and transport will be called. Each one of the mentioned *Get()* methods will deliver output objects describing the shower profile, photons in atmosphere and photons on pupil. The choice of the object oriented approach shows its power here where the call of several polymorphic *Get()* methods allows great flexibility.

Always inside the *SimuApplication::DoEvent()* method the virtual *Detector::Get()* method will be called. This method takes care of the entire detector simulation. Several choices are open at this stage between various detector configurations. The most important of them can be considered to be the *EusoDetector*, (activating the RIKEN ray trace code), the *G4Detector* (activating the Geant 4 optics) and other testing or debugging detector simulators. Calling one of the above described methods will activate both optics

### 3.1. THE EUSO SIMULATION AND ANALYSIS FRAMEWORK (ESAF)

and electronics simulators. As final output of the entire procedure a *Telemetry* object is produced.

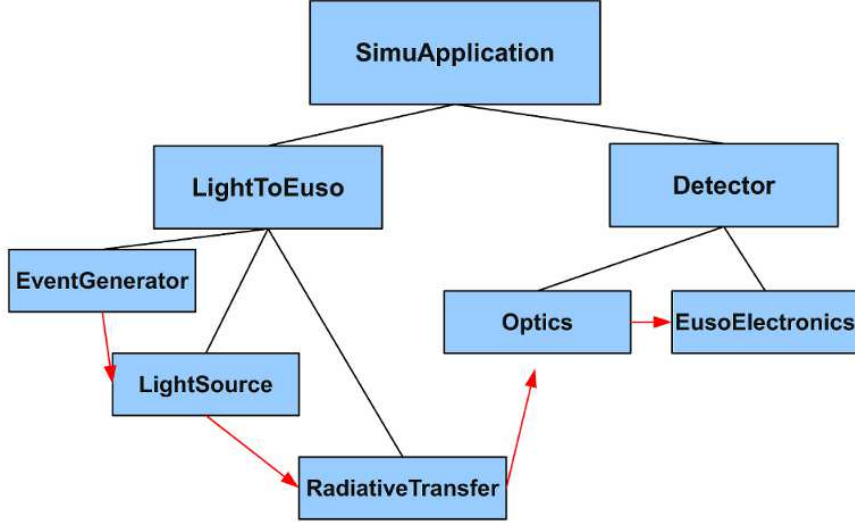


Figure 3.1: a schematic view of the ESAF Simu application structure. The main application is the so called *SimuApplication*. The *LightToEuso* application takes care of all the physical process from shower to detector. The *EusoDetector* application performs the simulation of optics and electronics. Black lines represent the calling hierarchy. Red arrows represent the flux of simulated input–output necessary for all the called applications.

The reconstruction procedure is activated in the *reco\_main.cc* file. Here an instance of the *RecoFramework* class is created and the method *RecoFramework::Execute()* is called. While in the constructor function *RecoFramework::RecoFramework()* the module chain is built, the *RecoFramework::Execute()* method performs the entire sequence of calls to reconstruct the event. In fact, the module sequence is first initialized through an iterative call of the *ModuleFactory::MakeModule()* method which allocates all the *RecoModule* objects requested by parameter files. Moreover, a *vector* named *fModules* with all the pointers to the created *RecoModule* objects is created. In the *RecoFramework::Execute()* method all the modules (which are inheriting from *RecoModule*) are initialized, called and cleared. Eventually all the output data are saved in the root file. For performing all the mentioned operations, the polymorphic methods *RecoModule::PreProcess()*, *RecoModule::Process()*, *RecoModule::PostProcess()* and *RecoModule::SaveRootData()* are declared in each module. Each of such modules has a specific function which can be either pattern recognition, direction fitting, profile reconstruction or  $X_{max}$  and energy reconstruction. Several modules have been

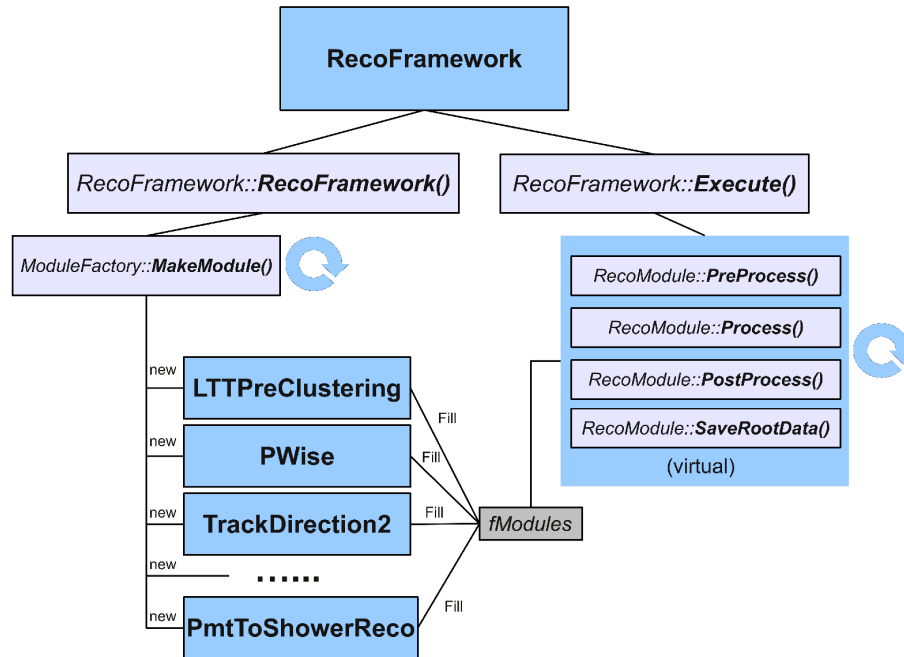


Figure 3.2: a sketch of the reconstruction framework. The main application *RecoFramework* calls iteratively the *MakeModule* method which allocates all the required modules. A *vector* of pointers to the allocated objects is saved under the name *fModules*. In the *Execute* method the operations of all the modules are performed. All the modules are inheriting from the *RecoModule* class. The virtual methods *PreProcess*, *Process*, *PostProcess* and *SaveRootData* are called for all the allocated modules. Note that blue boxes represent classes, blue-gray boxes methods, the gray box is a C++ *vector* and the circular arrow indicates iterative repetition of some method or sequence of methods.

implemented in the course of the years but the most actual and currently updated are the *LTTPreClustering* and *PWISE* for the pattern recognition, the *TrackDirection2* for the direction reconstruction and the *PmtToShowerReco* for the energy reconstruction. A schematic view of the above mentioned structure is shown in Figs. 3.1 and 3.2.

Another extremely important issue is the availability of the output information. The Simu executable produces a *.root* output file which is available for data analysis. Every user can develop specific root macros to open and read such files. The basic methods for such operations can be found in the *packages/common/root* directory. Each simulation root file contains a root *TTree* object called *etree*. Such an object can be retrieved after opening the root file, by means of the *TFile::Get()* method. Thanks to the ESAF *EEvent* class, the retrieval of all the *TBranches* objects of the tree is possible. By

### 3.1. THE EUSO SIMULATION AND ANALYSIS FRAMEWORK (ESAF)

---

calling the method `EEvent::EEvent()` the memory segment for the retrieval of all the branches is allocated. By calling the `EEvent::SetBranches()` the addresses for all the data objects is set. With the `TTree::GetEntry()` method the access of the single events is possible. This is by itself a very standard procedure to access root data. The interested reader can refer to root documentation<sup>2</sup> for more detailed information. Thanks to the retrieval methods of the `EEvent` class it is possible to access all the pointers to the available branches and consequently to the saved data. A small resume of the code lines necessary access the true primary energy is given here:

---

```
TFile * fsimu = new TFile("rootFile.root");
TTree * etree = (TTree*)fsimu -> Get("etree");
EEvent * evs = new EEvent();
evs -> SetBranches(etree);
etree -> GetEntry(eventNumber);
evsreco -> GetTruth().GetEnergy();
```

---

The same concept is valid for the Reco output file. In this case the output file would end with the `.reco.root` extension. Also here, after opening the file, it will be necessary to retrieve the `TTree` object called `recotree` always by means of the `TFile::Get()` method. Analogously to what has been done for the simulation it will be necessary to create a `RecoRootEvent` object and set the addresses of all the branches with the method `TTree::SetBranchAdress()`. The method `TTree::GetEntry()` will provide direct access to the single event data. In case of Reco output the directory under which all the output methods are defined is `packages/reconstruction/root/include`. Thanks to the `RecoRootEvent` methods then, the pointers to all the branches are made available. A small resume of the code lines necessary access the reconstructed energy is given here:

---

```
TFile * freco = new TFile("rootFile.reco.root");
TTree * recotree = (TTree*)freco -> Get("recotree");
RecoRootEvent * evsreco = new RecoRootEvent();
recotree -> SetBranchAdress("events", &evsreco);
recotree -> GetEntry(eventNumber);
evsreco -> GetRecoPmtToShower().GetEnergy();
```

---

<sup>2</sup>For documentation check <http://root.cern.ch/>

Of absolute importance is also the presence of all the available parameters under the *config* directory. Such parameters can be passed as command line parameters (by using the syntax `--Class.Parameter = value`) or grouped in a single user-defined config file. In such a case the file should be identified by means of the `--usrcfg = fileName` command line expression. Generally it must be considered that the priority order would be as follows: command line parameters first, then user file parameters and finally *config* directory parameters.

To conclude is mandatory to mention the fact that ESAF consists also of a collection of macros to perform several auxiliary operations. Between them the *opticsresponse.C*, the *MakePixelMapPhotonFile.C* and the *EEventViewer.C* can be mentioned. Aim of the previously mentioned macros is respectively, the production of the *OpticsResponse* map, of the so called *PixelAngleMap* and the management of a graphical interface for the event visualization.

## 3.2 Shower development

In this section a small review of both structure and physics of the shower generation in ESAF is given. As explained in the previous section by calling the *SimuApplication::DoEvent()* the shower generator will be first activated. Essentially, a call of the *StandardLightToEuso::Configure()* method will allocate an object of *EventGenerator* type. This operation will be performed thanks to the execution of *LightFactory::Get()*. The choice between all the different generators is made here. In fact, depending on the parameters, objects of type *SlastShowerGenerator*, *CONEXFileShowerGenerator* or *CORSIKAFileShowerGenerator*, (all of them inheriting from *EventGenerator*) will be allocated. At the following step, namely inside *StandardLightToEuso::Get()* the *EventGenerator::Get()* and *EventGenerator::DevelopShower()* methods will be called. Within these methods the shower is built. Parameters like slant depth, position, timing and number of charged particles will be calculated for each of the so called *Steps* of which the shower is made. A schematic view of the previously described process is shown in Fig. 3.3.

In the present work the *SlastShowerGenerator* [159] and *CONEXFileShowerGenerator* are described. The *SlastShowerGenerator* is the most widely used in the course of this thesis and has been implemented in ESAF by the ESA-EUSO developers. It consists of a series of analytical parameterizations for the shower profile like the GIL, Gaisser-Hillas and the Gaussian-Function-in-Age. However just the GIL function is ready for use since the remaining two are still in the debugging phase. As described by D. Naumov

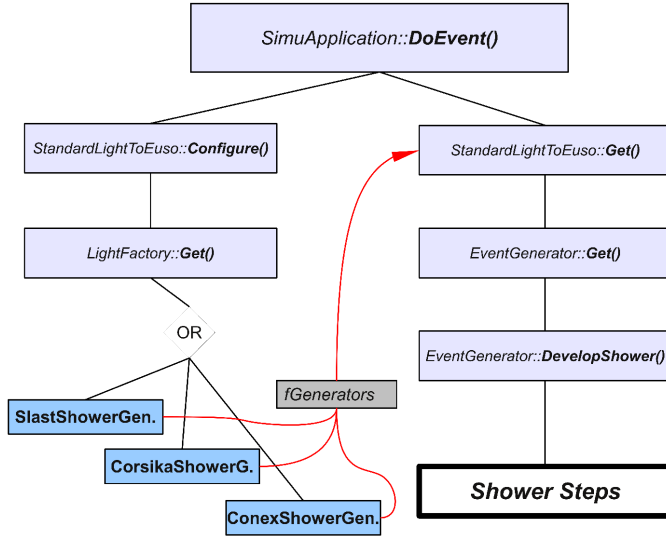


Figure 3.3: a schematic view of the shower execution process. The *SimuApplication::DoEvent()* method is calling first the *StandardLightToEuso::Configure()* and then the *StandardLightToEuso::Get()*. This will activate a sequence of calls which will respectively allocate one of the generators (blue boxes) and perform all the basic operations to build the shower steps.

in [159] the GIL function is essentially an analytical approximation of the shower longitudinal development based on the QGSJET model. Such an idea was developed by J. Linsley on the base of previous studies[169][170][171]. The GIL parameterization is implemented in ESAF as shown in Eq. 3.1

$$N_e = \frac{E}{1.45 \cdot 10^9 eV} \cdot e^{t - t_{max} - 2 \cdot t \cdot \ln \frac{2}{1 + \frac{t_{max}}{t}}} \quad (3.1)$$

whereas  $t = \frac{X}{37.5g/cm^2}$  is an expression of the slant depth in units of mean interaction length of protons in air ( $37.5 g/cm^2$ ),  $E$  is the primary energy and  $A$  the atomic mass of the particle. Furthermore  $t_{max}$  expresses the slant depth of the maximum of the shower (after the subtraction of the first interaction length) in units of mean interaction length and it has a form like shown in Eq. 3.2

$$t_{max} = 1.7 + 0.76 \cdot \left( \ln \frac{E}{8.1 \cdot 10^7 eV} - \ln A \right) \quad (3.2)$$

whereas  $A$  is the atomic mass of the particle. In the previous formulas the number of particles at each slant depth is univocally determined by just two parameters: the primary energy and the atomic mass of the particle. Once the first interaction point is fixed, this parameterization does not imply

any oscillation from shower to shower. Within the *SlashShowerGenerator* a random distribution for the first interaction point is implemented. Such a point is sampled randomly, as function of slant depth, according to an exponential distribution scaled by the mean hadronic interaction length. In order to calculate the mean interaction length in air, a parameterization of the nucleon–air cross section according to Mielke et al. [172]<sup>3</sup> and the average air composition are used. In such a parameterization, primary energy and atomic mass are therefore used as input parameters.

In the framework of ESAF also other non parametrical shower simulators have been implemented. For that purpose interfaces for both CONEX [160][161] and CORSIKA [162] have been introduced. The CONEX shower generator has been developed as a hybrid Monte Carlo air shower simulator for the extremely high energy<sup>4</sup>. Given the non parametrical nature of the CONEX simulator, the shower development will include some intrinsic statistical oscillation independently of the first interaction. This feature can be seen in Fig. 3.4 where the profiles of 10 SLAST (left panel) and CONEX (right panel) events are shown. In both plots the shower profiles have been shown as function of the slant depth. In both panels two sets of curves are visible. In the first case (red dots) the profile as function of slant depth is shown as itself. In the second case (black triangles) the first interaction depth is subtracted to the total slant depth.

As can be seen no oscillation is present anymore for the SLAST showers if the first interaction depth is subtracted while CONEX represents a more realistic shower simulator.

In Fig. 3.5 10 shower profiles both for CONEX (red circles) and SLAST (black triangles) have been plotted. In the left panel the profile is expressed in number of charged particles while in right panel in energy deposit<sup>5</sup>. As can be clearly observed a systematic in the maximum amplitude is visible. This feature is present in both plots but inverted. This apparently contradictory

<sup>3</sup>The nucleon–air cross section value would then be  $\sigma = 290 - 8.7 \cdot \ln \frac{E}{10^9 eV} + 1.14 \cdot \ln^2 \frac{E}{10^9}$  whereas  $\sigma$  is expressed in mbarn.

<sup>4</sup>Above a certain energy the simulation of the entire secondaries cascade is out of the capabilities of current calculators. For that reason in the course of years various approaches have been developed. The CORSIKA simulator, for example executes the Monte Carlo simulation of all the secondaries till a certain threshold. After that, just some sample of "average" particles is followed. Another approach is the one used in CONEX. In such a case the initial steps of the shower will be treated in a pure Monte Carlo approach like in the case of CORSIKA. In this simulator, however after a certain energy threshold is reached the corresponding sub-showers are developed following an analytical parameterization. From this feature therefore comes the "hybrid" definition.

<sup>5</sup>By energy deposit is meant the amount of energy lost by the shower during the propagation process in each slant depth unit.



### 3.2. SHOWER DEVELOPMENT

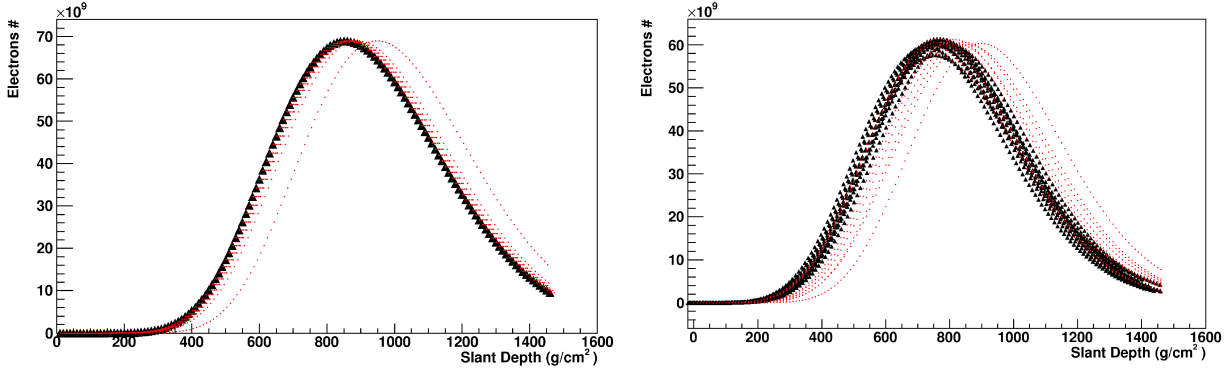


Figure 3.4: **Left panel:** a comparison between 10 SLAST profiles as function of slant depth. Red spots represent the shower profile as function of the slant depth while black triangles the slant depth after the subtraction of the first interaction point. **Right panel:** the same plot as in left panel but for 10 CONEX events simulated with the QGSJET-III interaction model.

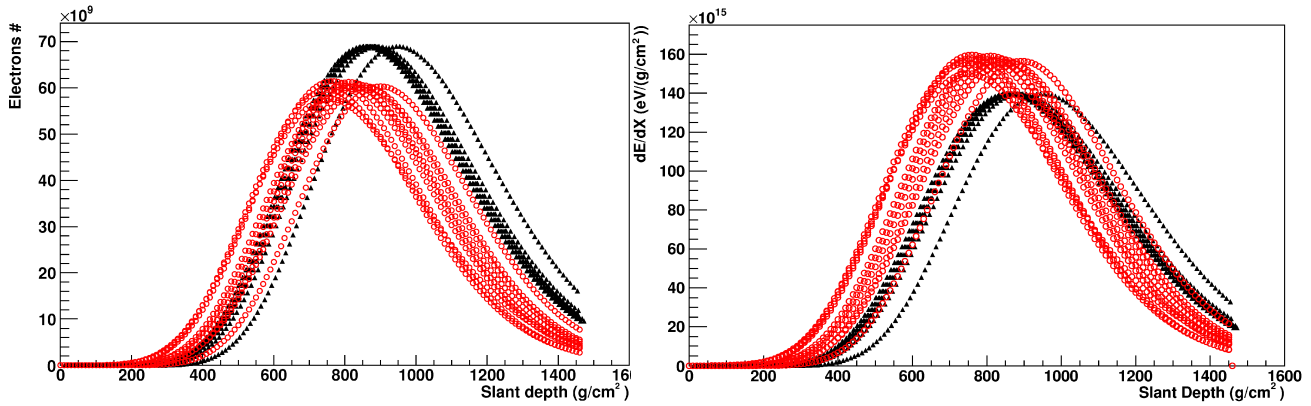


Figure 3.5: **Left panel:** a comparison between 10 CONEX and SLAST shower profiles. Black triangles represent GIL profiles while red circles CONEX (QGSJET-III). **Right panel:** energy deposit for 10 SLAST (GIL) and CONEX (QGSJET-III) showers. The assumed secondaries energy distribution for the GIL profiles is the so called Giller function. The integration range is between 0 and 10 GeV. The energy loss function is the standard energy loss function of electron in air also used in Kakimoto et al. [150]. All the showers have an inclination of 45 degrees and have been simulated with a  $10^{20}$  eV energy.

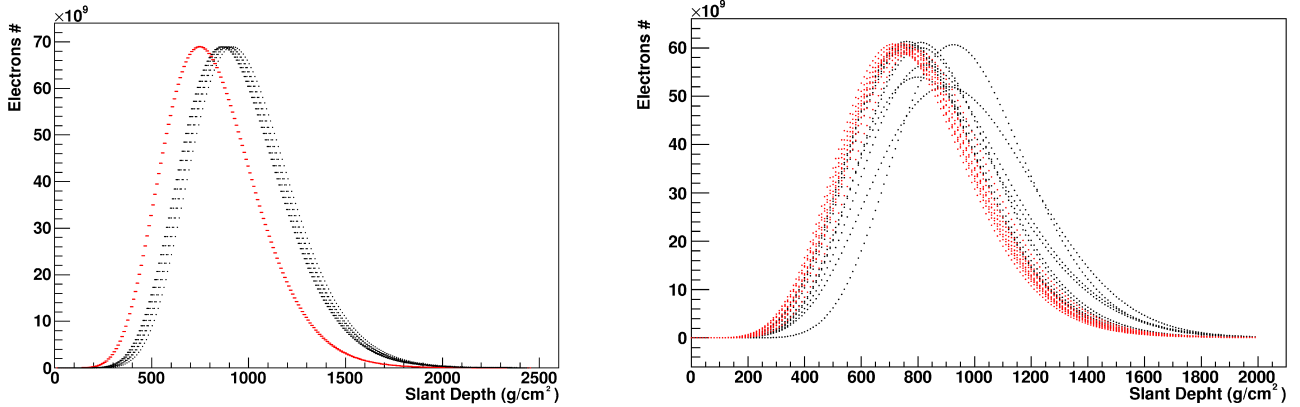


Figure 3.6: **Left panel:** a comparison between 10 proton (black dots) and 10 iron showers (red dots) simulated with SLAST. All the showers have been simulated for  $10^{20}$  eV and 65 degrees conditions. As can be clearly seen just a shift in the maximum position is visible. **Right panel:** same as left panel but simulated with CONEX.

behavior is due to the different electron energy distribution emerging in the two shower models. After integrating both curves in fact, we find the total deposited energy in CONEX simulator to be  $\sim 93\%$  of the primary energy. On the other hand GIL fraction remains limited to  $\sim 89\%$  (at 65 degrees)<sup>6</sup>. The lower integrated energy deposit in GIL is likely due to the lack of other ionizing particles in the energy loss. Such a parameterization, in fact, assumes just an electron curve while muons do not contribute to the total energy deposit. CONEX on the other hand considers muons in the energy deposition process. For this reason the energy deposited in atmosphere results to be larger.

A plot showing proton and iron primaries both for SLAST and CONEX is shown in Fig. 3.6. As to expect, the SLAST shower amplitude does not show any dependence on the primary type. In the present plot just a shift in the maximum depth can be observed when the primary is changed. On the other hand, CONEX simulations show some more complex features. As it clearly appears, the statistical oscillations on the shower structure are strongly reduced for heavier components both in amplitude and in  $X_{max}$  position. Moreover beside a clear shift in the maximum position the two species seem to be affected by systematics also in the amplitude.

Another very important point which can be observed in Fig. 3.4 and 3.5 is the presence of a systematic also in the  $X_{max}$  distribution. Such a feature can be observed in Fig. 3.7 where the expected maximum slant

<sup>6</sup>In both cases the missing energy is assumed to be carried by muons, neutrinos and hadrons to ground.

depth as function of energy is shown. Both the slant depth for GIL and CONEX events is shown here. For the SLAST parameterization the dotted area corresponds to the  $\pm\sigma$  interval on the  $X_{max}$  parameter given the random distribution on the first interaction point. For the CONEX showers on the other hand, for each condition 1000 events have been simulated and both average and  $\sigma$  have been calculated. As can be seen a clear systematic in the steepness of the two functions as well as a constant shift is present. This feature is particularly apparent for protons while for iron the two simulators can be considered almost in agreement. However, it can be seen that for both calculators the iron and proton species tend to be separated at a level of at least  $\sigma$ .

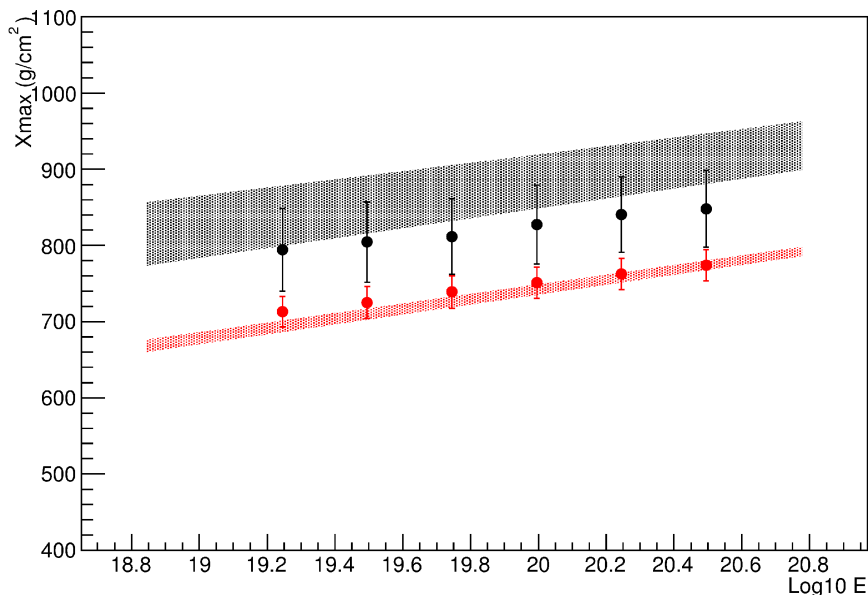


Figure 3.7: the slant depth of the maximum for various simulators and species. Dotted areas represent the GIL parameterization after adding the first interaction as parameterized in ESAF. The black area represent a proton parameterization while the red iron. Each dot represents  $X_{max}$  averaged over 1000 events in CONEX. Also here the black and red colors represent respectively proton and iron.

The energy distribution of the secondaries is also treated. Currently several parameterizations are implemented in ESAF. However just the so called Giller parameterization [173] is tested and fully operating. In the study by Giller et al. [173] the authors propose a parameterization for the energy spectrum of the extensive air shower secondaries. Such a formula can

be seen in Eq. 3.3

$$\frac{1}{N_e} \frac{dN_e}{d \ln E} = C(s) \cdot \left(1 - a \cdot \exp\left(-d(s) \frac{E}{E_{cr}}\right)\right) \left(1 + \frac{E}{E_{cr}}\right)^{s+b \ln \frac{E}{cE_{cr}}} \quad (3.3)$$

whereas  $E$  is the secondary particle's energy,  $E_{cr}$  is the critical energy in atmosphere (80 MeV) and all the shown parameters are either constants or dependent on the age parameter  $s^7$ . In Fig. 3.8 the shape of the spectrum for different shower ages is shown. As can be clearly observed the peak of the energy spectrum is around  $\sim 1$  MeV while at higher energy the spectrum decreases. Another interesting feature can be seen in the progressively

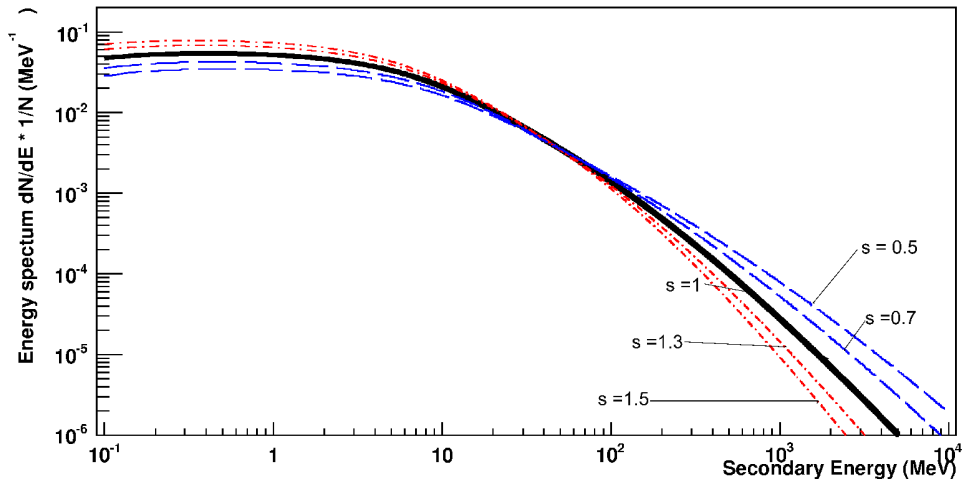


Figure 3.8: The secondary energy spectrum for an extended air shower. As can be seen the energy spectrum for 5 different ages is shown in different colors and line styles. In bold thick line the spectrum for the shower maximum ( $s = 1$ ) is shown.

softer spectrum toward the later stages of the shower. This is intuitively understandable since the entire shower process can be viewed as an energy dissipation process. For that reason the few high energy particles at the early shower stages will progressively loose their energy till the threshold is reached.

<sup>7</sup>Such a parameter is commonly used in cosmic ray science as an expression of the shower development. A shower in the early stage of its development would then have  $s < 1$ . At the maximum this parameter would assume a value = 1 while at later stages will grow  $>1$ . One possible definition of such a parameter (as given in Giller paper) is  $s = \frac{3X}{X+2X_{max}}$  whereas  $X$  represents the slant depth. To be mentioned is the different definition which is used in ESAF  $s = \frac{2X}{X+X_{max}}$

### 3.3 Photon production

In this section the photon production in ESAF is described. A call of the *SimuApplication::DoEvent()* method will again activate the *StandardLightToEuso::Configure()* method which takes care of the allocation of a *ShowerLightSource* object. Analogously to what previously seen the *StandardLightToEuso::Get()* will call the *LightSource::Get()* which will perform the entire chain of calls for the photons production. Such a method will create several bunches of photons (*BunchOfPhoton*). The *ShowerTrack* produced in the shower generator will be instead used as a input.

For each of the *ShowerSteps* the secondaries energy spectrum, the altitude, direction will be retrieved and according to such properties the *BunchOfPhoton* will be produced. More in detail part of the *Step* energy will be deposited according to the known functions of energy deposition of electrons in air. Part of this energy will then be converted in photons according to the previously mentioned Nagano [149] and Kakimoto [150] fluorescence parameterizations as well as to the standard Cherenkov parameterizations.

The concept of *Bunch* has been introduced to make possible the treatment of the photon production in a parametrical way. Therefore, the determination of the spectrum, timing, direction, will be performed in a parametrical way over the entire bunch. The population of *SinglePhotons* will be then extracted randomly according to the *Bunch* distributions and to the solid angle under which JEM-EUSO is visible. To be mentioned is also the fact that in the ESAF environment each *ShowerStep* will therefore host two bunches: one fluorescence and one Cherenkov bunch. A schematic view of the above mentioned processes is shown in Fig. 3.9.

The physical analysis of the above described process must start from the energy deposition in atmosphere. ESAF makes use of an interpolation of tabulated data. Such data are the one taken from Kakimoto et. al [150] which on its own report data tabulated in older studies. The resulting energy deposit can be seen in Fig. 3.10 (right panel). Such a quantity is considered generally to be linearly proportional to the fluorescence yield. Both the reference studies used in ESAF (Nagano and Kakimoto) assume the proportionality of the FY with the energy deposition.

Both Nagano and Kakimoto studies give a parameterization of the fluorescence yield in atmosphere which depends on parameters like temperature, air density and energy deposition. The Nagano formula implemented in ESAF is therefore as explained in the cited paper

$$\epsilon = \frac{\frac{dE}{dX}}{\frac{dE}{dX} 0.85MeV} \frac{A\rho}{1 + \rho B\sqrt{t}} \quad (3.4)$$

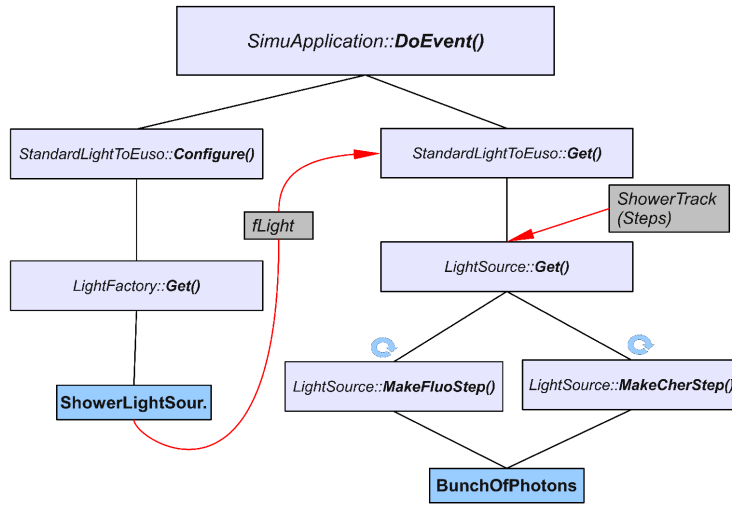


Figure 3.9: a schematic view of the light production process. The *SimuApplication::DoEvent()* method is calling first the *StandardLightToEuso::Configure()* and then the *StandardLightToEuso::Get()*. This activates a sequence of calls which first allocates the *ShowerLightSource* objects and then performs the generation of all the *BunchOfPhoton*.

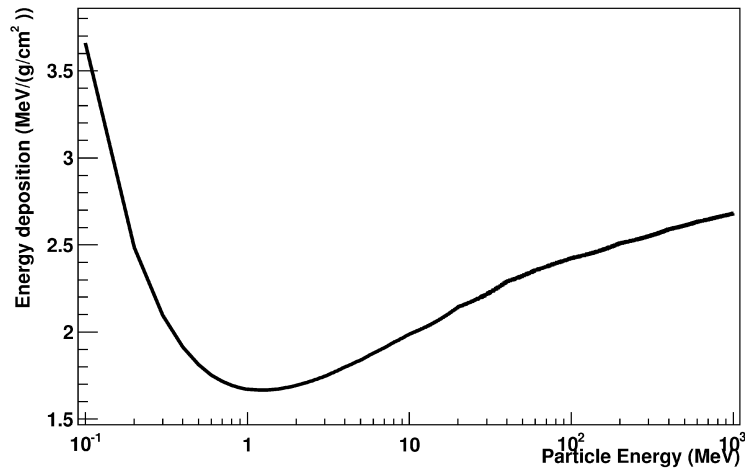


Figure 3.10: the energy loss as function of energy. The minimum ionization loss for electrons can therefore be found around 1 MeV while at higher energy the loss tends to increase.

whereas  $\rho$  is the density,  $t$  the temperature of air,  $A$  and  $B$  are wavelength

dependent tabulated parameters. The same formula can be reported for Kakimoto et al.

$$\epsilon = \frac{\frac{dE}{dX}}{\frac{dE}{dX}_{1.4MeV}} \rho \left( \frac{A_1}{1 + \rho B_1 \sqrt{t}} + \frac{A_2}{1 + \rho B_2 \sqrt{t}} \right) \quad (3.5)$$

whereas  $\rho$  and  $t$  are defined as in previous equation and  $A_1$ ,  $A_2$ ,  $B_1$ ,  $B_2$  are constants tabulated in Kakimoto's paper.

In Fig. 3.11 the two fluorescence yields parameterizations as calculated by ESAF are shown. The red curve represents Nagano's while the black one Kakimoto's parameterization. The chosen age parameter is 1. The energy spectrum and photon integration range assumed in the two studies are different. As can be noticed the decrease of the temperature in the first layers of the atmosphere causes the increase of the yield value. Above  $\sim 12$  km the temperature function flattens and in Eqs. 3.4, 3.5 the decrease of density becomes dominating. For this reason, the yield starts decreasing again.

In Fig. 3.12 the fluorescence yield as function of height can be seen for the Nagano parameterization. In this case the same function has been plotted for different shower ages. As can be clearly seen for early evolutionary stages the fluorescence yield tends to be larger. This is a consequence of the harder electrons spectrum which characterizes the earlier stages of the shower (see Fig. 3.8). In fact, as can be seen in Fig. 3.10, to higher electron energies are associated higher energy depositions and, as can be also seen in formulas 3.4 and 3.5, to higher energy deposition corresponds a linearly higher fluorescence yield.

In Fig. 3.13 the produced fluorescence spectrum according to the Nagano parameterization (Eq. 3.4) is shown. In this plot the integrated Nagano spectrum can be observed for a 45 degrees  $10^{20}$  eV shower.

The final part of this section is devoted to the Cherenkov production. The *SimpleCrkCalculator* calculator produces a Cherenkov output as function of altitude and secondary energy. The reference equation used in ESAF has such a shape

$$C_Y(E, h) = 2\pi\alpha \left( 2\delta - \left( \frac{m_e c^2}{E} \right)^2 \right) \left( \frac{1}{\lambda_{min}} - \frac{1}{\lambda_{max}} \right) \quad (3.6)$$

whereas  $\delta = n - 1$  (with  $n$  as refractive index),  $\alpha$  is the fine structure constant,  $E$  the electron's energy,  $\lambda_{min}$  and  $\lambda_{max}$  are the integration extremes in the produced spectrum (see also chapter 2). To get the total yield is necessary to perform the integration over the energy distribution of the secondaries. Therefore, performing the integration of Eq. 3.6, the Cherenkov yield as

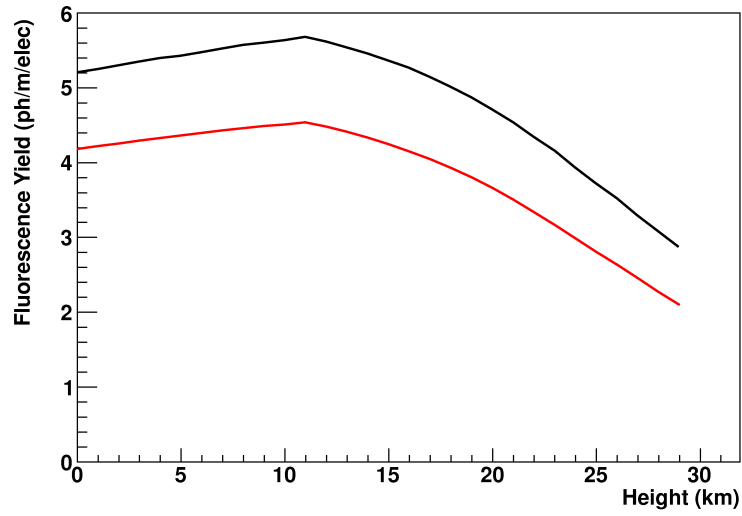


Figure 3.11: the comparison between Nagano and Kakimoto fluorescence yields as calculated by ESAF is shown here. The calculations have been performed for age parameter = 1 and with the Giller energy distribution. Nagano's integration is performed in the range 316–430 nm as in ESAF. On the other hand Kakimoto's spectrum is integrated in the range 298–306 nm.

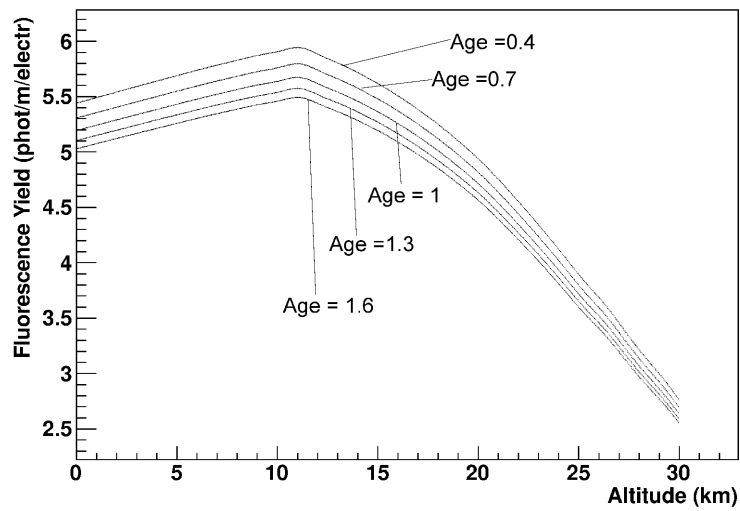


Figure 3.12: Nagano's fluorescence yield as function of altitude. Different ages are depicted. The integration is performed in the range 316–430 nm which includes all the produced lines.



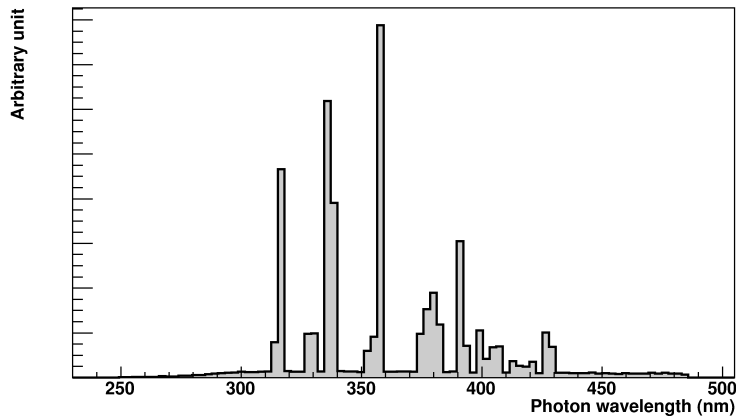


Figure 3.13: the simulated fluorescence spectrum according to Nagano integrated over the entire shower development. The shower is a  $10^{20}$  eV, 45 degrees proton. The electron energy distribution was according to Giller et al. Note that the low component superposed to the lines is the Cherenkov reflected in direction of the detector.

depicted in Fig. 3.14 (left panel) is obtained. In this case the integration has been performed between 250 and 450 nm over the energy distribution of electrons emerging at age  $s = 1$ . On right panel the Cherenkov yield can also be observed decomposed in wavelength units. As can be seen, the Cherenkov yield integrated over each 2 nm bin is depicted as a function of wavelength. The same value has been depicted for different altitudes in 1 km steps from 0 to 30 km. The altitude corresponding to each sequence of points is specified on the right side of the plot. As can be seen the highest yield values are produced at low altitude just as can be also seen on the left panel. Worth to note is how above a certain altitude the Cherenkov yield goes to 0.

A further aspect of the Cherenkov yield functions is shown in Fig. 3.15 where the dependence on the secondaries energy is shown. In left panel the yield can be observed as function of the electron energy and for different altitudes. As can be seen a plateau is reached after the rapid increase at low energies. Furthermore, it can be observed how the yield increases toward the lower altitudes. On right panel the Cherenkov yield can be also seen as function of the altitude for various electron's energies. The examples shown go from 24 to 100 MeV in 4 MeV steps. To be mentioned is the presence of a minimum energy threshold in order to produce Cherenkov light. In fact Cherenkov light can be produced just in case the particle's speed exceeds the speed of light in the medium.

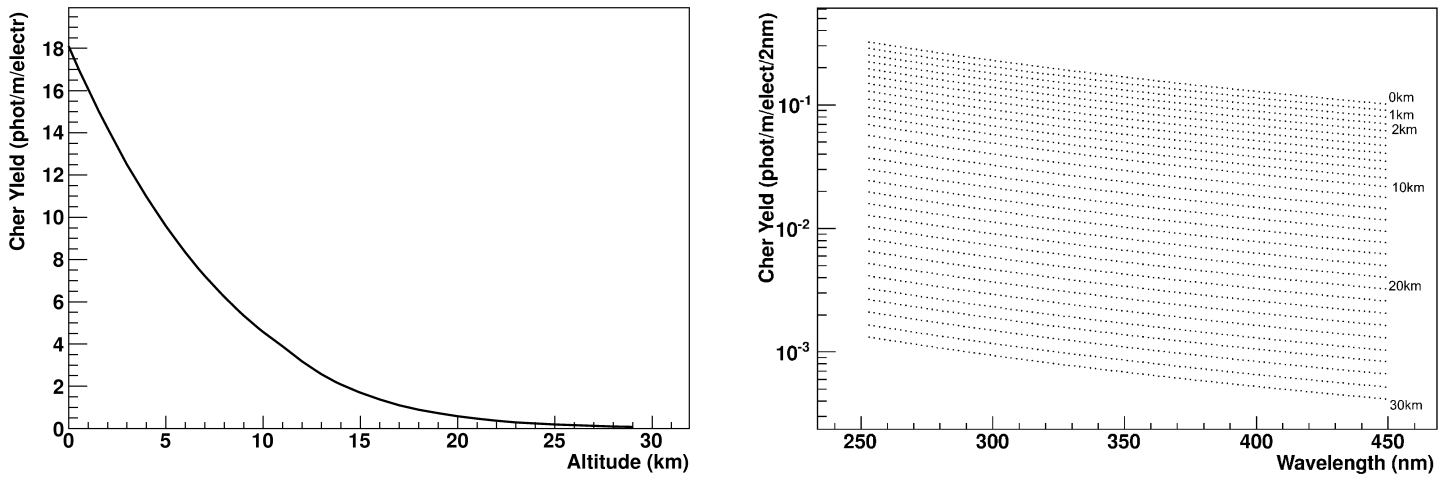


Figure 3.14: **Left panel:** Cherenkov photon yield as function of altitude given the electron's distribution at age 1. The integration range is between 250 and 450 nm. **Right panel:** the Cherenkov yield decomposed in spectral bins. Each bin represent the yield within 2 nm wavelength range. A sequence of points can be observed for different altitudes from 0 to 30 km in intervals of 1 km. The integration is performed between 250 and 450 nm.

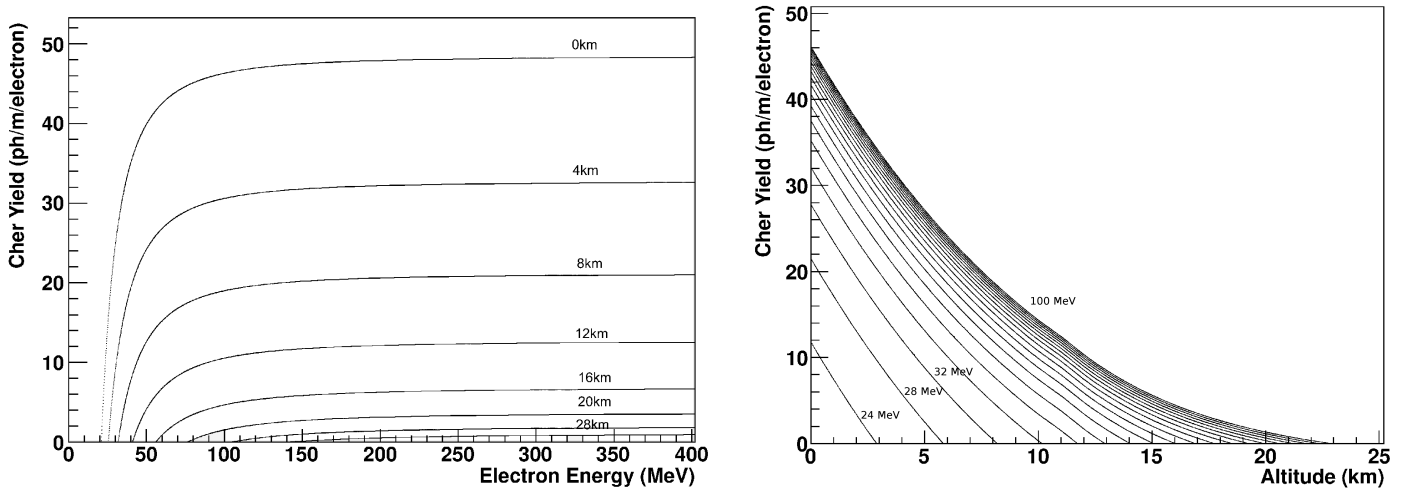


Figure 3.15: **Left panel:** the parameterized value of Cherenkov yield as function of electron's energy and for different altitudes. **Right panel:** the parameterized Cherenkov yield as function of altitude and for different electron's energy. Since Cherenkov can be produced just above a certain energy threshold the minimum energy represented is 24 MeV.

## 3.4 Atmosphere

In all the simulation steps from primary to detector, the atmosphere modeling is of extreme importance. In fact, almost every class regarding shower generators, fluorescence, Cherenkov production and photons transport makes a wide use of the *Atmosphere* class. In such a class methods to calculate the air density, humidity, temperature, slant depth, composition, amount of ozone are implemented. The US Standard 1976 Atmosphere is the default parameterization used in ESAF.

The ESAF atmospheric structure will be therefore shown here. In the following plots, important atmospheric parameters are depicted. In Fig. 3.16, for example, the profiles as function of altitude for the most important atmospheric components are shown. More in detail in the upper left plot the density (in  $\text{g}/\text{cm}^3$ ) for air, nitrogen and oxygen are shown for altitudes between 0 and 30 km. In the same way in the other plots air pressure, temperature and absolute humidity are depicted.

In Fig. 3.17 also the ozone profile is plotted. More in detail, in the left panel the ozone fraction in parts per million volume is depicted. As can be seen, the maximum fraction is observable around 37 km. In the right panel, the profile is also shown in terms of dobson units per km (black curve). The amount of ozone till the top of atmosphere in dobson units<sup>8</sup> is instead shown in red. As can be clearly seen the derivative of the dobson columnar density of ozone has its maximum at a different altitude than the ozone volume fraction plot. Such a difference is due to the altitude dependence of the temperature and pressure which on their own affect the volume fraction. In fact DU are expression of a volume under standard conditions while the volume fraction is expressed under "local" conditions. The same pattern is also followed by the particle density profile which follows a similar shape as the derivative of dobson columnar depth.

## 3.5 Photons propagation

Once photons are produced the next step would be their transport through the atmosphere and the application of all the interaction processes with air molecules. The entire procedure is started again in the *SimuApplication::DoEvent()* method. This method indirectly calls the *LightFactory::Get()*

---

<sup>8</sup>Such a parameter is expression of the column density of a gas over the entire atmosphere. More in detail it expresses the thickness of a gas column if compressed at standard temperature and pressure. As a matter of fact 1 DU corresponds to  $10\mu\text{m}$  column of gas at 273 K and 1013 hPa.

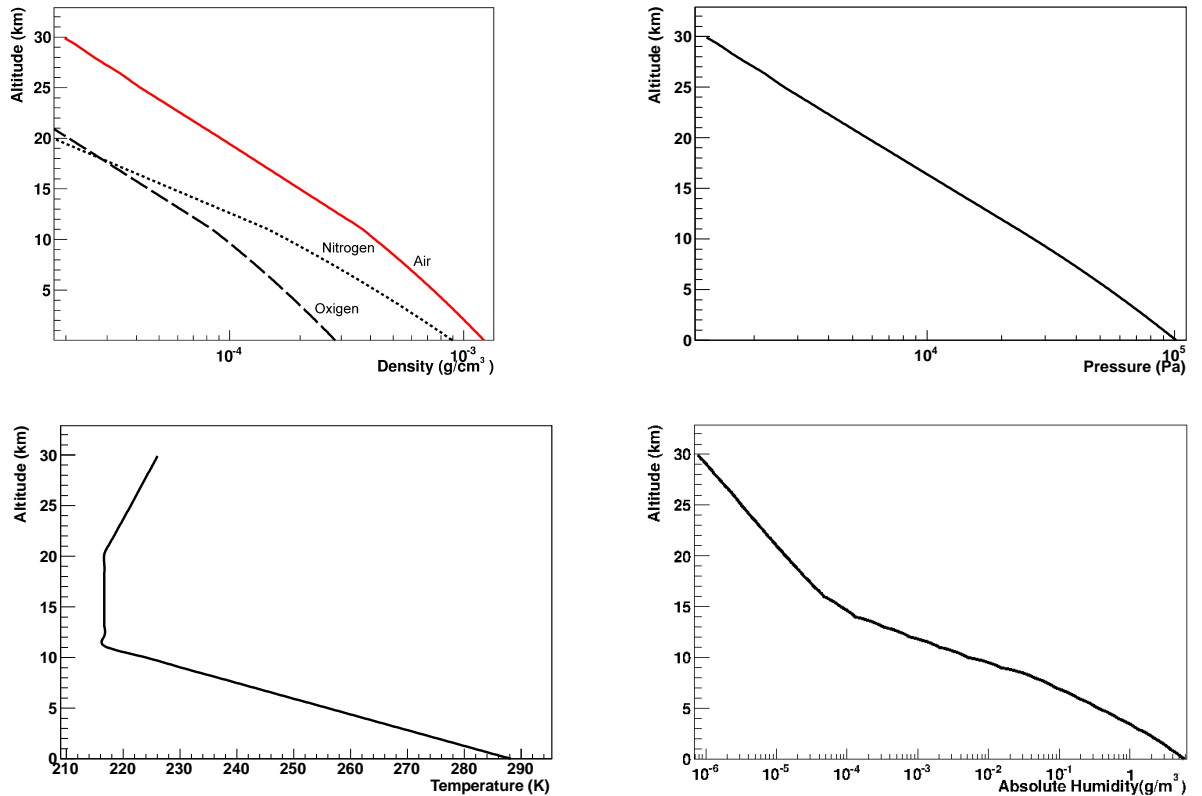


Figure 3.16: **Upper left panel:** the density profile of air (red curve), nitrogen and oxygen in  $\text{g}/\text{cm}^3$  as function of altitude. **Upper right panel:** the air pressure in Pa as function of altitude. **Bottom left panel:** the temperature distribution as function of altitude. **Bottom right panel:** the absolute humidity of air expressed in  $\text{g}/\text{m}^3$  as function of altitude.

which allocates all the *RadiativeTransfer* objects. In the default option the so called *BunchRadiativeTransfer* will be allocated. Always inside the *SimuApplication::DoEvent()* method the entire calls chain for the transport of photons is performed. First of all a call of the *StandardLightToEuso::Get()* method will (in the default configuration) activate on its own the method *BunchRadiativeTransfer::Get()*. This method will accept as input the *BunchOfPhotons* described in Sect. 3.3. Within such a method the bunch will be decomposed in several *SinglePhoton* objects.

For this purpose, parameters like angular direction toward JEM–EUSO, the solid angle under which JEM–EUSO is seen and the timing of the bunches are calculated. Therefore, within the methods *BunchRadiativeTransfer::DirectToEuso()* and *BunchRadiativeTransfer::GenerateDirectSingles()* all the single photons direction, timing and wavelength are sampled according to the distributions

### 3.5. PHOTONS PROPAGATION

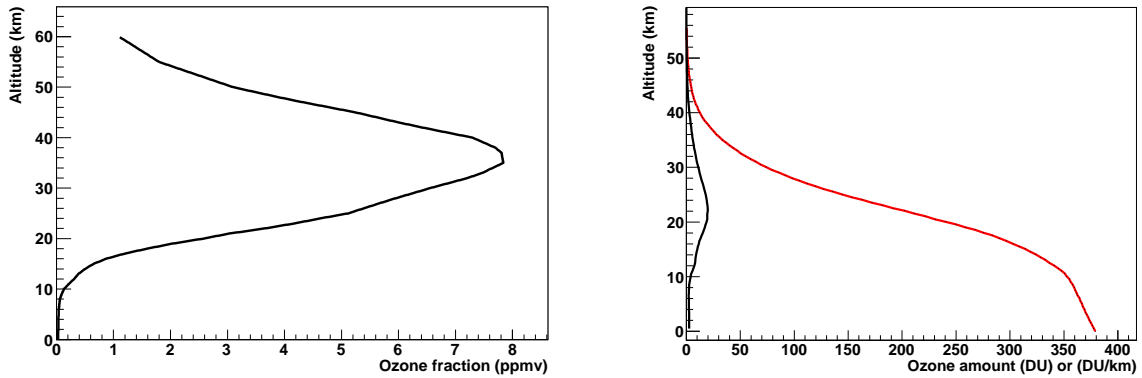


Figure 3.17: **Left panel:** the ozone fraction in parts per million volume as function of altitude. **Right panel:** the columnar density of ozone in dobson units (red curve). In black the derivative of such a function is also presented.

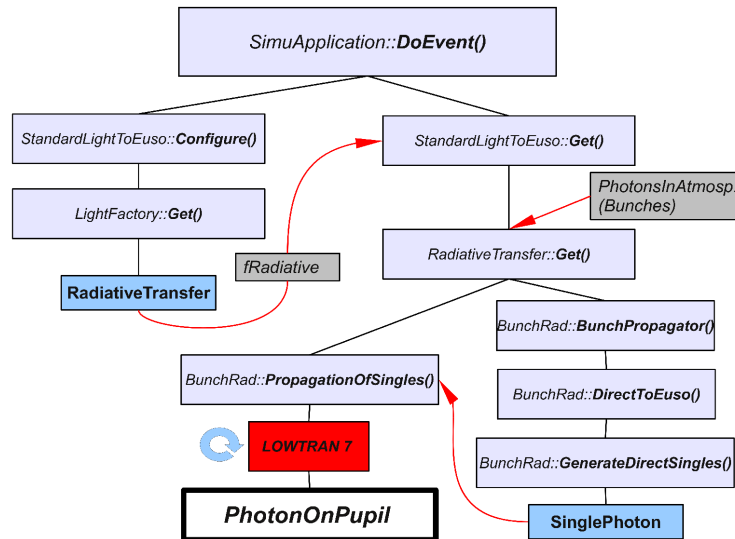


Figure 3.18: the photon propagation framework. The `SimuApplication::DoEvent()` method is the main calling function. This will allocate the new `RadiativeTransfer` objects which in default configuration will be `BunchRadiativeTransfer`. The `BunchRadiativeTransfer::Get()` method will first perform the decomposition of all the bunches in `SinglePhoton` objects. The propagation of each single photon will be performed by the `BunchRadiativeTransfer::PropagatioOfSingles()` method. By calling the `Lowtran 7` software the transmission of all the photons to the detector is performed. As a final result the list of `PhotonOnPupil` is delivered.

calculated for each bunch. At the end, several `SinglePhoton` objects are

allocated and the corresponding pointers are passed to the *BunchRadiative-Transfer::PropagationOfSingles()* method which performs the transport from shower to detector. For each of the produced photons the integrated transmittance up to the detector will be calculated as a superposition of Rayleigh, ozone and aerosol interactions. Thanks to a random rejection process all the photons will be then marked as *Absorbed*, *CloudAbsorbed* or as reaching the pupil. Once at the pupil then, parameters like the position and timing of the photon will be calculated. At the final step of such a process an object *ListPhotonsOnPupil* is produced. Within such a list all the photons who survived the transport till the detector are stored and passed to the detector simulation functions. The above described structure is depicted in Fig. 3.18.

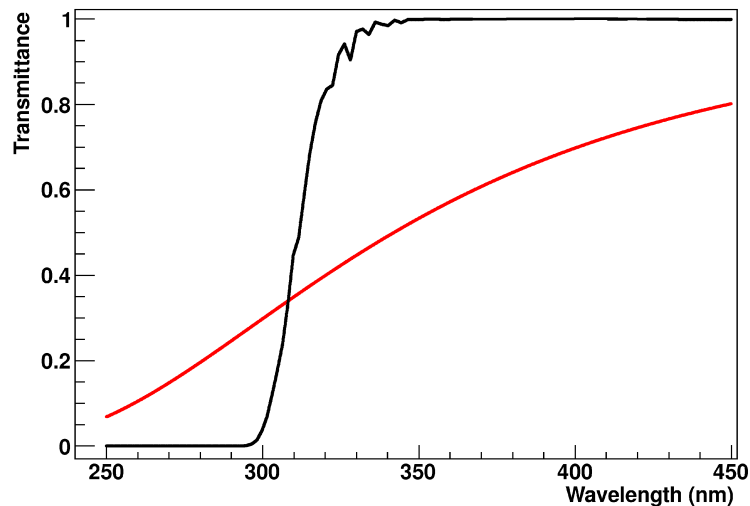


Figure 3.19: the transparency function for both Rayleigh and ozone absorption as function of wavelength. The function is calculated from ground to JEM–EUSO along a vertical path. Rayleigh transparency can be seen in red while ozone absorption in black.

In the present ESAF configuration the so called *lowtran 7* [164] package is used to simulate the entire photon propagation. Such a package makes also use of the so called *Standard US atmosphere* [163]. All the relevant interaction processes like Rayleigh scattering, ozone absorption and Mie scattering have been included in ESAF. Since the present thesis covers just the clear sky condition, the main focus of this section will essentially be on the Rayleigh scattering and on ozone absorption. In fact, a satisfactory treatment of the cloudy condition and aerosols (which involves mainly Mie scattering) is out of the scope of this work.

In Fig. 3.19 the atmospheric transparency for both ozone and Rayleigh

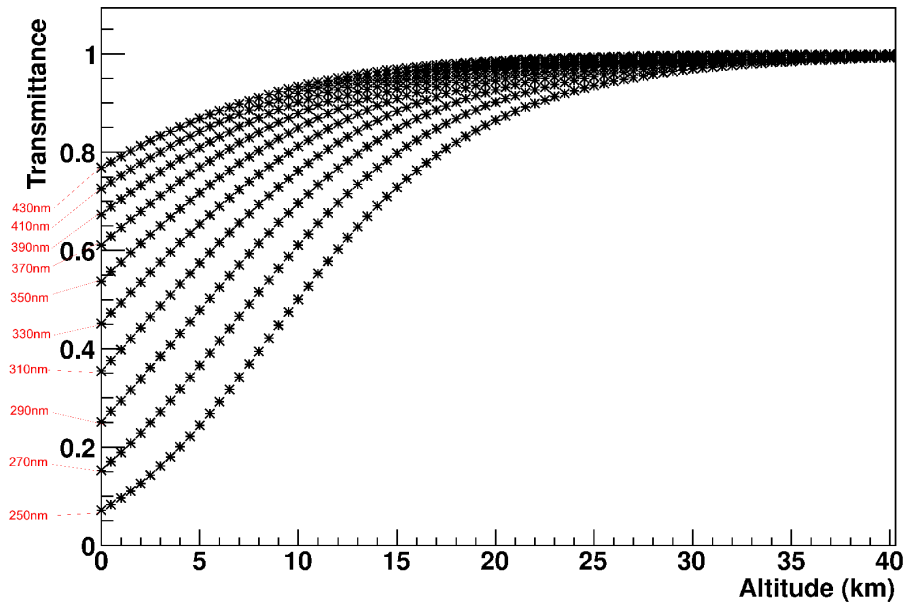


Figure 3.20: the Rayleigh transparency as function of altitude. The transparency is shown for different wavelengths from 250 to 430 nm in 20 nm intervals.

is shown. The calculation has been performed along a vertical path from ground till JEM–EUSO. The two curves have been distinguished by two colors: red for Rayleigh and black for ozone. As can be clearly seen, the ozone absorption processes start to be relevant just under 330 nm. While the Rayleigh transparency shows a smooth and constantly increasing tendency toward the higher wavelengths the ozone shows a rich wavy structure.

In Fig. 3.20 on the other hand, the transparency of the Rayleigh scattering can be seen as function of altitude. Additionally several curves are shown here to better express the different behavior according to wavelength. As can be seen here, each curve corresponds to a different wavelength which has been chosen in regular intervals of 20 nm from 250 to 330 nm. As it is clearly visible, short wavelengths show a stronger depletion.

The same kind of plot has been produced for ozone which can be seen in Fig. 3.21. The characteristic feature of this plot is the large difference between shorter and longer wavelengths. As can be seen for the three lower wavelengths the atmosphere remains totally opaque under 20 km. However, due to the very sharp transition observed also in Fig. 3.19 at 310 nm the entire atmosphere starts to be partially transparent. Above 330 nm, the atmosphere can be considered totally transparent to ozone at all altitudes.

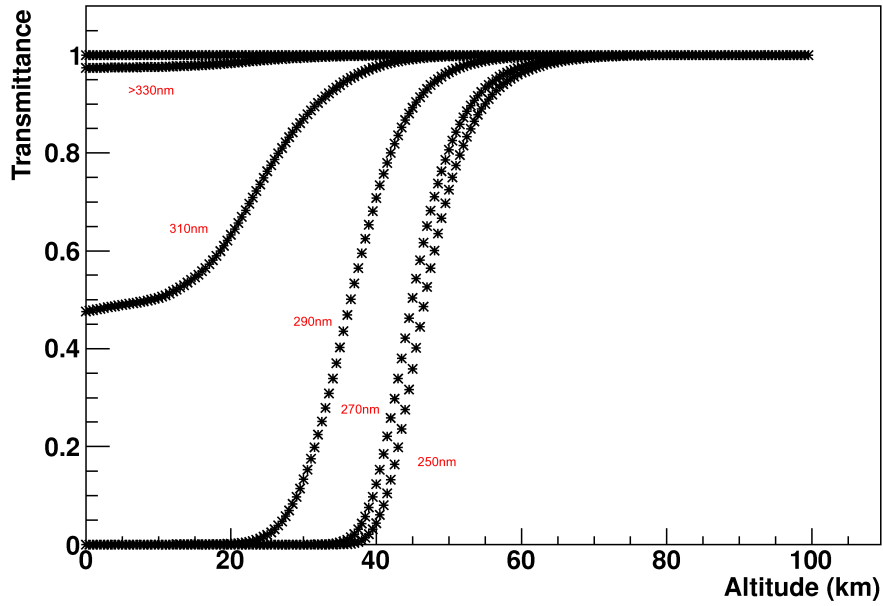


Figure 3.21: the ozone transparency as function of altitude. The transparency is shown for different wavelengths from 250 to 430 nm in 20 nm intervals.

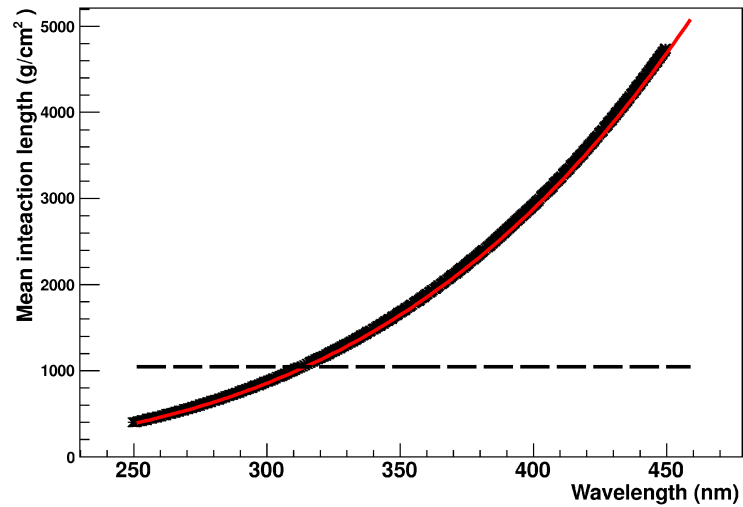


Figure 3.22: the mean interaction length for Rayleigh scattering as function of wavelength. The mean interaction length is shown in terms of slant depth in  $\text{g}/\text{cm}^2$ . The dashed line represents the total vertical slant depth of atmosphere. The red line represent a modeling of the Rayleigh scattering as shown in [174]



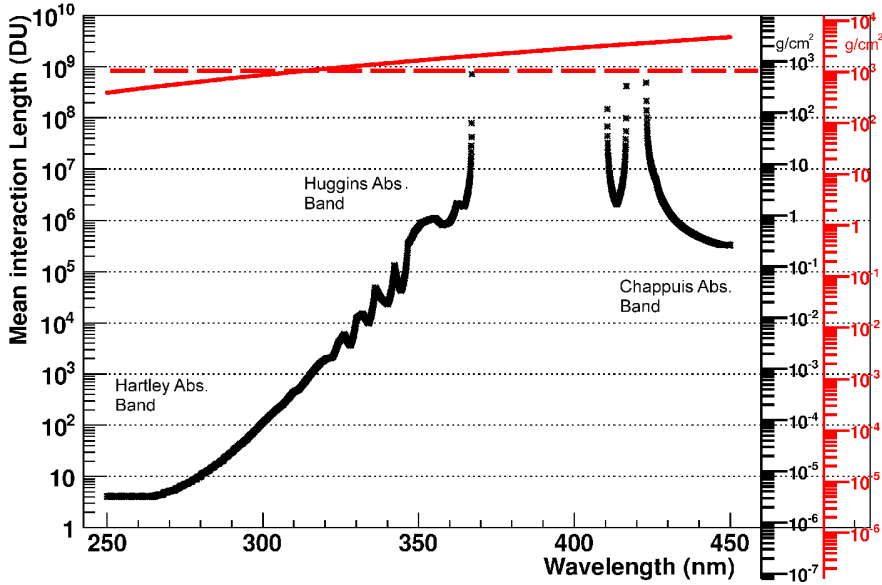


Figure 3.23: the mean interaction length for Rayleigh (red line) and ozone (black line) expressed in dobson units. Both plots have been expressed as function of wavelength. The red dashed line represents the total vertical columnar density of the atmosphere. On the right side the graduated scale indicate the columnar density expressed in slant depth ( $\text{g}/\text{cm}^2$ ) for both ozone and Rayleigh. To be stressed is the non unique conversion factor between dobson units and slant depth. Such a conversion factor in fact depends on the molar mass of the considered gas. The red axis corresponds to the columnar density of air (in  $\text{g}/\text{cm}^2$ ) and refers to the Rayleigh curve (red curve). The black axis corresponds to the columnar density of ozone (in  $\text{g}/\text{cm}^2$ ) and refers to the ozone curve (black curve).

In Fig. 3.22 the mean interaction length for Rayleigh scattering expressed in slant depth units ( $\text{g}/\text{cm}^2$ ) as function of wavelength is shown. The integration is started at ground level along the vertical till JEM-EUSO. The dashed line represents for visual comparison the vertical slant depth of the atmosphere. Clearly the increase of the interaction length agrees with the increase of atmospheric transmittance also shown in Fig. 3.20.

Furthermore a simplified formula has been also superposed to the *Lowtran 7* output. Such an equation is derived from Berat et al. [174] and expresses the mean interaction length of Rayleigh. Such a formula can be written like in Eq. 3.7.

$$\Lambda = 3102 \text{g}/\text{cm}^2 \left( \frac{\lambda}{400 \text{nm}} \right)^4 \cdot \left( 1 - 0.0722 \left( \frac{400 \text{nm}}{\lambda} \right)^2 \right) \quad (3.7)$$

The function seem to agree quite well with the used ESAF routines output and the deviation between the two models never exceeds more than  $\sim 1-2\%$ .

The last point concerns the relative comparison of the interaction lengths for ozone and Rayleigh. Because of the different distribution of ozone with respect to air the comparison must be done in columnar density units like Dobson units or slant depth. In Fig. 3.23 the Rayleigh mean interaction length can be observed in red. In black we can observe the same feature for ozone. The Y axis on the left represents the mean interaction length in DU of air (for Rayleigh) and of ozone (for ozone absorption). Moreover, the red dashed line represents the thickness of the atmosphere in DU ( $\sim 8.3 \cdot 10^8$ ). Such a value represents by definition an air column of 8.3 km at 273 K and 1 atm. On the right side on the other hand the columnar density in terms  $\text{g}/\text{cm}^2$  is shown. Because of the different molar mass of air with respect to ozone the conversion factor from DU to slant depth is different for the two gases. In fact, while DU is basically an integration of volume (which requires just the assumption of the ideal gas law), the slant depth is an integration of mass for which the knowledge of the molar mass is necessary. The red axis represents the mean free path in terms of slant depth in air. The black axis on the other hand represents the mean free path in terms of slant depth in ozone. As can be seen the axes are shifted by a factor  $\sim 1.6$  which is consistent with the ratio of the molar masses of ozone and air ( $\sim 1.6$ ).

A last consideration can be done about the rich structure of the ozone absorption as modeled by ESAF. As can be clearly seen in the plot several regimes can be identified. At the lowest wavelengths the so called *Hartley* absorption bands strongly constrain the transparency. Such a feature is dominant till 300 nm and show quite continuous structure. Above 300 nm the so called *Huggins* absorption bands are present. Although less strong they exhibit a band-like structure which can be clearly seen in the wavy structure of the plot. Following toward higher wavelengths between 330 and 410 nm ozone becomes totally transparent to show weak absorption features again in the visible range above 410 nm. Such absorption feature is known as *Chappuis* absorption band.

## 3.6 Optics

The second main task of the Simu framework is the simulation of the detector. At this point a list of photons is handled to the optics simulator. Each photon carries informations like position, direction and wavelength. The simulation will take care of the propagation of all the photons till the focal surface. After this point the surviving photons will be converted in electric signals and treated by the electronics.

As explained in Figs. 3.1 and 3.24 the *SimuMain.cc* will activate the simu-

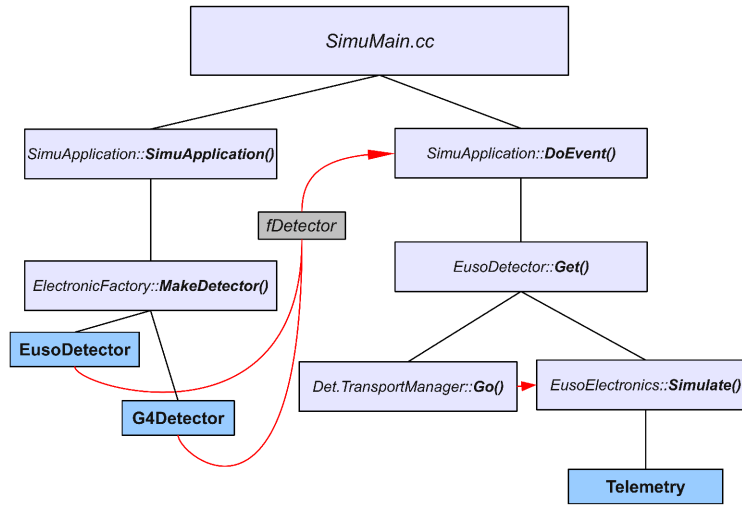


Figure 3.24: the ESAF detector simulation structure. The *SimuMain.cc* application will first allocate the *Detector* objects depending on whether the RIKEN or the Geant 4 [165] simulators are to be used. Thanks to the *SimuApplication::DoEvent()* and *EusoDetector::Get()* method both the optics and the electronics are simulated. The final output will be of *Telemetry* type.

lation of the detector after producing a list of photons on pupil. After calling the *SimuApplication::SimuApplication()* method a *Detector* object is allocated. Such an instance is created by the *ElectronicsFactory::MakeDetector()*. Depending on the input parameters either an *EusoDetector* or a *G4Detector* will be created. Other detector simulators are implemented for testing purposes. In the course of the thesis just the *EusoDetector* will be however considered. After the main detector instance has been created the *SimuApplication::DoEvent()* method will perform the actual simulation of all the detector components. For this purpose thanks to the *EusoDetector::Get()* method both the *DetectorTransportManager::Go()* and the *EusoElectronics::Simulate()* will be called for the simulation of optics and electronics respectively. The final returned object is of *Telemetry* type.

A more detailed view of the optics simulation is given in Fig. 3.25. We can see here the sequence of calls which is initiated by the methods *EusoDetector::EusoDetector()* and *DetectorTransportManager::Go()* of Figs. 3.24 and 3.25. After a long sequence of calls the *DetectorTransportManager::DetectorTransportManager()* will perform the allocation of all the relevant sub-components of the photon transport simulator. Therefore, at this point the *OpticsFactory* class methods will be called in order to initialize *Op-*

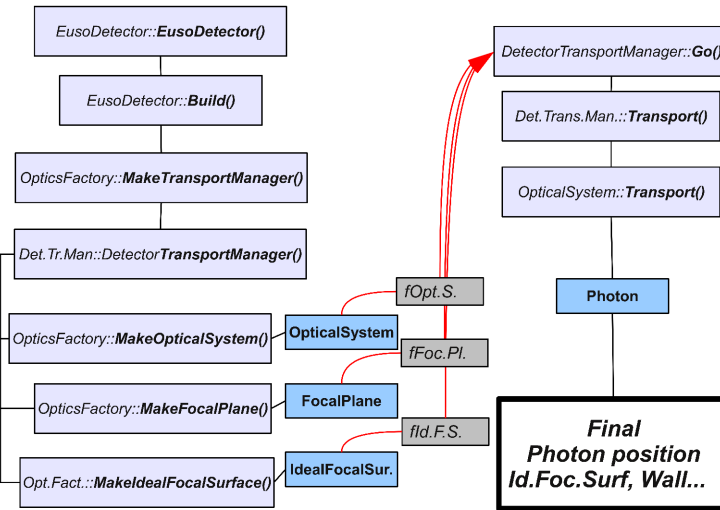


Figure 3.25: a more detailed sketch of the optics simulators. Such a structure applies for the *EusoDetector* simulator. The call of the method *EusoDetector::EusoDetector()* (see also Fig. 3.24) will start a sequence of calls that leads to the allocation of all the necessary components of the optics simulator. More in detail the *OpticalSystem*, the *FocalPlane*, the *IdealFocalSurface* and many other are allocated. The call of the method *DetectorTransportManager::Go()* will perform the simulation of the optics. One of the most important operations is performed by the *OpticalSystem::Transport()* method. The final output consists again in a list of photons each of one identified by a certain position, timing and fate (*absorbed, wall...*).

*ticalSystem*, *FocalPlane*, *IdealFocalSurface* and several others optics related classes. Depending on the parameter set one of the generators of the *RIKEN raytrace code* will be called. The most up to date function implemented in ESAF is the so-called *NOpticalSystem* which will be used in the course of the thesis. Both the JEM–EUSO PPP baseline and CPP advanced (see Chap. 2) optics are available for use. All the pointers to the allocated sub-components will be then passed to the *DetectorTransportManager::Go()* method where the calls chain for the real photons transport is started. In sequence the *DetectorTransportManager::Transport()* and the *OpticalSystem::Transport()* methods will bring all *PhotonsOnPupil* from pupil to the focal surface or to other internal parts of the detector like for example the *Wall*. The final result of this simulation is a list of photons which carries the information of position, direction, wavelength and so on. Such information will be used in the next step once the photons are transferred through the filter, the optical adaptor and the *PmtSignal* is produced.

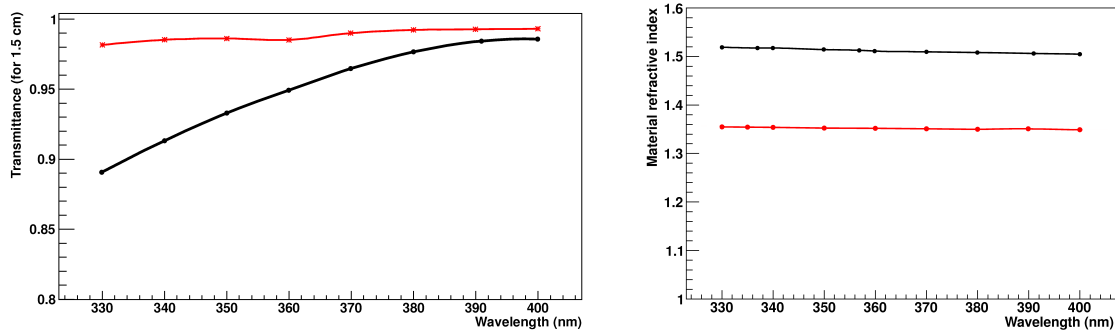


Figure 3.26: **Left panel:** the lenses material transmittance for different wavelengths. Both PMMA (black curve) and Cytop (red curve) material are shown. **Right panel:** the refractive index for both PMMA (black curve) and Cytop (red curve).

All the photons are going therefore to be transported and diffracted in the lens medium and delivered to the focal surface. At this stage the optical filter is implemented and the photons are either absorbed or transmitted to the PMT depending on their wavelength.

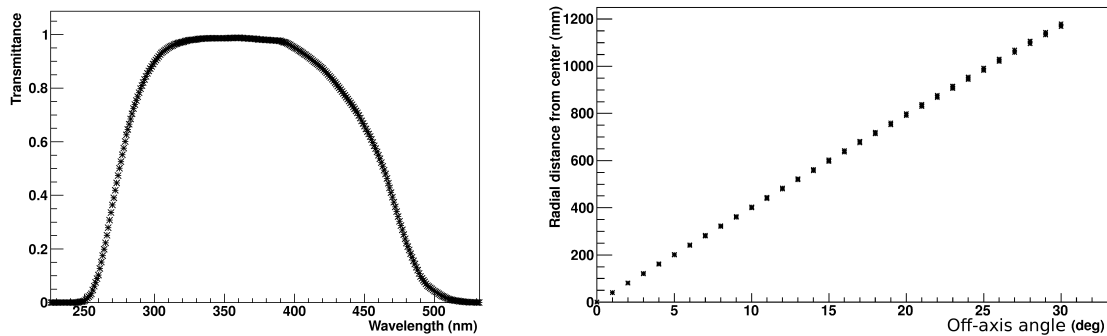


Figure 3.27: **Left panel:** the transmittance curve of the ESAF BG3 filter. **Right panel:** the image height of the JEM-EUSO PPP optics. The average radial distance from the central axis of photons coming from a point source in a particular direction is represented here. The average position is calculated after a preselection of all the photons within 20 mm from the maximum density bin.

In Fig. 3.26 the transmittance and the refractive index of the lenses is represented as function of wavelength. As can be clearly seen in left panel Cytop material has a much higher and constant transparency than PMMA. It can be also observed (right panel) how Cytop material is characterized by a lower refractive index than PMMA.

In Fig. 3.27 (left panel) the so called BG3 filter transmittance is depicted. Such a filter is implemented in order to reduce the background caused by photons outside the experimental wavelength range (300–400 nm). According to

the optics laws and to the tabulated lenses parameters photons are therefore scattered through all the three lenses and focused on the focal surface. In Fig. 3.27 (right panel) the center of mass of the photon spots generated as function of off-axis angle ( $\vartheta$ ) is shown. Such a parameter has been calculated as the average position of all the photons falling in a very large selection area having radius of 20 mm and centered on the maximum of the photon distribution. As can be seen a quasi-linear behavior can be observed.

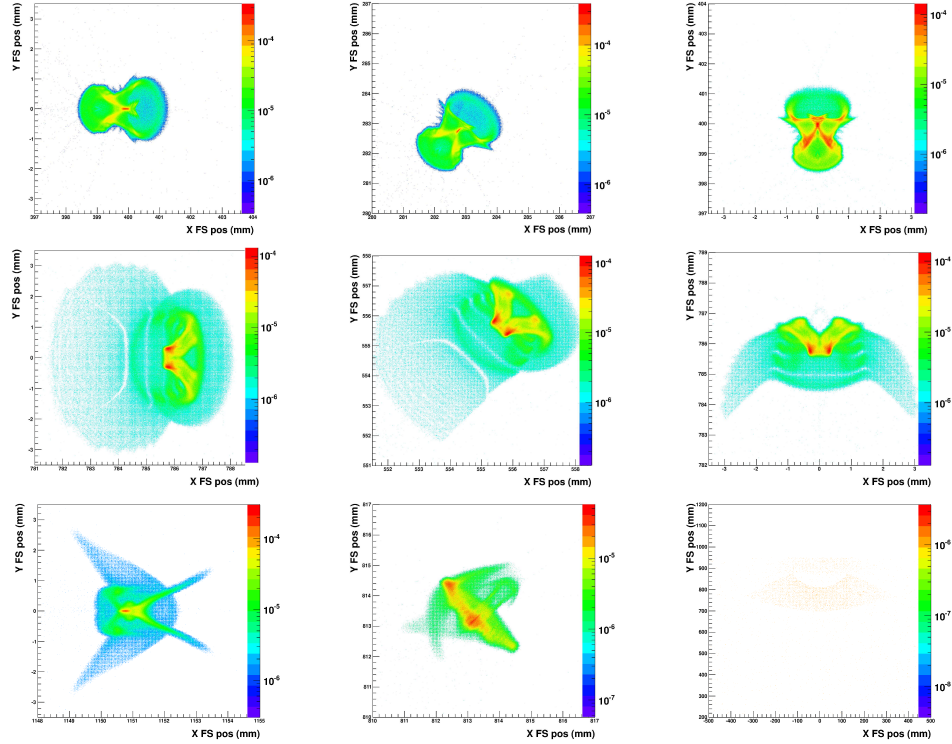


Figure 3.28: several spot images for different inclinations. The upper line represents the off-axis angle  $\vartheta=10$  degrees while the second and third respectively 20 and 30 degrees. The leftmost column represents the condition where  $\varphi=0$  degrees while the second and third column represent respectively 45 and 90 degrees. The chosen wavelength is 350 nm. The color scale represents the fraction of the photons reaching the  $4.5 \text{ m}^2$  which are being focused to a particular bin. Each plot has the same binning which corresponds to a bin of area of  $1.6 \cdot 10^{-5} \text{ mm}^2$ . Each plot corresponds to  $10^7$  photons shot on a circle of 1325 mm.

In Fig. 3.28 an example of the form of the JEM–EUSO optics spot is given for different condition of entrance direction. The simulated point sources are located to infinity and correspond to FOV angles of  $\varphi = 0, 45, 90$  degrees and  $\vartheta = 10, 20, 30$  degrees. The chosen wavelength is 350 nm. As can be clearly observed for the condition  $\varphi = 90 \vartheta = 30$  degrees no focusing is

possible because of the side-cut form of the JEM-EUSO optics. Another feature to observe is the axis-symmetric behaviour at low angles. In fact, for the conditions  $\vartheta=10$  degrees the spot keeps its shape for all the  $\varphi$  conditions except for a rotation around the central axis. On the other hand, as it can be seen, for increasing angles the spot shape tends to vary with the  $\varphi$  angle.

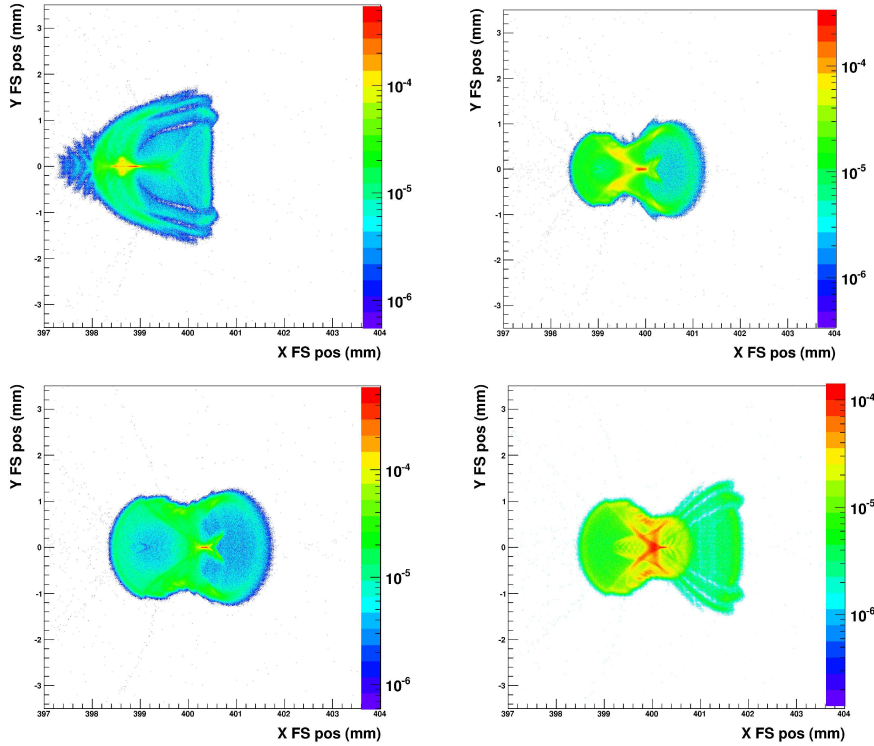


Figure 3.29: the spot shape for different wavelengths. The inclination condition is constant for all the plots and corresponds to the angles  $\vartheta=10$  and  $\varphi=0$  degrees. All the plots have been produced in the following conditions. **Upper left plot:** 330 nm. **Upper right plot:** 350 nm. **Bottom left plot:** 370 nm. **Bottom right plot:** 390 nm. The color scale represents the fraction of the photons reaching the  $4.5 \text{ m}^2$  which are being focused to one particular bin. Each plot has the same binning which corresponds to a bin of area of  $1.6 \cdot 10^{-5} \text{ mm}^2$ . Each plot corresponds to  $10^7$  photons shot on a circle of 1325 mm.

In Fig. 3.29 also the spot shape for the condition  $\varphi = 0$   $\vartheta = 10$  degrees and wavelengths  $\lambda=330, 350, 370$  and  $390$  nm is shown. As it clearly appears the shape is also wavelength dependent.

A more quantitative description of the arrival direction and wavelength dependence of the spot shape is shown in Fig. 3.30. Here the spot size as function of the off-axis angle is shown. The spot size has been defined as the radius within which is focused the 90% of the photons hitting the focal surface. The center of such an area is defined as the average position

of the photons focused on the focal surface after applying a 20 mm radius cut around the maximum bin. In left panel such a parameter is shown for several wavelengths (300, 325, 350, 375 and 400 nm) and for  $\varphi$  angle equal to 12 degrees. The short wavelengths show a factor 5 to 10 larger spot size compared to the other wavelengths. At all the other wavelengths, the spot size remains always confined within 2 mm radius. In right panel the same parameter is depicted for fixed wavelength (350 nm) and for several arrival  $\varphi$  angles (12, 36, 60 and 84 degrees). Being the spot not focused in the side-cut region no data are available for the angles  $\varphi = 60$  and 84 degrees for large  $\vartheta$ . Apart of that, given the described conditions the spot size remains always within the 2 mm radius. Near the center the spot is even concentrated within 0.5 mm.

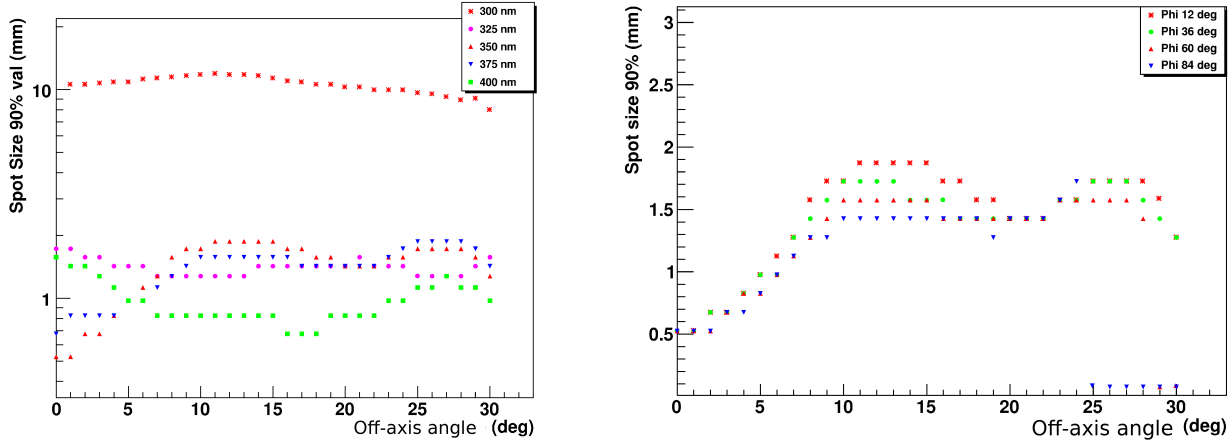


Figure 3.30: **Left panel:** the spot size as function of the off-axis angle. The same plot is shown for different wavelengths namely 300, 325, 350, 375 and 400 nm. **Right panel:** the spot size as function of off-axis angle. The plot for different  $\varphi$  angles are shown here. All the curves are produced at 350 nm. For both panels the spot size has been defined as the radius within which 90% of all the photons arriving on the focal surface fall. The center of such a radius is defined as the average after a preselection of 20 mm from the maximal density bin.

Another very important parameter is the so called ensquared throughput efficiency. Such a parameter observable in Fig. 3.31 is expression of the fraction of photons arriving within an area of  $\sim 8.7 \text{ mm}^2$  with respect to the photons arriving on the entrance pupil. This is comparable to the area of the present baseline pixel ( $\sim 2.9 \times 2.9 \text{ mm}^2$ ) and is of circular shape. This collection area is again centered on the center of mass of the spot obtained after a preselection of the photons falling inside 20 mm from the maximum bin. Such a definition is however appropriated just in the context of the optics performance evaluation. In fact, with such a parameter we express



the capability of the optics of generating signal above the background given a point source. In the framework of the event reconstruction on the other hand the spot size will not be determined by the optics but mainly by the size of the shower.

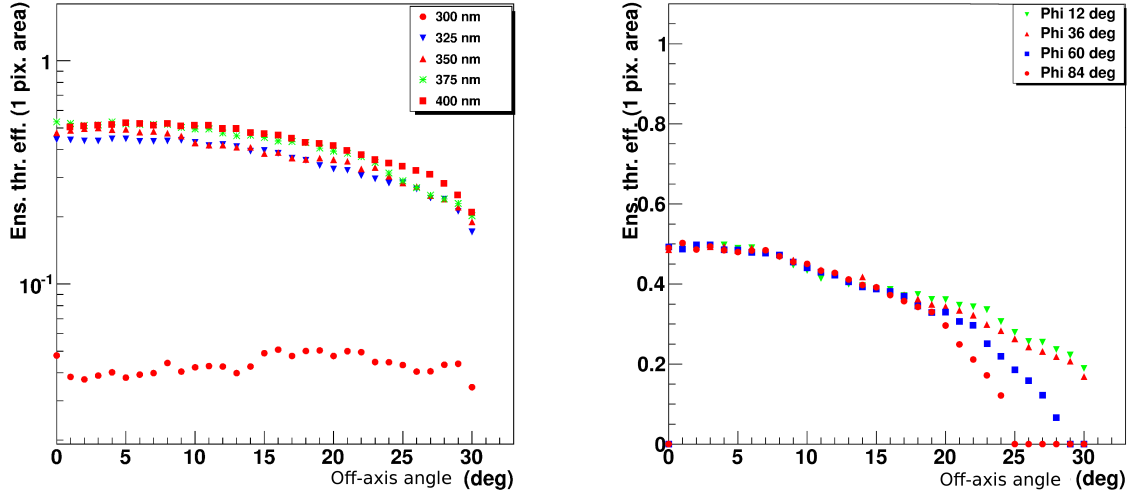


Figure 3.31: **Left panel:** the throughput efficiency as function of the off-axis angle. The plot has been performed for different wavelengths (300, 325, 350, 375 and 400 nm). **Right panel:** the throughput efficiency as function of the off-axis angle. The plots are shown for different  $\varphi$  (12, 36, 60 and 84 degrees). For both plots the throughput has been defined as the fraction of photons falling in an area of  $\sim 8.7 \text{ mm}^2$  radius with respect to the one impinging on the pupil ( $4.5 \text{ m}^2$ ). Such an area is equivalent to the area of a pixel. The surface has been chosen to be circular. The considered area is chosen to be centered on the average position of photons after a preselection of photons within 20 mm from the maximum density bin.

In Fig. 3.31 left panel the efficiency is depicted as function of the off-axis angle for different wavelengths (300, 325, 350, 375 and 400 nm) and fixed  $\varphi$  (12 degrees). As it is clearly visible the efficiency for the shorter wavelengths is poorer. Another very important feature is the lower efficiency observable toward the edges of the FOV. Furthermore we can observe a slightly higher efficiency for the highest wavelengths due to the better transparency of PMMA at higher wavelengths. In right panel the throughput efficiency has been depicted as function of the off-axis angle for a fixed wavelength (350 nm) but for different  $\varphi$ . As can be seen no significant deviation from spherical symmetry is observable till  $\vartheta \sim 20$  degrees. After such an inclination the effect of the cut section of the telescope starts to become relevant. Therefore for the  $\varphi$  angles 60 and 84 degrees a drop even to 0 of the efficiency is observed as the side cut is reached.

### 3.7 Electronics

In this section a brief description of the ESAF electronics is given. The event is therefore followed from the PMT signal till the telemetry. As can be seen in Fig. 3.32 (and Fig. 3.24) the call of the *EusoDetector::EusoDetector()* method will start a sequence of calls that will eventually lead to the allocation of the sub-components of the electronics. More in detail within the *EusoElectronics::Build()* the *ElectronicsFactory::MakeElementaryCell()*, the *ElectronicsFactory::MakeMacroCell()*, *ElectronicsFactory::MakePmt()* and several others will be called. As the names explain, such functions will allocate all the objects for the single components simulation. The allocated objects will therefore be of type *ElementaryCell*, *MacroCell* and *Photomultiplier*. The relative pointers to the allocated memory segments are then passed to the *EusoElectronics::Simulate()* method which will perform the simulation of all the components. The *EusoElectronics::Simulate()* method will however need the input of all the *PmtSignals* which will be generated after all the photons have been transported through the *OpticsAdaptor* simulator and delivered to the *Photomultiplier* routines.

One of the most important parts of the electronics simulation is performed within the *MacroCell::Simulate()* method since in this context the trigger algorithms will be performed. Eventually the final output of the electronics framework will be a *Telemetry* object. The information produced at this stage, which basically includes a table of counts with space and timing information, will be saved in the *.root* file together with all the trigger informations. Such operations conclude the *Simu* framework and all the informations are made available for the *Reco* framework.

The delivery of the photon to the *Photomultiplier* class will start the PMT simulation. The first step consists in the application of the detector efficiency. This will decide whether the photon can be converted to a signal or not. For this purpose three efficiencies coefficients are applied. The first one is the so called quantum efficiency and determines the fraction of photons to be converted in photoelectrons. In ESAF a parameterization of such an efficiency is implemented and plotted in Fig. 3.33 (left panel). In such a plot the efficiency is plotted as function of the photon wavelength and reaches its maximum between 300–320 nm. Another extremely important factor is the angular dependence of the quantum efficiency. As plotted in the right panel such an efficiency corresponds to an additional factor which depends on the inclination of the photon with the perpendicular axis of the PMT. Once the photoelectron has been produced, the PMT has to focus it to the anode. The fraction of produced photo electrons arriving to the anode is therefore expressed under the name of collection efficiency. In the current M64-PMT

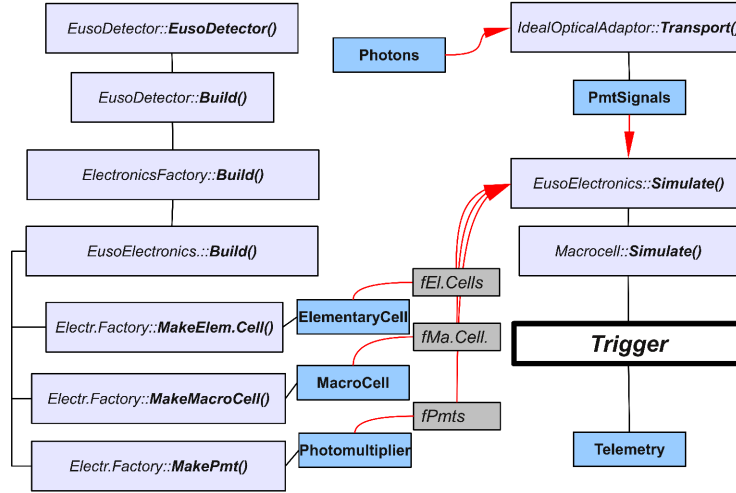


Figure 3.32: a sketch of the Electronics simulator. Such a scheme is valid for the *EusoDetector* configuration. The call of the *EusoDetector::EusoDetector()* method will activate the sequence of calls that will eventually lead to the allocation of all the necessary subcomponents of the electronics. As an example the *ElementaryCell*, the *MacroCell* and the *Photomultiplier* are represented here. The relative pointers are then passed to the *EusoElectronic::Simulate()* method which will, after accepting as input the *PmtSignal* objects, perform the calls for the *MacroCell* and *FrontEnd* simulation. The trigger will also be called here. The final output is a *Telemetry* object.

such a factor is taken as constant and equal to 0.8. A random number will be uniformly sampled and in all the cases where it exceeds the efficiency  $\epsilon_{det}$  a *PMTcount* will be produced.

$$\epsilon_{det} = \epsilon_{quant}(\lambda) \cdot \epsilon_{ang}(\vartheta) \cdot \epsilon_{coll}(Pixel) \quad (3.8)$$

ESAF allows also the treatment of the so called cross talk. This phenomenon describes the probability of a photoelectron to be focused on the anode of another pixel. The image will therefore result smeared by such an effect. For this purpose ESAF considers a matrix which determines for each pixel the probability of the signal to end up in another one. However, in the newest generations of EUSO PMT's such an effect is negligible and it is therefore considered to be 0 in the most up-to-date ESAF parameterizations.

The PMT converts the *PhotoElectron* in a current signal. Every PMT channel is therefore characterized by a gain factor which expresses the conversion factor from *PhotoElectron* to final pulse charge. In the baseline of M64-PMT implemented in ESAF the average gain is  $4.8 \cdot 10^6$  while the gaus-

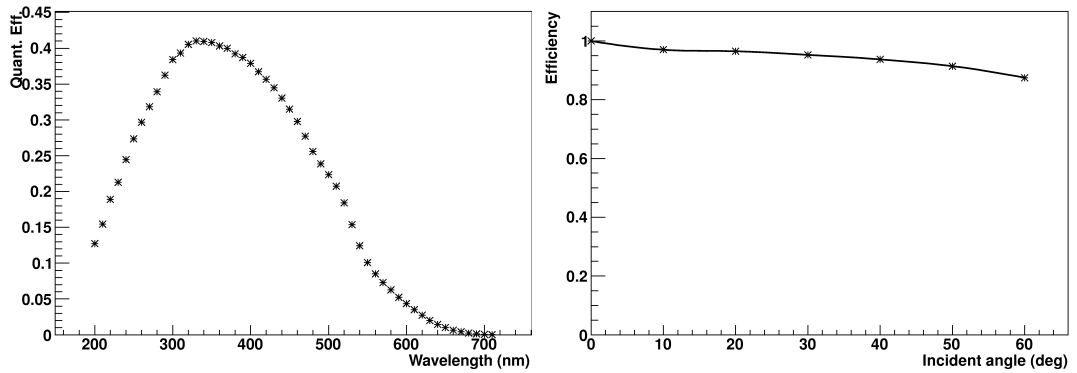


Figure 3.33: **Left panel:** the quantum efficiency for the JEM–EUSO M64–MAPMT as function of wavelength. **Right panel:** the additional efficiency factor depending on the inclination of the photon with respect to the vertical of the PMT.

sian fluctuation is  $9.1 \cdot 10^5$ . Each count is therefore amplified according to a random gaussian distribution and therefore the amplitude of the current pulse results to be also an average value with a gaussian  $\sigma$  fluctuation associated.

The signal shape as function of time is also set to be gaussian. In the present implementation status, this feature is however not relevant since the only feature presently taken into account by the *FrontEndElectronics* is the amplitude of the gaussian pulse. If such a parameter is larger than a pixel–preset threshold the PMT count is converted in a front–end count. The chosen threshold is assigned to each pixel in the building phase and is considered to have an average of  $54 \mu\text{A}$  with a gaussian fluctuation of  $5.4 \mu\text{A}$ .

Worth to mention is the presence at the *FEE* level of another gain factor which is set also to be of gaussian shape with average = 1 and  $\sigma$  0.05.

Of extreme importance is the generation of the background which is added at this level. In fact, since the simulation of each of the  $\sim 10^{12}/\text{s}$  night glow photons is computationally too heavy, the assignment of a certain amount of counts / (pixel·time) is made at the *FEE* level. The preset background is however still implemented as a constant average, varying from pixel–GTU according to a poissonian distribution. The implementation of background maps with average varying from pixel to pixel is left for future works.

Once both Front–End counts and background are generated, the further step includes the logic treatment of the count map. Several trigger algorithms will be therefore applied in order to reduce the data amount rate. The detailed treatment of this aspect is however left for the next chapters.

### 3.8 Reconstruction: pattern recognition

The general reconstruction structure is by far simpler than in the simulation case. As seen in Fig. 3.2 the entire reconstruction chain is build in such a way to be extremely flexible. In fact, all the modules will be allocated within the *RecoFramework::RecoFramework()*. The pointers to such objects will be then used in a recursive iteration for calling the initialization, execution and clearing methods. Each of the modules will have to be structured in such a way to have *RecoModule::PreProcess()*, *RecoModule::Process()*, *RecoModule::PostProcess()* and *RecoModule::SaveRootData()* methods. The order of execution of all the modules is decided at the level of parameter file but must respect the specific input–output demands of each module. Obviously any direction or energy reconstruction must get as input a cluster of pixel–GTUs. For that reason at the first step any reconstruction must be initiated by a pattern recognition. Other dependences must be checked from time to time depending on the chosen configuration.

As already explained, after the trigger signal is issued all data is sent to Earth for the reconstruction of the event properties. The JEM–EUSO data format has not been finalized yet but it can be thought as a table of pixel–GTUs carrying the information of how many counts are associated to each pixel for each time. The first necessary step would be the recognition of the signal inside the data. Additionally, at this stage some selection algorithm should be present in order to reject the large amount of fake trigger still keeping the real events. In fact beside a fake trigger rate of the order of  $\sim 0.1$  Hz, JEM–EUSO has a real event trigger rate of  $\sim 0.1$ – $1$  mHz. The selection algorithms should therefore prove the ability of rejecting the fake triggers with a reliability of at least a factor  $10^{-5}$ . Such a rejection performance is necessary to guarantee the presence of less than 1 fake reconstructed event over 100 real events. The test of such a rejection performance is however computationally very challenging. The simulation of a statistically sufficient sample of fake triggers will in fact require huge simulation times. In fact, it requires the generation of at least  $10^5$ – $10^6$  fake triggers and the processing of them through the filtering algorithms<sup>9</sup>. The preparation of such a rejection study is ongoing but will not be included in the present work.

In the present study the pattern recognition algorithms will be just used to identify the real signal inside the data sent at ground. Several approaches have been followed in the course of time for this purpose. The simplest one is the so called *LTPPreClusteringModule* developed by Bertaina and Gorgi.

---

<sup>9</sup>To be noticed is the fact that for each fake trigger  $\sim 10$  s of pure background on  $\sim 3 \cdot 10^5$  pixels, for  $4 \cdot 10^5$  GTU/s must be simulated. Such a task requires large amounts of CPU time since it implies the generation of  $\sim 1.2 \cdot 10^{12}$  random numbers.

Such a module performs an integration along several test tracks in order to select the most likely signal location in the data. The *LTTPreClustering-Module* is inspired by the *LTTTrigger* which will be described in the next chapter. In few words it looks for high density tracks of signal on the focal surface. The JEM–EUSO signal is in fact characterized by a spot moving on the focal surface with a speed equal to the projected speed of light.

The pattern recognition algorithms will start from an initial condition which is presently defined as the pixel–GTUs with the maximum counts density. Such a frame is defined as the  $3 \times 3$  box which realizes the highest count integration within 5 consecutive GTUs. This is done in order to reduce the probability of a random fluctuation of background. In fact the persistency over such a long time is very likely due to the presence of a signal spot. Other choices could be the pixel–GTU with the maximum trigger. In this case of course such an information must be provided by the telemetry. Following the initial condition selection an integration is started along several predefined directions. The integration box will have  $3 \times 3$  size and will be moved for the length corresponding to 200 GTUs. The speed of the integration box will be decided according to the projection on the focal surface of a set of predefined shower directions. The track which maximizes the integration is chosen as the center for the selection. All the pixels inside a preset distance will be therefore selected. Such a predefined distance is set from parameter and is expressed in terms of pixel size units. The radius of such an area must therefore be a tradeoff between the necessity of the maximal data reduction and the maximal signal collection. In Fig. 3.34 by Bertaina the fraction of collected signal can be seen as function of the selection parameter. As can be seen already a dimension of 3 pixel would allow a collected efficiency of  $\sim 90\%$ . This very simple algorithm allows therefore a massive data reduction since it can reject  $\sim 99\%$  of the background still accepting  $\sim 90\%$  of the signal. However this selected data is still much bigger than the real spot size and for that reason further, more refined search algorithms should be used together with the *LTTPreClusteringModule* to further improve the selection of the spot and also improve the following angular and energy reconstruction algorithms.

One of the possibilities is the so called *PWISE* selection algorithm developed by A. Guzman. Such an algorithm performs a search of the most likely signal pixels by means of an intensity and signal to noise ratio analysis. More in detail, the *PWISE* algorithm defines for each pixel the so called *Pixel Trace*. Such an object represents the front end counts history of each pixel or in other terms how many counts were selected by the FEE in each GTU for that pixel. After this definition, the *PWISE* searches for the maximum GTU within the *Pixel Trace*. Provided such a maximum is above a certain

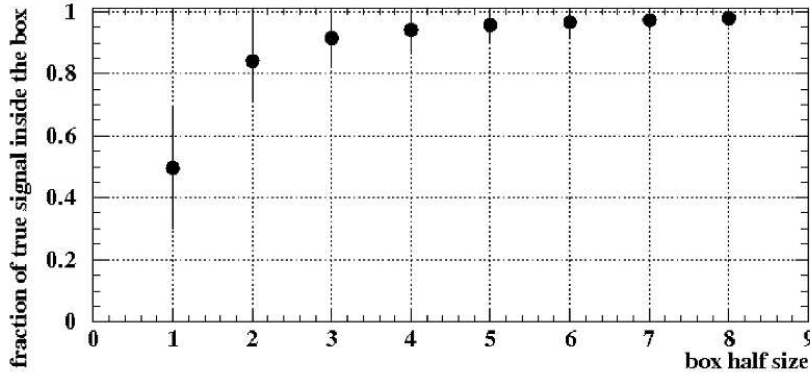


Figure 3.34: collected fraction of signal inside the *LTPPreClusteringModule* selection box as function of the selection box half size. Courtesy of Bertaina, Gorgi and Rossi.

threshold it selects it as a peak. Following this, a selection window is defined around the peak. Such a window will be chosen of variable width and the signal to noise ratio will be calculated for each condition. The signal to noise ratio is calculated as in Eq. 3.9

$$SNR = \frac{\sum_{\Delta\tau} counts}{\Delta\tau \cdot RMS} \quad (3.9)$$

whereas  $\Delta\tau$  is the window width, *counts* is the amount counts per pixel-GTU and *RMS* is the root mean square of the counts in the entire pixel trace. The window is therefore set at the beginning to be as large as the entire *Pixel Trace* and is progressively reduced till it only consists of the peak. The window having the maximum signal to noise ratio will be selected. At this point a further threshold on the SNR is applied and only those *Pixel Traces* having a SNR above threshold will be selected. All the pixel-GTU selected by such a procedure will be marked as part of the signal track and handled to the next reconstruction stages.

A visual example of the above described algorithms can be given in Fig. 3.35. Here one single proton shower ( $\theta = 65$  degrees) has been simulated and reconstructed. All the plots represent the integrated signal over the entire shower development.

The upper left panel of Fig. 3.35 depicts all data which have been sent by the telemetry. As can be clearly seen 2 entire PDMs have triggered and have been sent to Earth. As can be seen the background saturates the image and at least by eye no track recognition is possible. On the upper right plot on the just the signal pixels can be seen. This information is of course not available for any measurements since signal is not directly distinguishable by

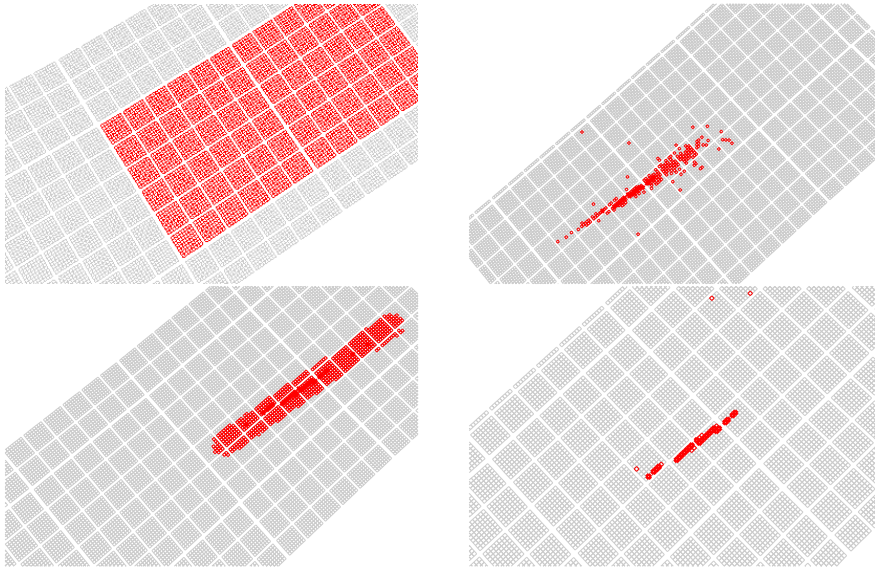


Figure 3.35: the telemetry data as received by the reco framework. The simulated event was a proton shower having an inclination of 65 degrees. Pixels which are selected are highlighted in red. Within the tracks pixels having more than 20 counts are depicted in bold red. **Top left panel:** the entire data bunch sent by the telemetry. **Top right panel:** the real signal counts. **Bottom left panel:** the pixel selected by the *LTTPreClusteringModule*. **Bottom right panel:** the data selected by the *PWISE*.

background. On the bottom left panel we can observe the *LTTPreClusteringModule* output. As can be seen the entire track is basically contained within the selected track and a very good rejection can be achieved. The application of the *PWISE* sequentially with the *LTTPreClusteringModule* allows a further narrowing of the selected data. As can be seen in the bottom right panel in fact the *PWISE* shows to be able of collecting just the Pixel-GTUs where the strongest part of the signal is.

### 3.9 Reconstruction: angular reconstruction

The direction reconstruction routines implemented in ESAF are the so called *TrackDirection2Module*, and the *TrackDetectorPlane*, *TrackDirection* module chain. In the present work however just the *TrackDirection2Module* is in use while the others are still in the debugging phase.

In order to perform any angular reconstruction at least two informations are necessary. The first is the already mentioned reconstructed track. The second fundamental information is a map which associates to each pixel a direction in the FOV. In ESAF such a map is called *PixelAngleMap* and



consists essentially of 5 columns:

$$\text{Pixel ID} \mid \vartheta \text{ angle} \mid \Delta\vartheta \mid \varphi \text{ angle} \mid \Delta\varphi$$

Such a table associates to each pixel ID a  $\vartheta$  and a  $\varphi$  angle. Associated with such an angle are also the relative sigmas expressing the width of the FOV associated with each pixel.

In Fig. 3.36 the *PixelAngleMap* is graphically represented. In the upper panels the  $\vartheta$  and  $\varphi$  angles are shown as function of the so called unique pixel ID which represents the identifier of each JEM–EUSO pixel and goes from 1 to 315648. The complex features seen in such plots are due to the non trivial order of the pixel identification number. In the lower panels the projection on the X–Y plane of the FOV angles can be observed first as a whole and then as a zoom on the central part.

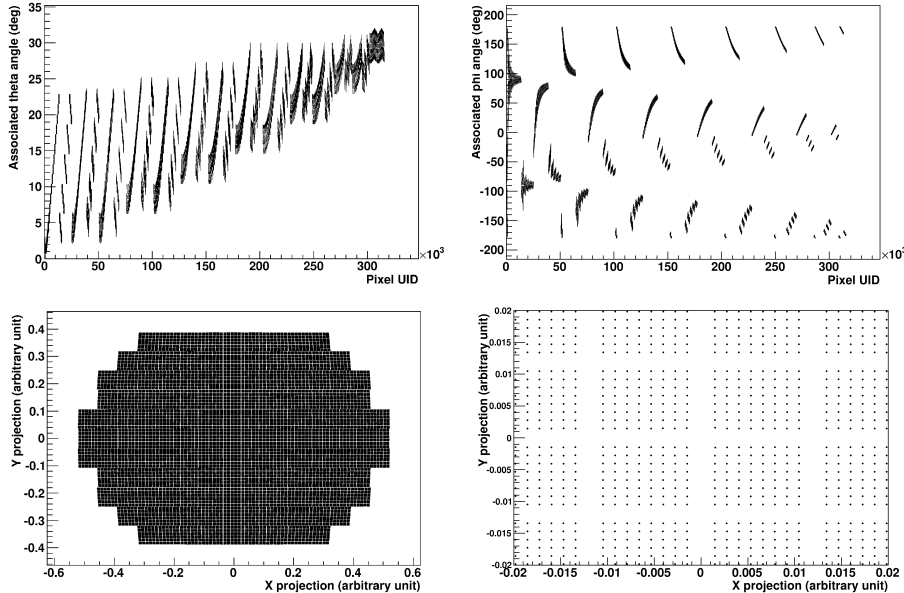


Figure 3.36: the *PixelAngleMap* function. **Top left panel:** the optics off-axis angle ( $\vartheta$ ) as function of the pixel ID. **Top right panel:** the optics rotational angle ( $\varphi$ ) as function of the pixel ID. The complicate patterns of both the upper panels is caused by the non trivial organization of the Pixel ID number. **Bottom left panel:** the projection on the X–Y plane of  $\vartheta$  and  $\varphi$  angles. **Bottom right panel:** a detailed view of the central part of the focal surface.

The *TrackDirection2Module* module includes several reconstruction algorithms. The two algorithms reaching the best performances are the so called *Numerical Exact 2* and the *Analytic Approximate 1 (AA1)* methods. In the first case the direction is reconstructed by means of several iterative tests.

The counts timing resulting from each test shower is compared with the data. The minimization of the  $\chi^2$  delivers the best direction. This method requires however the knowledge of at least one point of the real shower. For such a purpose the Cherenkov mark is the best candidate to justify the application of this method.

In present work however just the *AA1* will be treated in detail and is currently in use. This algorithm will first determine the so called *Track Detector Plane* which represents the plane where both shower and detector are located. Once this plane has been found the shower timing information is used to determine the inclination of the shower itself. Through all the steps of the *AA1*, the application of fit algorithms will be necessary both for the *TDP* and inclination determination. Within the *AA1* several fitting procedures are implemented. Between them the least square, median, the linear and the hough fitting procedures can be mentioned. In our specific case the so called median fitting is used<sup>10</sup>.

More in detail the *AA1* retrieves the identified cluster of data and by means of the available fit procedures finds the *TDP*<sup>11</sup>. For this purpose the knowledge of the position of the detector must be used as well as the informations coming from the *Pixel Angle Map*. The normal to such a plane  $\widehat{fNorm}$  will be then used for the calculation of other two vectors,  $\widehat{fW}$  and  $\widehat{fU}$ . The first one lies on the intersection between the *FDP* and the  $z=0$  plane and is calculated as:

$$\widehat{fW} = (0, 0, 1) \times \widehat{fNorm} \quad (3.10)$$

The  $\widehat{fU}$  vectors, on the other hand, is defined as

$$\widehat{fU} = \widehat{fNorm} \times \widehat{fW} \quad (3.11)$$

and lies on the *TDP* but is orthogonal to the horizontal plane intersection line (see Fig. 3.37). Such vectors define a base for the *TDP*. The following step consists in the definition of an  $\alpha$  angle between  $\widehat{fW}$  and the detector to shower vector<sup>12</sup>. The derivative of the  $\alpha$  angle will deliver therefore the information of the angular velocity of the shower with respect to the detector ( $\omega$ ) in the *TDP*.

Following this, an iterative procedure will be performed in order to calculate the relative inclination of the shower with respect to the detector and eventually the direction of the shower itself. As first approximation the height

<sup>10</sup>See the *MedianFit* class and the *MedianFit::Do()* method.

<sup>11</sup>See *TrackDirection2Module::FindPlane()*.

<sup>12</sup>See *TrackDirection2Module::AA1()*.

of the maximum of the shower will be assumed to be 5 km and consequently the distance  $R_{max}$  of the shower from the detector will be calculated<sup>13</sup>. Such a parameter will be used to calculate the linear tangential velocity of the shower like:

$$v_{tang} = R_{max} \cdot \omega \quad (3.12)$$

According to the trigonometric functions then, it can be derived that the the inclination of the shower with respect of the line of sight to JEM-EUSO is:

$$\beta' = \pi - 2 \cdot \arctan \frac{c}{v_{tang}} \quad (3.13)$$

By adding the average  $\alpha$  (which represents the angular position of the shower inside the  $TDP$  plane) to  $\beta'$  the angle  $\beta$  can be calculated.

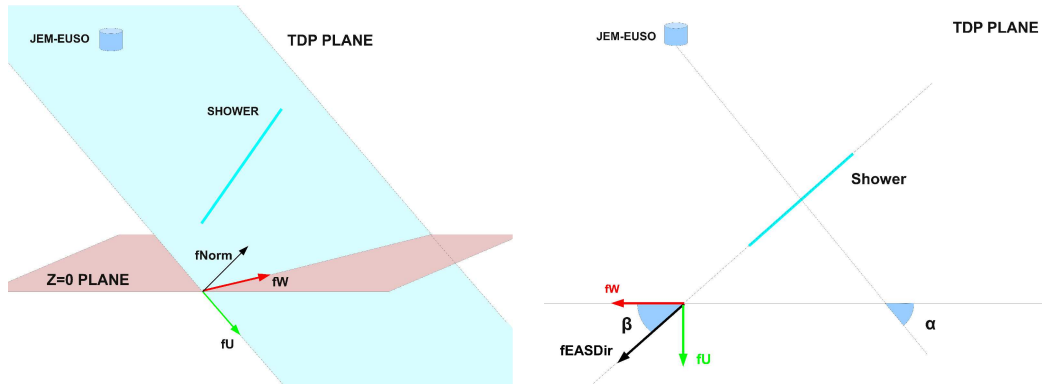


Figure 3.37: **Left panel:** the 3D representation of the direction reconstruction. Here both the  $TDP$  and  $z = 0$  planes are identified respectively with cyan and red colors. The normal vector, the  $\widehat{fW}$  and the  $\widehat{fU}$  vectors are identified in red and green. **Right panel:** the  $TDP$ -internal angles and the  $\widehat{fEASDir}$  vector.

The  $\beta$  angle represents therefore the inclination of the shower in the  $TDP$  plane with respect to the  $z = 0$  plane. Therefore by using the above defined  $\widehat{fW}$  and  $\widehat{fU}$ , the shower direction vector can be calculated as

$$\widehat{fEASDir} = \cos \beta \cdot \widehat{fW} + \sin \beta \cdot \widehat{fU} + \pi \quad (3.14)$$

where the additional  $\pi$  is just a rotation factor to respect the ESAF system orientation<sup>14</sup>.

The above calculated direction vector can be used now to give a more justified choice of the altitude of the maximum. Such a direction is therefore

<sup>13</sup>See `TrackDirection2Module::CalculateRmax()`.

<sup>14</sup>See `TrackDirection2Module::CalculatefromBetaEASdir()`.

used in combination with the  $X_{max}$  parameterization from Linsley to recalculate the altitude of the maximum and the distance of the shower to the detector. The process starts again from the definition of the  $\alpha$  angle till the determination of a new  $fEASDir$  vector. The process is repeated several times to allow convergence toward a most likely altitude value. A graphical representation of the above mentioned angles and vectors is given in Fig. 3.37.

## Chapter 4

# The JEM–EUSO Trigger Performances

As described in Chap. 2 the background is one of the critical items of the JEM–EUSO mission. The standard background is of the order of  $\sim 2 \cdot 10^{12}$  photons per second on the entrance pupil. Given an approximate factor 10 of reduction due to the detector inefficiencies JEM–EUSO is therefore expected to achieve some  $\sim 10^{11}$  counts per second over the entire Focal Surface. Given  $\sim 3 \cdot 10^5$  pixels and  $4 \cdot 10^5$  GTU/s about  $\sim 1$  counts/GTU/pixel is expected. Assuming 8 bits for each pixel/GTU the total amount of data generated by background can be estimated to be of the order of  $\sim 1$  Tb/s (Tb  $\equiv$  terabit)  $\sim 125$  GB/s (GB  $\equiv$  gigabyte). Obviously such an amount of data is not easily manageable unless some data reduction procedure is implemented. Such a difficulty is even more evident if we consider the very limited telemetry budget available for a mission on the ISS like JEM–EUSO. In fact, the amount of telemetry reserved for the JEM–EUSO mission is 3 GB/day. The use of solid state disks to be physically carried on the Soyuz capsule will increase the down–link rate by a factor of 3 bringing the available data amount up to 10 GB/day. Considering approximately 20% duty cycle this amount of data is however  $\sim 5 \cdot 10^{-6}$  of the total produced amount. To comply with such a requirement a data reduction algorithm chain has been designed in JEM–EUSO with the specific duty of reducing within the telemetry constraints and given limited computational resources, the produced data.

The present chapter is focused on the trigger algorithms and on their performances. First, a general description on their logic is given. The the average background rate is estimated together with some additional consideration about its distribution on the focal surface. The fake trigger rate associated with the calculated background and thresholds is estimated. The so called efficiency curve is presented and discussed for several conditions.

The study is also extended to the tilt mode conditions. The conclusions will be devoted to some consideration on the telemetry budgets.

The JEM–EUSO trigger system exploits the peculiarities of the signal morphology with respect to background. The background distributes almost uniformly on the entire FS. The statistical oscillations from pixel to pixel have a poissonian shape and the average value is maximum in the central part of the detector and tends to decline toward the edges. The signal, on the other hand, can be imagined as a spot moving on the focal surface. The apparent velocity of such a spot is equal to the projection on the focal surface of the shower’s trajectory. Different inclinations give different persistencies on the same elements. The trigger algorithms aim at the detection of patterns characterized by high concentrations of counts within a certain time window and in limited regions of the FS. Such a requirement will select the signal with higher probability than background oscillations.

The first trigger algorithm is performed by the FPGA in the PDM. In the baseline configuration this algorithm is the so called persistent tracking trigger (PTT) and verifies the occurrence of signal persistency on each of the 9 elementary cells controlled by one FPGA. Aim of this algorithm is the reduction of the trigger rate to  $\sim 1$  kHz/FS  $\sim 7$  Hz/PDM. The occurrence of a trigger event inside a PDM activates the next trigger algorithm at the cluster control board level (CCB.LTT). In the baseline such an algorithm is the so called cluster control board linear tracking trigger. Such a trigger will be performed by the so called cluster control board which is physically connecting groups of 8–9 PDMs. This trigger will be performed at the level of each single PDM but the possibility of larger scale analysis still remains under study. The basic idea is the search of patterns resembling EAS tracks by means of integrations along a set of predefined directions. This algorithm has to reduce the trigger rate by another 4 orders of magnitude. More in detail the trigger rate in output is set to be of the order of  $\sim 0.1$  Hz on the entire focal surface. In the following sections a brief description of the above mentioned algorithms will be given.

## 4.1 The Persistent Tracking Trigger

The first stage in the signal treatment is represented by the PTT algorithm which searches for persistent patterns inside single elementary cells. The PTT trigger has been developed by Catalano and optimized by Bertaina [177] and implemented in ESAF by the author. More in detail, the PTT sets a threshold on each pixel–GTU which defines a count excess. Following that, several  $3\times 3$  pixel boxes are defined. Each box consists of 9 pixels since

#### 4.1. THE PERSISTENT TRACKING TRIGGER

borders have been intentionally excluded. For this reason, the elementary cell is divided in  $14 \times 14$  boxes. All the excess inside such boxes is integrated and assigned to the central pixel. At the same time, the presence of at least one pixel above threshold inside the EC is the condition for the incrementation of a persistency counter. The absence of such a condition will, on the contrary, cause the reset of the persistency counter to 0. The persistency counter will be therefore incremented till no pixel above threshold is verified within an EC. Provided the persistency condition is verified, the entire excess map is saved in a ring buffer. The lack of persistency will force the reset of the entire buffer. Furthermore a persistency threshold is set on the number of active GTUs. If the persistency threshold is exceeded the excess inside each box is integrated for all the previous GTUs in the buffer. The summation is performed for a depth equal to the persistency threshold. Finally, if the integration value exceeds a preset threshold, the trigger signal is issued. As already said the expected fake trigger rate after this first stage is set to 7 Hz/PDM. A sketch of the algorithm is given in Fig. 4.1 where a reduced

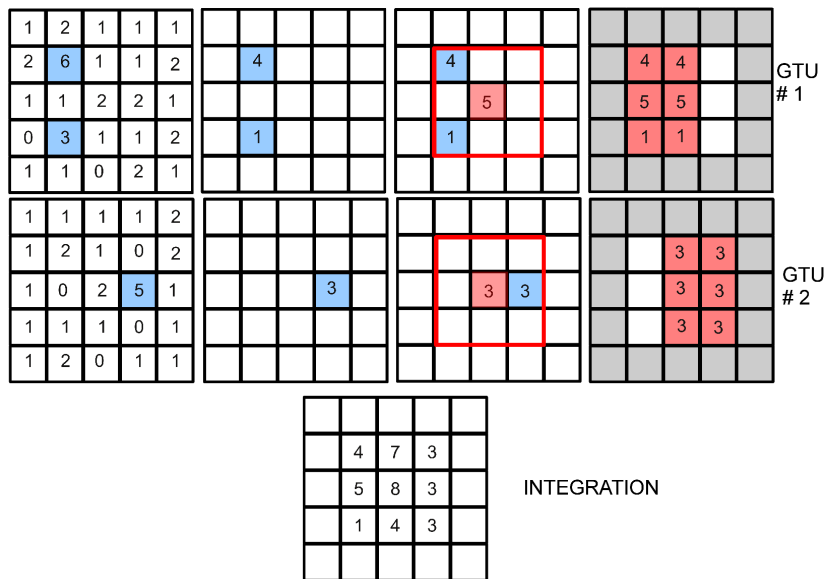


Figure 4.1: the first two GTUs of the PTT trigger logic. The left column represents the signal detected at each GTU. The second column shows the excess in each pixel while the third an example of  $3 \times 3$  integration box. The last column represents the resulting integration on the entire element. The lowest panel integrated the result for both GTUs. In blue are represented pixels with excess given a threshold of 3. In red all the integrated excesses over a  $3 \times 3$  box are shown. In gray is marked the edge where no  $3 \times 3$  box can be defined.

5×5 EC is shown. The upper row shows the first GTU while the middle one the second. The left panel shows the pure counts map in each of the two GTUs. Moving toward right we respectively encounter, the excess map, one example of integration box and the resulting integrated signal over all the pixels. The pixels having excess (thr=3) are highlighted in blue while the integrated excess values are underlined in red. The bottom panel represents the integration over two GTUs. Provided at least another pixel has excess in the following GTU the process repeats until the persistency threshold is reached. Once this condition is met also the integration threshold is applied.

## 4.2 The CCB–Linear Tracking Trigger

After the PTT trigger signal has been issued the electronics scheme implies the activation of the CCB level logic. The basic idea consists in the integration of the counts collected inside a box moved along predefined directions. The signal from a track implies a signal excess in the data map. Background cannot reproduce such features. For that reason a higher amount of counts is expected in the case of a real event. Such an algorithm has been developed by M. Bertaina [177] and implemented in ESAF in the course of this doctoral work. The *CCB\_LTT* algorithm requires far more computational resources than the PTT and cannot be applied at the first level.

The pixel–GTU where the PTT trigger signal was issued, serves as starting condition for the application of the entire CCB trigger procedure. Following that, the definition of a set of pixel–GTUs around the above mentioned starting condition is done. In the present configuration a data box having a size of 3×3 and spanning through ±7 GTUs around the PTT trigger is selected.

All the pixel–GTUs inside such a range (135 pixel–GTUs) serve as initial condition for a series of test integrations. In each of them 324 integration directions are defined. Each direction is defined as the projection on the focal surface of an ideal shower inside the FOV. The direction list must take into account the possible arrival direction of EASs. Low zenith angle ( $\theta$ ) showers will therefore be projected as a standing integration while an horizontal one will cross larger fractions of focal surface. The integration will be performed in the range ±7 GTUs with respect to the starting condition. In every GTU, the box moves according to the Eq. 4.1 and 4.2

$$\Delta_x = \Delta_t * K_x \tag{4.1}$$

$$\Delta_y = \Delta_t * K_y \tag{4.2}$$



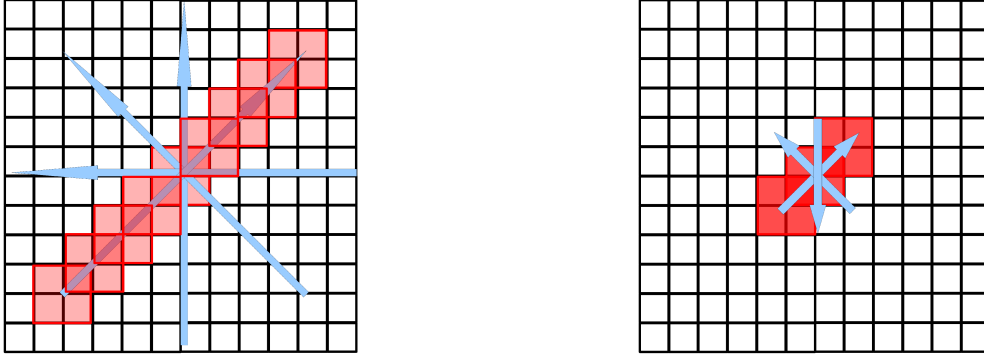


Figure 4.2: **Left panel:** a set of projected LTT directions (blue arrows). In red we see an example of translated integration box. The very long tracks are representing horizontal showers. **Right panel:** a set of projected test LTT directions (blue arrows). In red we see an example of translated integration box. The very short tracks are representing vertical showers. In this case the integration will insist longer on the same pixels.

where  $\Delta_x$  and  $\Delta_y$  are the offsets on each axis expressed in pixel numbers with respect to the integrations starting position and  $\Delta_t$  is the offset in GTUs with respect to the integration starting time.  $K_x$  and  $K_y$  are defined as follows

$$K_x = \sqrt{\frac{\tan^2 \frac{\hat{\theta}}{2}}{\left(\frac{\Delta_{Pix}}{GTU_{Light}}\right)^2 * (1 + \tan^2 \hat{\phi})}} \quad (4.3)$$

$$K_y = K_x * \tan \hat{\phi} \quad (4.4)$$

In Eq. 4.3 and 4.4  $\hat{\theta}$  and  $\hat{\phi}$  represent the polar and azimuthal angle in a polar coordinate system whose polar axis is the shower-to-detector line. Both of such parameters are listed in a predefined 324 lines table. The parameters  $\Delta_{Pix}$  and  $GTU_{Light}$  represent respectively the size on the ground of a pixel and the distance traveled by light in one GTU. In this way we can calculate for each of the  $\pm 7$  GTUs the position of the  $2 \times 2$  pixels, integration box<sup>1</sup>. All the counts inside this box and exceeding the pixel threshold are then integrated. If the collected signal exceeds the preset integration threshold a trigger signal is issued.

In Fig. 4.2 is shown the integration box moved according to a set of directions. The blue arrows are examples of projected directions. In the left panel we can see the projection of a set of horizontal showers while in the right panel a sample of vertical test integration is depicted. In right panel

<sup>1</sup>This is actually not the most up-to-date version of the algorithm. In fact, a times a  $3 \times 3$  box is used together with a reduced number of integration directions.

the tracks are shorter which implies a longer permanence of the box over the same pixels.

### 4.3 Average background and fake trigger rates

The first step in order to assess the trigger performances of JEM–EUSO is to estimate the background rate. In the JEM–EUSO collaboration several studies have been performed in order to give realistic estimates of the background rate at the pupil. The default value is assumed to be 500 ph/(m<sup>2</sup>·sr·ns) which translates to approximatively 20% of the observational duty cycle [177].

The simulation of all background photons through the optics is not an option given the enormous required computational resources. ESAF simulates the background just at the level of front end electronics. A model of the background distribution is developed. Such a model is detector dependent and describes how many counts of background are associated to each pixel given a certain radiance<sup>2</sup> at the pupil.

In the present work a Monte Carlo approach has been followed in order to calculate such a distribution. As a matter of fact, several billions photons have been simulated having random direction and position on the pupil. The off-axis angle ( $\vartheta$ ) has been chosen randomly according to a  $\sin 2\theta$  distribution in the range 0–39 degrees<sup>3</sup>. Several different wavelengths have been simulated. The resulting distribution of counts per pixel is measured. This distribution is used for calculating the ratio of counts in one pixel with respect to the total amount of photons reaching the pupil

$$\chi = \frac{Counts_{pix}}{Photons_{pupil}}. \quad (4.5)$$

This map provides the information on the distribution of counts for any radiance at the pupil. In fact, multiplying  $\chi$  times the radiance of photons  $B_{rad}$ , the integrated solid angle  $\Omega_{sr}$ , the area of the pupil  $A_{pup} \cos \theta$ , and time span  $\Delta_t$ , the counts expected in each pixel within a certain time are obtained.

$$B_{pix} = \chi \cdot B_{rad} \cdot \Delta_t \cdot \Omega_{sr} \cdot A_{pup} \quad (4.6)$$

In Fig. 4.3 is shown the background distribution per pixel. Left and right panel represent the 332 and 382 nm photons distribution respectively. In

<sup>2</sup>Radiance is the amount of radiation falling in a certain area from a solid angle unit in a particular time. (it is expressed in photons/(m<sup>2</sup>·sr·s))

<sup>3</sup>This choice is done given the negligible contribution of the background in the range 39–90 degrees. Moreover such a value has been chosen to maintain consistency with some past study.

### 4.3. AVERAGE BACKGROUND AND FAKE TRIGGER RATES

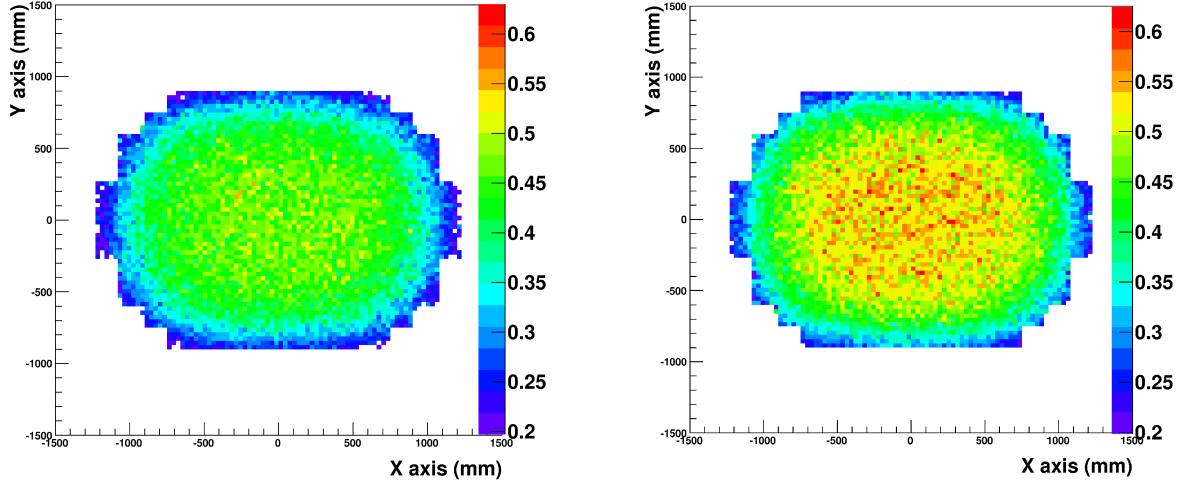


Figure 4.3: **Left panel:** the background map in Counts/ $(\mu\text{s}\cdot\text{pixel})$  corresponding to 500  $\text{ph}/(\text{m}^2\cdot\text{sr}\cdot\text{ns})$ . The values shown here are referred for 332 nm photons. **Right panel:** the background map in counts/ $(\mu\text{s}\cdot\text{pix})$  corresponding to 500  $\text{ph}/(\text{m}^2\cdot\text{sr}\cdot\text{ns})$ . The values shown here are referred for 382 nm photons.

Wavelength (nm)	Background Rate counts/ $(\mu\text{s}\cdot\text{pix})$
332	0.38
357	0.43
382	0.44
407	0.43

Table 4.1: the average background rates per  $\mu\text{s}\cdot\text{pix}$  for different wavelengths.

the present version of ESAF the simulation of variable background maps is not allowed. The background is set to a constant average value for all the pixels. The average background for wavelengths 332, 357, 382 and 407 nm is shown in the following table. A more realistic estimate can be given if the calculation is done for photons in the range 300–400 nm or for completeness 250–500 nm. Obviously, a radiance  $B_{rad} \sim 500$  photons/ $(\text{m}^2\cdot\text{sr}\cdot\text{ns})$  in the range 300–400 nm corresponds to 1250 photons/ $(\text{m}^2\cdot\text{sr}\cdot\text{ns})$  between 250 and 500 nm. Assuming a flat spectrum therefore the results we obtained are respectively: 0.42 and 0.64 counts/ $(\mu\text{s}\cdot\text{pix})$ . This result can be partially considered to be a cross check for the usually assumed JEM-EUSO standard background rate which has been calculated by the collaboration to be  $\sim 0.42$  counts/ $(\mu\text{s}\cdot\text{pix})$  [177].

The thresholds of the JEM-EUSO trigger electronics must be estimated. For this purpose ESAF allows the simulation of pure background events.

Thanks to this tool the thresholds associated to each background level can be adjusted to the level where the trigger rate comply with the default values of 7 Hz/PDM for the PTT and 0.1 Hz/FS for the CCB.LTT. In Tab. 4.2, partially shown here and developed by M. Bertaina, has been used in the course of this doctoral work. To cross check these results the trigger scheme has been also directly tested for the conditions corresponding to 1.05 and 2.1 counts/ $(\mu\text{s}\cdot\text{pix})$ . The test for the background value  $B_{pix} \sim 1.05$

$B_{pix}$ counts/ $(\mu\text{s}\cdot\text{pix})$ .	$Thr1_{PTT}$	$Pers_{PTT}$	$Int_{PTT}$	$Thr1_{CCB\_LTT}$	$Int_{CCB\_LTT}$
1.0	2	5	52	2	115
1.1	3	5	32	3	97
...	...	..	...	...	...
2.0	4	5	44	4	153
2.1	4	5	48	4	158
2.2	4	5	51	4	171
...	...	..	...	...	...
4.1	6	5	72	6	283
4.2	6	5	75	6	289
4.3	6	5	79	6	304
...	...	..	...	...	...

Table 4.2: the thresholds for the JEM-EUSO trigger electronics system for different background conditions. Results are published according to Bertaina. In the table we can see from left to right, the background per pixel per GTU ( $B_{pix}$ ), the pixel threshold, the persistency and the integration value of the PTT algorithm (respectively  $Thr1_{PTT}$ ,  $Pers_{PTT}$  and  $Int_{PTT}$ ). The last two columns are then the single pixel threshold and the integration value ( $Thr1_{CCB\_LTT}$  and  $Int_{CCB\_LTT}$ ) of the CCB.LTT trigger.

counts/ $(\mu\text{s}\cdot\text{pix})$  (0.42 counts/ $(\mu\text{s}\cdot\text{pix})$ ) delivers rates of 3.91 Hz/PDM at the PTT level and 0.2 mHz/PDM ( $\sim 0.03$  Hz/FS) for the CCB.LTT. The final rates achieved for  $B_{pix} \sim 2.1$  counts/ $(\mu\text{s}\cdot\text{pix})$  (0.84 counts/ $(\mu\text{s}\cdot\text{pix})$ ) are 3.205 Hz/PDM for the PTT and  $\sim 0.07$  Hz/FS for the CCB.LTT trigger. The thresholds used in such conditions are equal: which fully confirms the

$B_{pix}$ (counts/pix/GTU)	$Thr1_{PTT}$	$Pers_{PTT}$	$Int_{PTT}$	$Thr1_{CCB\_LTT}$	$Int_{CCB\_LTT}$
1.05	2	5	54	2	115
2.1	4	5	48	4	158

Table 4.3: the test for the trigger thresholds for two different background levels.

results of Tab. 4.2. As it can be clearly seen the values for 1.05 slightly exceed the thresholds corresponding to  $B_{pix} = 1$ . This is obviously due to the higher trigger rate implied by the higher background (1.05 instead of 1 counts/ $(\mu\text{s}\cdot\text{pix})$  ) As for the background 2.1 ph/ $(\text{m}^2\cdot\text{sr}\cdot\text{ns})$ the thresholds result to be exactly the same.

## 4.4 Trigger performances

Once the trigger background rejection performances have been assessed the next step is to quantify the associated real event acceptance. With the thresholds presented and tested in the previous section a set of real events has been simulated. The events had random energy between  $[10^{19}, 10^{21}]$  eV and were distributed according to a power law with index -1. This index has been chosen in order to cope with computational resources limitations and does not have any physical meaning. In fact, a too steep spectrum would imply a strong overabundance of low energy events while a flat spectrum a too large fraction of high energy events and consequently too heavy computations. By using a logarithmic binning, then, a uniform statistics in the bins over the entire energy range is obtained. All the events have been randomly distributed within the FOV following a uniform distribution. More in detail the impact point is sampled within the interval from -270 to 270 km and from -200 to 200 km.

The angular distribution is also chosen randomly from 0 to 90 degrees in zenith angle  $\theta$  and 0 to 360 degrees in azimuth  $\phi$ .  $\theta$  is distributed according to a  $\sin 2\theta$  distribution to take into account the solid angle integrated in each  $\theta$  bin and the inclination of the impact area<sup>4</sup>. In this way the  $\theta$  distribution has a maximum at 45 degrees and declines toward 0 and 90 degrees. The amount of events from vertical and horizontal directions will therefore be smaller.

The trigger probability is defined as the ratio of events triggering with respect to those falling inside the above mentioned area. A normalization factor has been applied for the full FOV case.

$$\epsilon_{FOV} = \frac{N_{trigg}}{N_{inject}} \cdot \frac{A_{inject}}{A_{FOV}} \quad (4.7)$$

$\epsilon_{FOV}$  is the trigger probability,  $N_{trigg}$  and  $N_{inject}$  are respectively the triggered and simulated number of events and  $A_{inject}$  and  $A_{FOV}$  the sampling and FOV area.

Three different values of backgrounds have been considered 500, 1000 and 2000 ph/(m<sup>2</sup>·sr·ns) corresponding to 0.42, 0.84 and 1.26 counts/( $\mu$ s·pix). In Fig. 4.4 the trigger probabilities as function of the energy are shown. As can be seen in order to maintain the constant trigger rate a loss in the real event efficiency must be accepted. It can be roughly noticed how the 50% efficiency is reached at  $\sim 3-4 \cdot 10^{19}$ ,  $\sim 4-5 \cdot 10^{19}$  and  $\sim 7 \cdot 10^{19}$  eV for respectively 500,

<sup>4</sup>Such an expression is obtained after the integration  $\int \sin \theta \cos \theta d\theta$  has been performed. Here the  $\cos \theta$  takes into account the cross section of the pupil from a particular direction while the  $\sin \theta$  of the integrated solid angle.

1000 and 2000  $\text{ph}/(\text{m}^2\cdot\text{sr}\cdot\text{ns})$ . In the same way the full efficiency is reached around  $10^{20}$  eV for the 500  $\text{ph}/(\text{m}^2\cdot\text{sr}\cdot\text{ns})$  condition. Higher backgrounds will imply and increase in the full efficiency energy respectively to  $\sim 1\text{--}2\cdot 10^{20}$  and  $\sim 3\cdot 10^{20}$  eV.

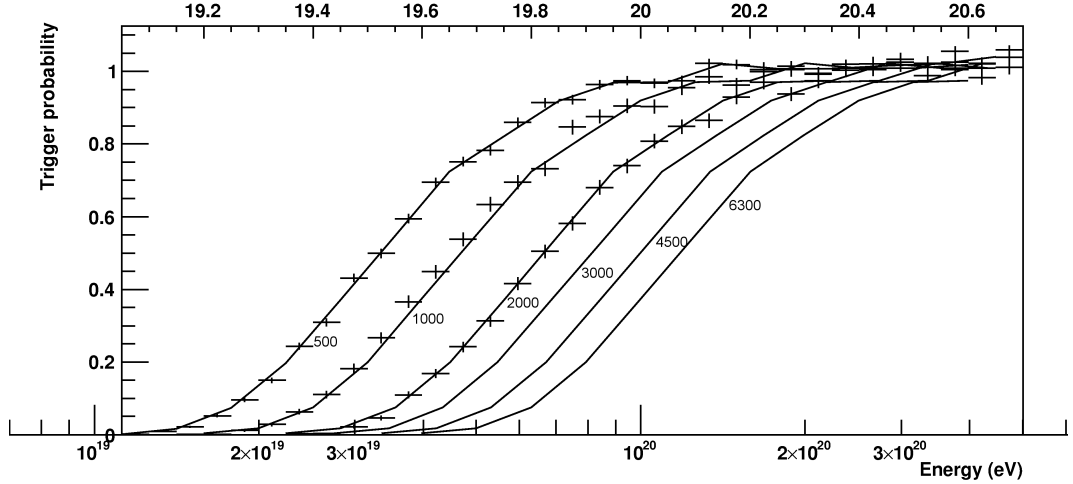


Figure 4.4: the trigger efficiency curve for JEM-EUSO. Points represent real simulated efficiency curves. From left to right we can therefore see the trigger efficiency curve for 500, 1000 and 2000  $\text{ph}/(\text{m}^2\cdot\text{sr}\cdot\text{ns})$  background condition. The continuous lines represent the scaled version of the points obtained at 500  $\text{ph}/(\text{m}^2\cdot\text{sr}\cdot\text{ns})$ . From left to right 500, 1000, 2000, 3000, 4500 and 6300  $\text{ph}/(\text{m}^2\cdot\text{sr}\cdot\text{ns})$  efficiency curves can be observed.

In parallel to the pure Monte Carlo approach a parameterization of the trigger performances has been developed in order to optimize the use of computational resources. The one shown here assumes the trigger probability to be scaled with the square root of the background radiance. This is intuitively due to the lower signal to noise ratio which can be achieved for the higher background values. Statistical oscillations on the background will therefore compete with the signal and make the event recognition more difficult. The curves will be therefore scaled along the energy axis of a quantity equal to  $\sqrt{\frac{B}{B_0}}$  whereas  $B$  is the analyzed background and  $B_0$  is the reference background (500  $\text{ph}/(\text{m}^2\cdot\text{sr}\cdot\text{ns})$ ). Under this approximation the simulated 500  $\text{ph}/(\text{m}^2\cdot\text{sr}\cdot\text{ns})$  curve has been scaled in order to obtain the parameterized curves for 1000, 2000, 3000, 4500 and 6300  $\text{ph}/(\text{m}^2\cdot\text{sr}\cdot\text{ns})$ <sup>5</sup>. The parameterized efficiencies are shown in Fig. 4.4 as continuous lines. Worth to notice is

<sup>5</sup>6300  $\text{ph}/(\text{m}^2\cdot\text{sr}\cdot\text{ns})$  is assumed in JEM-EUSO to be the operational background limit. In fact, such a high radiance will imply a large PMT current and consequently a degradation of the PMT.

how at least the two simulated efficiency curves match with the parametrical approximations. The very small deviation from the parameterization of the points for 1000 ph/(m<sup>2</sup>·sr·ns) is most likely due to the slightly smaller fake trigger rate which is associated to this curve with respect to the 500 ph/(m<sup>2</sup>·sr·ns) curve. This parameterization has been therefore accepted in this study for the generation of the efficiency curve for any arbitrary background value. The systematic verification of this parameterization within the whole operational range and the quantification of the deviation from the real simulated curves is left for future works.

An important task of JEM–EUSO is to prove the ability to detect a sufficiently large number of low energy events to overlap with ground based experiment and allow an important cross check test. For this reason, the uncertainty on the exposure must be minimal. To reduce the uncertainty on the exposure the 100% trigger probability plateau should be reached in the range under analysis. In this way at least the uncertainty on the trigger probability curve will be removed in order to obtain a more reliable flux estimate. A possible way to overcome this limitation is to set cuts on the whole JEM–EUSO events sample. By selecting subsamples of events with higher trigger efficiency it is therefore possible to extend the full efficient range to lower energies and guarantee a solid exposure determination at low energies.

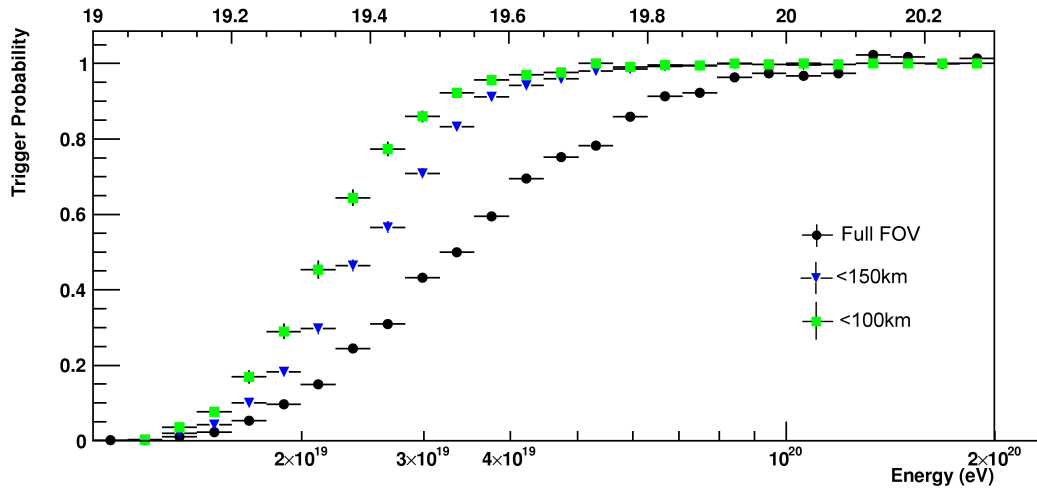


Figure 4.5: the JEM–EUSO trigger probability. Both full FOV and sub–selections are visible. More in detail the blue triangles represent the trigger efficiency for events with impact point within 150 km from the center. Green squares represent the trigger efficiency for events with core within 100 km from the center.

Within this work two types of cuts have been applied. The first one is

on the zenith angle ( $\theta$ ) of the shower while the second on the position within the FOV. In Fig. 4.5 the efficiency curve of the full field of view is shown together with the curves obtained from events within 150 and 100 km from the center. As it can be clearly observed the full efficiency regime, which for the entire sample starts at  $\sim 10^{20}$  eV, is lowered at  $5 \cdot 10^{19}$  and  $4 \cdot 10^{19}$  eV. Already such cuts allow to enter in the ground detectors range with full efficiency.

In Fig. 4.6 cuts on the zenith angle ( $\theta$ ) have been applied. The events having zenith angle ( $\theta$ ) larger than 60 degrees have been selected both for the full FOV or the 100 km cut. These cuts clearly imply an even higher efficiency allowing the full efficient energy range to go down to  $3 \cdot 10^{19}$  eV. Furthermore it can be clearly seen how the cuts in FOV achieve a much lower energy threshold than cuts in angle.

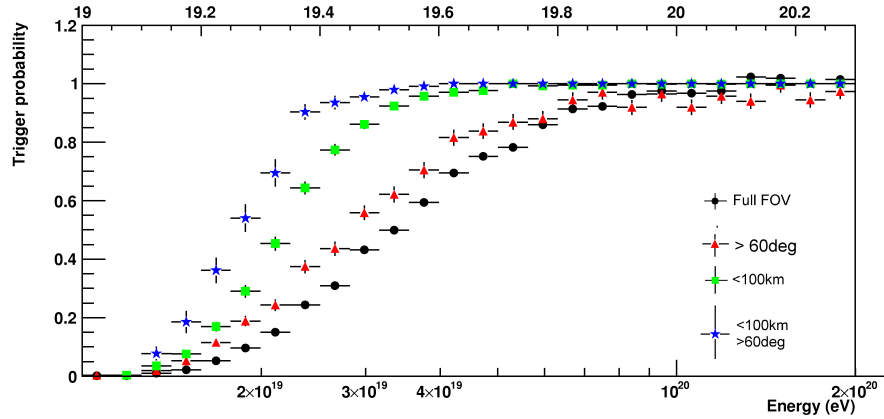


Figure 4.6: the JEM-EUSO trigger probability. Both full FOV and sub-samples are visible. More in detail the green squares represent the trigger efficiency for events with impact point within 100 km from the center. Red triangles represent the trigger efficiency for full FOV events from the center and zenith angle greater than 60 degrees. Blue stars represent events falling in the innermost 100 km of the FOV and having inclination angles larger than 60 degrees.

In the present study extensive studies have been carried out estimating the trigger efficiency for Iron nuclei. Some example is given to how the triggering performances differs depending on the primary. In Fig. 4.7 the efficiency curves for JEM-EUSO in case of iron primaries are shown. The efficiency curve for nadir mode and 3 background conditions has been simulated. Clearly the iron curve results to be shifted to lower energies by a factor of roughly 10%. Such a feature is due to the shorter development of iron showers compared to protons. For this reason iron showers are modeled to be developing higher in the atmosphere and therefore to be affected by less



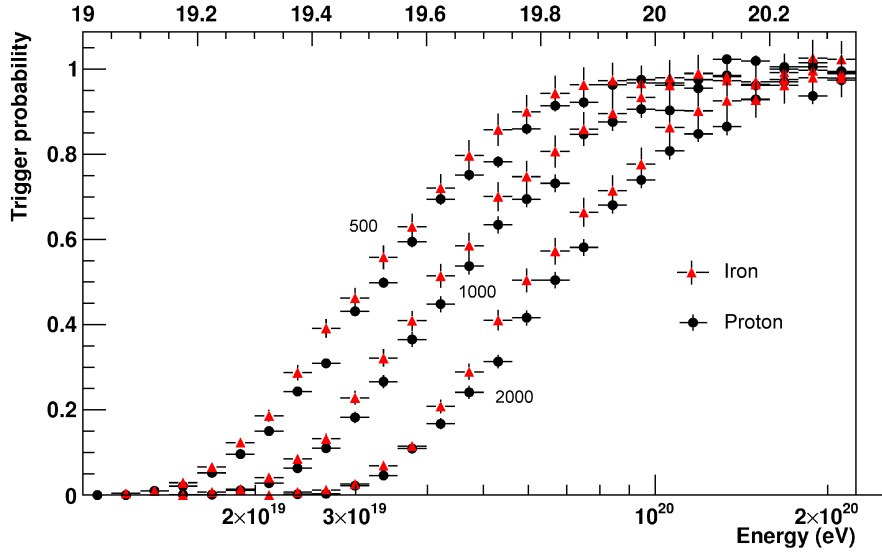


Figure 4.7: trigger probability curves for protons (black dots) and iron (red triangles). Three background conditions namely 500, 1000 and 2000 ph/(m<sup>2</sup>·sr·ns) are represented.

atmospheric absorption. It can be therefore stated that protons represent a more conservative estimation of the triggering performances.

## 4.5 Exposure

The exposure is commonly used to express the experimental "size" of an UHECR detector. The exposure is in fact used to establish the mission performances without referring to the flux. The exposure is expressed in  $km^2 \cdot sr \cdot yr$  and is calculated according to the following equation:

$$\Psi(E) = A_{geo}(E) \cdot t \cdot DC \quad (4.8)$$

whereas  $A_{geo}(E)$  is the geometrical aperture as function of the energy,  $t$  the mission duration and  $DC$  the so called observational duty cycle.  $A_{geo}$  and is given by:

$$A_{geo}(E) = \int_{S_{test}} dS \int_0^{2\pi} d\phi \int_0^{\frac{\pi}{2}} d\theta \cos \theta \cdot \sin \theta \cdot \epsilon(E, S, B_{rad}). \quad (4.9)$$

whereas  $\theta$  and  $\phi$  represent the arrival direction angles,  $S_{test}$  a test area sufficiently larger than the visible FOV surface ( $S_{fov}$ ) and  $\epsilon(E, S, B_{rad})$  the average efficiency of the detector at a given energy ( $E$ ), background ( $B_{rad}$ )

and at a certain position in the FOV. The integration on  $\theta$  and  $\phi$  is performed over the entire celestial sphere namely from 0 to  $2\pi$  for  $\phi$  and from 0 to  $\frac{\pi}{2}$  for  $\theta$ . The integration on the surface  $S$  is performed over the entire test surface  $S_{test}$ . The  $S_{test}$  area is chosen large enough to avoid border effects. The  $\epsilon(E, \gamma, B_{rad})$  factor is defined as

$$\epsilon(E, S, B_{rad}) = \frac{N_{trigg}}{N_{tot}} \quad (4.10)$$

whereas  $N_{trigg}$  and  $N_{tot}$  are respectively the number of triggering events and the total number of injected events. The duty cycle associated to each background has been chosen always according to the JEM-EUSO collaboration [177].

As already mentioned one possible alternative to this definition is the definition according to the volume.

$$A_{geo}(E) = \int_{S_{test}} dS \int_0^{h_{max}} dh \int_0^{2\pi} d\phi \int_0^{\theta_{horizon}(h)} d\theta \sin \theta * \sigma_{vol}(\theta) * \epsilon(E, S, h). \quad (4.11)$$

This definition takes into account the vertical development of the atmosphere in its entire structure from sea level to a maximum altitude. The integration on the  $\theta$  angle goes from zenith (0 degrees) to horizon (for  $h > 0$   $\theta > 90$  degrees). The  $\sigma_{vol}$  parameter represents the cross section area of the volume seen from a particular direction. As in the case of planar geometry both base and altitude should be chosen of sufficient size to include the most complete sample of potentially triggering showers still keeping a reasonable computational time demand. Given a certain flux, the choice of a 3D detector volume would most likely imply a slightly larger number of detected events than in the 2D case. This is due to the neglect of the events without a geometrical intersection with the earth's surface in the standard exposure definition. A consequence of such a definition lies in the different unit in which the flux must be expressed namely in  $\text{ph}/(\text{km}^3 \cdot \text{sr} \cdot \text{yr})$ . However, the calculation of  $\epsilon(E, S, \gamma)$  following the tridimensional geometry would require a huge amount of computational resources since the generated event distribution is characterized by an additional degree of freedom in the  $z$  direction. For this reason the estimate of the deviation from planar assumption is left for future work.

Given the definition of Eq. 4.9 and the efficiency curves calculated in the previous sections, the geometrical aperture of the JEM-EUSO mission can be calculated.

In Fig. 4.8 the JEM-EUSO geometrical aperture is shown for the full FOV and for several cuts. Events with impact point at less than 150 km or

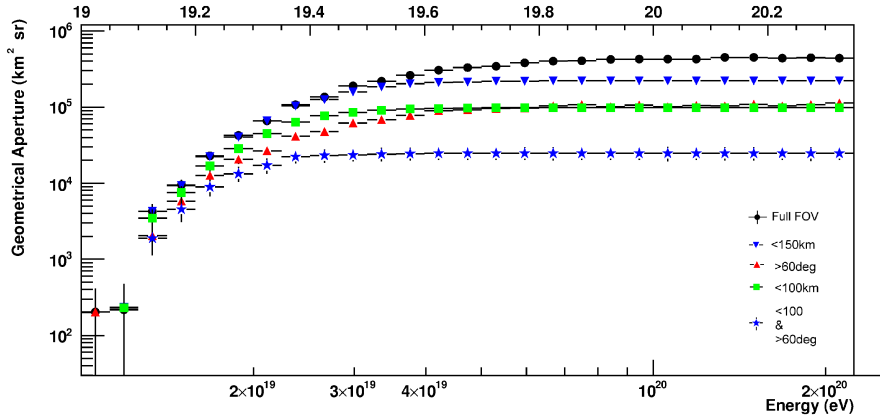


Figure 4.8: the geometrical aperture curves for the JEM-EUSO mission. As black dots the aperture for the full field of view can be seen. Blue triangles and green squares represent the selection on the position and respectively correspond to a 150 and 100 km cut. Red triangles represent a 60 degrees cut on the zenith angle ( $\theta$ ) of the showers. Blue stars combine a 100 km cut with the 60 degrees cut.

100 km from the center have been selected as well as events with inclination larger than 60 degrees. The most restrictive condition is taking the events within 100 km from the center of the FOV and with inclinations larger than 60 degrees.

As can be expected, the samples with stronger cuts reach the full efficiency plateau at lower energy. On the other hand it appears totally clear how a cut implies a dramatic loss in the aperture. The full efficiency plateau corresponds to a value of  $\sim 4.5 \cdot 10^5 \text{ km}^2\text{sr}$ . The stronger cut reduces the aperture to  $2.5 \cdot 10^4 \text{ km}^2\text{sr}$ . Also the shape of the curve is affected. The two curves related to the 60 degrees (red triangles) and 100 km (green squares) have a different shape although almost the same amplitude. As a matter of fact, the 60 degrees cut implies an aperture reduction of a factor 4 with respect to the full FOV case because of the solid angle reduction. Similarly the 100 km cut reduces the aperture of a factor 4.5 this time because of the loss of geometrical area. The two curves will therefore asymptotically converge to very close values although the 100 km will be a bit lower. Despite that, below  $4 \cdot 10^{19} \text{ eV}$  the situation seems to be reversed. Here in fact, the 100 km cut seems to be more efficient in accepting low energy events even with a lower total aperture. Such a feature can be a very great advantage in the effort to extend toward lower energy the full efficiency range and suggests that a deeper study is needed to optimize the trigger performances. The cut must be therefore chosen in order to get the highest exposure at the low

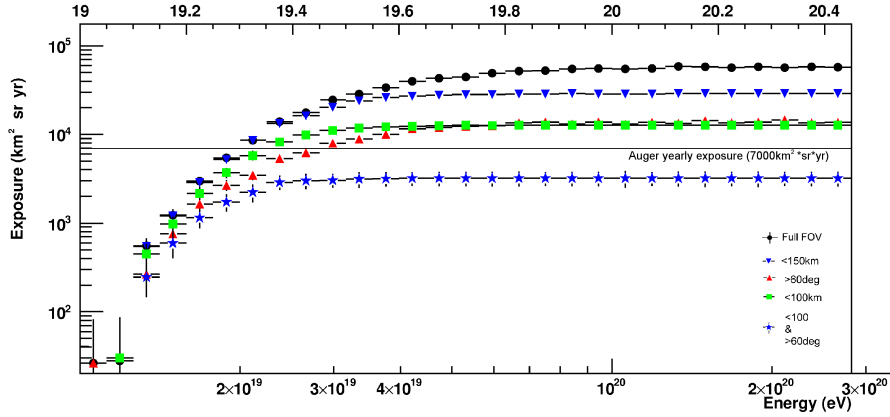


Figure 4.9: the yearly exposure curves as calculated for the JEM-EUSO detector. The curve for full FOV is shown as black dots. Blue triangles and green squares represent the selection on the position and respectively correspond to a 150 and 100 km cut. Red triangles represent a 60 degrees cut on the zenith angle ( $\theta$ ) of the showers. Blue stars combine the 100 km with the 60 degrees cut. The full FOV exposure curve for JEM-EUSO reaches a plateau at  $\sim 6 \cdot 10^4 \text{ km}^2 \cdot \text{sr} \cdot \text{yr}$ . For comparison the Auger yearly exposure is also depicted and corresponds to roughly  $7000 \text{ km}^2 \cdot \text{sr} \cdot \text{yr}$ .

energies without penalizing too much the asymptotic aperture.

An essential factor for the estimate of the exposure is the so called duty cycle. Such a parameter has been defined as the fraction of mission lifetime under which the the expected background is lower than a certain threshold. The collaboration has provided studies [177] to assess the duty cycle for each background threshold. The choice which has been adopted here assumes a constant air glow background superposed with moon's related variations. This leads for example to a duty cycle of 17.5% for  $B < 500 \text{ ph}/(\text{m}^2 \cdot \text{sr} \cdot \text{ns})$  increasing up to 34% for  $B \lesssim 15000 \text{ ph}/(\text{m}^2 \cdot \text{sr} \cdot \text{ns})$  which has been claimed to be the background for full moon at zenith. A further loss in the duty cycle due to clouds, lightnings, cities and other luminous atmospheric events is to be expected [177]. Such a loss is quantified by detailed collaboration's works to be 0.72 as for clouds and 0.9 for all the other light sources<sup>6</sup>.

Furthermore, the background averaged over the interval  $B < 1500 \text{ ph}/(\text{m}^2 \cdot \text{sr} \cdot \text{ns})$  is  $\sim 550 \text{ ph}/(\text{m}^2 \cdot \text{sr} \cdot \text{ns})$  [177]. This implies that the aperture curve for  $500 \text{ ph}/(\text{m}^2 \cdot \text{sr} \cdot \text{ns})$  can be combined with the duty cycle for  $B < 1500 \text{ ph}/(\text{m}^2 \cdot \text{sr} \cdot \text{ns})$  namely  $\sim 0.2$ . The resulting exposure curve is extremely similar to the one calculated after integrating over the differential duty cycle for  $B < 1500 \text{ ph}/(\text{m}^2 \cdot \text{sr} \cdot \text{ns})$ . Therefore, the simulated  $500 \text{ ph}/(\text{m}^2 \cdot \text{sr} \cdot \text{ns})$  samples can still

<sup>6</sup>Mainly cities. Lightnings also imply a significant loss.

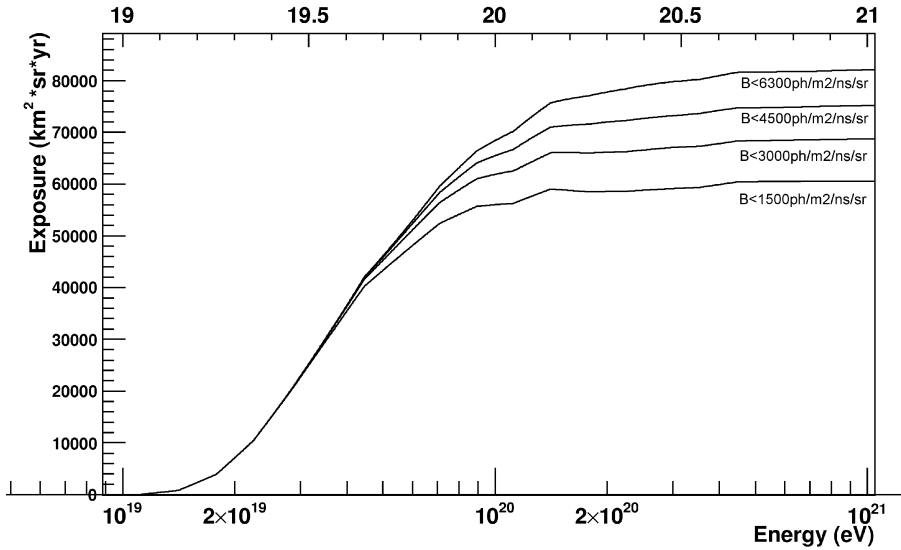


Figure 4.10: JEM-EUSO yearly exposure obtained over the entire background range. Four curves corresponding to the thresholds  $B < 1500$ ,  $B < 3000$ ,  $B < 4500$  and  $B < 6300$   $\text{ph}/(\text{m}^2 \cdot \text{sr} \cdot \text{ns})$  are represented here. The curve for  $B < 1500$   $\text{ph}/(\text{m}^2 \cdot \text{sr} \cdot \text{ns})$  converges toward  $60000 \text{ km}^2 \cdot \text{sr} \cdot \text{yr}$  and is remarkably near to the full FOV exposure as observed in the previous section.

be used as an approximation for the  $B < 1500$   $\text{ph}/(\text{m}^2 \cdot \text{sr} \cdot \text{ns})$  range by considering a duty cycle  $\sim 0.2$ .

Following this approach the curves of Fig. 4.8 can be therefore multiplied by the observational duty cycle, cloud and lightning factors (namely 0.2, 0.72 and 0.9) to obtain the curves of Fig. 4.9. We can observe here the cumulated exposure in one year for the JEM-EUSO detector for a background  $< 1500$   $\text{ph}/(\text{m}^2 \cdot \text{sr} \cdot \text{ns})$  with all the already explained cuts. The full FOV JEM-EUSO exposure is at the highest energies  $\sim 6 \cdot 10^4 \text{ km}^2 \cdot \text{sr} \cdot \text{yr}$ . For comparison we introduced in the plot the yearly exposure of the Auger detector which corresponds to  $\sim 7000 \text{ km}^2 \cdot \text{sr} \cdot \text{yr}$ . In the full efficiency range  $> 10^{20}$  eV therefore JEM-EUSO (in nadir mode and with a background threshold of 1500  $\text{ph}/(\text{m}^2 \cdot \text{sr} \cdot \text{ns})$ ) turns out to be  $\sim 8-9$  times larger than Auger. JEM-EUSO finally turns to be of a size comparable to Auger around  $\sim 2 \cdot 10^{19}$  eV both for full FOV and for almost all the cuts.

As already explained JEM-EUSO has the advantage with respect to the ground arrays of a possible increase in the exposure. Two possibilities are open and consists essentially in the increase of the accepted background threshold or in the tilted configuration. The increase in background threshold will be considered now. The integration of the exposure cumulated in

each background condition must be therefore performed. For each of the thresholds the interval from 500 ph/(m<sup>2</sup>·sr·ns) up to the maximum, has been covered in steps of width equal to 50 ph/(m<sup>2</sup>·sr·ns). For each of such conditions the corresponding efficiency curve has been generated according to the scaling parameterization shown in the previous section. This allows the calculation of a sample of exposure curves thanks to the differential duty cycle distribution as a function of background [180]. Each of these exposure curves corresponds to the exposure in each background bin and, by performing the integration over the entire background range, the final exposure curve can be calculated. The above described procedure can be resumed in Eq. 4.12

$$\Psi(E, < I_{BG}^{thr}) \propto \int_0^{I_{BG}^{thr}} A_{geo} \left( E \cdot \sqrt{\frac{\langle I_{BG} \rangle}{I_{BG}}} \right) p(I_{BG}) dI_{BG}. \quad (4.12)$$

The entire exposure is integrated from 0 to threshold. In Fig. 4.10 the exposure is shown as a function of energy for different background thresholds. The curve corresponding to the case B<1500 ph/(m<sup>2</sup>·sr·ns) flattens at  $\sim 6 \cdot 10^4 \cdot \text{km}^2 \cdot \text{sr} \cdot \text{yr}$  and refers to the maximum exposure achievable for the 1500 ph/(m<sup>2</sup>·sr·ns) case. Such a value must be compared with the plateau of the full FOV exposure of Fig. 4.9 ( $\sim 6 \cdot 10^4 \text{km}^2 \cdot \text{sr} \cdot \text{yr}$ ) and gives a useful check of the duty cycle assumption used to produce these exposure curves. We can therefore confirm that no significant difference in the exposure can be expected in the cases where  $B = 500$  or B<1500 ph/(m<sup>2</sup>·sr·ns) are used. Another very useful feature is the increase in the exposure which can be achieved by JEM–EUSO at the highest energies. Such an increase amounts, for the highest acceptable threshold, to  $\sim 40\%$  at the highest energies and  $\sim 20\%$  around  $10^{20}$  eV. Another important fact is that such an increase does not come at cost of any exposure loss at the lowest energies as could be for tilting. This is due to the obvious consideration that the wider background bands totally include the narrower allowing exactly the same performance cumulated with some additional bonus at the highest energies.

## 4.6 Triggered events energy distribution

In this section the so called triggered spectrum is estimated. Such an estimate depends however on the modeled flux to get an estimate of the number of triggered events. For the flux the published Pierre Auger and Telescope Array spectra are used. The triggered spectra is calculated for all the conditions shown before. The published spectra have been taken from [179] and [145] for Auger and Telescope Array respectively.

## 4.6. TRIGGERED EVENTS ENERGY DISTRIBUTION

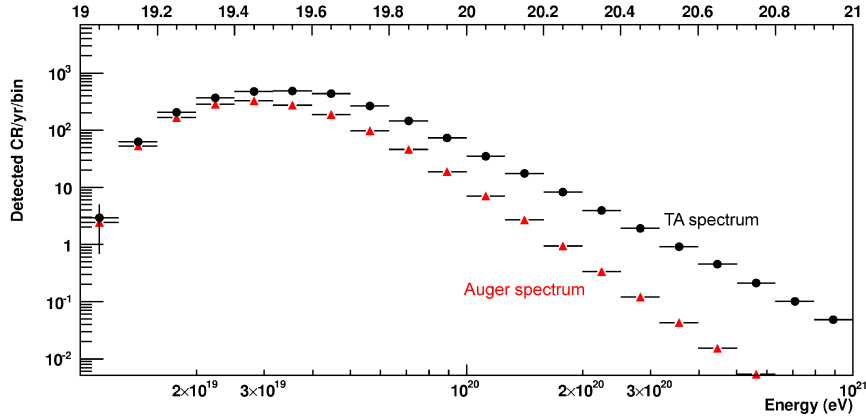


Figure 4.11: the expected triggered JEM-EUSO spectrum. The JEM-EUSO exposure has been combined with both the Pierre Auger and Telescope Array fluxes. Depicted here we observe the number of events detected per bin in one year for Auger (red triangles) and TA (black dots). Bins are chosen to have a width of 0.1 in logarithmic scale.

The equations

$$\Phi(E) = A \cdot E^{-2.63} \cdot \frac{1}{1 + \exp \frac{\log E - 19.63}{0.15}} \quad (4.13)$$

for Auger and

$$\Phi(E) = B \cdot E^{-2.68} \text{ for } E < 4.8 \cdot 10^{19} \text{ eV} \quad (4.14)$$

$$\Phi(E) = C \cdot E^{-4.2} \text{ for } E > 4.8 \cdot 10^{19} \text{ eV} \quad (4.15)$$

for Telescope Array represent therefore the flux of incoming particles and is expressed in particles/(km<sup>2</sup>·sr·yr·eV). All the parameters have been taken exactly as expressed in the publications apart for the normalization factors A, B and C which have been fitted by the author from the plots in the cited papers. Here the parameters assume values of  $A=4.5 \cdot 10^{30}$  particles·km<sup>-2</sup>·sr<sup>-1</sup>·yr<sup>-1</sup>·eV<sup>1.63</sup>,  $B=4.7 \cdot 10^{31}$  particles·km<sup>-2</sup>·sr<sup>-1</sup>·yr<sup>-1</sup>·eV<sup>1.68</sup> and  $C=3.89 \cdot 10^{61}$  particles·km<sup>-2</sup>·sr<sup>-1</sup>·yr<sup>-1</sup>·eV<sup>3.2</sup>. In this way the differential spectra can be estimated for all energies.

In Fig. 4.11 the triggered JEM-EUSO spectra assuming the Auger and Telescope Array flux are shown. More in detail the number of triggered events per energy bin per year can be observed.<sup>7</sup>

<sup>7</sup>Note: the binning of such plots is double with respect to all the previous plots. Such a choice has been taken simply to be consistent with the binning traditionally used in cosmic ray science. In fact, commonly CR collaborations plot 10 bins per decade for estimating the number of detected particles at various energies. This choice allows therefore to directly

The JEM–EUSO mission will clearly allow access to much higher energies than present ground arrays. As can be seen in Fig. 4.11 several particles per year in each bin can be expected at energies larger than  $10^{20}$  eV. Such a feature will be fundamental in order to reconstruct the spectrum at high energies.

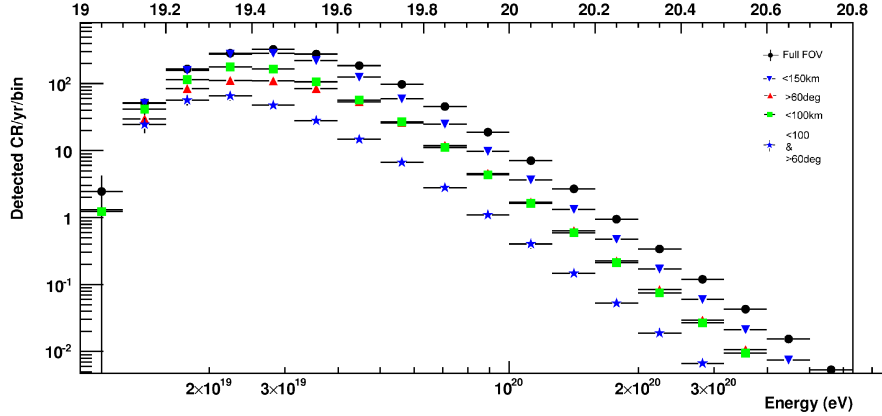


Figure 4.12: the triggered JEM–EUSO spectrum assuming the Auger flux. As black dots the full FOV is shown. Blue triangles represent the triggered spectrum for the cut at 150 km while green squares for 100 km. Red triangles depict the cut for events with zenith larger than 60 degrees while blue stars combine the 100 km and the 60 degrees cut. Bins are chosen to have a width of 0.1 in logarithmic scale.

Another very interesting study is related to the cuts previously presented. In Figs. 4.12 and 4.13 it can be observed the number of particles per bin according respectively to the Auger and TA fluxes. In each of those cases the triggered curves for all the different cuts can be seen. Within such plots we can appreciate the different position of the peaks for all the distributions. Moreover different cuts deliver different maximal energies and different amplitudes.

To have a statistically significant overlap with ground arrays the presence in a full efficient bin of at least 50 events per bin is required. Such assumption implies a statistical uncertainty of 15%. In addition, since we require the bin to be in the full efficient range we define for each cut a minimum energy threshold above which bins can be considered to be full efficient. Such thresholds are  $3 \cdot 10^{19}$  eV for the 100 km–60 degrees selection,  $4 \cdot 10^{19}$  eV for the 100 km,  $5 \cdot 10^{19}$  for the 150 km and  $7\text{--}8 \cdot 10^{19}$  eV for the 60 degrees cut

compare JEM–EUSO numbers with the one produced by other collaborations. As for the previous plots they just represent functions which do not depend on the binning. For esthetic reasons they have been therefore left with a thinner binning.



#### 4.6. TRIGGERED EVENTS ENERGY DISTRIBUTION

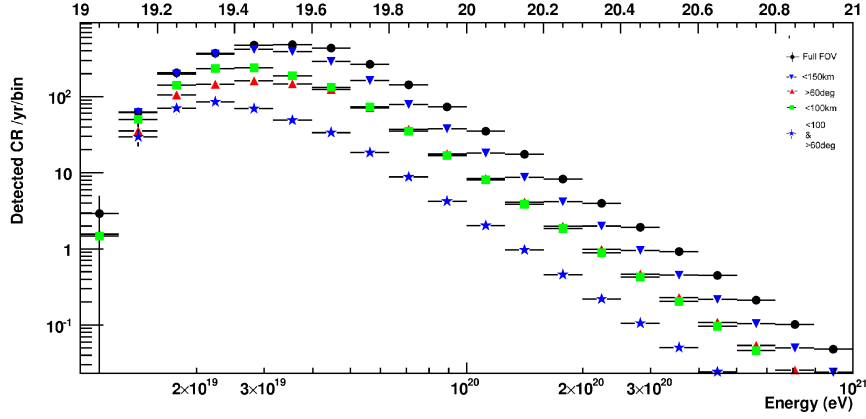


Figure 4.13: the triggered JEM-EUSO spectrum assuming the Telescope Array flux. As black dots is shown the full FOV. Blue triangles represent the triggered spectrum for the cut at 150 km while green squares for 100 km. Red triangles depict the cut for events with zenith angles larger than 60 degrees while blue stars combine the 100 km and the 60 degrees cut. Bins are chosen to have a width of 0.1 in logarithmic scale.

(see Figs. 4.5 and 4.6).

The first study has been performed for the Auger flux assuming protons. In this case, merging 2 bins of the plots in one is necessary in order to achieve a sufficient statistics. With a bin width of 0.2, therefore, just one point could be found satisfying the above mentioned conditions. More in detail the 100 km selection achieves the first full efficient bin with at least 50 events roughly around  $5 \cdot 10^{19}$  eV. Between all the cuts this was the only bin which was completely above the already mentioned full efficient threshold. In fact, such a bin consisting of 84 events had its lower edge at  $4 \cdot 10^{19}$  eV. Extremely important is the fact that several other bins were found to be very near to the above mentioned requirements. This suggests that a small adjustment in the bin position or width can for sure increase the number of superposition bins.

In the case of TA flux, the number of accepted bins increases significantly and spreads over a wider range. After a 2 fold bin with respect with the plots the cut 100 km-60 deg offers 155 events bin at  $5 \cdot 10^{19}$  eV. The 100 km cut gives even 2 bins at  $5 \cdot 10^{19}$  and  $8 \cdot 10^{19}$  eV with respectively 200 and 50 events. Moreover the 150 km cut delivers one full efficient bin at  $8 \cdot 10^{19}$  eV with roughly 120 events. Finally even the full FOV spectrum could guarantee a full efficiency point with more than 50 events although at very high energy. In fact in the bin around  $1.5 \cdot 10^{20}$  eV JEM-EUSO could provide 50 triggering events. The TA assumption delivers therefore at least

5 full efficient bins with at least 50 events in one year time distributed in the range  $E > 4 \cdot 10^{19}$  eV till  $\sim 10^{20}$  eV.

Applying therefore a two–fold rebinning the triggered spectra deliver respectively 1 and 5 calibration bins in the full efficiency region. Worth to mention is that the measured points are relative just to 1 year measurement. In this view the collaboration could even extend the nadir mission phase if the collected statistics is considered to be unsatisfactory to provide superposition with the ground detectors. Moreover such exercises can be repeated in a systematic way trying to maximize both number and significance of cross correlation bins. In fact both varying bin size and position can affect the previous results. This results show however how the superposition is already achievable even in such a simple situation.

To avoid confusion it should be also stressed that the minimal detectable energy will be certainly lower than the thresholds mentioned here. In fact, such thresholds do not represent minimal triggerable energies but rather the minimal full efficient energies. As can be seen in 4.12 and 4.13 JEM–EUSO can probably detect particles even slightly above  $10^{19}$  eV. Once the spectrum has been calibrated around  $4\text{--}6 \cdot 10^{19}$  eV it can be extended both to higher and lower energies.

## 4.7 Tilt mode

A key feature of the JEM–EUSO mission is the possibility of operating in tilt mode. In such a way, the increase of observational area increases the observed statistics. However, the larger distance under which showers appear make them dimmer increasing the energy threshold. For this reason the advantages of the tilted mode are not obvious by itself and the improvement in exposure depends on the energy in a non trivial way. For this reason a specific study must be performed to find a trade–off between increased exposure and reasonably low energy threshold. In the present section results for nadir, 20, 30 and 40 degrees tilting have been presented.

The first step in this direction is to estimate how the surveyed area increases with the tilting angle. In Fig. 4.14 the FOV area is represented as function of the tilting angle. The two curves represent two different altitudes for the JEM–EUSO mission. In fact, the ISS orbit is limited to 330–460 km [176] but in the recent history such a variation has been limited between 340 and 420 km. As of January 2013 for example the ISS flies at an altitude of  $\sim 410$  km. At the moment it is not possible to foresee the altitude of the ISS in 2017–2022 but a reasonable assumption is 400 km. The 350 km altitude case can be on the other hand considered as a conservative estimate. The

tilting angle ranges from 0 to 50 degrees. As it can be seen, the surveyed area increases from 140.000 km<sup>2</sup> at 0 degrees up to  $2 \cdot 10^6$  km at 50 degrees for the 400 km case. At 350 km the area ranges from  $\sim 100.000$  to  $\sim 1.5 \cdot 10^6$  km<sup>2</sup>. Worth to mention is that the horizon is touched for the first time at 40.2 degrees tilting from 400 km and at 41.4 degrees from 350 km.

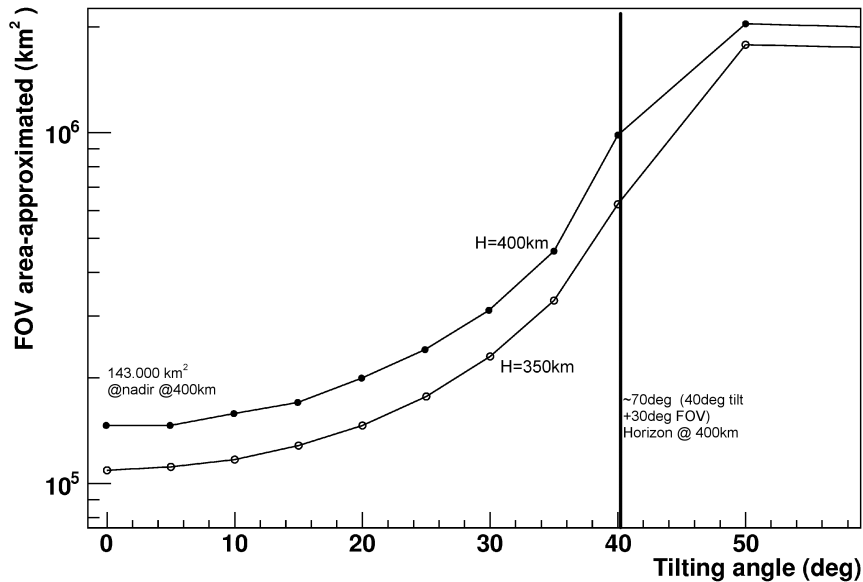


Figure 4.14: the JEM-EUSO surveyed area as function of the tilting angle. Both curves for 400 and 350 km are shown. The tilting angle (40.2 degrees) where the horizon is touched by the edge of the FOV at 400 km is shown.

For the exposure evaluation however a full FOV simulation is necessary. As shown in Fig. 4.15 the efficiency curves for different tilt inclinations are plotted. In the present study the background has been assumed to be constant over the entire FOV. Most likely such an assumption is too optimistic since the background radiance depend on the inclination under which the atmosphere is observed. However at a very first approximation and especially for low tilting angles we can consider the shower to detector distance to be the leading factor affecting the energy threshold. In fact, the shower signal can be expected to decrease proportionally to the inverse square of the distance which is much stronger than any reasonable inclination dependent variation in the background rate. Moreover the increase of the background by a factor  $n$  corresponds to an energy threshold a factor  $\sqrt{n}$  higher while the signal variations affect linearly the energy threshold. Efforts are ongoing within the collaboration for a more realistic estimation of the tilting angle

background dependence.

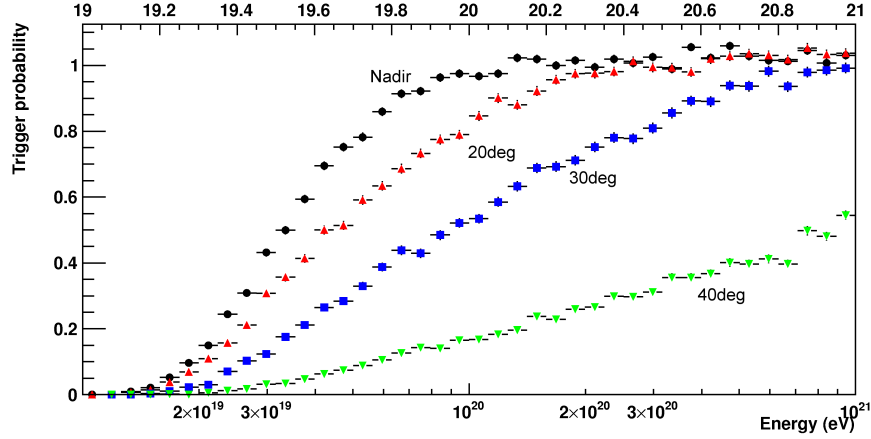


Figure 4.15: the JEM–EUSO trigger probability for nadir, 20, 30 and 40 degrees tilting.

The efficiency has been defined as in the nadir mode case. However the sampling range must be considerably enlarged because of the much larger FOV area. More in detail the used ranges are  $(-550-100, -250-250)$  km for 20degrees tilting,  $(-850-50, -320-320)$  km for 30 degrees tilting and  $(-1950-0, -430-430)$  km for 40 degrees tilting. This must be compared with the nadir mode range of  $(-270-270, -200-200)$  km. The Earth’s curvature is taken into account and it represents a deviation of 1.5% with respect to the flat sampling area even in the 40 degrees tilting case. The efficiency is therefore calculated as fraction of triggering events with respect to the total number of events in one bin. A normalization factor equal to the ratio between FOV and sampling area for each case is used.

As shown in Fig. 4.15 the efficiency curves tend to be lower for higher inclinations. More in detail the curves reach the full efficiency at  $\sim 10^{20}$ ,  $3 \cdot 10^{20}$ ,  $10^{21}$  eV for nadir, 20 and 30 degrees tilting. As for the 40degrees tilting the full efficiency is expected to be reached just around  $10^{22}$  eV.

The advantage of the tilting mode appears just above a certain energy depending on the inclination as can be seen in Fig. 4.16. Here, the JEM–EUSO exposure as function of energy can be observed for four different tilting angles. The aperture has been defined as in the previous section as observational area multiplied by solid angle integration and trigger efficiency. The assumed background is  $500 \text{ ph}/(\text{ns}\cdot\text{sr}\cdot\text{m}^2)$  which according again to the previous sections implies an observational duty cycle of 20% plus clouds lightnings and cities effects.

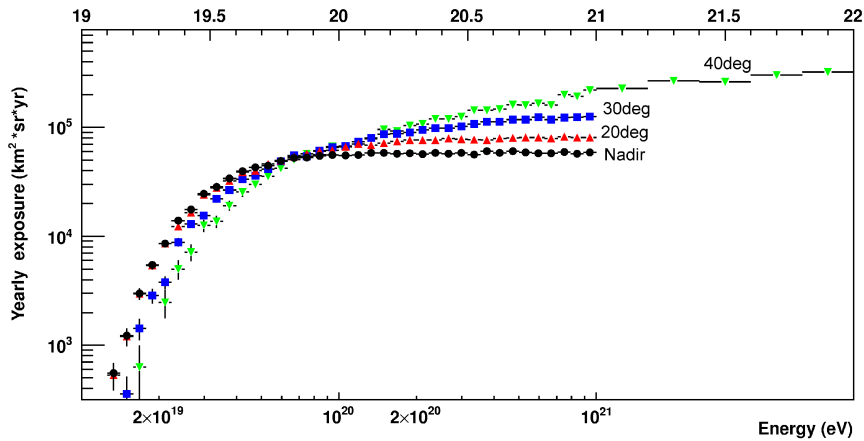


Figure 4.16: the JEM–EUSO trigger exposure. Four tilting angles, nadir, 20, 30 and 40 degrees are represented. The duty cycle is 0.2 (plus clouds and cities effects). A background of 500 photons/(ns·sr·m<sup>2</sup>) (or < 1500 photons/(ns·sr·m<sup>2</sup>)) has been assumed. The 40 degrees tilting requires an extension of the energy range in order to reach the full efficiency.

Tilting JEM–EUSO implies a loss in the exposure at low energies. On the opposite, at the highest energies a clear increase in exposure is achieved. As can be seen in Fig. 4.16, the maximal exposure is reached at higher energies as the tilting angle increases. For the 40 degrees sample an additional statistic of events has been simulated between  $10^{21} \sim 10^{22}$  eV. Such a high energy is however fully speculative and no scientific case has been developed in such a range. To be noticed is however the fact that an increase in the tilting angle brings to an increase already in the  $10^{20} \sim 10^{21}$  eV decade which falls in the JEM–EUSO interest range. Interestingly, given the present assumptions, around  $7 \cdot 10^{19}$  eV tilting does not affect the exposure in significant way. Above such energy tilting brings to a considerable increase in exposure while a loss has to be expected at the lower energies. However in the tilting phase, no significant loss is expected slightly above the cutoff ( $4 \cdot 10^{19}$  eV) if we limit the tilting to 30 degrees. Already above  $7 \cdot 10^{19}$  eV the exposure starts to increase significantly with the tilting angle. Worth to notice is the extremely low energy where tilting is bringing just moderate loss. Already at  $4 \cdot 10^{19}$  eV, moderate tilting reduces the exposure by 25%. The minimal achievable energy is shifted to higher energies by a large factor. Therefore tilting more than 20 degrees will make the trigger blind below  $2\text{--}3 \cdot 10^{19}$  eV. These considerations tell us, however, how the end of nadir mode mission does not immediately mean the end of the ”middle energy” mission. In fact

even in tilting configuration the mission will be able to collect a significant amount of statistics around  $4\text{--}5 \cdot 10^{19}$  eV. An extremely interesting consideration is how a moderate 20 degrees tilting will almost not affect the exposure even at the lowest detectable energies.

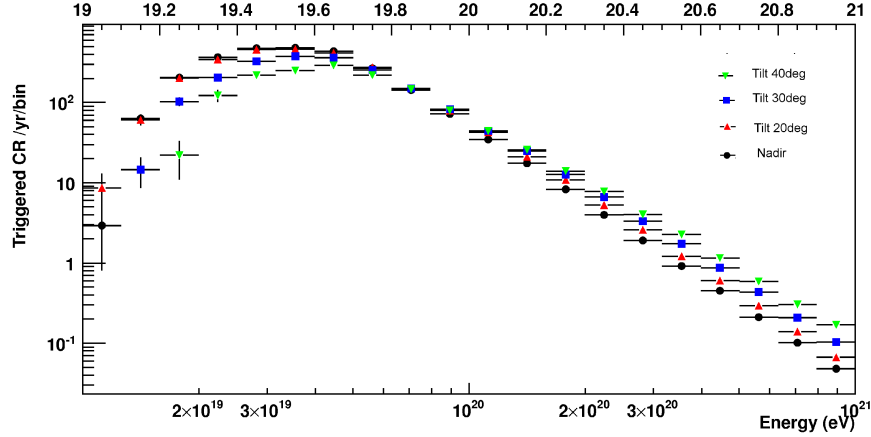


Figure 4.17: the JEM-EUSO triggered spectrum as expected by assuming the TA flux. All the considered tilting angles are represented here. As to expect the highest gain in number of triggered particles is at the highest energies while at the lowest a clear loss is observed above 20 degrees tilting.

Another way of evaluating the tilting impact is to estimate the number of triggered particles per bin and above a certain threshold. As it can be seen in Fig. 4.17 the higher the tilting angle the larger is the loss of events in the bins below  $6 \cdot 10^{19}$  eV. Around such an energy no significant variation is expected while at higher energies tilting will increase the number of triggered events. Another interesting aspect is related to the maximum energy achievable in such conditions. The maximal achievable energy increases therefore with the tilting angle according to both fluxes. Such a feature makes JEM-EUSO an extremely valuable mission since it allows the exploration of the highest energies ever detected.

The effects of cuts cut in the FOV position for the tilt mode has been investigated. Again a cut parameter is the distance from the center of the FOV. The FOV is divided in several stripes of increasing distance and area. More in detail the sample has been divided according to the distance of the shower impact point assuming the radius (0,100), (100,200), (200,300), (300, 400), (400, 600), (600, 1000) and (1000,  $\infty$ ) km as limits. In the present thesis we limited the study to the 30 degrees tilting case. In Fig. 4.18 the annual exposure for the 30 degrees tilting case is shown for all the above mentioned cuts. The chosen background is always  $500 \text{ ph}/(\text{ns}\cdot\text{sr}\cdot\text{m}^2)$  and corresponds

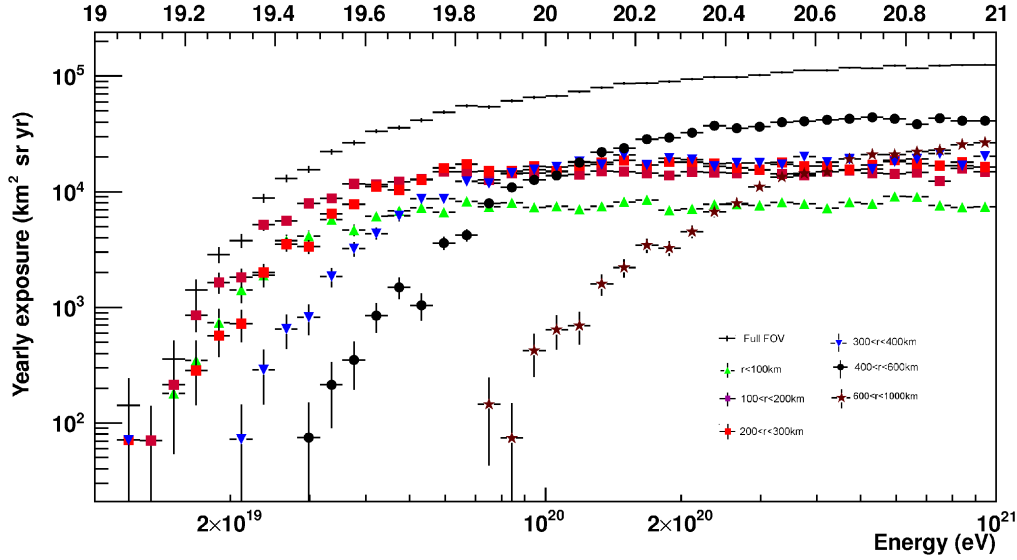


Figure 4.18: the exposure for the JEM-EUSO mission assuming 30 degrees tilting. A background of  $500 \text{ ph}/(\text{m}^2 \cdot \text{ns} \cdot \text{sr})$  and a duty cycle of 0.2 are assumed. Several FOV cuts are assumed in the present plot. More in detail the events have been selected according to the position of the impact point in the FOV. Cuts have been selected as follows: (0~100), (100~200), (200~300), (300~400), (400~600) and (600~1000) km.

to a 20% (plus clouds and cities) observational duty cycle. One extremely interesting feature is the relatively low full efficiency threshold which can be achieved across the most internal parts of the FOV. Also interesting is the limited range where all the exposure curves reach the full efficiency. In fact all the curves from 0 to 300 km reach the full efficiency already around  $5 \cdot 10^{19}$  eV. Such a feature is due to the compensation of the distance loss with an increase in the optics efficiency for the middle distances. In one word the energy threshold gets higher because of the increased distance but this effect is compensated by the fact that the ranges between 300–400 km are now surveyed by the best part of the optics. For this reason the detector can be considered to be very uniform till at least 300 km. For this part of the FOV it must be also noted how the asymptotic exposure is exceptionally similar for all the ranges from 100 to 300 km and at higher energies up to 400 km. Such a feature is due to the non dramatic increase in observed area as far as the distance is not above 400 km. A significant loss can be observed just under 100 km since the FOV border falls around nadir. Therefore, because of geometrical reasons a significant loss in the detector area can be observed in this parts of the FOV. The biggest contribution to the gain at higher energies

comes however from the 400–600 km range. It appears clearly how such a region is contributing to a significant increase in exposure at the highest energies and to a depletion at the lowest. At such an angle the ranges above 600 km are not relevant although they bring a significant contribution to the exposure just above  $5 \cdot 10^{20}$  eV.

## 4.8 Data rate studies

To complete this analysis of the JEM–EUSO performances an assessment of the expected data rates has been presented. This is essential to estimate constraints and performances of the telemetry. The number of triggering PDMs will be then estimated for each event together with the number of PDMs with signal and with the event duration. If the total available data budget reserved for each event is smaller than what can be reasonably defined as the event size, either a selection on the data or a reduction of the trigger rate must be done. If the data available for each event is larger than the average event the trigger thresholds can be relaxed or a more conservative selection of the event can be done.

As previously described the available JEM–EUSO telemetry is of the order of  $\sim 3$  GB/day. This limit can be extended up to 10 GB/day by means of solid state hard discs hosted on the ISS. Assuming a 20% duty cycle and the already mentioned 0.1 Hz/FS trigger rate, we can estimate the amount of triggering events to be of the order of  $\sim 1700$  triggers/day. Given the above mentioned telemetry constraints this respectively corresponds to  $\sim 1.7$  MB and  $\sim 5.7$  MB of data for each event.

Now, the estimation of the relevant data amount for each event must be performed. Given the projected size of the PDM on Earth and knowing the speed of a shower we can calculate the maximum time persistency of signal on each single PDM. More in detail, given the 37 km diagonal size of the PDM projected on Earth, the vertical shower development of a shower (which typically is confined in the lowest 30 km of the atmosphere) and the shower speed (0.75 km/GTU) it can be calculated that a spot cannot insist on the JEM–EUSO PDM for longer than  $\sim 65$  GTUs.<sup>8</sup> In other terms the insisting time in GTUs is

$$GTU_{PDM} = \frac{\sqrt{l_{PDM}^2 + h_{atm}^2}}{c} / 2.5[s/GTU] \quad (4.16)$$

whereas  $l_{PDM}$  is the diagonal length of a PDM on Earth (37 km),  $h_{atm}$  is a

---

<sup>8</sup>We will define here the 64 GTUs time span since it is a more reasonable number in hardware. In fact 64 is a power of 2 and can be expressed as a binary of 6 bits.



30 km altitude roughly assumed as the altitude under which the largest part of the shower is going to develop and  $c_{km}/GTU$  is the speed of light.

Therefore, once a trigger in a PDM occurred, a window around it having size  $2 \cdot GTU_{PDM}$  must be chosen in order to include the entire signal. The factor 2 derives from the consideration that the knowledge of the timing position of the trigger might not be known in real time. Said in other terms the CPU might not have the information on whether the trigger was at the end or at the beginning of the shower track.

Given the previous considerations and given the 2304 pixel of a PDM each triggering PDM is associated to  $\sim 300$  kB of data. Therefore the JEM-EUSO telemetry can send up to 5.6 PDMs for each triggering event. After including also the solid state disc this number can potentially increase up to 18.6 PDMs<sup>9</sup>.

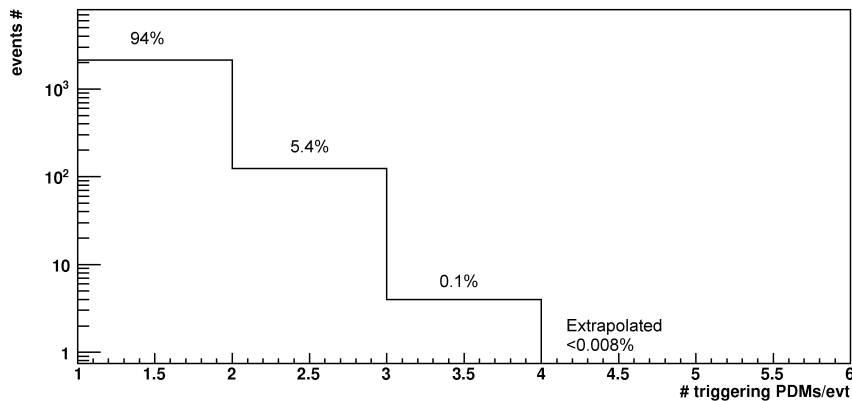


Figure 4.19: the distribution of the number of triggering PDMs for each event. The simulated sample delivered  $\sim 2200$  triggering events. The simulated sample includes energies from  $10^{19}$  to  $10^{21}$  eV. The assumed spectrum has a power law shape with index -4. The angular distribution is like  $\sin 2\theta$  from 0 to 90 degrees.

The size of the typical event on the focal surface can now be assessed. A distribution of proton showers on the entire focal surface has been simulated. The angular distribution has been chosen as  $\sin 2\theta$  as in the case of the normal trigger studies. The energy spectrum however has been chosen as power law with spectral index -4 within the range  $10^{19}$ – $10^{21}$  eV. Such a choice has been taken in order to have a more realistic ratio of low and high energy events

<sup>9</sup>Such numbers are however not considering any telemetry required by other instrument functions. This is clearly an overestimation but all these results can be easily scaled once the real available telemetry is known.

and the very steep index is describing the part of the spectrum above the cutoff.

In Fig. 4.19 the distribution of the number of triggering PDMs for each event is given. Of the simulated events  $\sim 2200$  triggered in at least one PDM. Of the triggering events 94.3% trigger in one PDM, 5.4% in 2 and 0.17% in 3. Due to the large statistics needed, the fraction of events triggering on 4 PDMs could not be estimated in the scope of this doctoral work. However, a preliminary estimation could be done after considering the relative amplitude of the bins and extrapolating such a tendency to higher PDMs numbers. The number of events triggering over 4 PDM has been estimated to be of the order of 1 event every ten thousand.

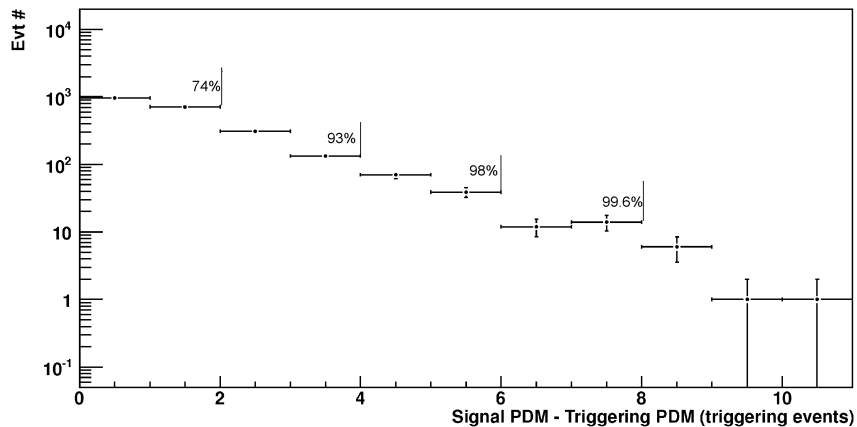


Figure 4.20: number of PDMs with signal in addition to the triggering PDMs. The first bin represents all the events with no PDM having signal other than the triggering ones. The fraction of events having less than a certain amount of triggering PDMs is superposed on the plot.

Another feature to estimate the event size is shown in Fig. 4.20. Here the amount of PDMs with signal additionally to the triggering PDMs can be observed. This is done to estimate the number of PDMs which carry information additionally to the triggering PDMs. In fact, triggering PDMs will be identified univocally while the additional PDMs with signal will be unknown. Worth to note is that in Fig. 4.20 no information is given on the amount of signal in each PDM. The only considered condition is that at least 3 photoelectrons are collected in each PDM. Such an estimate is therefore largely conservative. Whether some information can be extracted from the selected PDMs or not can be regarded as a reconstruction related problem. As can be seen, of the 2264 triggering events, almost 1000 do

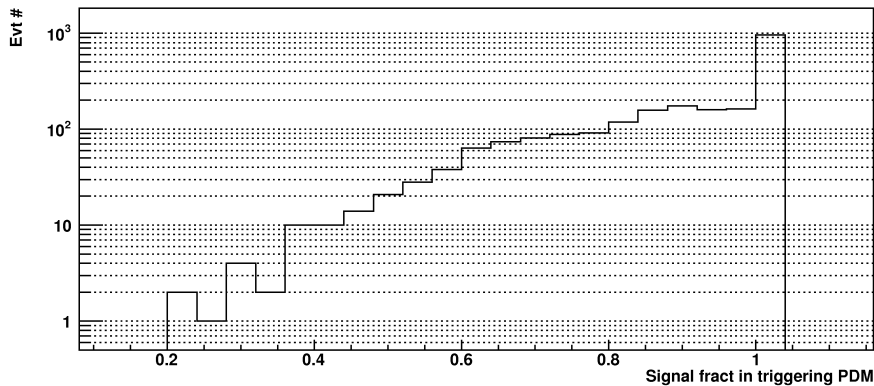


Figure 4.21: the fraction of the signal which is included in triggering PDMs.

not have any appreciable signal on not triggering PDMs. The 74% of the events have 1 or no additional PDM with signal. The 93, 98 and 99.6% of the events have respectively at most 3, 5 or 7 PDMs with signal. The probability of having more than 10 PDMs with signal is expected to be very small. In this case however the extrapolation of the tendency suggests a non negligible probability of having a large number of PDMs with signal. Assuming 10000 triggering events as the total JEM-EUSO sample and the tendency of a reduction of an order of magnitude every 3 additional PDMs we might expect some event to have till 12–13 PDMs in addition to the triggering one at least once in the mission time.

Fig. 4.21 shows the fraction of the total signal which falls on triggering PDMs. As can be seen the majority of the signal falls inside the triggering PDMs. Remarkably even almost 1000 of the 2264 triggering events does not have any signal at all outside the triggering PDMs. Moreover the 76% of the events loose less than 20% of the signal while 95% are within 40%. Such a plot however tells that a relevant fraction of the potentially interesting signal might be lost. In the most extreme cases some event might even loose up to 80% of the signal. A more detailed study is necessary in order to identify which events are characterized by such losses for and which part of the event is going to be lost. However it can be expected that the neglectation of the non triggering PDMs could harm the scientific output of the mission.

The signal duration both on the single PDM and on the entire FS is also shown. In Fig. 4.22 the time difference between trigger and counts can be observed. The considered pixel-GTUs must belong to the same triggering PDM to be considered. This condition is chosen in order to measure the time persistency of the signal on a single triggering PDM. Such a plot expresses

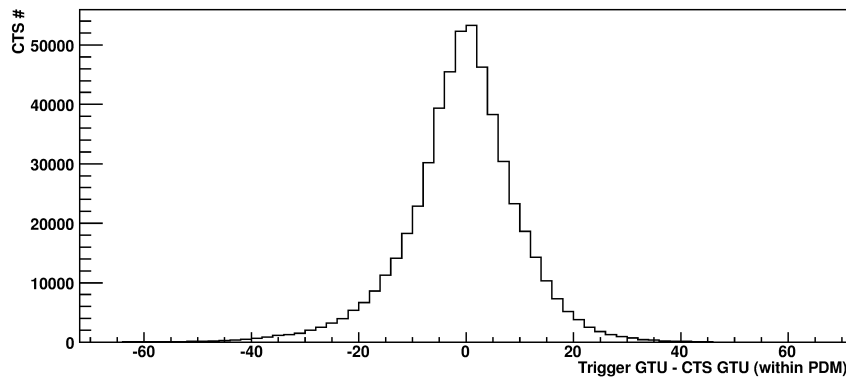


Figure 4.22: difference between the GTU of the maximum *CCB\_LTT* trigger and the GTU of the counts. The pixel-GTU plotted here represent just those belonging to triggering PDMs.

therefore the time window where most likely a spot insists on the same PDM where the trigger occurred. As can be seen the persistency on the same PDM is typically under 60 GTUs. However, the lack of information on the trigger timing with respect to the rest of the signal in the PDM forces the choice of a window of  $\pm 64$  GTUs centered on the trigger. Taken the above mentioned conditions the amount of signal out of the selected window could be estimated to be negligible. The average of the distribution does not change if instead of maximum trigger all the triggers are included since regardless of the position in the shower development the spot will always leave the PDM within 65 GTUs and cannot have entered before 65 GTUs in the past.

Also the time duration of the event on the entire focal surface can be estimated. In Fig. 4.23 the time difference between the first and the last EC signal is plotted. The event duration is expressed in GTUs. As it can be seen the largest fraction of the events insists on the focal surface for less than 120 GTUs. However a long tail on the right part of the plot signalizes the presence of a large fraction of events having very long duration. Such events are typically the very inclined showers which evolve high in the atmosphere and are characterized by slow evolutions and do not display impact point. Moreover the potential presence of long neutrino events makes the need for the largest coverage of such events very urgent.

Again as in the case of the geometrical extension of the events, the fraction of signal falling in a specific time window can be estimated in Fig. 4.24, which shows the fraction of the total signal (Y axis) falling after a certain GTU threshold (X axis). In this way by setting a time threshold it can be estimated which is the fraction of signal lost after that time. To estimate

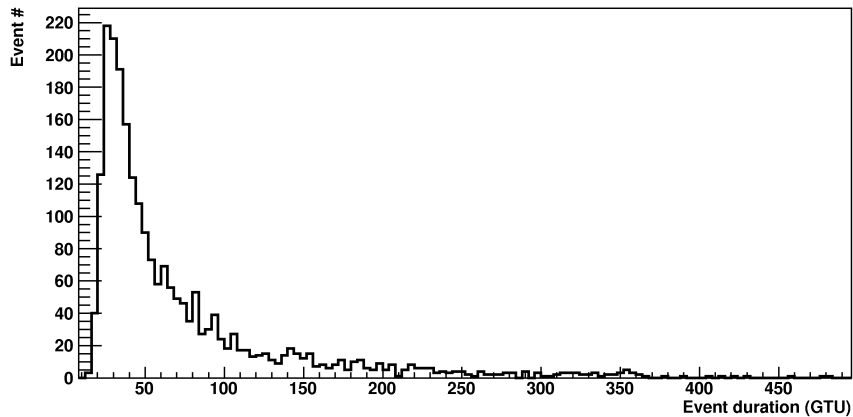


Figure 4.23: number of GTUs between the timing of the first and the last EC signal. Such a time span expresses the total duration of the event but not its detectability.

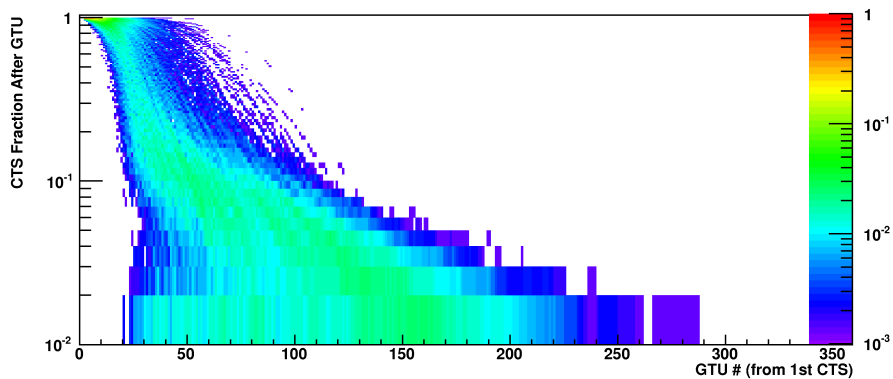


Figure 4.24: lost fraction of signal (Y axis) for each time threshold (X axis). The color scale represents the frequency of a particular condition.

how many events share the same bin a color scale has been introduced. In this plot the rare conditions are represented by violet–blue colors while red orange represent states which are shared by many showers. Obviously by setting GTU 0 as the threshold requires that all the events have the entire signal still to come. It can be also seen for example how all the events never loose more than 7–8% of the signal if a  $\sim 128$  GTU threshold is set. By setting a threshold of  $\sim 256$  GTUs the totality of the events will never loose more than 2% of the signal. Worth to mention is the fact that the binning in Y of such a plot has been chosen in such a way that fractions just down to 1% can be appreciated. In fact many of the single photons which contribute

to the very long tail in Fig. 4.23 cannot be seen in Fig. 4.24.

The very last part of the section is devoted to the extremely luminous events. The most scientifically interesting task for the JEM-EUSO mission is the detection of the extreme energies. For this purpose a statistic of  $10^{21}$  eV events has been chosen. This is meant to test the case most challenging conditions for the JEM-EUSO hardware. Nevertheless the JEM-EUSO electronics must be able to cope with such events given the extremely high value they would deliver.

In Fig. 4.25 the distribution of the number triggering PDMs can be seen for 534  $10^{21}$  eV triggering events. Such events have been distributed according to the  $\sin 2\theta$  angular distribution and are scattered across the FOV ( $\pm 270, \pm 200$ ) km. These extreme events can achieve a much larger number of triggering PDMs. In fact given the chosen statistic  $\sim 1\%$  of the events have been triggering over 5 PDMs. Still a significant fraction of such events ( $\sim 10\%$ ) can trigger on 3 or more PDMs.

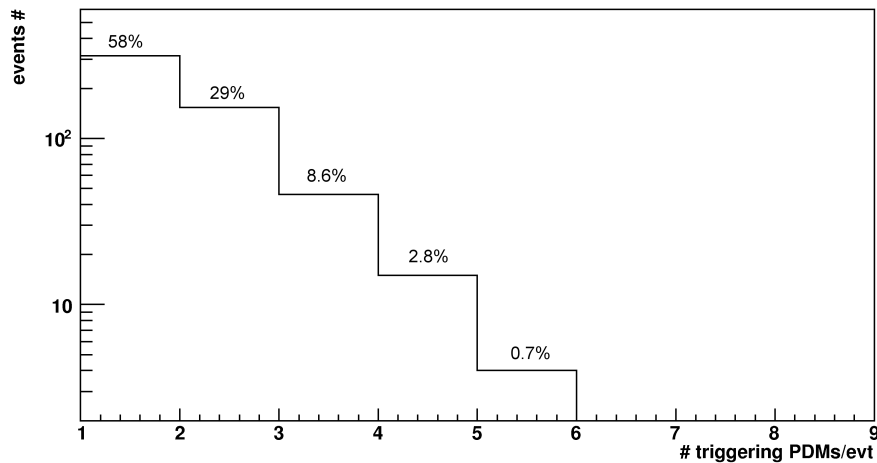


Figure 4.25: number of triggering PDMs per event. The 534 triggering events have an energy of  $10^{21}$  eV and are distributed in all directions and FOV positions. The percentage of the triggering events in each bins is also depicted.

Another very important feature is shown in Fig. 4.26 where the number of non triggering PDMs with signal is plotted. An extremely large number of PDMs can be involved (up to 25 PDMs) without a related trigger. A striking feature of such a plot is also the almost total lack of events with no significant signal out of the triggering PDMs. Such events seem therefore to involve large fractions of the focal surface.

In Fig. 4.27 on the other hand the fraction of signal collected in the

triggering PDMs reveals a more relaxing scenario. In fact, in the totality of the cases the fraction of non triggering signal never exceeds 25%. This is a consequence of the extremely strong signals associated to such showers. For this reason whenever the spot enters a PDMs it will most likely trigger it. The extremely large numbers of triggering PDMs is due to the large amount of light scattered in the optics.

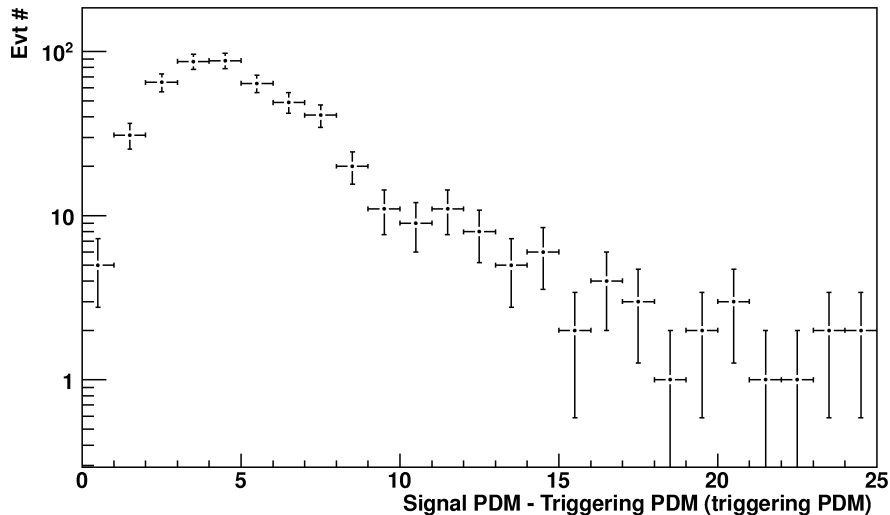


Figure 4.26: number of non triggering PDMs which collect at least 3 photoelectrons. As can be seen a very large fraction of the focal surface can be involved if a  $10^{21}$  eV event is detected.

In Fig. 4.28 the persistency of the signal on a single triggering PDM can be seen. No significant difference can be appreciated with respect to Fig. 4.22 despite the very high energy. This feature is due to the speed of the spot which can never allow the signal to persist on the same PDM for more than  $\sim 64$  GTUs.

In Fig. 4.29 the total duration of the event on the focal surface can be seen for the high energy sample: the time delay between first and last count is significantly larger than in the previous case. As already shown, the signal duration is significantly reduced once the signal threshold is considered. As shown in Fig. 4.30 the fraction of signal which can be lost with a 128 GTU cut can be larger than 10% in a very significant number of cases. The 256 GTU cut seems to offer a better performance although not as safe as in the normal event condition. In fact, in some small fraction of events even up to 4% of the signal can be lost.

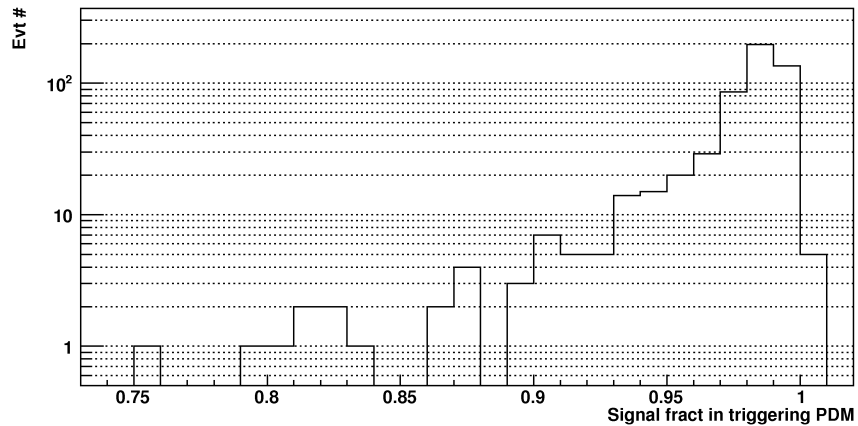


Figure 4.27: fraction of signal collected inside the triggering PDMs for the  $10^{21}$  eV sample.

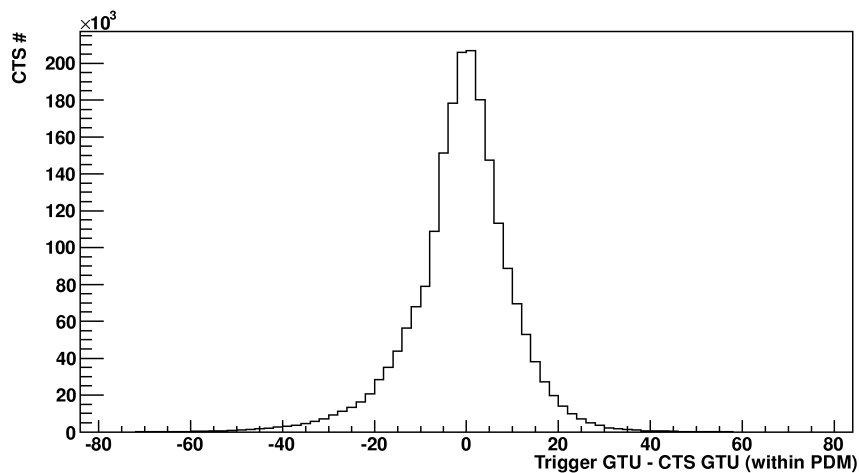


Figure 4.28: signal persistency over a single triggering PDM for the  $10^{21}$  eV sample. No significant difference can be seen with respect to the realistic sample.

To conclude, the amount of triggering PDMs is compatible with the telemetry limits. In fact, almost all the events trigger with less than 2 PDMs. In the high energy sample we see that the number of triggered PDMs is significantly larger and up to 4 PDMs can trigger in a significant fraction of cases. However the rarity together with the unrealistically high energy of these events make the overall contribution of such sample manageable. Nevertheless the JEM-EUSO electronics must be ready to accept large numbers



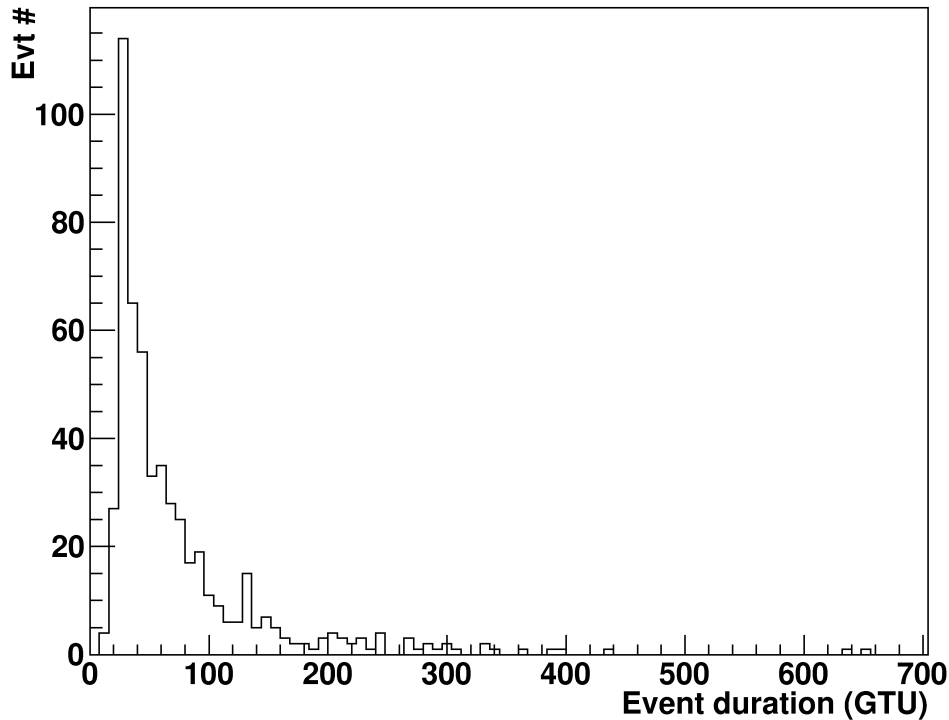


Figure 4.29: number of GTUs between the timing of the first and the last EC signal for the  $10^{21}$  eV case. Such a time span expresses the total duration of the event but not its detectability.

of triggering PDMs.

Also the persistency time within one PDM is compliant with the expectations. Therefore we can assume that the 128 saved GTUs are certainly sufficient for the single PDM level. We can also observe in Fig. 4.22 and 4.28 how the time distribution of the signal with respect to the triggering GTU is centered on 0. These considerations are made on the maximum trigger achieved in one PDM but are easily extendible on the multiple trigger flag case. This is because, independently of the position of the trigger with respect to the shower maximum the spot will leave the PDM within 64 GTUs or alternatively it must have entered the PDM at earliest 64 GTUs before. The cumulated distribution of the timing within one PDM will be always centered on 0.

The total event duration however exceeds the 128 GTUs span in a very relevant fraction of cases both for the low and high energy sample. For this reason given the limited ring buffer depth triggering PDMs must be treated

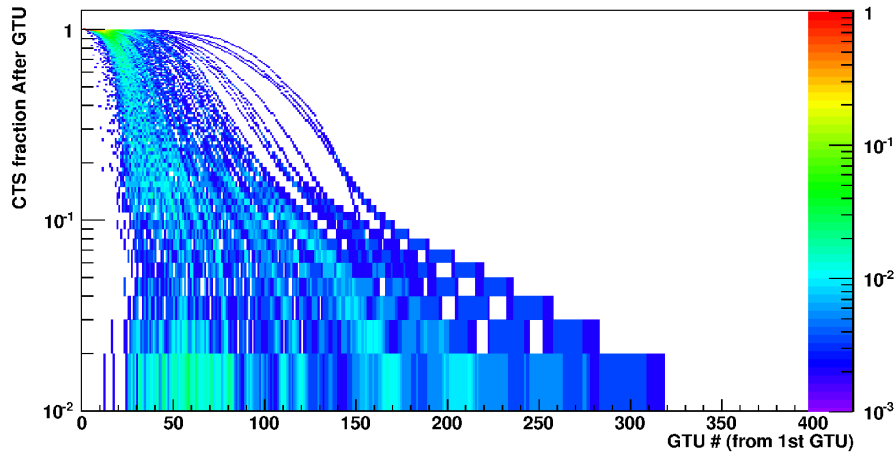


Figure 4.30: lost fraction of signal (Y axis) for each time threshold (X axis) for the  $10^{21}$  eV sample. The color scale represents the frequency of a particular condition. In color scale is the frequency of a particular condition.

independently. The *CCB-LTT* should be able therefore to cope with triggers in such a way to save 128 GTUs for each PDM at different times. This is needed especially for the most important high inclination and high energy events crossing several PDMs. Alternatively it can be also said that a 256 GTU window could be well enough to include almost all the signal for the vast majority of events (see Figs 4.24 and 4.30).

The case of non triggering PDMs is however more complicated. In Figs. 4.20 and 4.26 the number of PDMs with signal in addition to the triggering PDMs has been shown. In this case no time information is available and it must be considered as impossible to recognize the signal since the trigger algorithms failed to do so<sup>10</sup>. The time window to be selected has to be therefore defined according the timing of the trigger issued in neighboring PDMs. Provided no logic is available for the direction determination of the shower the needed time window to be covered is however double than what necessary for the triggering PDMs. In fact, assuming a trigger happens at a GTU  $X$  we can estimate the latest time the spot will leave the triggering PDM as  $X+64$  GTUs. The signal can then insist on the contiguous non triggering PDM for additional 64 GTUs (GTU  $X+128$ ) always for the above mentioned spot speed reasons. This idea works also for the past GTUs. In fact the signal must have entered the triggering PDM at earliest at GTU

<sup>10</sup>Alternatively some logic has to be developed in order to recognize non triggering signal by using the correlation with other triggering PDMs.

X-64 and the non triggering adjacent PDM at GTU X-128. This implies the very wide time span (from X-128 to X+128) which can in principle host signal in any of the adjacent PDMs.

The most reasonable approach could be the implementation of some logic to select just some of the adjacent PDMs and either past or future GTUs depending on the direction of the track. Another possibility could be the extension of the buffer in order to include the maximum length of the shower event. For this purpose an increase up to 256 GTUs could be enough given the low fraction of signal surviving after such time. If none of these options is available it might be possible that some information is lost even if the adjacent GTUs are sent to ground. In this case it might be more appropriated the relaxation of the triggering conditions to accept a higher rate of triggering events and to fill the gap between allowed and produced PDMs.

Interestingly, the extremely high energy events seem to be characterized by large fractions of signal included within the triggering PDMs (see Fig. 4.27). This is probably due to the high capability of the high energy signal to trigger if a PDM is encountered. This consideration might mitigate the challenges related to the event size and available telemetry.

The present study should be repeated in case of a wider range of possible spectra in order to find if significant deviations from the presented results can be found. Moreover the reconstructability of the non triggering signal must be assessed to test up to which extent is necessary to consume available telemetry. In the present discussion no additional telemetry is assumed to be consumed by any other function of the instrument. Such an assumption is obviously not correct and must be checked in the future. The presented numbers can be however easily rescaled once the non available fraction has been defined.



## Chapter 5

# The Energy and $X_{max}$ Reconstruction Algorithms

Aim of this chapter is the description and the validation of the JEM–EUSO energy and  $X_{max}$  reconstruction algorithms. Several algorithms have been developed in this work. From the detector response map, the information of the incoming flux on the pupil can be reconstructed. This information is used to calculate the luminosity of the shower. This however requires the knowledge of additional information like the direction of arrival of the photons and the response of the optics. The correlation of the arrival direction with the pixel is then mapped to perform a fast photon off–axis angle ( $\vartheta$ ) reconstruction. Given the arrival direction, the geometrical projection on ground of the track can be also determined. Several algorithms have been developed to reconstruct the altitude of the shower at each step. Using a parameterization of the atmospheric transmittance and the position of the shower at each time, the shower luminosity is eventually calculated. An estimate of the electron’s number for each step is made taking into account the Cherenkov light contamination.

The final electron profile is then fitted with a shower parameterization function to obtain the energy and  $X_{max}$  parameters. A general overview of the above mentioned process is shown in Fig. 5.1.

The obtained values can be then used as initial conditions for an iterative process in order to obtain the best set of parameters and a parameter confidence range. In fact, as a result of the statistical uncertainty no unique answer can be given on the energy and  $X_{max}$  parameters.

In this chapter the steps needed to reconstruct the shower parameters are described. An extensive study on the systematics of the procedure as well as an estimation on the statistical uncertainty is also performed.

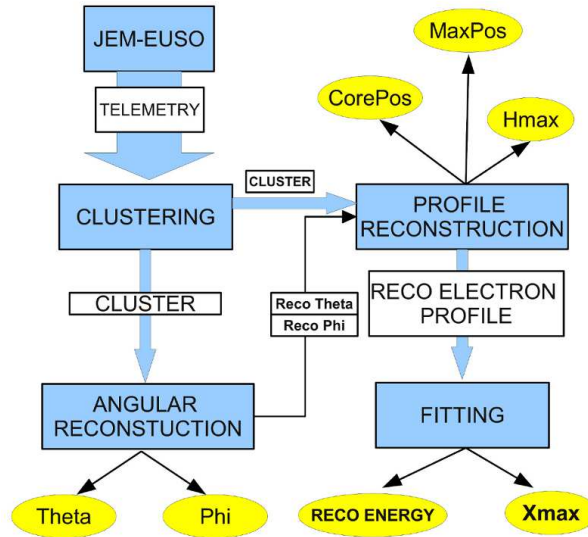


Figure 5.1: The basic concept of the reconstruction process is shown here. The JEM-EUSO detector response is analyzed by the pattern recognition algorithms (called clustering here). Once the signal has been recognized this information is used for the angular and profile reconstruction. The altitude ( $H_{max}$ ) of the maximum and the position of core and maximum are reconstructed. Thanks to a fit on the reconstructed profile parameters like energy and  $X_{max}$  can be calculated.

## 5.1 The PmtToShowerReco algorithm

The *PmtToShowerReco* is the energy and  $X_{max}$  reconstruction algorithm developed in the framework of this doctoral work. The algorithm is structured in several subsequent steps. A very schematic view of the *PmtToShowerReco* algorithm is given in Fig. 5.2.

As previously described the *PmtToShowerReco* receives as input the information on the timing and on the position for all the counts. Just triggered events are analyzed since the trigger is the condition for the data table to be sent to ground. The first step consists in the reconstruction of a *count curve*. The information of the reconstructed track will be therefore read-out and the timing of all the pixel-GTUs is used to reconstruct the signal intensity as function of time. The spatial information is retrieved in order to assess the possible signal losses due to the voids of the focal surface. More in detail for each GTU the center of mass of the spot is calculated. All the GTUs where the center of mass falls in proximity of a gap must be carefully treated since they are affected by signal loss. For this purpose, several approaches have been followed. The easiest option simply removes the points generated

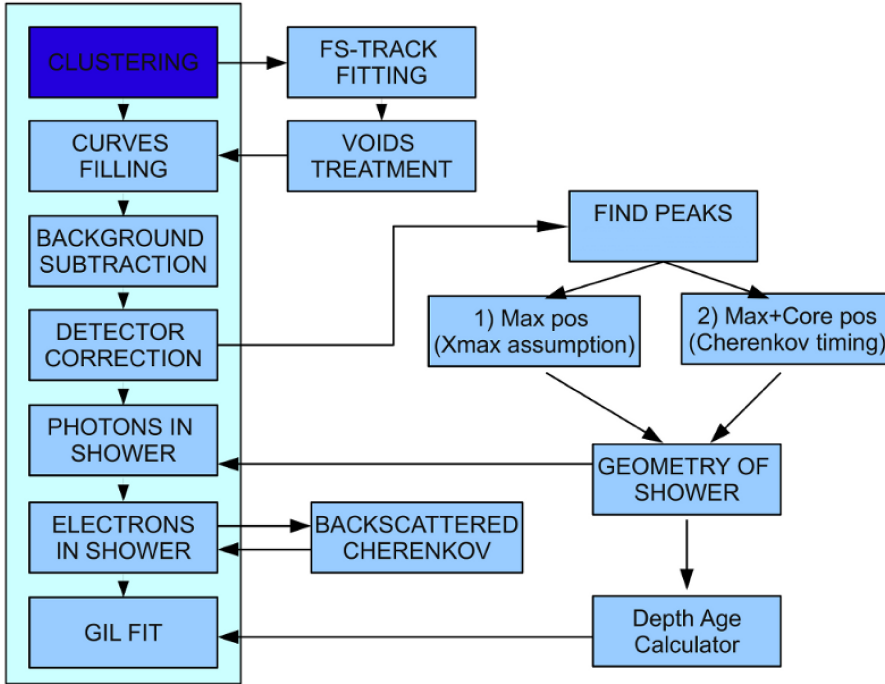


Figure 5.2: a simplified view of the *PmtToShowerReco* reconstruction. The input information is represented by the blue box marker with the title *Clustering*. Here information like the amount of counts for each time and position is given. Following the vertical path underlined in cyan the counts curve the electron curve is obtained from the counts following several steps. Complementary operation are executed on the right side of the diagram.

by a spot in the vicinity of a focal surface gap. Another approach corrects the missing signal. This is significantly more complex since it requires the knowledge of the spot shape. The parameterization presently implemented includes however just a uniform distribution of circular shape and uses a correction factor proportional to the ratio between sensitive area and total circular area. The removal option is used in the present study. At a very first approximation, the exclusion area is circular with radius  $\sim 3$  mm. This implies that the center of mass of the spot must be at least one pixel far away from the border of the focal surface component. Such a radius can be justified by considering that the projection of the exclusion circle in nadir mode is  $\sim 500$  m and therefore comparable to the standard shower size. The ESAF default parameterization (following Gora et al. [178]) implies a shower lateral development which confines most part of the generated electrons within  $< 500$  m. Already few hundreds meters from the shower axes the shower's

charge exceeds the 90–95% of the total charge. The optics doesn't present a limitation from the point of view of spot size. In fact, as already shown in Chap. 3, assuming point-like sources the 90% of the focal surface photons are falling inside 1 or 2 mm radius for most of the conditions.

An essential step of the reconstruction is the background subtraction. This amounts to the number of pixel selected in the GTU multiplied by the average background on each pixel–GTU. Before subtracting the background as fixed amount for each pixel–GTU the error bars associated with each GTU will be calculated as the root square of the amplitude value. The absolute error bars will be preserved after the background subtraction. For all the following steps the error bars must be scaled according to the conversion factors applied in each step.

A second key step of the procedure is the identification of the maximum and of the Cherenkov peak in the reconstructed light curve. The nature of the JEM–EUSO detected signal makes the search for such a signal not trivial. The first difficulty lies in the relatively low measured signal. As it will be shown later, a typical shower ( $10^{20}$  eV) produces a maximum  $\sim 50$  counts/GTU. Moreover gaps cause sudden drops in the light intensity which can totally deplete the light curve. A further limitation lies in the wide area over which the Cherenkov reflection is spread. This causes the signal to noise ratio on the Cherenkov signal to be further reduced. For these reasons the automatic recognition of a physical peak is not trivial and not always possible. First a cleaning of the signal is performed to avoid the detection of fake peaks especially in fractions of the curve where low signal is present. The chosen approach counts, in a  $\pm 2$  window around the analyzed GTU, the number of GTUs different from zero. Provided neither 2 additional bins different from zero are within this window nor the central bin is larger than 10 the central bin is neglected in the peak analysis. This is done to avoid detection of peaks in the later evolutionary stages of a shower where Cherenkov signal is massively spread out and where the detection of a large number of single isolated peaks of low intensity is still possible. In fact the present peak search algorithm can be heavily affected by such a small and discontinuous signal tail.

The following step is the retrieval of all the peaks in the counts curve. The peak has been defined as the maximum between the  $\pm 2$  adjacent bins. In general the identification of one single peak is considered as detection of the maximum while two peaks are generally identified as maximum and Cherenkov. All such situations must be however treated carefully since a limited number of peaks is most likely caused by a poor quality signal.

The presence of more than 2 peaks triggers a more complex analysis. More in detail each peak is numbered according to its amplitude compared with



the other peaks. The highest will be marked with *rank* 0, the second highest with *rank* 1 and so on. Moreover the timing of the peaks is used to give a first estimation of the Cherenkov peak. More in detail, the latest or the second latest peak is assumed to be the first guess for the Cherenkov peak. The peak *rank* is used in the process for the maximum analysis. In normal conditions the peak with highest *rank* previous to the Cherenkov peak is identified as maximum. If two or more maxima have the same height the maximum GTU will be assumed as the average of the maximum peaks. If the maximum is near a gap an average between the minor peaks having at least 90% of the maximum amplitude is calculated. In fact, in these cases no guarantee is given that the observed maximum is not a fake detection since the curve could be depleted by the gap. The reconstructed arrival direction is used to verify the consistency of Cherenkov and fluorescence peaks. If for example the maximum and the Cherenkov were too close for a "reasonable" proton shower with a given inclination the Cherenkov peak must be neglected. This consistency check requires however the knowledge of a reconstructed arrival direction and assumes a priori the nature of the particle.

The next step of the procedure consists in obtaining the focal surface photon's curve. The parameterization of the photo detector includes the efficiency of the PMTs, of the front end and the transmittance of the optical filter. At the present stage all the three features have been implemented just in form of single factors. Following that, the correction for the optics response is performed. At the end of this stage a photon curve at the entrance pupil is obtained. The so called *OpticsResponse* is therefore calculated. To calculate the *OpticsResponse* map several point sources are simulated following a set of predefined  $\vartheta$  and  $\varphi$  FOV angles. Incoming photons are simulated according to a predefined set of wavelengths. Given a certain number of photons two factors are calculated. The first one is the ratio of photons reaching the focal surface with respect to the one incident on the detector's entrance.

$$Eff = \frac{\gamma_{fs}}{\gamma_{opt}} \quad (5.1)$$

The second factor expresses the ratio between the photons reaching inside a predefined radius with the photons incident on the detector.

$$Eff_{trigg} = \frac{\gamma_{encirc}}{\gamma_{opt}} \quad (5.2)$$

It must be stressed how the second factor is more relevant since it expresses the validity of a focal surface section as signal collector. The so called trigger throughput is affected by both the optics capabilities and physical width of the shower.

A selection radius of 3 mm has been chosen in the present work. The choice is justified by the confinement of most part of the signal in such a radius. Once the signal inside such an area is estimated the throughput is used to estimate the flux reaching the pupil<sup>1</sup>.

Note that the definition of a 3 mm radius collection area assumes that the area selected by the pattern recognition is comparable to this circular area ( $A \sim 28 \text{ mm}^2$ ). With a  $9 \text{ mm}^2$  pixel is assumed that the pattern recognition algorithms select an average of  $\sim 3$  pixels every GTU. Every deviation from this average causes systematics effects. This can be explained by the intuitive argument that the reconstruction throughput efficiency has been calculated for  $A \sim 28 \text{ mm}^2$  and it cannot be applied over a different area. For this reason the clustering (the *PWISE* in this case) will be used as a basis for the track selection. All the pixel-GTUs whose center is falling within 3.5 mm from the center of the selected spot are used for the curve construction. The average number of pixels selected in this way turns out to be  $\sim 3$  making the selected area comparable to the *OpticsResponse* trigger throughput area.

Another fundamental information is the mapping of the arrival directions as function of the pixel identification number namely the *PixelAngleMap*. This map, described in Chap. 3, allows the reconstruction of the arrival direction of the photons depending on the pixel under analysis.

The aforementioned maps allow the calculation of an efficiency factor for each time of the event development. After calculating the average FOV angle of the UV photons at each time, an average optics efficiency is retrieved from the map. This efficiency factor is needed to obtain the photon curve at the pupil.

The reconstruction of the shower's luminosity will follow next. Precondition to such a calculation is however the knowledge of the shower position at each time to calculate the distance of the shower from the detector and consequently the total amount of photons produced. Given the total number of photons at the pupil and the  $\frac{1}{d^2}$  flux decrease the number of photons at the shower site can be calculated. The knowledge of the position in the atmosphere is also needed to properly apply the atmospheric transmission correction.

Within the following doctoral work two methods have been developed to determine the altitude of the maximum. The first uses the Cherenkov reflection mark while the second assumes a parameterization for the depth of the maximum ( $X_{max}$ ) and relies on the direction delivered by the direction

---

<sup>1</sup>More in detail, the so called *OpticsResponse* will perform a preselection of all the photons within 20 mm from the maximal photons density concentration. Following this selection the center of mass of the selected photons distribution will be calculated. Finally the fraction of the photons falling inside 3 mm radius will be calculated.

reconstruction algorithms.

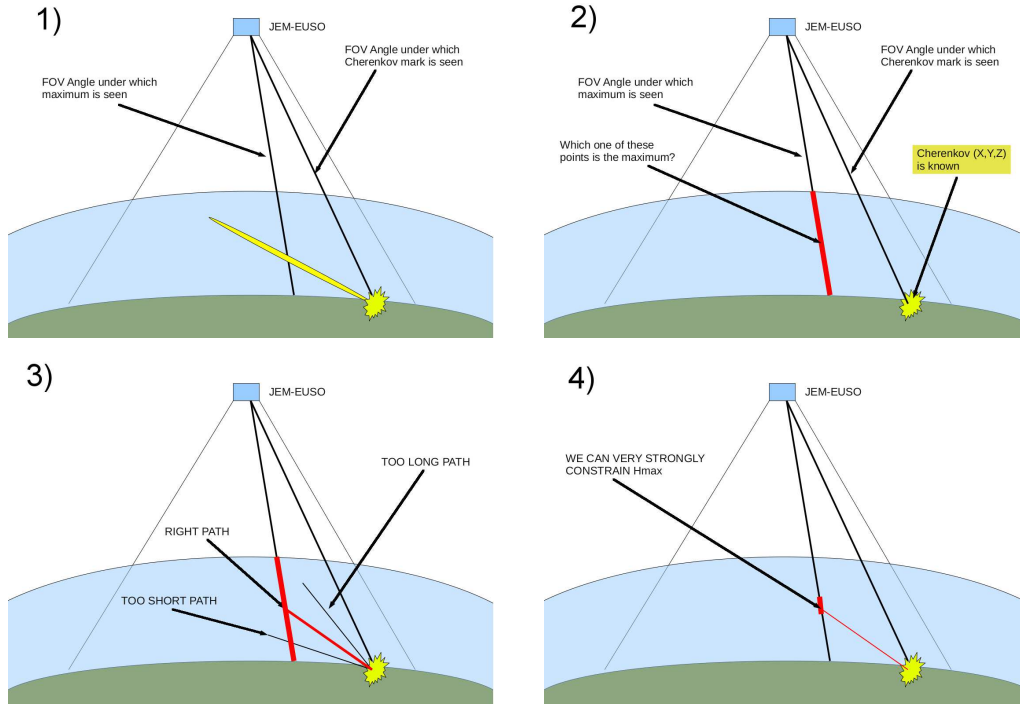


Figure 5.3: the Cherenkov  $H_{max}$  reconstruction method. **Upper-left panel:** the shower with the FOV angles for both maximum and Cherenkov. **Upper-right panel:** the unknown position of the maximum (in red). **Bottom-left panel:** several geometrical trials are shown. Knowing the time which intercurrs between maximum and Cherenkov just a limited set of trials can be accepted to identify the proper  $H_{max}$ . **Bottom-right panel:** The most likely  $H_{max}$  interval is identified.

The first method shown in Fig. 5.3 assumes the identification of a Cherenkov mark within the light curve. The time delay between shower maximum and Cherenkov reflection provides the distance traveled by the shower. Both the propagation time of the photons and of the shower must be taken into account. Knowing the projection of the maximum and of the Cherenkov bump on Earth is possible to calculate the altitude of the maximum.

In Fig. 5.4 a second method, based on the direction reconstruction, is shown. Both direction and maximum projection on the field of view are assumed to be known. A range of  $H_{max}$  is then selected according to the depth of the projected maximum ( $X_{max}^{GEO}$ ). Note that a high  $H_{max}$  implies a very low  $X_{max}^{GEO}$  while a very low  $H_{max}$  implies a high  $X_{max}^{GEO}$ . In this study the GIL parameterization has been used but any other parameterization for  $X_{max}$  can be chosen. The constrains on  $X_{max}^{GEO}$  are therefore used to constrain the altitude.

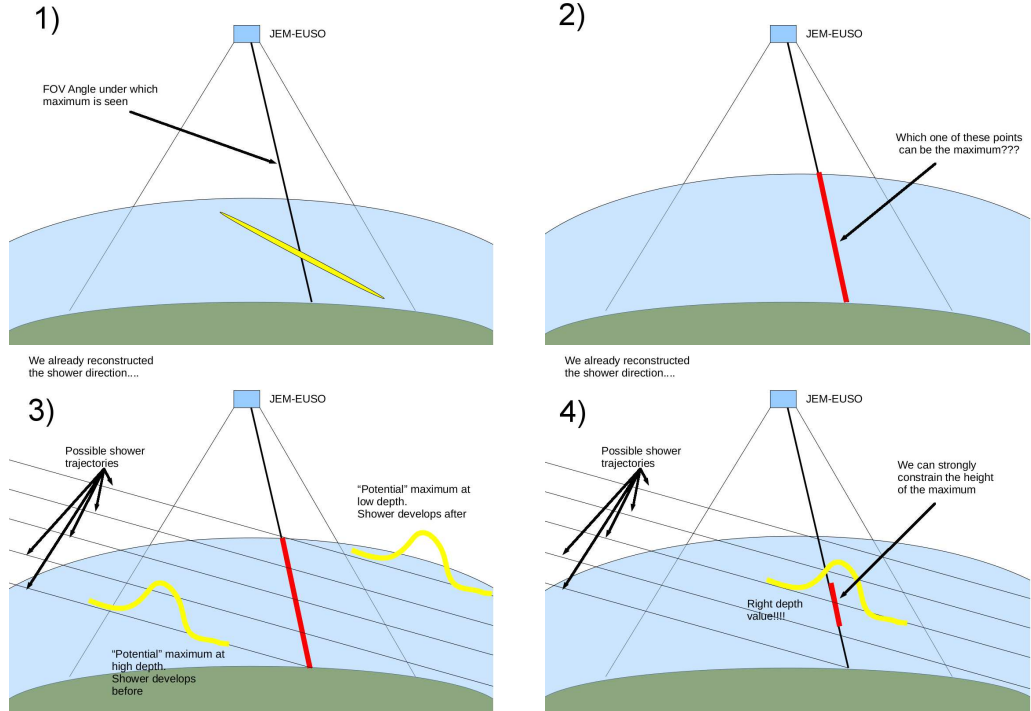


Figure 5.4:  $X_{GEO}^{max}$  approximation altitude determination method. **Upper-left panel:** a shower is represented whereas just the maximum is identified. The maximum cannot be identified a priori within the red line of the upper right panel. **Bottom-left panel:** the assumption of a reconstructed direction and of a profile is made. **Upper-right panel:** the most likely range in  $X_{max}$  is used to constrain the range for  $H_{max}$ . **Bottom-right panel:** the best guess for such a range is identified.

Once the tridimensional position of the maximum has been determined the position of the shower for each time can be derived and an estimation of the slant depth for each step of the shower can be also calculated. We use the atmospheric profile together with the reconstructed shower's direction and position to integrate the atmospheric density till the top of the atmosphere. The shower age is also calculated from the the maximum depth.

The knowledge of the position and of the age of a shower allows the estimate of the energy distribution of the secondary electrons. The used parameterization is the one developed by Giller [173], extensively described in Chap. 3. Such a distribution is used to estimate the fluorescence and Cherenkov yields, and the relative the scattering and absorption.

Eventually the shower's luminosity is obtained and the modeling of the atmospheric transmission can be applied. In this study the standard *lowtran* software has been chosen.

At the end of this process the curve of photons at the shower location

for each time is reconstructed. Unfortunately no distinction is possible on whether the reconstructed photons are fluorescence or Cherenkov. In fact the two components result to be entangled since the knowledge of the number of electrons is necessary in order to estimate the production of Cherenkov photons. On the other hand the number of electrons can be estimated only if the Cherenkov contamination is known. To this aim an iterative process has been developed.

No Cherenkov contamination is assumed at the first shower step. The shower luminosity together with the Nagano's fluorescence yield will therefore deliver an electron number associated to the first step. Such electrons will produce a certain amount of photons distributed like shown in Chap 3. This component is transmitted to the second step. The produced Cherenkov will suffer of absorption and scattering. The scattered fraction is assigned as contamination to the following step. In this treatment also ozone absorption will be taken into account. The surviving component (neither scattered nor absorbed) goes to the next step. The corrected photon number is used together with the fluorescence yield to obtain the number of electrons of the next step. The process is repeated iteratively till the last step of the shower.

The result is the shower's electron curve. Such a curve can be fitted by a shower function in order to obtain the energy and  $X_{max}$  parameters. The chosen function is again the so called GIL function (see Chapt. 3) but any other function is equally applicable. The fit parameters of such a function are simply the energy and the  $X_{max}$  but a width oscillation parameter might also be included. The fit procedure will converge on a particular set of values.

A syntetic way of describing the process of Fig. 5.2 is shown in Eq. 5.3.

$$\begin{aligned} \frac{dN_{pe}}{dL} = \int_{\lambda_{min}}^{\lambda_{min}} & \left\{ N_e \left( X(L), X_{max}, E \right) \epsilon_{FY}^\lambda \left( H(L), s(L) \right) \frac{1}{4\pi} \right. \\ & + \Psi_{CH}(\lambda, \vec{P}(L)) \left. \right\} \frac{A_{opt} \cos \theta}{R^2} T_s \left( \lambda, \vec{P}(L), \vec{D} \right) \\ & \cdot T_a \left( \lambda, \vec{P}(L), \vec{D} \right) \epsilon_{opt} \left( \lambda, \theta, \pi \right) T_{BG3} \left( \lambda \right) \epsilon_{PMT} \left( \lambda \right) \epsilon_{FED} d\lambda \end{aligned} \quad (5.3)$$

The present equation shows the amount of counts detected by JEM-EUSO for every element  $dL$  of shower development. First of all, this number depends on the number of electrons in the shower  $N_e \left( X(L), X_{max}, E \right)$  which on its own is parameterized as function of the energy  $E$ , of the slant depth of the maximum and of the single step. Another fundamental factor is the  $\epsilon_{FY}^\lambda \left( H(L), s(L) \right)$  or the so called fluorescence yield (in differential notation)

which depends both on altitude and on shower age. The dimension of the entrance pupil of the detector is expressed by the area  $A_{opt}$  which includes also a  $\cos(\theta)$  factor for taking into account the arrival direction of the photons. The efficiency of the detector is taken into account with the  $\epsilon_{opt}(\lambda, \theta, \pi)$ ,  $\epsilon_{PMT}(\lambda)$ ,  $\epsilon_{FE}$  and  $T_{BG3}(\lambda)$  which respectively represent the throughput efficiency of the optics, the detector efficiency of the PMT, the losses of the front end electronics and the transmittance of the optical adaptor. Finally the Rayleigh and ozone absorption are taken into account with the parameters  $T_s(\lambda, \vec{P}(L), \vec{D})$  and  $T_a(\lambda, \vec{P}(L), \vec{D})$  which depend on wavelength, shower and detector position.

A separate treatment is however needed for the Cherenkov contamination  $\Psi_{CH}(\lambda, \vec{P}(L))$ . In Eq. 5.4 the additional counts component due to Cherenkov for each shower step is given.

$$\begin{aligned} \Psi_{CH}(\lambda, \vec{P}(L)) = \int_0^L \left[ N_e(X(l), X_{max}, E) \epsilon_{CH}^\lambda(H(l), s(l)) \right. \\ \left. \cdot T_s(\lambda, \vec{P}(l), \vec{P}(L)) T_a(\lambda, \vec{P}(l), \vec{P}(L)) \right] dl \quad (5.4) \\ \cdot \left( -\dot{T}_s(\lambda, \vec{P}(L)) dl \right) \alpha_{anys} \end{aligned}$$

Here the number of electrons for each of the past steps of a shower  $N_e(X(l), X_{max}, E)$  must be considered together with the differential Cherenkov yield  $\epsilon_{CH}^\lambda(H(l), s(l))$ . For each of the  $dl$  elements the produced photons must be carried till the  $L$  point. Such a transmittance will be affected by losses  $T_s(\lambda, \vec{P}(l), \vec{P}(L)) T_a(\lambda, \vec{P}(l), \vec{P}(L))$  respectively for scattering and ozone absorption. The derivative of the the scattered fraction  $(-\dot{T}_s(\lambda, \vec{P}(L)))$  calculated at the  $L$  position multiplied by the differential  $dl$  tells how much of the transmitted light is scattered in the interval  $dl$ . As last point it must be kept in mind that the Rayleigh scattering is not isotropic and therefore a component  $\alpha_{anys}$  must account for the asymmetry of the scattered photons.

## 5.2 Procedure systematics

An essential step of the reconstruction procedure and a central part of this thesis has been the evaluation of the uncertainties involved in the aforemen-

tioned steps. All the models used to describe the process from step to step must be therefore confronted with Monte Carlo simulations, assumed to be (for the moment) the "truth".

The approach which has been followed evaluates the deviation of the modeled system from the simulated one. In Fig. 5.5 a schematic representation of the process is shown.

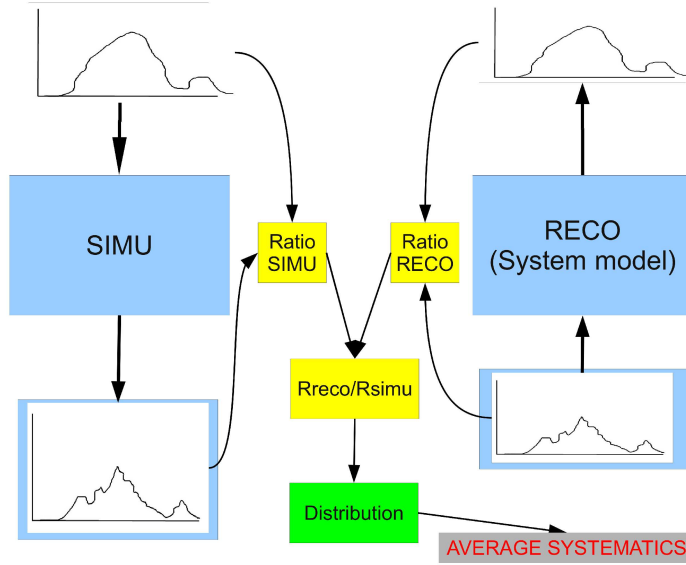


Figure 5.5: the logic of the systematic estimation algorithm. A generic step is depicted. The ratio between input and output will be calculated for both reconstruction and simulation. The discrepancy of each reconstructed step from the simulated will be estimated for each event. The median on the distribution of the deviations will be defined as systematics (see gray box).

For each step of the simulation process the ratio between input and output curve must be calculated for all the times.

$$\epsilon_{sim}(t, evt) = \frac{N_{sim}^{out}(t, evt)}{N_{sim}^{in}(t, evt)} \quad (5.5)$$

$$\epsilon_{reco}(t, evt) = \frac{N_{reco}^{in}(t, evt)}{N_{reco}^{out}(t, evt)} \quad (5.6)$$

The ratios of Eq. 5.5 and 5.6 are then used for the calculation of 5.7

$$\Delta^k(evt) = \frac{\sum_{t=0}^{t_{max}} \frac{\epsilon_{reco}(t, evt)}{\epsilon_{sim}(t, evt)}}{t_{max}} \quad (5.7)$$

This parameter is expression of the deviation of the model from the "truth". The distribution of such a parameter over a large number of events will be calculated. The median of the distribution

$$\mu_{\frac{1}{2}}(\Delta^k(evt)) \quad (5.8)$$

quantifies the quality of the model in a particular experimental condition  $k$ . However, the systematics might change depending on the experimental conditions. For this reason the same assessment must be repeated by changing the relevant simulation parameters. In the present work the systematics are estimated for all the relevant reconstruction steps and for several zenith angles ( $\theta$ ), energies and position in FOV. Moreover, the impact of neglecting the Cherenkov correction has been estimated together with the impact of the clustering and of the geometrical reconstruction. Several tables have been produced accounting for all the conditions. This information will allow the application of a correction factor to every event according to inclination, energy and position. However, the non application of such correction on a single event basis will translate to an uncertainty on the simulated sample which can be defined as systematic. Therefore the average over all the conditions gives the average shift while the RMS will give the variation of such a factor inside the analyzed sample. Extremely important is to remember that given the non uniform event distribution depending on the various simulation parameters a weighted average and RMS must be calculated.

$$\frac{\sum_k \alpha^k \cdot \mu_{\frac{1}{2}}(\Delta^k)}{\sum_k \alpha^k} \quad (5.9)$$

The  $\alpha^k$  factor will therefore express the frequency of the  $k^{th}$  condition in the sample. Such an average must be calculated separately for each different event selection. For example, each of the cuts described in Chap. 4 will be associated to a different systematic.

More in detail in Tab. 5.1 the systematics of the reconstruction algorithm have been estimated for the most simple case. Samples of showers of different inclinations and of energy  $10^{20}$  eV have been simulated in the vicinity of the center of FOV. To avoid confusion the backscattered Cherenkov has been temporarily removed. Moreover this table is produced just considering all those pixels-GTU where signal is present<sup>2</sup>. The geometry of the shower has been forced to be the same as the simulated one. In the second column (Cts)

---

<sup>2</sup>Which does not mean just signal but pixel-GTUs with signal. This is the so-called ESAF debug mode.



Zenith (deg)	Cts	Det	Opt	Trans	FY	Prod	Erec Ratio
30	1.01	0.95	1.18	0.96	0.99	0.95	0.95
40	1.01	0.95	1.18	0.97	0.99	0.94	0.96
45	1.01	0.94	1.18	0.97	0.99	0.95	0.96
50	1.02	0.93	1.18	0.98	0.99	0.96	0.95
60	1.02	0.93	1.18	0.98	0.99	0.96	0.94
70	1.02	0.94	1.18	0.99	0.99	0.94	0.92
80	1.01	0.96	1.15	1.01	1	0.9	0.92

Table 5.1: the systematic uncertainty for several samples of events. The chosen energy  $10^{20}$  eV, the events are impacting in the square ( $\pm 20, \pm 20$ ) km and the  $\phi$  angle has been chosen from 0 to 360 degrees. No backscattered Cherenkov has been simulated and the so called debug mode is used. In order from left to right the columns represent: the event zenith angle ( $\theta$ ), the deviation of the reconstructed from the simulated counts, the deviation of the focal surface correction, of the optics, the transmittance and the fluorescence yield. Under "Prod" the product of the various factor as shown in the text is shown. The last column represents the median on the energy distribution.

is shown the median over all the events of the average ratio distribution

$$\Delta^k(evt) = \frac{\sum_{t=0}^{t_{max}} \frac{counts_{reco}(t,evt)}{counts_{sim}(t,evt)}}{t_{max}} \quad (5.10)$$

As a matter of fact, even considering just pixel-GTUs with signal a systematic of 1–2% is obtained. Reason of such a shift might be a non optimal background correction which has been applied to reconstructed counts curve. The following columns represent the systematic effects calculated according to Eq. 5.5 to 5.8 on the focal surface (Det), optics (Opt), atmospheric transmission (Trans) and fluorescence yield (FY). The seventh column (Prod) defined as in Eq. 5.11 represents the product between all the previously mentioned factors.

$$Prod = Cts \cdot Det^{-1} \cdot Opt^{-1} \cdot Trans^{-1} \cdot FY^{-1} \quad (5.11)$$

The Prod factor expresses the relative shift of the reconstructed energy (plotted in the last column as Erec ratio). This correction is applied to the denominator to obtain the curves from detector to shower.

To maximize the statistical quality of the reconstructed parameters, a  $\chi_{red}^2 < 1$  cut has been introduced. The median on the reconstructed energy distribution has been calculated and reported in the last column.

Non negligible systematic shifts affect each reconstruction step. Such systematics however do not significantly change with the angle and therefore

a single correction factor can be applied. The overall systematic shift is around 0.95 for almost all the conditions. The good agreement between Prod and Erec Ratio shows that the systematics on the energy parameter are under control. The systematics on the optics, on the detector and on the transmittance are most likely due to a mismatch between simulated and reconstructed photons spectra.

Zenith (deg)	Cts	Det	Opt	Trans	FY	Prod	Erec Ratio
30	1.01	0.95	1.18	0.97	0.99	0.94	1.27
40	1.01	0.94	1.18	0.97	0.99	0.95	1.25
45	1.01	0.95	1.18	0.97	0.99	0.94	1.2
50	1.01	0.95	1.18	0.98	0.99	0.93	1.19
60	1.02	0.95	1.18	0.98	1	0.93	1.1
70	1.03	0.95	1.19	0.99	0.99	0.93	1.01
80	1.01	0.96	1.15	1.01	0.99	0.91	0.97

Table 5.2: the systematic uncertainty for several samples of events. The chosen energy  $10^{20}$  eV, the events are impacting in the square  $(\pm 20, \pm 20)$  km and the  $\phi$  angle has been chosen from 0 to 360 degrees. The backscattered Cherenkov has been simulated but not corrected. The so called debug mode is used. In order from left to right the columns represent: the event zenith angle ( $\theta$ ), the deviation of the reconstructed from the simulated counts, the deviation of the focal surface correction, of the optics, the transmittance and the fluorescence yield. Under "Prod" the product of the various factor as shown in the text is shown. The last column represents the median on the energy distribution.

Tab. 5.2 is produced in the same conditions as Tab. 5.1. However in this table the backscattered Cherenkov has been simulated but not corrected. The systematics on the single reconstruction steps must be assessed again since the simulated spectra is different with respect to the case of Tab. 5.1. The response of optics, focal surface and the transmittance might be affected by the different spectrum. However, all the factors do not change dramatically from the pure fluorescence case. A significant difference arises however between the two last columns. Such a difference can amount up to  $\sim 30\%$  for vertical and  $\sim 5 - 6\%$  for horizontal showers. Such a discrepancy is clearly due to the neglect of the Cherenkov correction in this study. The non symmetric nature of Rayleigh scattering makes the fraction of light contamination reaching JEM-EUSO larger for vertical showers than for horizontal.

The same study applied on the FOV position implies however a larger variation of the systematics. In both Tab. 5.4 and 5.3 several sets of shower have been simulated in different positions of the FOV. More in detail the average X and Y coordinates of the impact point are reported. All the events have energy of  $10^{20}$  eV and a zenith angle ( $\theta$ ) of 60 degrees. As can be seen

Posit (km)	Cts	Det	Opt	Trans	FY	Prod	Erec Ratio
(0,0)	1.02	0.93	1.18	0.98	0.99	0.96	0.94
(50,50)	1.03	0.93	1.16	1	0.99	0.96	0.96
(100,0)	1.03	0.92	1.13	1.01	0.99	0.96	0.95
(0,100)	1.03	0.92	1.13	1.01	0.99	0.97	0.97
(100,100)	1.03	0.92	1.09	1.04	1	0.99	0.99
(150,0)	1.03	0.9	1.14	1.04	1	0.97	0.98
(150,100)	1.03	0.91	1.05	1.07	0.99	1.01	1.02
(200,0)	1.04	0.9	1.07	1.09	0.99	0.96	0.98
(200,50)	1.03	0.88	1.11	1.08	1.01	0.97	0.96

Table 5.3: the systematic uncertainty for several samples of events. The chosen energy  $10^{20}$  eV, the events are simulated with a zenith angle ( $\theta$ ) of 60 degrees, the  $\phi$  angle has been chosen from 0 to 360 degrees. The backscattered Cherenkov has not been simulated. The so called debug mode is used. In order from left to right the columns represent: the average impact point, the deviation of the reconstructed from the simulated counts, the deviation of the focal surface correction, of the optics, the transmittance and the fluorescence yield. Under "Prod" the product of the various factor as shown in the text is shown. The last column represents the median on the energy distribution.

already at the counts level an excess in the reconstructed curve up to 4% can be expected. Focal surface and optics correction variate respectively in the range 0.88–0.93 and 1.05–1.18 which correspond to 6 and 11% systematic variation. The transmittance will also variate in the range 0.98–1.08 with a relative variation of 10%. Unlike in the previous case the application of a single correction factor is here more difficult given the wider variation span. Again as in the previous cases a good agreement can be found between the last two columns showing an acceptable understanding of the systematics.

The introduction of backscattered Cherenkov in Tab. 5.4 does not dramatically change the general trends of Tab. 5.3 apart again in the last two columns. More in detail it can be seen how the deviation on the focal surface factor seem to decrease by 2–3% in the central part of the field of view and to remain almost unvariated in the outer part. For this reason the variation in the FOV of the focal surface correction factor amount here to  $\sim 8\%$ . The energy overestimation due to the neglect of the Cherenkov component remains over the entire sample  $\sim 18\%$  with respect to the one calculated in Tab. 5.4.

The non linear response of the detector depending on the shower's luminosity has been estimated. In Tab. 5.5 several samples of showers having different energies have been simulated. The zenith angle ( $\theta$ ) angle is 60 degrees and the impact point is near the center of the FOV. As it can be seen,

CHAPTER 5. THE ENERGY AND  $X_{MAX}$  RECONSTRUCTION  
ALGORITHMS

Posit (km)	Cts	Det	Opt	Trans	FY	Prod	Erec Ratio
(0,0)	1.02	0.95	1.18	0.98	1	0.93	1.1
(50,50)	1.01	0.95	1.17	1	1	0.91	1.11
(100,0)	1.02	0.94	1.14	1.01	1	0.94	1.14
(0,100)	1.02	0.94	1.15	1.01	1	0.93	1.12
(100,100)	1.03	0.93	1.09	1.04	1	0.98	1.15
(150,0)	1.02	0.92	1.09	1.04	0.99	0.99	1.18
(150,100)	1.03	0.91	1.06	1.07	0.99	1.01	1.17
(200,0)	1.03	0.89	1.08	1.1	0.99	0.98	1.13
(200,50)	1.03	0.88	1.12	1.1	1.01	0.94	1.11

Table 5.4: the systematic uncertainty for several samples of events. The chosen energy is  $10^{20}$ eV, the events are simulated with a zenith angle ( $\theta$ ) of 60 degrees and the  $\phi$  angle has been chosen from 0 to 360 degrees. The backscattered Cherenkov has been simulated but not corrected. The so called debug mode is used. In order from left to right the columns represent: the average impact point, the deviation of the reconstructed from the simulated counts, the deviation of the focal surface correction, of the optics, the transmittance and the fluorescence yield. Under "Prod" the product of the various factor as shown in the text is shown. The last column represents the median on the energy distribution.

there seem to be a strong variation depending on the primary energy in the focal surface correction. Such a fact is most likely due to the neglect in the reconstruction procedure of nonlinear effects in the phototube. For this reason the true efficiency tends to decline with the increasing energy while the reconstructed remains constant. The ratio will therefore increase with the energy. The variation between the extremes amounts to  $\sim 25\%$ . The deviation in the counts curves (Cts) seem to be reducing with the increasing energy. In fact the higher luminosity improves the signal to noise ratio and therefore the error in the background correction is minimized for the highest energy showers. All the other factors do not change significantly apart the last two columns where a mismatch between Prod and the energy column is observed. In fact for energy  $E > 2 \cdot 10^{20}$  eV the median of the reconstructed energy tends to drop strongly than the simple product of the systematics. The reason for this is not yet understood. Most likely some kind of systematic in the fitting procedure could be present. A further verification can be done on the non linear effects involved in showers with backscattering Cherenkov. As it can be seen in Tab. 5.6 the focal surface correction factor seems to increase faster than in the Cherenkov free curve. Another difference is again in the systematics between the last two columns. Such a systematic decreases with the energy.

A further aspect to consider is related to the impact of the signal selection

Energy (eV)	Cts	Det	Opt	Trans	FY	Prod	Erec Ratio
$2 \cdot 10^{19}$	1.07	0.85	1.2	0.93	0.99	1.14	1.12
$4 \cdot 10^{19}$	1.03	0.91	1.18	0.97	0.99	1	0.96
$6 \cdot 10^{19}$	1.03	0.93	1.18	0.97	0.99	0.98	0.95
$8 \cdot 10^{19}$	1.02	0.93	1.18	0.98	0.99	0.96	0.94
$10^{20}$	1.02	0.93	1.18	0.98	0.99	0.96	0.94
$2 \cdot 10^{20}$	1.02	0.96	1.17	0.98	0.99	0.94	0.89
$4 \cdot 10^{20}$	1.02	1.02	1.17	0.98	0.99	0.88	0.79
$6 \cdot 10^{20}$	1.01	1.08	1.17	0.98	0.99	0.82	0.71

Table 5.5: the systematic uncertainty for several samples of events. The events are simulated with a zenith angle ( $\theta$ ) of 60 degrees and are impacting in the square ( $\pm 20, \pm 20$ ) km. The  $\phi$  angle has been chosen from 0 to 360 degrees. The backscattered Cherenkov has not been simulated. The so called debug mode is used. In order from left to right the columns represent: the simulated energy, the deviation of the reconstructed from the simulated counts, the deviation of the focal surface correction, of the optics, the transmittance and the fluorescence yield. Under "Prod" the product of the various factor as shown in the text is shown. The last column represents the median on the energy distribution.

on the energy parameter. A preliminary way to assess the impact of such an algorithm is the evaluation of the reconstructed energy in the clustering mode with respect to the debug mode. Several samples of events with simulated but not corrected Cherenkov have been simulated and shown in Tabs 5.7, 5.8 and 5.9. The median of the reconstructed energy for different conditions has been shown. To notice is the lower energy ratio which can be observed in all the tables with respect to Tab. 5.2, 5.6 and 5.4 respectively. Such tables represent the simulation in analogous conditions but in debug mode. This is clearly understandable since the loss in the collected signal is affecting the reconstructed energy.

The impact of the geometrical uncertainty on the reconstructed energy has been eventually estimated. To give a preliminary assessment of the systematics the deviation of the energy parameter with respect to the events with simulated backscattered Cherenkov, active *PWISE* but real geometry has been calculated. The factors on the second column of Tab. 5.10 and 5.11 represent the ratio

$$\Delta E = \frac{E_{reco}^{VAR}}{E_{reco}^{FIX}} \quad (5.12)$$

Where  $E_{reco}^{FIX}$  represent the reconstructed energy in the fixed geometry case and  $E_{reco}^{VAR}$  the energy with variable geometry. A sample of  $10^{20}$  eV, 60 degrees events has been simulated in the center of the FOV. The Cherenkov

CHAPTER 5. THE ENERGY AND  $X_{MAX}$  RECONSTRUCTION  
ALGORITHMS

Energy (eV)	Cts	Det	Opt	Trans	FY	Prod	Erec Ratio
$2 \cdot 10^{19}$	1.08	0.86	1.19	0.96	1	1.1	1.21
$4 \cdot 10^{19}$	1.04	0.92	1.19	0.98	1	0.97	1.12
$6 \cdot 10^{19}$	1.02	0.94	1.19	0.98	1	0.93	1.12
$8 \cdot 10^{19}$	1.02	0.95	1.19	0.98	1	0.92	1.12
$10^{20}$	1.01	0.96	1.18	0.98	1	0.91	1.12
$4 \cdot 10^{20}$	1.01	1.08	1.17	0.98	0.99	0.82	0.84
$6 \cdot 10^{20}$	1.01	1.07	1.17	0.98	0.99	0.83	0.87

Table 5.6: the systematic uncertainty for several samples of events. The events are simulated with a zenith angle ( $\theta$ ) of 60 degrees and are impacting in the square ( $\pm 20, \pm 20$ ) km. The  $\phi$  angle has been chosen from 0 to 360 degrees. The backscattered Cherenkov has been simulated but not corrected. The so called debug mode is used. In order from left to right the columns represent: the simulated energy, the deviation of the reconstructed from the simulated counts, the deviation of the focal surface correction, of the optics, the transmittance and the fluorescence yield. Under "Prod" the product of the various factor as shown in the text is shown. The last column represents the median on the energy distribution.

Zenith (deg)	Ereco Ratio
30	1.16
45	1.11
60	0.99
70	0.91

Table 5.7: the systematic uncertainty originated by the collection inefficiency. The events are  $10^{20}$  eV and impacting in the square ( $\pm 20, \pm 20$ ) km. The backscattered Cherenkov has been simulated but not corrected. The median on the energy distribution can be seen.

backscattering and the *PWISE* algorithm have been included. The reconstructed geometry has been modified in a controlled way to asses the impact on the final energy value with respect to the case with fixed geometry. The basic parameters which have been changed are the altitude of the maximum and the zenith angle ( $\theta$ ). In Tab. 5.10 after fixing the arrival direction the altitude has been changed. In Tab. 5.11 the maximum has been fixed and the zenith angle ( $\theta$ ) has been varied. The increase in the reconstructed altitude causes a decrease in the reconstructed energy. On the opposite a "deeper" shower results in a higher energy shower. This is a direct consequence of the larger absorption of light from the lower layers of the atmosphere. In a similar way can be interpreted the results of Tab. 5.11. In fact an increase in the zenith angle corresponds to a higher shower. A

Energy (eV)	Ereco Ratio
$4 \cdot 10^{19}$	1.02
$6 \cdot 10^{19}$	0.99
$8 \cdot 10^{19}$	1
$10^{20}$	0.99
$2 \cdot 10^{20}$	0.93
$4 \cdot 10^{20}$	0.78
$6 \cdot 10^{20}$	1

Table 5.8: the systematic uncertainty originated by the collection inefficiency. The events are 60 degrees and impacting in the square ( $\pm 20, \pm 20$ ) km. The backscattered Cherenkov has been simulated but not corrected. The median on the energy distribution can be seen.

Pos FOV (km)	Ereco Ratio
(0,0)	0.99
(50,50)	1
(0,100)	1.01
(200,0)	1

Table 5.9: the systematic uncertainty originated by the collection inefficiency. The events are 60 degrees and  $10^{20}$  eV The backscattered Cherenkov has been simulated but not corrected. The median on the energy distribution can be seen.

more vertical shower is on the other hand deeper. The reconstructed energy is smaller for the more horizontal while larger for the more vertical shower.

A key feature of the JEM–EUSO mission is the capability to identify the primary type. As already explained the fundamental parameter for this purpose is the so called  $X_{max}$ . The discussion on the capability to determine the average mass of the population is left to the next chapter. The sources of systematics on  $X_{max}$  are analyzed here. The  $X_{max}$  reconstruction algorithms developed in the context of this work are essentially the slant depth and the Cherenkov method. In the first case the altitude of the maximum is reconstructed according to a parameterization of the assumed  $X_{max}^{GEO}$  given a reconstructed direction. The reconstructed  $X_{max}^{FIT}$  used in the following studies is the one resulting from the fit on the electrons curve. Potential systematics arise in the reconstructed direction or in the  $X_{max}^{GEO}$  parameterization. In Tab. 5.12 the systematics on X and Y maximum position  $H_{max}$ , the averaged  $X_{max}^{GEO}$  and the fitted  $X_{max}^{FIT}$  are shown. These parameters have been calculated both assuming the true and the reconstructed direction for several samples of showers of different zenith angle, energies of  $10^{20}$  eV and impact

$\Delta h$ (km)	variation E
+2	0.92
+1	0.96
+0.5	0.97
-0.5	1.01
-1	1.02
-2	1.03

Table 5.10: the systematic uncertainty originated by the  $H_{max}$  resolution. All the events have been chosen of  $10^{20}$  eV energy, 60 degrees zenith angle, 0–360 degrees  $\phi$  and impact point is chosen in the interval  $(\pm 20, \pm 20)$  km. Backscattered Cherenkov has been included and *PWISE* selection is activated. The first column represents the variation of the reconstructed  $H_{max}$  with respect to the simulated one. The second column represents the variation of the energy value with respect to the events real geometry.

point near the center the FOV. As can be seen the X,Y geometry seem to be on average properly reconstructed. This aspect requires however a deeper study since no guarantee is given that systematic effects are not present on each  $\phi$  direction. The average over the  $2\pi$  angle could compensate such a systematic making it not visible in a  $0-2\pi$  sample. However within this study it could be confirmed that the sigma on the maxima X and Y distributions are significantly smaller than 1 km.  $X_{max}^{GEO}$  is slightly overestimated. This parameter has been set according to the GIL parameterization and averaged over the interval  $10^{19}-10^{21}$  eV, to cover a wide range of shower's energies. Under all the conditions  $X_{max}^{GEO}$  is slightly overestimated and consequently a lower shower maximum is reconstructed. Assuming the arrival direction to be the same as the real one imposes therefore a systematically lower maximum altitude  $H_{max}$ . This feature appears also in the case of reconstructed geometry although a small difference in  $X_{max}^{GEO}$  is observed. Such a difference is not clearly understood and still under investigation. However it must be noted how such a difference amounts to  $\sim 10$  g/cm<sup>2</sup> while the maximum depth traveled in 1 GTU is  $\sim 75$  g/cm<sup>2</sup>. This discrepancy is therefore small. Finally it can be seen how the fitted  $X_{max}^{FIT}$  tends to converge toward higher depths both for real and reconstructed direction. There is a good agreement between the real and reconstructed direction cases apart in the 45 degrees case. The reason for this discrepancy is not understood yet.

In the Cherenkov method the timing information is used for the calculation of the distance between the impact point and the maximum. Such a method has the advantage of being free from any previous assumption on the maximum slant depth. For this purpose a Cherenkov peak and a maximum



$\Delta \theta$ (deg)	variation E
+10	0.92
+5	0.95
+2	0.97
-2	1.01
-5	1.04
-10	1.07

Table 5.11: the systematic uncertainty originated by the  $\theta$  resolution. All the events have been chosen of  $10^{20}$  eV energy, 60 degrees zenith angle ( $\theta$ ), 0–360 degrees  $\phi$  and impact point is chosen in the interval  $(\pm 20, \pm 20)$  km. Backscattered Cherenkov has been included and *PWISE* selection is activated. The first column represents the variation of the reconstructed  $\theta$  with respect to the simulated one. The second column represents the variation of the energy value with respect to the events with real geometry.

must be identified in the counts curve. The timing difference taking into account the time of flight of the photons is used to calculate the geometrical distance between the maximum and the impact point. Knowing the position of Cherenkov mark and the angular position of the maximum, the position of the maximum can be calculated and consequently can be the  $X_{max}$ . The systematics analysis is in this case significantly more difficult than in the  $X_{max}$  case. First, the angular position of the Cherenkov mark and of the maximum are not free of uncertainty. Moreover the timing of the two peaks is also affecting the relative distance calculation. The parameters to evaluate are the timing of maximum, of Cherenkov and their relative separation. In the first column of Tab. 5.13 the difference in GTUs of the reconstructed maximum and the arrival time of photons from the shower maximum is reported. The reconstructed maximum is slightly anticipated with respect to the arrival time of the real maximum photons. The Cherenkov peak seems to be not affected by such systematics. The combination of the two factors makes the reconstructed time difference between Cherenkov and maximum to be slightly larger than the real one (see third column of Tab. 5.13). Worth to notice is the much stronger systematics measured for angles above 50 degrees.

In Tab. 5.14 several other key parameters are reported. In the first two columns the average X and Y position both for maximum and Cherenkov are shown. The estimated distance between maximum and Cherenkov mark  $l_{Cher-Max}$  seems to be underestimated. This might not be in contradiction with the previous table where the maximum–Cherenkov timing difference was overestimated. This is because the Cherenkov–maximum time separation at the detector results from the time of flight of both shower and photons. In

CHAPTER 5. THE ENERGY AND  $X_{MAX}$  RECONSTRUCTION  
ALGORITHMS

Zenith (Deg)	(X,Y) (km)	$H_{max}$ (km) fixed dir	$H_{max}$ (km) free par	$X_{max}^{Geo}$ (g/cm <sup>2</sup> ) fixed dir	$X_{max}^{Geo}$ (g/cm <sup>2</sup> ) free par	$X_{max}^{FIT}$ (g/cm <sup>2</sup> ) fixed dir	$X_{max}^{FIT}$ (g/cm <sup>2</sup> ) free par
30	(0,0)	-0.23	-0.32	25	25	83	82
45	(0,0)	-0.18	-0.21	20	9.5	46	80
60	(0,0)	-0.19	-0.35	23	16	45	45.9
70	(0,0)	-0.14	-0.29	18	16	31	34

Table 5.12: the  $X_{max}$  systematics study on samples of events having different zenith angle. Events of energy  $10^{20}$  eV, having impact points in the interval  $(\pm 20, \pm 20)$  km and  $\phi$  0–360 degrees have been simulated. The so called  $X_{max}$  method is applied for the geometry reconstruction. In order from left to right can be seen the zenith angle of the events, the average X–Y reconstruction of the maximum, the  $H_{max}$  systematic using the true direction, the  $H_{max}$  systematic using the reconstructed direction, the geometrical  $X_{max}^{GEO}$  using the real and reconstructed direction and finally the  $X_{max}^{FIT}$  with both real and reconstructed angles.

fact, also the inclination of the shower can affect the time of the photons as the track length itself. Clearly a deeper study is needed to understand the reason of such a small discrepancy. A much stronger deviation can be seen for the events above 50 degrees. This fact was suggested also in the previous table where the strongest systematics on the maximum timing were present therefore it seems the Cherenkov method might not be reliable above 50–60 degrees.

The shorter path is typically reflected in a smaller maximum altitude for the vertical showers. Generally, the position of the reconstructed maximum can be considered to be extremely near to the real value. On the other hand the geometrical  $X_{max}^{GEO}$  seems to be slightly underestimated. Such a fact is also not immediately in contradiction with the lower  $H_{max}$  since a more vertical reconstructed inclination could result in a smaller  $X_{max}$ . Another important point is related to the value of the fitted  $X_{max}$ . As it clearly appears also for the Cherenkov method the fit seems to converge toward higher depths making the reconstructed value much more compliant with the simulated one. A last point to notice is how the fraction of detected Cherenkov events drops dramatically above 60 degrees. This is a consequence of the larger surface where the Cherenkov light is distributed at such angles.

Zenith (Deg)	$T_{Max}^{reco} - T_{Max}^{real}$ (GTU)	$T_{Cher}^{reco} - T_{Cher}^{real}$ (GTU)	$T_{Cher}^{reco} - T_{Max}^{reco}$ (GTU)
30	-3	-1	1
35	-2	0	1
40	-3	-1	1
45	-3	0	2
50	-4	-1	2
60	-5	-1	0
70	-6	-3	3

Table 5.13: the timing systematics study on samples of events having different zenith angle. Events of energy  $10^{20}$  eV, having impact points in the interval  $(\pm 20, \pm 20)$  km and  $\phi$  0–360 degrees are simulated. In particular the Cherenkov geometrical reconstruction method is shown here. From left to right are shown the zenith angle of showers, the timing difference between reconstructed maximum and arrival time of photons from the maximum, the timing difference between the reconstructed Cherenkov peak and the arrival time of Cherenkov bump photons. The final column represents the difference in time interval between maximum and Cherenkov for the reconstructed and simulated case.

### 5.3 Iterative procedure

The procedure described in section 5.1 must be seen just as a way to obtain a first guess on the basic shower’s parameters. In fact even if the systematics are corrected the procedure is affected by the statistical uncertainty. An iterative variation of the shower’s parameters to define the best set of parameters response and a confidence interval can improve our estimates. The Cherenkov method has been used here.

In this work two procedures have been developed. The first one aims at the determination of a parameter range where the detector response remains confined within some limited range with respect to the true one. The procedure repeats the entire reconstruction chain however reversed. Such an approach has the advantage of not being affected by the statistical error of the counts curve. In fact, once the basic set of parameters has been assigned, the application of all the correction steps consists just of a series of multiplication factors. The basic parameters will be therefore variated according to fixed intervals and the deviation from the real detector response is measured as:

$$\chi^2 = \frac{1}{N_{tot}} \sum \left( \frac{counts^* - counts^{sim}}{\Delta counts^{sim}} \right)^2 \quad (5.13)$$

whereas  $N_{tot}$  is the total number of GTUs of the real curve with at least 5 counts,  $counts^{sim}$  is the simulated counts curve and  $\Delta counts^{sim}$  the error

CHAPTER 5. THE ENERGY AND  $X_{MAX}$  RECONSTRUCTION  
ALGORITHMS

Zenith (Deg)	(X,Y) Max(km)	(X,Y) Core(km)	Hmax (km)	EffCher (%)	$l_{Cher-Max}$ (km)	XmaxGeo (g/cm <sup>2</sup> )	XmaxFit (g/cm <sup>2</sup> )
30	(0,0)	(0,0)	-0.1	73%	-0.1	-30	-0.5
35	(0,0)	(0,0)	-0.1	78%	-0.18	-35	-7.5
40	(0,0)	(0,0)	-0.07	82%	-0.19	-45	-11
45	(0,0)	(0,0)	0.07	86%	0	-56	-10
50	(0,0)	(0,0)	0.07	79%	-0.1	-48	-6
60	(0,0)	(0,0)	-0.95	19%	-1.9	65	103
70	(0,0)	(0,0)	-2.8	3.2%	-7.7	446	133

Table 5.14: the  $X_{max}$  systematics study on samples of events having different zenith angle. Events of energy  $10^{20}$  eV, having impact points in the interval  $(\pm 20, \pm 20)$  km and  $\phi$  0–360 degrees are simulated. In particular the Cherenkov geometrical reconstruction method is shown here. In order from left to right it is shown the shower’s zenith angle, the average X–Y position of maximum and Cherenkov, the systematics on the  $H_{max}$  parameter, the fraction of events for which a Cherenkov bump has been detected, the systematic on the maximum–Cherenkov distance, the geometrical and fitted  $X_{max}^{GEO}$  and  $X_{max}^{FIT}$ .

associated to it and *counts\** the modeled detector response. For each set of parameters a  $\chi^2$  value is calculated and a  $\chi^2$  map is created. This map is used to identify the set of parameters with the lowest  $\chi^2$  and a range of parameters with a limited deviation from this minimum. The contour where  $\chi^2$  reaches an excess of 1 with respect to the minimum is considered from statistical arguments to be enclosing the true value<sup>3</sup> with a predefined probability.

Another possibility to estimate the statistical uncertainty on the reconstruction is the repetition of the simulation procedure by simulating a large amount of events with the exact reconstructed parameters. Performing the reconstruction in the standard way on each of the newly simulated showers will result in a distribution of the reconstructed parameters whose width will be expression of the statistical uncertainty.

Both the above mentioned iterative processes are shown in Fig. 5.6.

As an example we applied the first procedure to one  $10^{20}$  eV,  $\theta$  60 degrees,  $\phi$  90 degrees event. The impact point has been chosen (20,25) km. The reconstruction procedure has been first applied in a standard way and it delivered an energy of  $9.1 \cdot 10^{19}$  eV and  $X_{max}$  of 788 g/cm<sup>2</sup> (56 g/cm<sup>2</sup> smaller than the real one). In Fig. 5.7 the first reconstruction is depicted as a black star in the central part of the plot. Such value of  $X_{max}$  and energy has then be used for an iterative process where the E and  $X_{max}$  values have been

---

<sup>3</sup>Once systematics have been corrected.

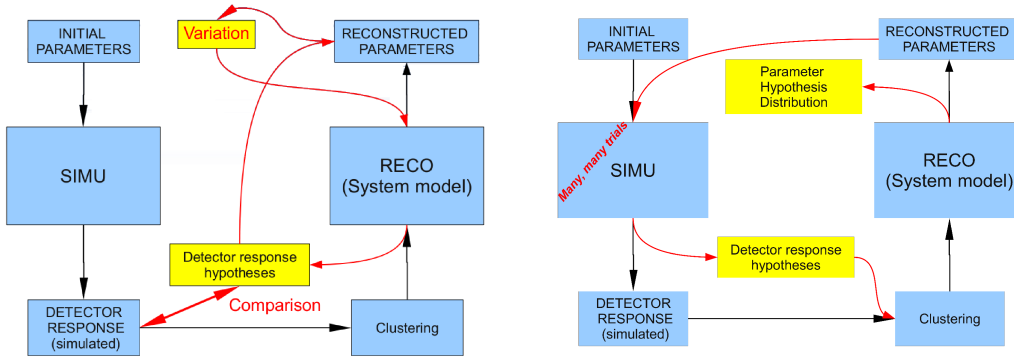


Figure 5.6: **Left panel:** the iterative procedure to constrain a range of parameter space which minimizes the deviation from the measured detector response. **Right panel:** the iterative procedure to evaluate the impact of the statistical uncertainty on the reconstructed parameters.

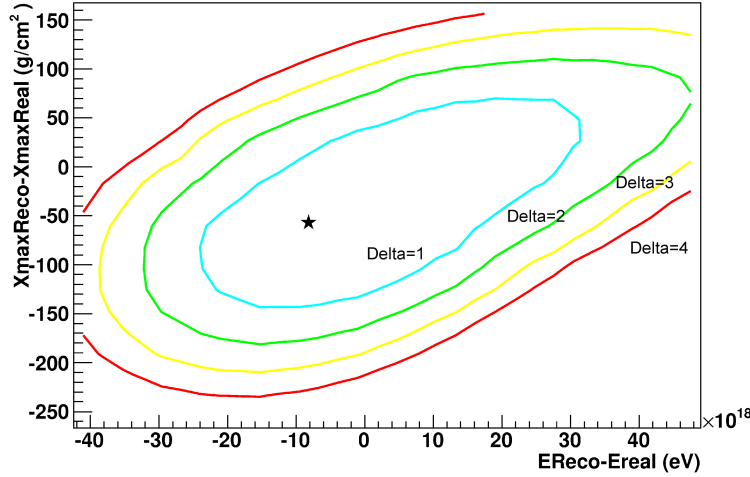


Figure 5.7: the  $\Delta\chi^2$  map for an event having energy  $10^{20}$  eV 45 degrees zenith angle ( $\theta$ ) and 90 degrees  $\phi$ . The star represents the reconstructed energy and  $X_{max}$  parameters and correspond to  $9.1 \cdot 10^{19}$  eV and and  $X_{max}$  of  $788 \text{ g/cm}^2$  ( $-56 \text{ g/cm}^2$ ). All the contours refer to an excess of 1,2,3,4 with respect to the minimum  $\chi^2$  measured in the map.

variated on fixed intervals. The reconstruction procedure has been reversed in order to obtain a test detector response. The  $\chi^2$  has been evaluated on the counts curve as expressed in Eq. 5.13. The contour in Fig. 5.7 represents the regions which delimit the  $\chi^2$  smaller than a certain value. More in detail the cyan curve represents the minimum  $\chi^2 + 1$ , the green  $\chi^2 + 2$ , the yellow  $\chi^2 + 3$  and red  $\chi^2 + 4$ . In order to define a confidence limit both in X and Y the projection of the contours on the axis has been performed. The  $\Delta\chi^2=1$  has

been considered. As explained in Numerical Recipes[181] the 1-dimensional projection of the  $\Delta\chi^2=1$  contour corresponds to the 68.3% of the events. Moreover the  $\Delta\chi^2=4$  (red curves) represent the 95.4% of the events. As can be noticed in this particular case the first reconstruction guess was falling in the  $\Delta\chi^2=1$  interval. Therefore we define as statistical uncertainty on this particular event the projection on the axis of the  $\Delta\chi^2 = 1$  contour. As a result of that the  $(-1.5, +4) \cdot 10^{19}$  eV and  $(-88,127)$  g/cm<sup>2</sup> can be regarded as 68% confidence intervals in energy and  $X_{max}$  for the specifically analyzed event.

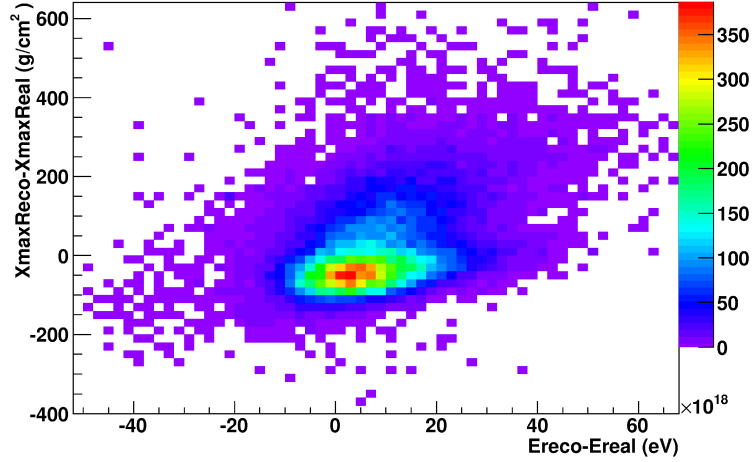


Figure 5.8: the energy and  $X_{max}$  value for a sample of  $\sim 5 \cdot 10^4$  events having exactly the same zenith angle(45 degrees),  $\phi$ , (90 degrees) energy ( $10^{20}$  eV) and  $X_{max}$ . The simulation-reconstruction chain is performed in order to assess the event to event statistical oscillation.

A second possibility which has been explored is the iteration of the simulation and reconstruction of a sample of events having exactly the same parameters. The reconstructed parameters will then give a valid expression of the statistical fluctuations from which every shower is affected. Several events have been simulated fixing the direction of the shower to exactly 45 degrees in  $\theta$  and 90 degrees in  $\phi$ . The energy has been chosen to be  $10^{20}$  eV. Furthermore the first interaction point has been fixed to some reasonably chosen value which automatically translates in a fixed  $X_{max}$ . The event has been repeated on the order of  $4 \cdot 10^4$  times and each reconstructed energy and  $X_{max}$  has been plotted in Fig. 5.8. The finite statistical quality of the counts curve in the end results in a distribution of both the energy and  $X_{max}$ . The projection of the distributions along the X and Y axis is used for the calculation of the  $\sigma$  both in Energy and  $X_{max}$ . In this way the events of

this condition are characterized by a statistical uncertainty of  $\pm 1.2 \cdot 10^{19}$  eV in energy and  $\pm 105$  g/cm<sup>2</sup> in  $X_{max}$ . It must be stressed how such values are not in contradiction. This is because the single event has its own  $\Delta\chi^2$  map since each event is characterized by its own morphology. This must be distinguished by the general statistical uncertainty.

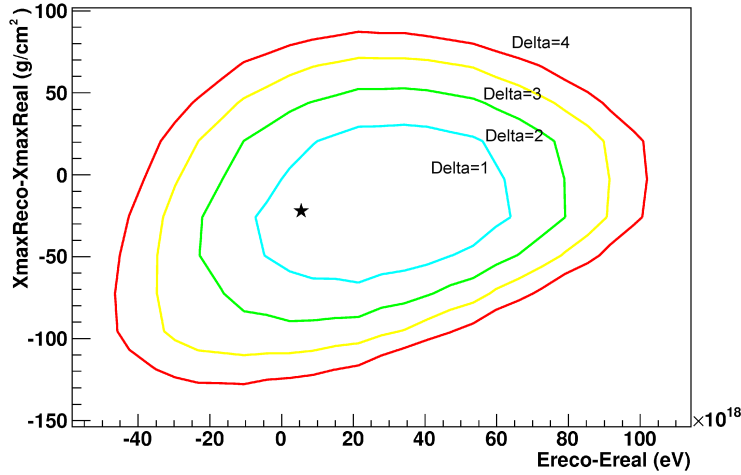


Figure 5.9: the  $\Delta\chi^2$  map for an event having energy  $2 \cdot 10^{20}$  eV 45 degrees zenith angle ( $\theta$ ) and 90 degrees  $\phi$ . The star represents the couple of reconstructed energy and  $X_{max}$  parameters and correspond to  $2.054 \cdot 10^{20}$  eV and  $X_{max}$  of  $844$  g/cm<sup>2</sup> ( $-22$  g/cm<sup>2</sup>). All the contours refer to an excess of 1,2,3,4 with respect to the minimum  $\chi^2$  measured in the map.

As can be seen in Fig. 5.9 and 5.10 other 2 events with energy  $5 \cdot 10^{19}$  and  $2 \cdot 10^{20}$  eV respectively have been simulated and reconstructed according to the previously mentioned  $\Delta\chi^2$  method. The showers are always 45 and 90 degrees in  $\theta$  and  $\phi$  inclined. The position of the impact point in the FOV is the same as seen in the previous examples. The reconstructed energy and  $X_{max}$  for the high energy event are  $2.054 \cdot 10^{20}$  eV and  $844$  g/cm<sup>2</sup> (implying a deviation of  $-22$  g/cm<sup>2</sup> from the real  $X_{max}$ ). The basic parameters for the low energy event are  $5.4 \cdot 10^{19}$  eV and  $835$  g/cm<sup>2</sup> (with a deviation of  $-13$  g/cm<sup>2</sup> from the real value). As can be seen the highest energies are characterized by smaller uncertainties than in the case of low energies. Applying the same procedure previously explained the uncertainties can be defined to be  $(-50, +50)$  g/cm<sup>2</sup> and  $(-1.7, +6.2) \cdot 10^{19}$  eV for the  $2 \cdot 10^{20}$  eV and  $(-239, +426)$  g/cm<sup>2</sup> and  $(-2, +3) \cdot 10^{19}$  eV for the  $5 \cdot 10^{19}$  eV event.

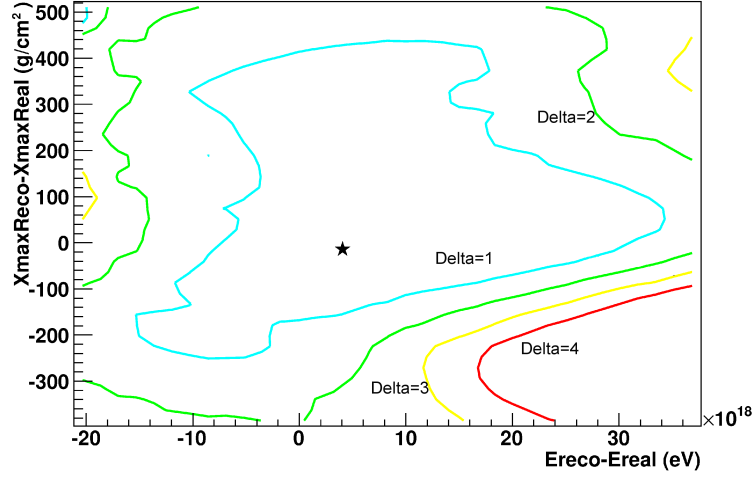


Figure 5.10: the  $\Delta\chi^2$  map for an event having energy  $5 \cdot 10^{19}$  eV 45 degrees zenith angle and 90 degrees  $\phi$ . The star represents the couple of reconstructed energy and  $X_{max}$  parameters and correspond to  $5.4 \cdot 10^{19}$  eV and  $X_{max}$  of 835 g/cm<sup>2</sup> (-22 g/cm<sup>2</sup>). All the contours refer to an excess of 1,2,3,4 with respect to the minimum  $\chi^2$  measured in the map.

## 5.4 Conclusions

The main purpose of this chapter was the description and validation of the *PmtToShowerReco* algorithm. Furthermore the systematics in the reconstruction procedure have been assessed. In most cases systematics are estimated and controlled. In fact, the quite stable and non varying nature of most of the considered factors makes their correction very easy. As a matter of fact, the most dangerous systematics sources are of course the one which are varying in the samples. Moreover, in establishing whether such factors can potentially harm the JEM-EUSO resolution, an evaluation over the controllability of the basic event parameters must be done. In fact, if the parameters can be determined with good resolution, a single event correction can be performed.

The basic shower parameters which affect the reconstruction are the position in the FOV, the energy of the shower, the real direction, the reconstructed altitude and the direction. The position in the FOV can be determined with very good precision and therefore no strong uncontrolled systematic is expected. As it appears in Tab. 5.3 and 5.4 the amplitude of the variation of the factors is limited to maximum 10–12% over a variation of tenth or hundreds of kilometers. The largest variations in the just mentioned tables occur between the center and the external part of the FOV. Over such



a long distances a 10% systematic will correspond to a variation of the order of  $<0.1\%$ /km. Being the JEM–EUSO X–Y resolution of the order of 1 km, all the variations dependent on the position can be neglected and considered as single event correction factors.

The shower inclination can significantly affect the Cherenkov contamination and the transmittance. In fact, Tab. 5.1, 5.2 and 5.11 show how no other significant variation can be observed if the zenith angle ( $\theta$ ) is changing. The Cherenkov contamination can be influenced by the different inclinations due to the anisotropy of the Rayleigh scattering. More in detail the Cherenkov contamination changes roughly by a  $\sim 1\%$  every degree. For this reason assuming a worst case scenario of 5 degrees angular uncertainty it can be expected that a non correction of the Cherenkov might imply a systematic effect up to  $\pm 5\%$ .

The misreconstruction of the shower’s inclination brings a significant source of uncertainty. In fact, as shown in Tab. 5.11 an uncertainty in the reconstructed zenith angle ( $\theta$ ) determines a systematic on the reconstructed energy. Given the 5 degrees worse scenario reconstruction, an estimate of the uncorrectable systematic can be done also here. In this case a rough  $(-5,+4)\%$  uncertainty can be expected as a result of the angular uncertainty.

The energy of the events impacts also in significant way on the procedure given the much wider parameter span. In fact the energy variates over almost two orders of magnitude. The main aspects which are affected by the reconstruction are at the level of background correction, signal selection and focal surface correction. In fact, in Tab. 5.5 and 5.6 the first column changes by 7%. Such a variation is likely due to a small misreconstruction of the background amplitude. Such a fact impacts on the reconstruction at low energies where the signal to noise ratio is worse. For this reason at low energies  $\sim 4 \cdot 10^{19}$  eV assuming a worst case reconstruction of 50% such a correction factor can impact on the energy itself by  $(-2,+4)\%$ . This systematic is even larger at lower energies but negligible at higher where the resolution is expected to be better and the variation is smaller.

The signal selection is also affected by the primary energy. Assuming a 50% energy resolution at  $4 \cdot 10^{19}$  eV this brings at least 2% systematic uncertainty. Applying an interpolation and assuming a 30% resolution at  $10^{20}$  eV the uncertainty can be estimated to be  $\sim 2\%$  also at  $1-2 \cdot 10^{20}$  eV. At the highest energies the systematics will however diminish.

The focal surface signal correction is also energy dependent. As shown in Tab. 5.5 and 5.6 variations up to 25% are observed through the entire energy range. Such an uncertainty is on the contrary of what previously presented particularly strong at the highest energies. This is most likely due to the neglectation within the reconstruction of nonlinear effects of pileup

of the electronics. For this reason, the factor tends to increase toward the higher energies. At the lowest energies an opposite trend seems to be present. A 50% and 30% energy resolution at  $4 \cdot 10^{19}$  and  $10^{20}$  eV converts (after interpolation) into a (-5,+2)% and  $\pm 1\%$  systematic. At higher energies the uncertainty is of the order of  $\sim 1\%$  given the non negligible variation of the focal surface factors and despite the smaller energy resolution.

A key source of systematics in the energy reconstruction is the uncertainty in the maximum altitude. In Tab. 5.10 we see how a misreconstruction in the altitude parameter impacts on the energy parameter. An altitude resolution of the order of  $\pm 1$  km it converts into a systematic uncertainty of (-4,+2)%.

The previous discussion can be therefore resumed in Tab. 5.15 where all the systematic uncertainty components have been reported as shown in the previous paragraphs. It must be again stressed how such systematics include

Source	Systematic %	Systematic % @ $4 \cdot 10^{19}$ eV
Angular (Cher)	$\pm 5\%$	$\pm 5\%$
Angular (Geo)	(-5,4)%	(-5,4)%
Backgr Corr	negligible	(-2,4)%
Sig Select (PWISE)	$\pm 2\%$	$\pm 2\%$
Focal surf Det	$\pm 1\%$	(-5,2)%
Altitude reco	(-4,2)%	(-4,2)%
$\Sigma^2$	(-8,7)%	(-10,8)%

Table 5.15: the different energy systematic sources. The systematics effects have been considered as non controllable. More indetail the Angular (Cher) represents the component originated from the uncertainty on the direction because of the non correction of the cherenkov. Angular (Geo) represents the component originated from the uncertainty on the direction caused by the wrong geometrical reconstruction. Backgr Corr is the uncertainty brought by the background correction. Focal surf Det represent the systematics from the focal surface correction and the last line represents the uncertainty brought by the  $H_{max}$  resolution.

just the uncertainties related to the present reconstruction procedure. Other external sources of systematics are present. As an example the flurescence yield is assumed in literature to be uncertain at the 20% level. Moreover the atmospheric condition can be sampled just with limited precision and therefore the energy value must be considered affected by such an uncertainty.

The  $X_{max}$  is also affected by systematics. The so called  $X_{max}$  method can be affected by the  $H_{max}$  determination which is in turn direct consequence of the reconstructed direction and of the assumed  $X_{max}^{GEO}$ . As shown in Tab. 5.12 both in case of real or reconstructed direction seems to deliever a slightly underestimated maximum altitude. This might be explained by the slightly

overestimated  $X_{max}^{GEO}$ . Finally it can be seen how the final fit tends to converge toward higher values of depth. The final  $X_{max}^{FIT}$  value results to be from 30 to 80 g/cm<sup>2</sup> overestimated. It must be stressed again how the maximal slant depth traversed in 1 GTU cannot exceed the 90 g/cm<sup>2</sup> and therefore the systematics for the mentioned conditions are in the best case of the same order of 1 GTU.

In the case of the Cherenkov method, it seems clear how the systematics are much smaller even though not totally understood. Such a method can be used just below 60 degrees. At the higher inclinations both unacceptably strong systematics and a very low efficiency is present. The method has also the advantage of being open for cross check. In fact, despite the  $X_{max}$  method where the  $X_{max}^{GEO}$  was imposed no assumption is done here on the maximum depth. Therefore beside the  $X_{max}^{FIT}$  also the  $X_{max}^{GEO}$  can be used for confirming the final result. Despite some systematic in the shower timing is found (see Tab. 5.13) it seems that a quite limited  $X_{max}^{GEO}$  systematic appears. As shown in Tab. 5.14, if the angles above 50 degrees are excluded, it clearly appears how the slant depth is slightly underestimated. The fit, also in this case, converges toward higher value but in this case the discrepancy with the true value is reduced to less than 10 g/cm<sup>2</sup>.

The last section of the chapter has been devoted to some demonstration of the method for the assessment of the statistical uncertainty. The definition of statistical uncertainty can be distinguished on single event and population uncertainty. A more extensive study is of course necessary but, in our examples, it can be seen how the 10<sup>20</sup> eV 45 degrees single event is affected by a (-17,+40)% and (-88,127) g/cm<sup>2</sup> uncertainty in energy and  $X_{max}$ . The 2 · 10<sup>20</sup> eV event seems on the other hand to be affected by a (-9,+30)% and ± 50 g/cm<sup>2</sup> in energy and  $X_{max}$ . The 5 · 10<sup>19</sup> eV event is affected by (-39,+55)% and (-240,+430) g/cm<sup>2</sup> uncertainty in energy and  $X_{max}$ . The above mentioned values are referred to specific events and not to the entire population. In fact, such events might be characterized by a peculiar morphology making their uncertainty map very different from the one of the typical event having the same characteristics. However it seems clear how the higher energies are characterized by better statistical uncertainty.

Another more general approach is the one which simulates a large number of events having exactly the same parameters and applies the standard reconstruction on each of them. The limited statistical quality of the signal on the focal surface delivers an oscillation on the reconstructed shower's parameter. In Fig. 5.8 the distribution of ~ 5 · 10<sup>4</sup> events having direction angles of 45 and 90 degrees and 10<sup>20</sup> eV energy is visible. On the entire population the uncertainty is of the order of ±12% and ±105 g/cm<sup>2</sup> in energy and  $X_{max}$  respectively.

It must be however stressed that in order to produce such plots a very large amount of computing time is necessary. In fact for a single event map of the shown quality at least 3 hr/event are necessary. For the large sample the time required amounts to  $\sim 160$  hr/condition. For this reason it is not possible to extend such methods to all the events in the present performance assessment phase. Such methods should be applied on the real event sample given the smaller numbers which will be involved in this phase.

# Chapter 6

## JEM–EUSO Reconstruction Performances

In this chapter we study the methods and the capability to reconstruct the energy and the  $X_{max}$  of events observed by the JEM-EUSO mission. First, we present all the steps to reconstruct a single event. Second, the energy and  $X_{max}$  resolutions are presented for events of predefined position, zenith angle ( $\theta$ ) and energy. In the second part of the study, we assess the energy and  $X_{max}$  reconstruction performances, discussing the cuts that can be applied to the event sample. The dependence of the resolution and of the triggered exposure on the cuts parameters is also discussed. Eventually, the reconstructed JEM–EUSO spectrum is presented for a possible realization of the observed sample. The work in progress on the iterative parameter optimization is summarized at the end of the Chapter.

### 6.1 The reconstructed event

In this section we present the steps of the reconstruction procedure for a "standard" event: a proton with energy  $10^{20}$ eV and zenith angle ( $\theta$ ) of 60 degrees. The impact point is inside the  $\pm 20$  km from the center of the FOV. The projection onto the focal surface of the shower's track is shown in Fig. 6.1 with no background. The color of each pixel gives the counts in that pixel integrated in the time window.

The simulated and reconstructed curves for the same event, relative to the different steps of the reconstruction procedure, are shown in Fig. 6.1.

In the top left panel of Fig. 6.2 the simulated (histogram) and reconstructed (points with bars) curves of the counts are shown. The upper right plot shows the photon curve at the focal surface, while the bottom left curves

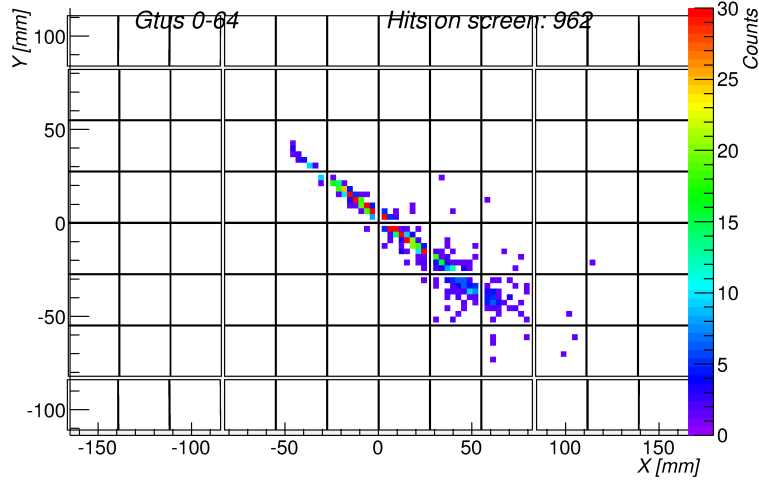


Figure 6.1: simulated counts track on the focal surface. This event has an energy of  $10^{20}$  eV, a zenith angle of 60 degrees and is impacting near the center of the FOV. Black squares represent the PMTs and the active pixels are shown. No background is shown.

show the photon distribution at the entrance pupil. Finally, after the geometry has been reconstructed, the curve of photons at the shower location is obtained.

Eventually, after applying the model for the fluorescence yield, we obtain the shower electron profile shown at the bottom of Fig. 6.2. We fit the reconstructed profile with the GIL function, that in the specific example gives a best-fit energy of  $1.10378 \cdot 10^{20}$  eV and  $X_{max}$  948.057 g/cm<sup>2</sup> (to be compared with the 967.943 g/cm<sup>2</sup> of the simulated event). The reduced  $\chi^2$  was 0.736343 for 20 DOF.

The relatively small systematic shift toward the high energies is due to the lack of Cherenkov correction. Signal gaps are visible as sudden drops in the intensity of the light. In fact, the present configuration sets to 0 all the GTUs in the vicinity of gaps. Such points will not be considered in the fit. As can be seen, the latest stages of the curve cannot be reconstructed given the non zero shower opening angle. Such a fact is however not immediately negative given the high contamination of backscattered and reflected Cherenkov in the latest stages of the shower.

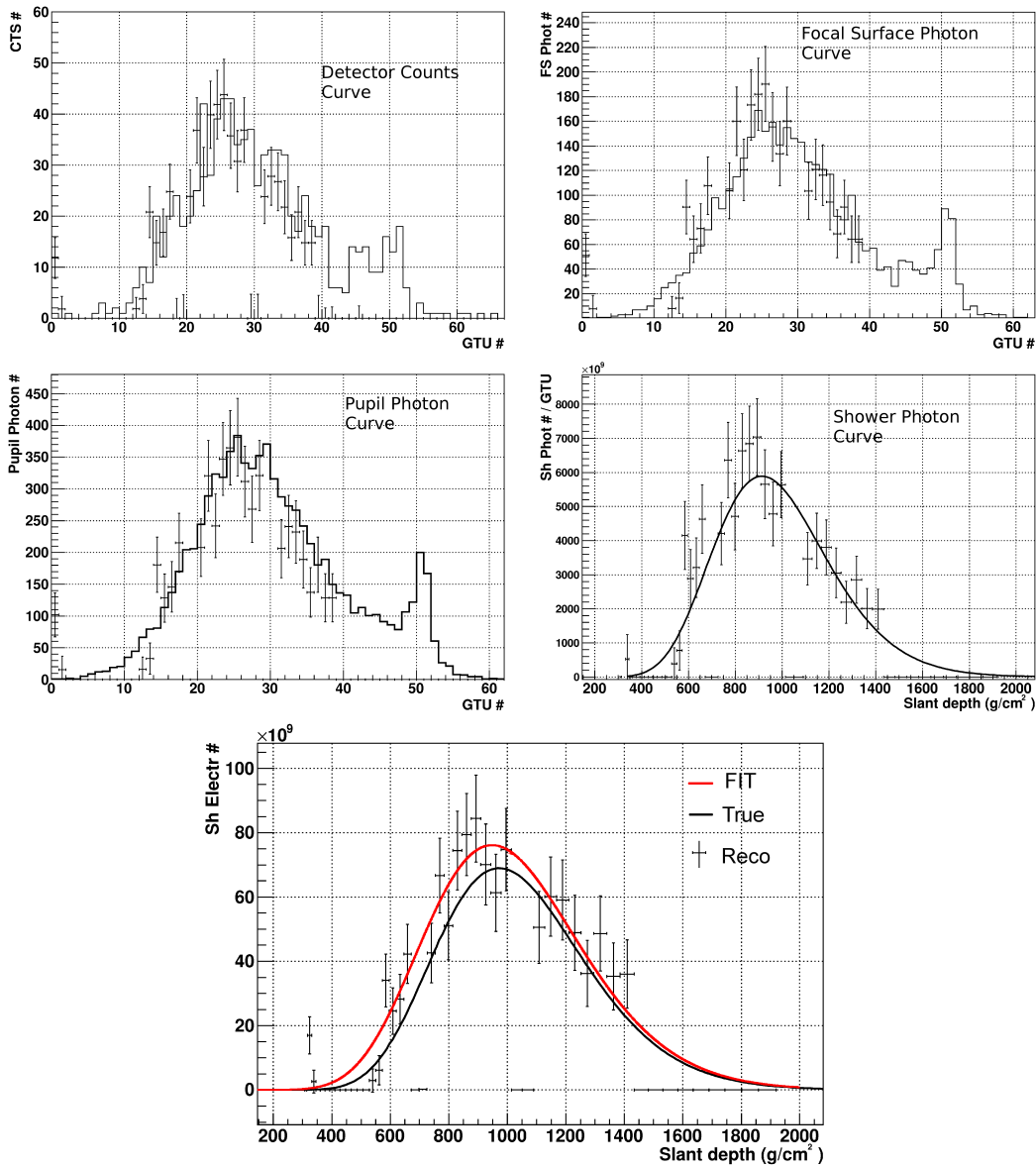


Figure 6.2: simulated and reconstructed curves for the various steps of the reconstruction procedure. From the upper left to the bottom right plot the profiles of the event are reconstructed from the focal surface signal to photons in atmosphere. More in detail counts, focal surface photons, pupil and shower photons. The bottom plot represents the shower electron curve. Points show the reconstructed electron curve and the black continuous lines refer to the real simulated data. The red curve shows the best-fit of the reconstructed points.

## 6.2 Energy reconstruction

### 6.2.1 Fixed condition

To debug the reconstruction algorithms and to understand the current limits of the procedure, we studied the reconstruction of a sample of events simulated at certain fixed energies, inclinations and impact points. We have also corrected the systematics according to the study presented in the previous chapter, that is according to the tables 5.7, 5.8 and 5.9 of Chap. 5. Given the limited number of conditions under which the systematics have been calculated, to estimate the proper correction factor we have used, in a few cases, some approximation like the combination and extrapolation of different factors in the tables.

In Fig. 6.3 we show, the energy reconstruction performances for protons of energy  $10^{20}$  eV arriving at various zenith angles. The impact point is in the innermost  $\pm 20$  km from the center of the FOV. The points show the median of the distributions for each single condition while the errors show the  $\pm 34\%$  confidence intervals (68% or  $\sigma$ ). Both the slant depth and Cherenkov methods are shown in the plot, respectively identified by black and red lines.

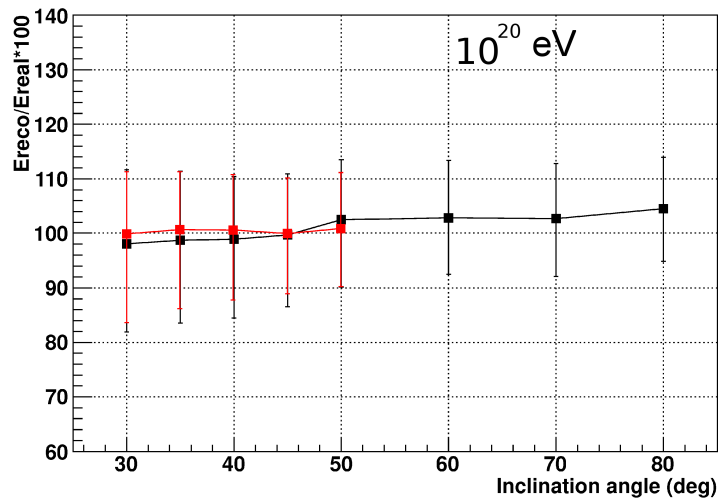


Figure 6.3: reconstruction performances for protons of energy  $10^{20}$  eV arriving at different zenith angles. The red and black curves represent the reconstruction performances according respectively to the Cherenkov and slant depth method. Points represent the median of the distribution while bars the  $\pm 34\%$  values of the distributions. For each case, 8000 events have been simulated.

As it can be seen, at  $10^{20}$  eV the energy reconstruction is very good. Residual systematics on the median, after correction, are less than 5%. The



## 6.2. ENERGY RECONSTRUCTION

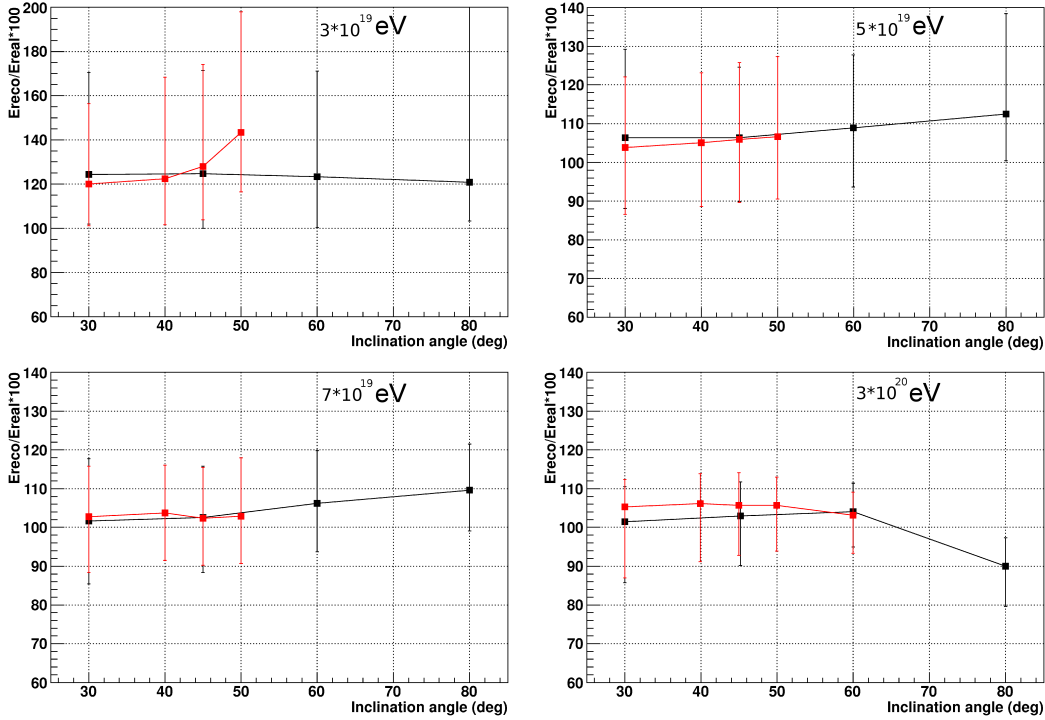


Figure 6.4: reconstruction performances for sample of events at  $3 \cdot 10^{19}$ ,  $5 \cdot 10^{19}$ ,  $7 \cdot 10^{19}$  and  $3 \cdot 10^{20}$  eV. The red and black curves are for the Cherenkov and slant depth method respectively. Points indicate the median of the distribution for each condition while bars the  $\pm 34\%$  values. For each sample 8000 events have been simulated.

$\pm 34\%$  width is  $\pm 10\%$  above 60 degrees and  $\pm 15\%$  for the other events. A summary of the distribution widths is given in Tab. 6.1. To be noticed is also the slightly higher quality of the reconstruction performed with the Cherenkov method, which improves the systematic shift and the resolution (see Tab. 6.2). At higher zenith angles, no reconstruction with the Cherenkov method is possible due to the opening angle of the Cherenkov emission which spreads over a large area on the Earth surface making the reflected component below the level of detectability.

In Fig. 6.4, we show the reconstruction of samples of events with energies  $3 \cdot 10^{19}$ ,  $5 \cdot 10^{19}$ ,  $7 \cdot 10^{19}$  and  $3 \cdot 10^{20}$  eV, each for different zenith angles. As in the previous case, the events impact near the center and both the slant depth and Cherenkov method are used.

For events at  $3 \cdot 10^{19}$  eV, the reconstruction performances are limited. This is not surprising given the weak signal received at these energies. A systematic shift of the order of  $+20\%$  is observed for all zenith angles. Moreover the distributions are asymmetric and the energy resolution is  $(-20, +40)\%$ . The

## CHAPTER 6. JEM-EUSO RECONSTRUCTION PERFORMANCES

Condition	30 deg	35 deg	40 deg	45 deg	50 deg	60 deg	70 deg	80 deg
$3 \cdot 10^{19}$ eV	(-0.23,0.46)	–	–	(-0.25,0.46)	–	(-0.23,0.47)	–	(-0.18,1.14)
$5 \cdot 10^{19}$ eV	(-0.18,0.23)	–	–	(-0.16,0.18)	–	(-0.15,0.19)	–	(-0.12,0.25)
$7 \cdot 10^{19}$ eV	(-0.16,0.17)	–	–	(-0.14,0.13)	–	(-0.13,0.14)	–	(-0.1,0.12)
$10^{20}$ eV	(-0.16,0.13)	(-0.15,0.12)	(-0.14,0.11)	(-0.13,0.11)	(-0.12,0.11)	(-0.1,0.1)	(-0.1,0.1)	(-0.09,0.09)
$3 \cdot 10^{20}$ eV	(-0.16,0.09)	–	–	(-0.13,0.09)	–	(-0.09,0.07)	–	(-0.1,0.07)

Table 6.1: the distribution width of the energy reconstruction with slant depth method (see Figs. 6.3 and 6.4). Numbers are expressed as  $\pm 34\%$  values and are defined as  $\frac{\Delta_{34}}{E_{reco}}$ .

Condition	30 deg	35 deg	40 deg	45 deg	50 deg	60 deg
$3 \cdot 10^{19}$ eV	(-0.18,0.36)	–	(-0.24,0.46)	(-0.24,0.46)	(0.26,0.54)	–
$5 \cdot 10^{19}$ eV	(-0.16,0.16)	–	(-0.15,0.17)	(-0.16,0.19)	(-0.17,0.2)	–
$7 \cdot 10^{19}$ eV	(-0.14,0.13)	–	(-0.12,0.12)	(-0.12,0.13)	(-0.12,0.15)	–
$10^{20}$ eV	(-0.16,0.11)	(-0.14,0.11)	(-0.13,0.1)	(-0.11,0.1)	(-0.1,0.1)	–
$3 \cdot 10^{20}$ eV	(-0.18,0.07)	–	(-0.14,0.08)	(-0.13,0.08)	(-0.12,0.07)	(-0.1,0.06)

Table 6.2: the distribution width of the energy reconstruction with cherenkov method (see Figs. 6.3 and 6.4). Numbers are expressed as  $\pm 34\%$  values and are defined as  $\frac{\Delta_{34}}{E_{reco}}$ .

asymmetry increases even more at 80 degrees till it reaches (-20,+114%). This feature is due to the worse quality of the optics in the external parts of the FOV. In fact inclined showers impacting near the center will be developing more on the external side of the FOV. The Cherenkov method seems also to show a poor performance especially at the highest zenith angles where the Cherenkov pulse recognition is more problematic.

At  $5 \cdot 10^{19}$  eV, systematics reduce to +5–15%. The width of the distribution is  $\sim 15$ –20%. The Cherenkov method can be used up to 50 degrees. At  $7 \cdot 10^{19}$  eV the residual systematics is around +10% while the width does not exceed the 15% (with the exception of the events with 30 degree zenith angle).

At  $3 \cdot 10^{20}$  eV, reconstruction is of course very good. However, a systematic shift of the energy appears for events inclined at 80 degrees. We discuss later the possible sources of this systematic effect.

### 6.2.2 Full field of view

In this section the energy reconstruction on the entire FOV will be analyzed. As first step the reconstruction in fixed points in the FOV will be calculated for different inclinations. On the left panel of Fig. 6.5 can be seen the performances obtained with the slant depth method while on the right with the Cherenkov method. The events have an energy of  $10^{20}$  eV and are of different inclinations. As can be seen no significant difference can be observed for both Cherenkov and  $X_{max}$  methods if the central curve is compared with

## 6.2. ENERGY RECONSTRUCTION

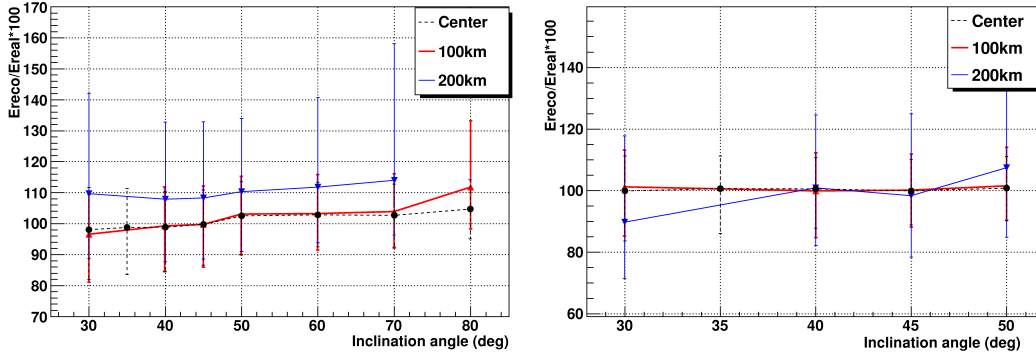


Figure 6.5: energy reconstruction performances in different locations of the FOV for  $10^{20}$  eV events. Points represent the median while error bars the  $\pm 34\%$  value. **Left plot:** energy reconstruction for the slant depth method. **Right plot:** energy reconstruction for the Cherenkov method.

Condition	30 deg	35 deg	40 deg	45 deg	50 deg	60 deg	70 deg	80 deg
cent.	(-0.16,0.13)	(-0.15,0.12)	(-0.14,0.11)	(-0.13,0.11)	(-0.12,0.11)	(-0.1,0.1)	(-0.1,0.1)	(-0.09,0.09)
100 km	(-0.16,0.13)	–	(-0.15,0.13)	(-0.14,0.12)	(-0.13,0.12)	(-0.12,0.13)	(-0.11,0.12)	(-0.14,0.21)
200 km	(-0.21,0.32)	–	(-0.2,0.25)	(-0.2,0.25)	(-0.19,0.24)	(-0.18,0.29)	(-0.18,0.44)	–

Table 6.3: distribution width of the energy reconstruction with slant depth method (see Fig. 6.5). Numbers are expressed as  $\pm 34\%$  values and are defined as  $\frac{\Delta_{34}}{E_{reco}}$ . Showers of energy  $10^{20}$  eV are simulated.

the one at 100 km. The only exception is given by the very extreme zenith angles where border effects start to become relevant. For the 200 km curve instead, a consistent shift can be observed, showing how other systematics appear in the external regions of the FOV. These systematics have to be investigated in the future. The reconstruction above 70 degrees has not been included given the border effects in this region.

The widths of the distribution are reported in Tabs. 6.3 and 6.4. As can be seen near the center a very good resolution ( $\pm 10\text{--}15\%$ ) is achieved, while the resolution at 200 km is, as expected, slightly worse, achieving  $\pm 20\text{--}30\%$  depending on the angle. At lower angles border effects also appear. The Cherenkov method is generally characterized by slightly better performances

Condition	30 deg	35 deg	40 deg	45 deg	50 deg
$10^{20}$ eV cent.	(-0.16,0.11)	(-0.14,0.11)	(-0.13,0.1)	(-0.11,0.1)	(-0.1,0.1)
$10^{20}$ eV 100 km	(-0.16,0.12)	–	(-0.15,0.12)	(-0.12,0.12)	(-0.11,0.13)
$10^{20}$ eV 200 km	(-0.18,0.28)	–	(-0.19,0.23)	(-0.2,0.26)	(-0.23,0.28)

Table 6.4: distribution width of the energy reconstruction with Cherenkov method (see Fig. 6.5). Numbers are expressed as  $\pm 34\%$  values and are defined as  $\frac{\Delta_{34}}{E_{reco}}$ . Showers of energy  $10^{20}$  eV are simulated.

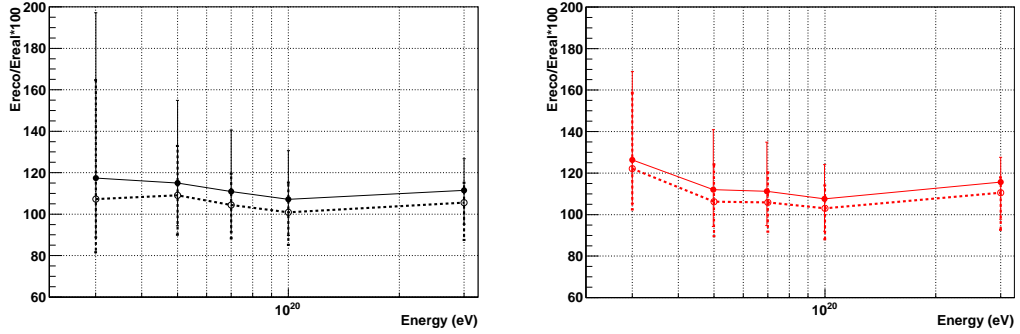


Figure 6.6: energy reconstruction performances for showers impacting in the  $(\pm 270, \pm 200)$  km box with a zenith angle of 30 degrees. **Left panel:** energy reconstruction performed according to the slant depth method. **Right panel:** energy reconstruction performed according to the Cherenkov method. Dashed lines represent a cut for  $r < 100$  km.

at all the angles especially at the center of the FOV.

The energy reconstruction has been also evaluated for several shower samples randomly distributed on the whole FOV. In Fig. 6.6 the ratio  $\frac{E_{reco}}{E_{real}} \cdot 100$  for 30 degrees showers impacting in the range  $(\pm 270, \pm 200)$  km can be seen as continuous line. In the left panel the reconstruction according to the slant depth method is shown. On the right panel, the reconstruction performed according to the Cherenkov method is presented. A sample with impact point within  $r < 100$  km from the center is shown as dashed line. The correction of the systematics has been performed as previously shown.

As it can be seen in Tab. 6.5 the reconstruction improves at the higher energies. This applies also for the systematic shift which is generally decreasing with the energy with the significant exception of the  $3 \cdot 10^{20}$  eV case. The reconstruction improves slightly in the central part due both to the reduced systematics and to the better quality of the signal.

The reconstruction performances seem to improve in terms of distribution width as the zenith angle is increased to 45 degrees. In fact, as it can be observed in Fig. 6.7 the width of the distribution tends to decrease particularly for the low energy case. However, no significant change can be observed in the systematic shift of the 45 degrees plots with respect to the 30 degrees case. The selection of the 100 km cut brings to an improvement of the reconstruction performances both from the point of view of shift and of systematic width.

In Fig. 6.8 the energy reconstruction for events with a 60 degrees zenith angle is shown. No Cherenkov method is presented given the non recognizable Cherenkov peak at such inclinations. The energy reconstruction perfor-

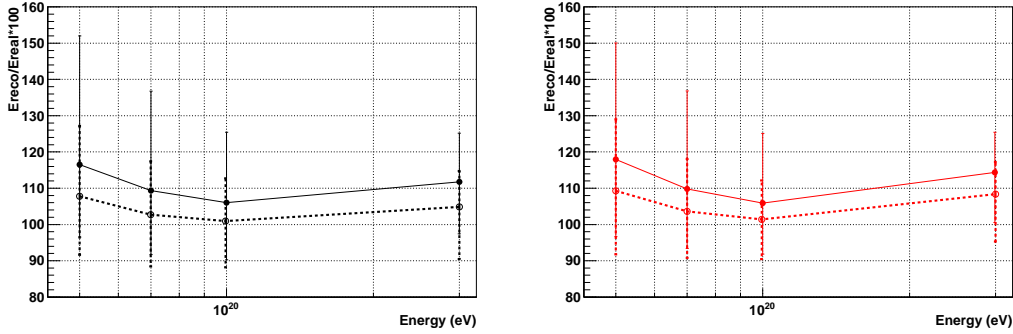


Figure 6.7: energy reconstruction performances obtained on the full FOV. The impact point has been simulated inside the  $(\pm 270, \pm 200)$  km box. All the showers have a zenith angle of 45 degrees. **Left panel:** reconstruction according to the slant depth method. **Right panel:** reconstruction according to the Cherenkov method. Dashed lines represent the cut for  $r < 100$  km.

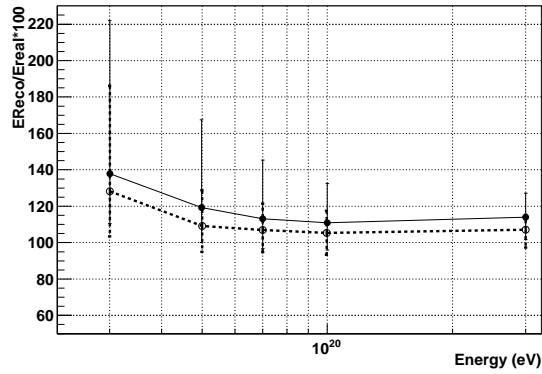


Figure 6.8: reconstruction performances for the 60 degrees sample of events. Given the poor recognizability of the Cherenkov peak just the slant depth method can be used. On the left panel the energy reconstruction performances can be observed.

manances are significantly improving as the energy increases. The systematic shift is around 10–15% at the highest energies. Again the central part of the FOV is characterized by a much better residual systematic shift. The distribution width improves further with the increasing zenith angles however just at the highest energies. In fact, in Tab. 6.5 at the lowest energies, for both methods and regardless of the cut no improvement is observed if the angle is increasing. Assuming equal conditions the cut will however always imply a much better distribution width given the much better signal quality.

Condition	$3 \cdot 10^{19}$ eV	$5 \cdot 10^{19}$ eV	$7 \cdot 10^{19}$ eV	$10^{20}$ eV	$3 \cdot 10^{20}$ eV
30 deg	(-0.28,0.8)	(-0.2,0.4)	(-0.19,0.3)	(-0.17,0.23)	(-0.16,0.15)
45 deg	(-0.28,0.6)	(-0.2,0.36)	(-0.17,0.27)	(-0.16,0.19)	(-0.14,0.13)
60 deg	(-0.27,0.84)	(-0.19,0.48)	(-0.16,0.32)	(-0.15,0.21)	(-0.12,0.13)
30 deg (< 100km)	(-0.26,0.58)	(-0.19,0.24)	(-0.16,0.15)	(-0.16,0.14)	(-0.18,0.1)
45 deg (< 100km)	(-0.28,0.47)	(-0.16,0.19)	(-0.14,0.15)	(-0.13,0.11)	(-0.14,0.1)
60 deg (< 100km)	(-0.25,0.58)	(-0.14,0.2)	(-0.12,0.15)	(-0.12,0.12)	(-0.1,0.08)
30 deg (Cher)	(-0.21,0.43)	(-0.18,0.29)	(-0.17,0.24)	(-0.16,0.17)	(-0.18,0.12)
45 deg (Cher)	(-0.25,0.62)	(-0.21,0.32)	(-0.16,0.27)	(-0.14,0.19)	(-0.13,0.11)
30 deg (Cher < 100km)	(-0.2,0.36)	(-0.17,0.18)	(-0.14,0.15)	(-0.15,0.11)	(-0.18,0.07)
45 deg (Cher < 100km)	(-0.25,0.6)	(-0.18,0.2)	(-0.13,0.14)	(-0.11,0.11)	(-0.13,0.09)

Table 6.5: distribution width of the energy reconstruction (see Figs. 6.6 6.7 and 6.8). Numbers are expressed as  $\pm 34\%$  values and are defined as  $\frac{\Delta_{34}}{E_{reco}}$ .

### 6.2.3 Full sample

In this section the energy reconstruction performances on events distributed as in the expected sample observed by JEM–EUSO will be presented. The proton events have been simulated in a range ( $\pm 270, \pm 200$ ) km with a zenith angle ( $\theta$ ) between 0 and 90 degrees. The events are distributed according to the  $\sin(2\theta)$ <sup>1</sup>. The energy spectrum covers the interval from  $10^{19}$  to  $10^{21}$  eV and follows a power law spectrum of index  $\alpha = -1$  (in differential notation). In the present study just the slant depth method is used for the performances estimation. In Fig. 6.9 the reconstructed energy (in Y axis) as function of the real energy (in X axis) for  $\sim 2 \cdot 10^4$  events. All the triggering events have been reconstructed and analyzed by the pattern recognition algorithms. In the present plot just the events where the signal has been properly identified have been included. For this reason all the events represented here have been successfully identified both by trigger and by the *PWISE* algorithm. Unlike in the previous plots, the systematics correction has not been performed given the very wide range of simulated conditions and the limited set of conditions for the study of the systematics. Future studies will have to perform an event by event correction in order to totally unbiased the entire sample.

Above  $3 \cdot 10^{19}$  eV the fraction of reconstructed events steadily increases with the increasing energy. Tails can be also observed at the highest and lowest energies of the plots while the main peak seems to indicate the presence of systematics shifts in different energy ranges. In fact, under  $10^{20}$  eV the energy is slightly overestimated while above  $\sim 2 \cdot 10^{20}$  eV is underestimated. Such a features might be due to the presence of uncorrected Cherenkov contamination and by the onset of non–linear effects (like PMT pile–up) at the

<sup>1</sup>This distribution takes into account the integration over the entire solid angle and the cross section of the FOV.

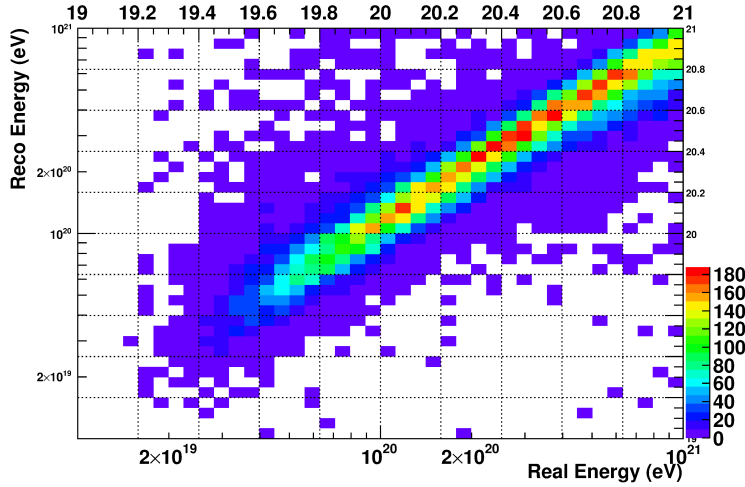


Figure 6.9: full FOV reconstruction performances. The reconstructed energy parameter can be seen as function of the real energy. The events are simulated in the  $(\pm 270, \pm 200)$  km. The zenith angle has been chosen between 0 and 90 degrees. The correction of the systematics has not been performed given the limited set of conditions analyzed in the previous chapter. The color scale represents the number of events integrated in each bin.

highest energies.

In Fig. 6.10 the  $\pm 34$  and  $\pm 45$  % contours are shown. More in detail, the median of the reconstructed energy distribution has been calculated for each true energy bin. Fig. 6.9 has been therefore divided in vertical stripes, the median has been calculated and consequently the  $\pm 34$  and  $\pm 45$  % ranges have been identified.

Such a map expresses the width of the reconstructed energy distribution for the entire energy range. As can be seen the  $\sigma$  of the distribution varies from the  $\pm 60\%$  at  $3 \cdot 10^{19}$  eV, to  $\pm 30\%$  at  $10^{20}$  eV and  $\pm 20\%$  at  $2 \cdot 10^{20}$  eV. At the highest energies, on the other hand, the distribution widens again. The potential reason of such a feature will be explained in the later sections.

## 6.3 $X_{max}$ reconstruction

### 6.3.1 Fixed condition

We present in this section a preliminary study of the  $X_{max}$  reconstruction performances. These results depend on the first assumptions made on the maximum and Cherenkov line of sight, on the inclination and, for the slant depth method, on the shower parameterization. Unlike the energy, the  $X_{max}$

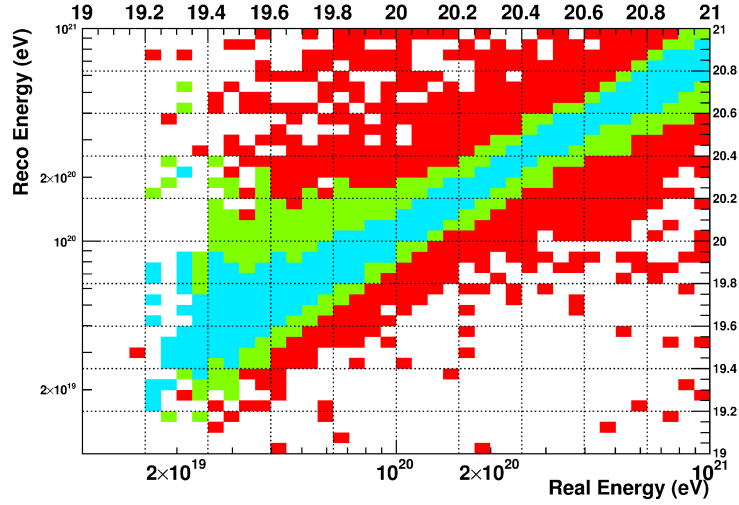


Figure 6.10:  $\pm 34$  and  $45\%$  values with respect to the median for each real energy. Such a graph expresses the width of the reconstructed energy distribution. In cyan green and red can be respectively identified the  $\pm 34$ ,  $45$  and  $> 45\%$  intervals. Such intervals corresponds to  $\sigma$ ,  $2\cdot\sigma$  and  $> 2\cdot\sigma$ .

parameter is very sensible to the assumptions on the geometry. To decouple the final result from the initial assumptions through an iteration procedure is a necessary task for future studies.

In the following plots, for each condition, 8000 events are simulated. The error bars give the  $\pm 34\%$  of the distribution. The median value has been corrected according to the tables 5.12 and 5.14 of Chapter 5.

In Fig. 6.11 the  $X_{max}$  reconstruction performances are shown for events of energy  $10^{20}$  eV and having different inclinations. Both the Cherenkov mark and slant depth methods are used. Systematic shifts are corrected, at all the inclinations, within  $50 \text{ g/cm}^2$ . The Cherenkov method delivers an even better result with a systematic shift always of the order of several  $\text{g/cm}^2$

In Fig. 6.12, we show the  $X_{max}$  resolution for events of different energy and arriving in the central part of the FOV. For events with energy  $3 \cdot 10^{19}$  eV, the Cherenkov method show large width and systematic effects. The slant depth method appears to be more robust even if systematics are around  $80 \text{ g/cm}^2$ .

The performances improve already at  $E = 5 \cdot 10^{19}$  eV. The Cherenkov method is still affected by strong systematic effects, especially at higher zenith angles. The slant depth method is again robust at all inclinations the systematics are here smaller than  $50 \text{ g/cm}^2$ . The  $X_{max}$  reconstruction for events at  $7 \cdot 10^{19}$  eV shows better performances for both the Cherenkov



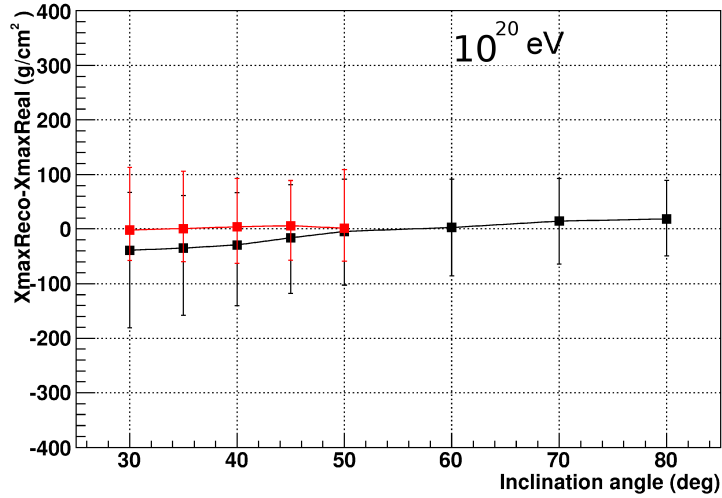


Figure 6.11:  $X_{max}$  reconstruction performances for protons with energy  $10^{20}$  eV. The red and black curves refer to the Cherenkov and slant depth method respectively. Points give the median of the distribution while bars the  $\pm 34\%$  values of the distributions.

Condition	30 deg	35 deg	40 deg	45 deg	50 deg	60 deg	70 deg	80 deg
$3 \cdot 10^{19}$ eV	(-173 ,183)	–	–	(-174 ,167)	–	(-157 ,160)	–	(-115 , 120)
$5 \cdot 10^{19}$ eV	(-152 , 143)	–	–	(-118 ,128)	–	(-105 ,113)	–	(-92 ,93)
$7 \cdot 10^{19}$ eV	(-147 ,117)	–	–	(-110 ,106)	–	(-93 ,103)	–	(-80 , 74)
$10^{20}$ eV	(-142 ,105)	(-123 ,96)	(-111 ,96)	(-102 ,96)	(-98 ,95)	(-89 ,99)	(-79 ,78)	(-68 , 71)
$3 \cdot 10^{20}$ eV	(-130 ,86)	–	–	(-98 , 75)	–	(-76 , 70)	–	(-60 , 56)

Table 6.6: distribution width of the  $X_{max}$  reconstruction with slant depth method (see Figs. 6.11 and 6.12). Numbers are  $\pm 34\%$  values. Numbers are expressed in  $\text{g}/\text{cm}^2$ .

and slant depth methods. The Cherenkov method, in fact, is almost totally unbiased up to 40–45 degrees while the slant depth method reconstructs well for all the inclinations. Systematic shifts in fact, never exceed 20–30  $\text{g}/\text{cm}^2$  for the slant depth method. At the highest energies the  $X_{max}$  reconstruction systematics range from 80 to 30  $\text{g}/\text{cm}^2$  for the slant depth method and from 0 to 30  $\text{g}/\text{cm}^2$  for the Cherenkov method.

In case of the slant depth method, the resolution narrows toward the higher zenith angles and energies (see Tabs. 6.6 and 6.7). In fact, horizontal shower will typically develop higher in the atmosphere and therefore the uncertainties in the position of the geometry are corresponding to a smaller uncertainty in  $X_{max}$ . At the higher energies showers will deliver a better signal and the uncertainty on the position of the maximum is further reduced.

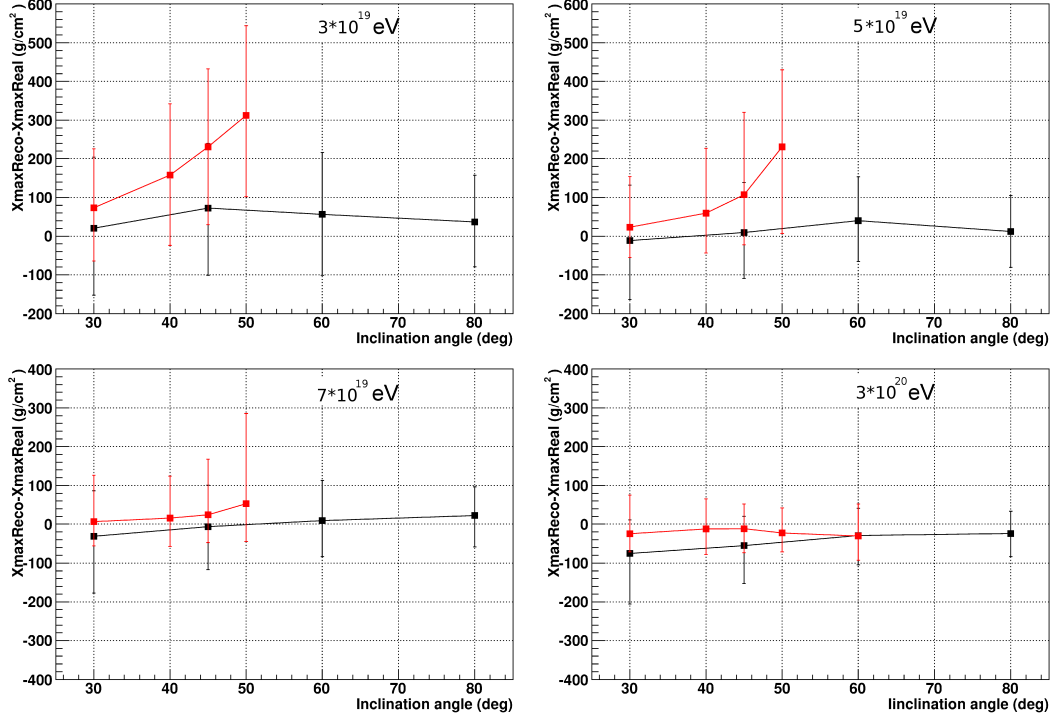


Figure 6.12:  $X_{max}$  reconstruction for samples of events with energy  $3 \cdot 10^{19}$ ,  $5 \cdot 10^{19}$ ,  $7 \cdot 10^{19}$  and  $3 \cdot 10^{20}$  eV. The red and black curves refer to the Cherenkov and slant depth method respectively. Points represent the median of the distribution while bars the  $\pm 34\%$  values of the distributions.

Condition	30 deg	35 deg	40 deg	45 deg	50 deg	60 deg
$3 \cdot 10^{19}$ eV	(-138 , 151 )	–	(-181,184 )	(-201 ,201 )	(-210, 232)	–
$5 \cdot 10^{19}$ eV	(-78 , 131)	–	(-103 ,167 )	(-129 , 212)	(-223 ,199)	–
$7 \cdot 10^{19}$ eV	(-62 , 119)	–	(-73 , 108)	(-71 , 143)	(-97 , 232)	–
$10^{20}$ eV	(-55 , 114)	(-61 ,104)	(-67 , 88)	(-62 , 82)	(-60 ,107)	–
$3 \cdot 10^{20}$ eV	(-47 , 100)	–	(-66 , 78 )	(-62 , 64 )	(-49 , 64 )	(-63 , 82 )

Table 6.7: distribution width of the  $X_{max}$  reconstruction with Cherenkov method (see Figs. 6.11 and 6.12).

### 6.3. $X_{MAX}$ RECONSTRUCTION

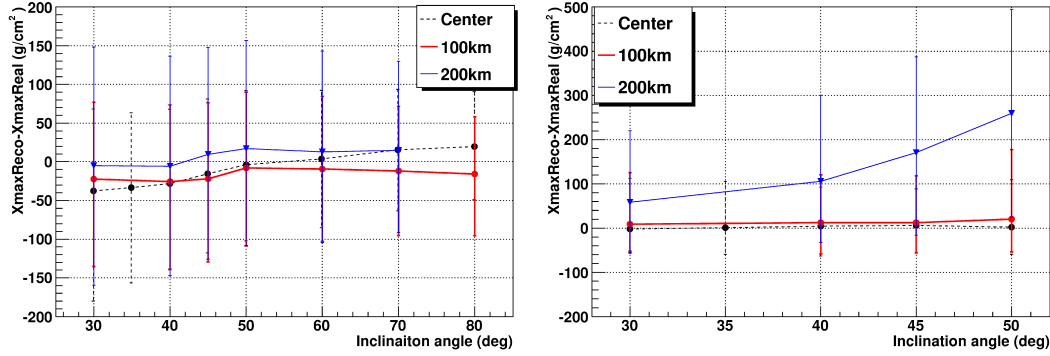


Figure 6.13: reconstruction performances in different locations in the FOV. Points represent the median while error bars the  $\pm 34\%$  value. The dashed lines represent the curves for the innermost 100 km. **Left plot:**  $X_{max}$  reconstruction performances for the slant depth method. **Right plot:**  $X_{max}$  reconstruction performances for the Cherenkov method.

Condition	30 deg	35 deg	40 deg	45 deg	50 deg	60 deg	70 deg	80 deg
cent.	(-142 ,105)	(-123 ,96)	(-111 ,96)	(-102 ,96)	(-98 ,95)	(-89 ,99)	(-79 ,78)	(-68 , 71)
100 km	(-113 , 99)	-	(-113 , 99)	(-107 , 98)	(-100 , 98)	(-93 , 93)	(-83 , 83)	(-80 , 73)
200 km	(-154 , 154)	-	(-141,142)	(-135,138)	(-125 , 139)	(-117 , 130)	(-106 , 114)	-

Table 6.8: distribution width of the energy reconstruction with slant depth method (see Fig. 6.13). Numbers are  $\pm 34\%$  values. Showers of energy  $10^{20}$  eV have been simulated.

#### 6.3.2 Full field of view

In this section the  $X_{max}$  reconstruction for events distributed on the entire FOV will be presented. The  $X_{max}$  reconstruction for events of different inclination impacting on different fixed positions in the FOV are presented. Left panel of Fig. 6.13 refers to the performances obtained with the slant depth method while right panel with the Cherenkov method. The systematics of the slant depth method are under  $50 \text{ g/cm}^2$  in all the cases. However, at 200 km no good quality reconstruction is obtained anymore.

In Tab. 6.8 the  $X_{max}$  resolution for the slant depth method is given. The resolution is to improving at the highest zenith angles. It can be also said that the resolution tends to worsen toward the external regions of the FOV because of the worse signal quality.

Condition	30 deg	35 deg	40 deg	45 deg	50 deg
cent.	(-55 , 114)	(-61 ,104)	(-67 , 88)	(-62 , 82)	(-60 ,107)
100 km	(-60 ,116)	-	(-70 ,108)	(-67 ,106)	(-74 ,157)
200 km	(-113 ,161)	-	(-138 ,194)	(-187,216)	(-234 ,235)

Table 6.9: distribution width of the  $X_{max}$  reconstruction with Cherenkov method (see Fig. 6.13). Numbers are  $\pm 34\%$  values. Showers of energy  $10^{20}$  eV have been simulated.

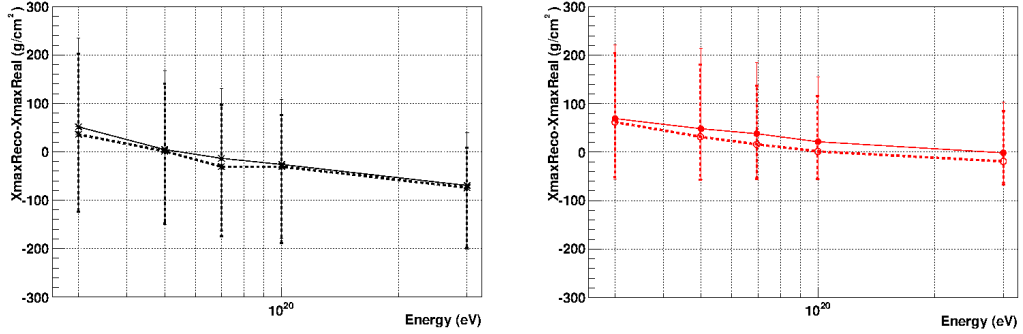


Figure 6.14:  $X_{max}$  reconstruction performances obtained on the full FOV. The impact point has been simulated inside the  $(\pm 270, \pm 200)$  km box. All the showers have a zenith angle of 30 degrees. **Left panel:** reconstruction performed according to the slant depth method. **Right panel:** reconstruction performed according to the Cherenkov method. Dashed lines represent the cut for  $r < 100$  km.

The reconstruction performances have been also assessed for different energies and inclinations scattered on the whole FOV and on the  $r < 100$  km sample.

In Fig. 6.14 the  $X_{max}$  reconstruction for 30 degrees events on the entire FOV has been represented as continuous line. In right panel the events are reconstructed with the slant depth method. The width of the distribution slightly improves with the increasing energy. On the other hand, the systematics seem not to be properly correctable even they still remain within 70-80  $\text{g}/\text{cm}^2$ . On right panel the reconstruction according to the Cherenkov method is shown. The main difference with respect to the slant depth method is the reduction of the systematics at the highest energies.

In Fig. 6.15 the  $X_{max}$  reconstruction for 45 degrees events is shown. No significant difference with respect to the 30 degrees case is observed. For the Cherenkov method (right panel) even a worsening of the performances can be observed especially at low energies. Moreover, the systematic shift obtained with the Cherenkov method at high energies seems to tend to 0. A significant improvement is achieved also for the reduced FOV ( $r < 100$  km).

In Fig. 6.16 the  $X_{max}$  reconstruction for events with 60 degrees zenith angle can is shown. No Cherenkov method could be applied anymore at such inclinations given the spread of the reflection on a larger surface. The  $X_{max}$  reconstruction is significantly improved as the energy increases. However, as in the previous cases no significant improvement in the width distribution is obtained at low energies. Results are summarized in Tab. 6.10.

### 6.3. $X_{MAX}$ RECONSTRUCTION

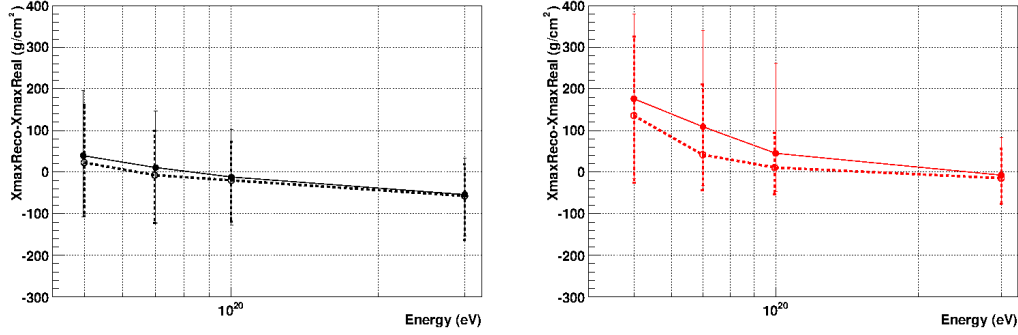


Figure 6.15:  $X_{max}$  reconstruction performances obtained on the full FOV. The impact point has been simulated inside the  $(\pm 270, \pm 200)$  km box. All the showers have a zenith angle of 45 degrees. **Left panel:** reconstruction performed according to the slant depth method. **Right panel:** reconstruction performed according to the Cherenkov method. Dashed lines represent the cut for  $r < 100$  km.

Condition	$3 \cdot 10^{19}$ eV	$5 \cdot 10^{19}$ eV	$7 \cdot 10^{19}$ eV	$10^{20}$ eV	$3 \cdot 10^{20}$ eV
30 deg	(-177 , 183)	(-155 , 162)	(-149 , 144)	(-152 , 134)	(-131 , 109)
45 deg	(-180 , 182)	(-147 , 155)	(-134 , 135)	(-116 , 114)	(-101 , 88)
60 deg	(-170 , 191)	(-132 , 146)	(-117 , 129)	(-104 , 113)	(-84 , 84)
30 deg (< 100km)	(-160 , 167)	(-149 , 139)	(-144 , 127)	(-157 , 106)	(-124 , 83)
45 deg (< 100km)	(-176 , 180)	(-128 , 139)	(-115 , 106)	(-99 , 94)	(-106 , 76)
60 deg (< 100km)	(-167 , 175)	(-106 , 109)	(-98 , 101)	(-88 , 94)	(-71 , 76)
30 deg (Cher)	(-125 , 151)	(-105 , 166)	(-91 , 146)	(-77 , 133)	(-61 , 105)
45 deg (Cher)	(-189 , 188)	(-192 , 203)	(-140 , 231)	(-92 , 215)	(-68 , 91)
30 deg (Cher < 100km)	(-113 , 141)	(-88 , 149)	(-72 , 120)	(-58 , 115)	(-47 , 104)
45 deg (Cher < 100km)	(-180 , 198)	(-161 , 189)	(-86 , 169)	(-64 , 84)	(-62 , 71)

Table 6.10: distribution width of the energy reconstruction (see Figs. 6.14 6.15 and 6.16). Numbers are  $\pm 34\%$  values.

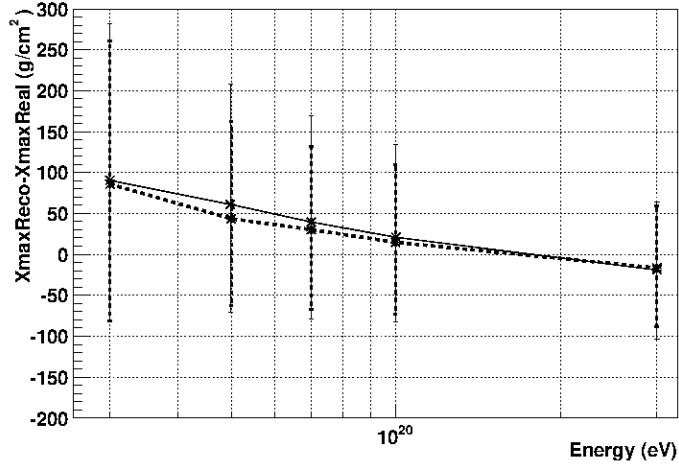


Figure 6.16:  $X_{max}$  reconstruction performances for the 60 degrees sample of events. Given the poor recognizability of the Cherenkov peak just the slant depth method can be used.

## 6.4 The quality of the event reconstruction

The values shown in the previous sections must be validated by quality checks. In fact, independently of the final result no guarantee is given that the chosen model properly describes the process. To assess the quality of the results obtained from the GIL fit on the shower electron curve, the  $\chi^2$  and the number of DOF of the fit can be used.

In Fig. 6.17 the average  $\chi^2$  of the fits obtained for different energies and angles is shown for the slant depth method. For each condition 8000 events were simulated and the impact point was close to the center of the FOV.

For most of the conditions average  $\chi^2$  better than 1.5–1.6 are obtained. At  $3 \cdot 10^{20}$  eV the average  $\chi^2$  of the fits increases to 2–3 indicating that the model is not perfectly describing the data, even if the results of the reconstruction are not much worse than the  $10^{20}$  eV case. Even though the model does not perfectly describe the data the fit converges toward a relatively narrow range of energy and  $X_{max}$  parameters.

In Fig. 6.18, we show the number of DOF as function of energy and zenith angles for the slant depth method. The number of DOF given by the number of selected points the free parameters of the fit. The points to be fitted are chosen to be at at least 20% of the maximum and within a limited range from the maximum. The width of such a maximum is adapted to the duration of the event.

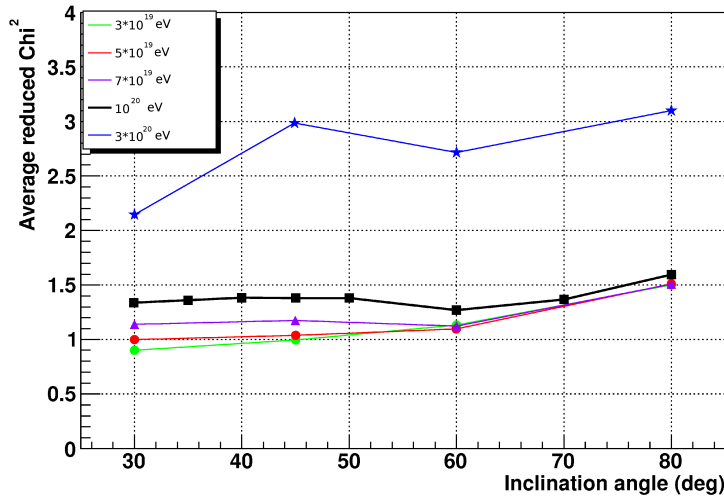


Figure 6.17: average reduced  $\chi^2$  calculated over 8000 events for different energies and inclinations.

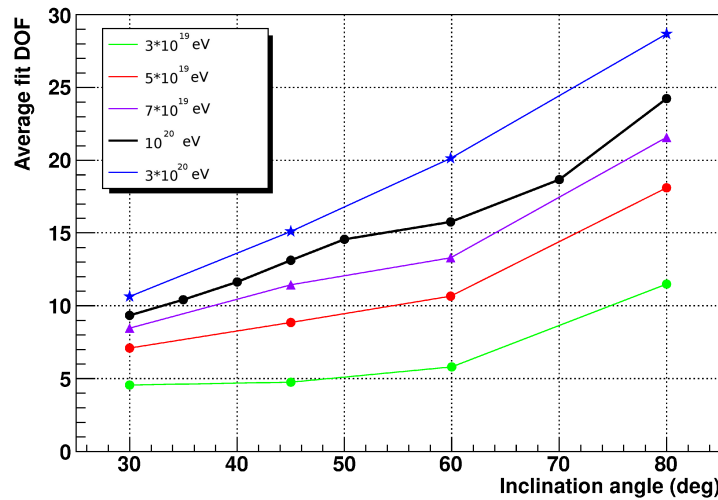


Figure 6.18: average over 8000 events of the number of DOF as function of energy and zenith angle.

The number of DOF increases with the zenith angle and with the energy. This is not surprising since more data points are used. While for showers at  $3 \cdot 10^{19}$  eV a minimum of 4 and a maximum of 11 DOF is involved, at energies around  $3 \cdot 10^{20}$  eV this number increases to 11–29 DOF.

In Fig. 6.19, we show the average  $\chi^2$ , obtained with the Cherenkov

method. The average  $\chi^2$  is slightly better (generally below 1.3) in comparison to the slant depth method. At  $3 \cdot 10^{20}$  eV, a worse  $\chi^2$  is obtained for all angles. For the same samples of events the number of DOF is shown in Fig. 6.20. Results are similar to the ones of the slant depth method.

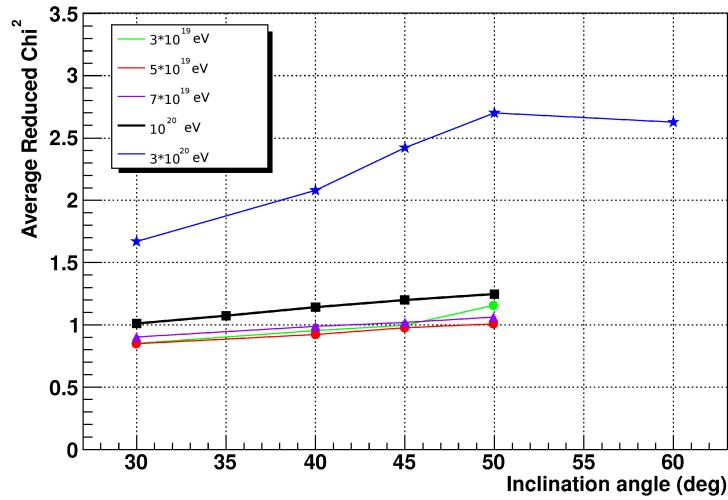


Figure 6.19: average reduced  $\chi^2$  calculated over 8000 events for different energies and inclinations. Reconstruction performed with the Cherenkov method.

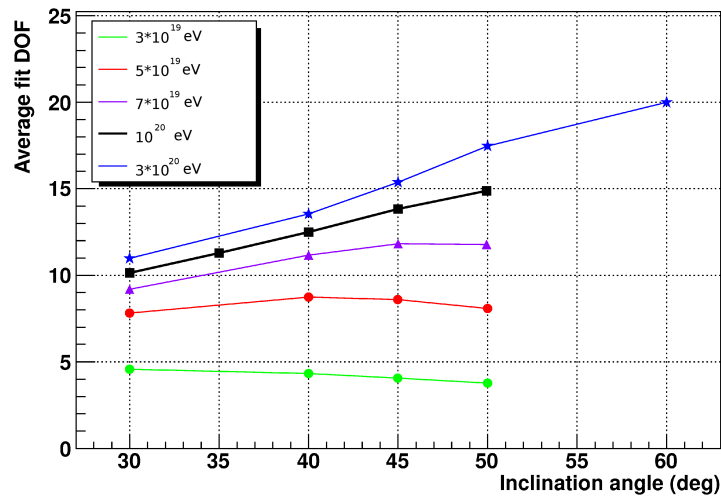


Figure 6.20: average over 8000 events of the number of DOF as function of energy and zenith angle. Reconstruction performed with the Cherenkov method.



To evaluate the quality the fraction of events with the Cherenkov mark has been estimated. In fact, the identification of a Cherenkov mark provides an independent method for the reconstruction of the geometry. For this reason the geometry can be cross-checked with two independent methods.

In Fig. 6.21 we show the fraction of triggered events reconstructed with a Cherenkov mark. All the events are impacting near the center of the FOV. The fraction of events showing Cherenkov mark increases with the energy. The current algorithm in most cases fails to reconstruct events above 50 degrees. Only at higher energies events up to 60 degrees can be reconstructed using the Cherenkov mark. The lower fraction of Cherenkov events at the lowest energies is also due to the weaker Cherenkov emission. All the curves however saturate around  $\sim 85\%$ . Such a value is most likely due to the fraction of non sensible area on the focal surface. Part of the Cherenkov marks seem therefore to be falling in the gaps.

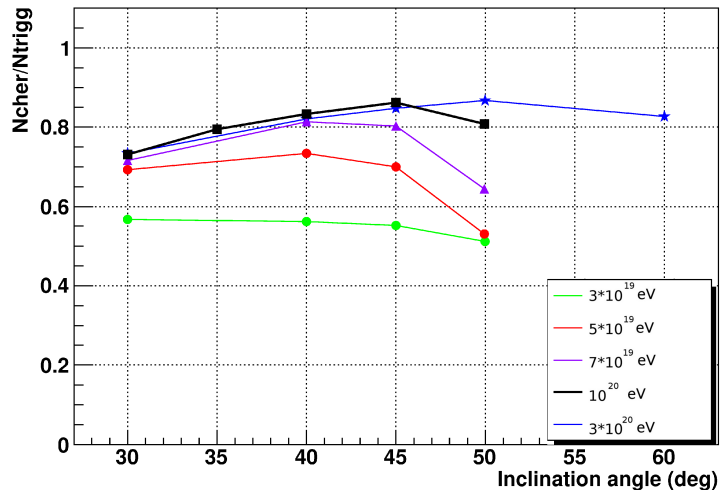


Figure 6.21: fraction of triggered events which have been identified with Cherenkov mark. Several samples of 8000 events of different energy and inclinations are shown.

In Fig. 6.22 it can be also seen how the performances of the Cherenkov recognition peak change within the FOV. Here is depicted the real impact position for all the events for which a Cherenkov peak has been found. All the events have an zenith angle of 45 degrees and energies equal to  $3 \cdot 10^{19}$  (in red) and  $3 \cdot 10^{20}$  eV (in black). For the low energies, the Cherenkov method seem to be successful just in the central part of the FOV. At the higher energies instead, the Cherenkov mark is detected on the whole FOV.

Gaps in the PMTs and PDMs limit the quality of the events. The per-

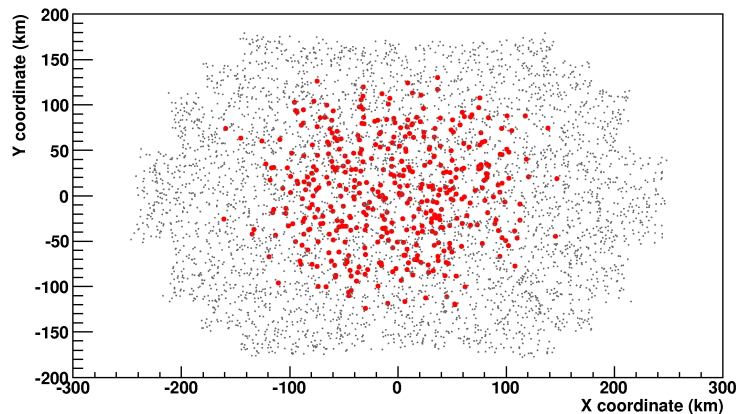


Figure 6.22: position of the real impact point of several 45 degrees showers. Condition for a shower to be included in such a plot is the recognition of a Cherenkov peak in the reconstruction algorithms. Red dots represent the  $3 \cdot 10^{19}$  eV while black points represent the  $3 \cdot 10^{20}$  eV events.

sistency of the signal in the vicinity of a gap makes the reconstruction of the track difficult. In fact, the signal can be totally or just partially depleted by the gaps. The near-gap fraction has been therefore estimated. We can then define cuts on the events on the base of their proximity to the gaps. An exclusion area up to 3.5 mm from the border of each PMT has been therefore defined. In the present ESAF implementation the PMT has a square shape with a non-sensible border of 1.5 mm and therefore the exclusion area extends only 2 mm in the sensible area. Whenever the center of mass of a spot is falling in the described area all the counts belonging to that GTU will be marked as near-gap signal. Because of the particular choice of the exclusion area the results must be therefore considered as preliminary.

More in detail in Fig. 6.23 the fraction of signal not affected by gaps with respect to the total reconstructed signals is shown. This ratio is defined according to Eq. 6.1.

$$\rho = \frac{counts_{far}}{counts_{reco}} \quad (6.1)$$

All signals belonging to a spot whose center of mass is not within the 3.5 mm from the border of the PMT is considered as far from the gap.

As shown in Fig. 6.23, the horizontal showers feature a more constant signal selection than vertical showers. This is explained by the consideration that vertical showers have higher probability of being either completely included or excluded from the near-gap region. Large zenith angles make possible a very long track which crosses internal and edge regions as well.

#### 6.4. THE QUALITY OF THE EVENT RECONSTRUCTION

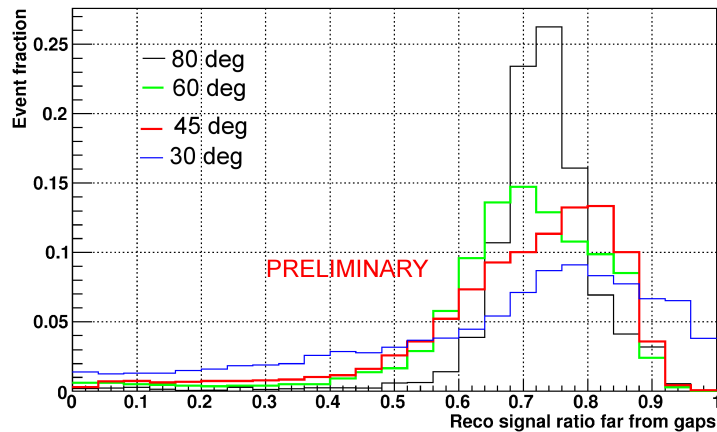


Figure 6.23: fraction of signal not falling in the exclusion region (X axis). Curves for several inclinations are shown here for 8000 events of  $10^{20}$  eV. On the Y axis the fraction of events characterized by such a signal exclusion is shown.

For this reason horizontal showers lose a rather uniform fraction of signal compared to the vertical showers. The 80 degrees showers can be observed in the plot as a peak marked in black with its maximum value around 0.75. All the lower zenith angles deliver a flatter distribution.

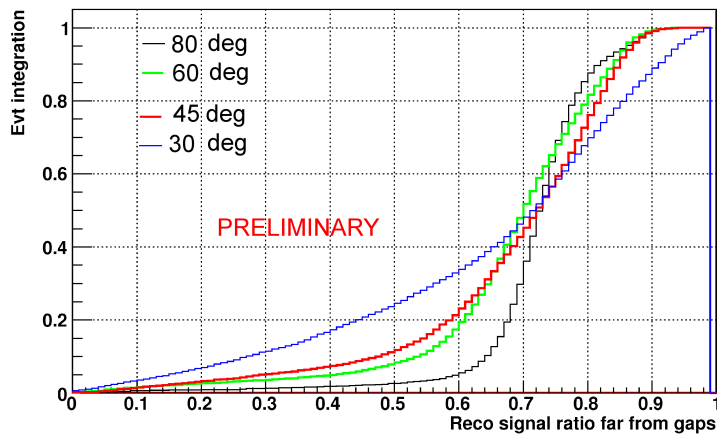


Figure 6.24: fraction of signal not falling in the exclusion region (X axis). Curves for several inclinations are shown here for 8000 events of  $10^{20}$  eV.

In Fig. 6.24, the integrals of the curves of Fig. 6.23 from 0 to 1 are shown. Vertical showers have a more equally distributed population than the horizontal ones. Such a plot can be used to study the impact of a potential

quality cut on the excluded signal. In fact, the fraction of the event out of the selection region can be used as a criterion to evaluate the quality of the event. It must be however stressed how such a cut does not preclude a priori the possibility of reconstruction.

## 6.5 Reconstruction quality cuts

In this section the impact of quality cuts on the full FOV–all inclinations reconstruction performances will be assessed. In the present work several parameters have been used to determine the statistical quality of the events. The most commonly used parameters are of course the  $\chi^2$  and the number of DOF of the fit. In addition to that the fraction of near-gap signal has been presented as event quality estimator. The application of a quality cut in the all-event sample implies however a reduction of the number of accepted events and for this reason, the reconstruction efficiencies associated to each cut are also presented.

Fig. 6.25 shows the reconstruction performances for the events with at least 6 DOF. The wide tails of Fig. 6.9 are not present anymore. This cut is extremely efficient to reduce the numbers of outliers in the distribution. The linearity of the reconstructed energy with respect to the simulated one is not affected by the presence of the cut.

In Fig. 6.26 the confidence intervals of the reconstructed energy distribution are shown. The events distribution is significantly narrower with respect to the full sample case. In fact, the width of the distribution will be reduced to  $\pm 40\%$  around  $\sim 3 \cdot 10^{19}$  eV and  $\pm 20\%$  between  $10^{20}$  and  $2 \cdot 10^{20}$  eV. The resolution however slightly worsen at the highest energies. As a matter of fact this cut seem to have a higher impact at the energies lower or equal to  $10^{20}$  eV.

In Fig. 6.27 it can be seen how the selection of a minimum DOF number reduces the reconstruction efficiency. In the figures the trigger efficiency is represented in black while the red triangles are the events recognized by the pattern recognition. The curve relative to the DOF cut is represented as blue squares. The curves have been defined as in Chapter 4.

The pattern recognition delivers a large exposure. In fact, the ratio of accepted events increases with the energy and ranges from a factor 0.5 at the lowest energies up to  $\sim 0.9$  or even higher at  $10^{20}$  eV and above.

The loss by the DOF cut amounts, with respect to the pattern recognition case, to a factor 2 around  $3 \cdot 10^{19}$  eV and to 10–15% above  $10^{20}$  eV. Most likely the fraction of rejected events belong are vertical events which encounter very soon the ground. Moreover the events largely affected by gaps are also

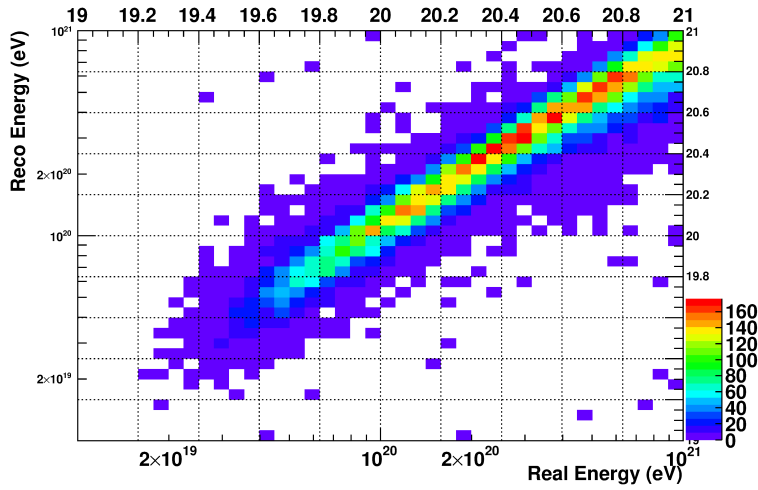


Figure 6.25: reconstructed energy with respect to the real energy. The events are simulated in the  $(\pm 270, \pm 200)$  km. The zenith angle has been chosen between 0 and 90 degrees. A  $\text{DOF} > 5$  cut has been applied here. The color scale represents the number of events integrated in each bin.

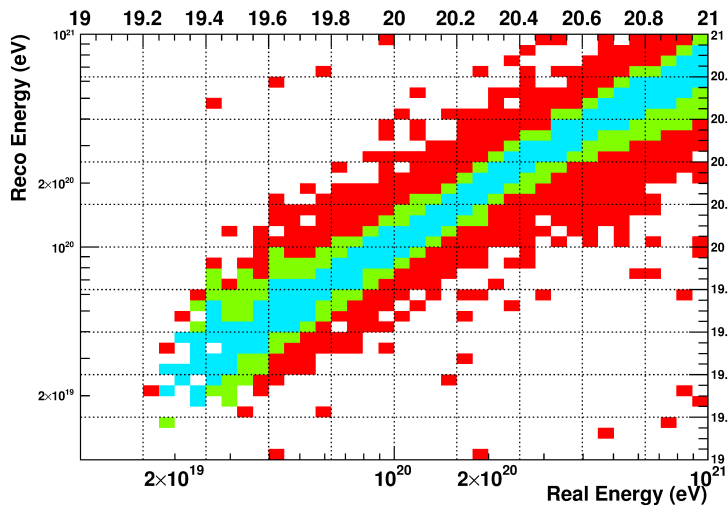


Figure 6.26: confidence intervals with respect to the median energy. In cyan green and red can be respectively identified the  $\pm 34$ ,  $45$  and  $> 45\%$  intervals. The  $\text{DOF} > 5$  cut has been applied here.

characterized by a smaller number of DOF. Eventually, a major improvement of the performances is obtained just under  $10^{20}$  eV. For this reason such a

cut is of limited use for the highest energies. A detailed study should be performed in the future in order to better characterize the rejected vents.

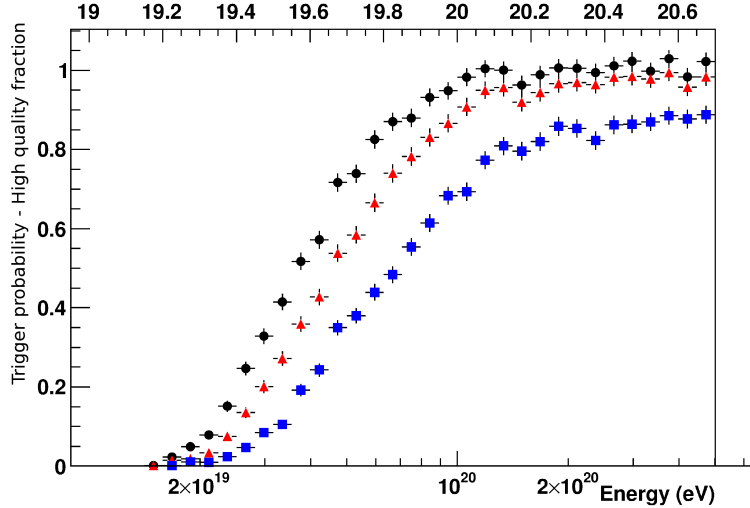


Figure 6.27: efficiency curves associated to different types of cuts. In black can be observed the trigger curve. The curve for the events identified by the pattern recognition and for the events passing the  $\text{DOF} > 5$  cut can be respectively observed in red and blue.

Another potential cut is the near-gap signal fraction. This aspect analyzed in the previous sections is expression of how much signal is in the vicinity of a gap. A possible threshold has been chosen to be equal to a 0.5 fraction.

In Fig. 6.28 the distribution of the reconstructed energy as function of the real is shown for events having a gap fraction smaller than 0.5. No significant difference can be observed with respect to the all-event sample (Fig. 6.9). In fact, apart from the removal of some outlier especially in the lower part of the plot the selection appears to be quite uniform.

In Fig. 6.29, the  $\pm 34\%$  values can be seen to be essentially equivalent to the full sample case except for the most extreme energies where a slight narrowing of the distribution can be observed.

The efficiency curves for the near-gap cuts are superposed on the efficiency curves shown before. The empty circles of the plot represent the near-gap cut (black circles) and the near-gap additionally to the DOF cut (blue circles). In both cases no significant decrease in efficiency are observed with respect to the cut free case. However, such a cut still allows the exclusion of a limited number of potentially biased events. The impact of stronger selection criteria must be also assessed in future studies.

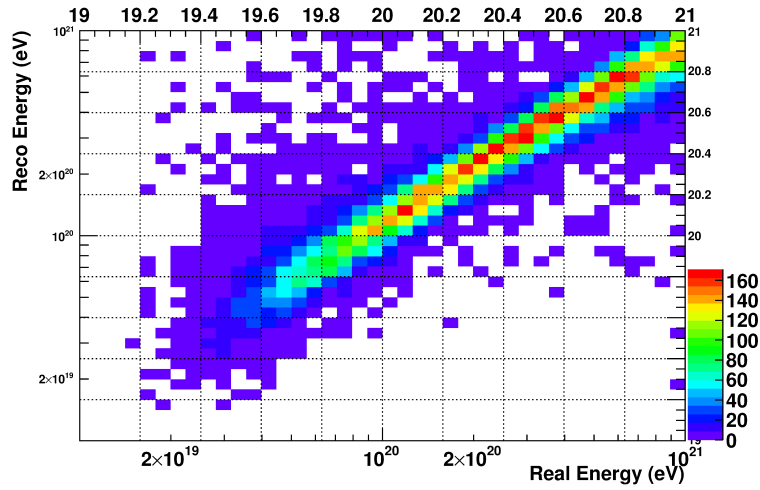


Figure 6.28: reconstructed energy as function of the real energy. The events are simulated in the  $(\pm 270, \pm 200)$  km. The zenith angle has been chosen between 0 and 90 degrees. The near-gap fraction  $< 0.5$  cut has been applied to the sample. The color scale represents the number of events integrated in each bin.

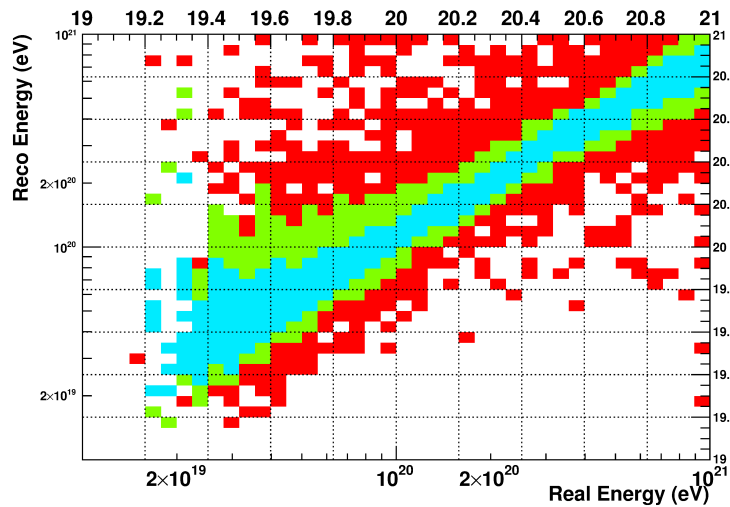


Figure 6.29: confidence intervals with respect to the median energy. In cyan green and red can be respectively identified the  $\pm 34$ ,  $45$  and  $> 45\%$  intervals. The near-gap fraction  $< 0.5$  cut has been applied here.

The cuts on the  $\chi^2$  parameters require a specific discussion. As previously observed an excellent fitting is not guaranteed anymore once the energy grows

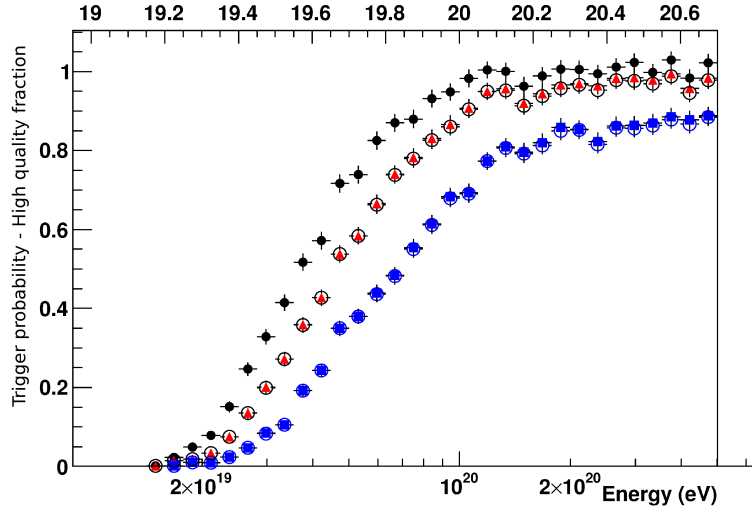


Figure 6.30: efficiency curves associated to different types of cuts. In black can be observed the trigger curve. The curve for the events identified by the pattern recognition and for the events passing the near-gap fraction  $< 0.5$  cut can be respectively observed in red and blue.

above  $2 \cdot 10^{20}$  eV. Obviously the application of a cut in  $\chi^2$  implies a decrease in the efficiency toward the higher energies given the increase in the average  $\chi^2$ . This bad  $\chi^2$  is caused by lacks in the modeling at the highest energies. In the following possible sources of this problem are identified and potential corrections are identified.

In Fig. 6.31 and 6.32 the energy reconstruction performances for the events after applying a cut of  $\chi^2 < 2$  are shown. As expected a depletion of the distribution is visible at the highest energies due to the worsening of the  $\chi^2$ . The overall shape of the distribution does not change in a significant way showing again an overestimation at lower energies and an underestimation at the highest. The confidence intervals shown in Fig. 6.32 seem to be slightly narrower at the highest energies than in the all-event sample. Such a feature seems to suggest how the performances can be improved at the highest energies once the systematics on the fitting are solved.

Finally in Fig. 6.33 the efficiency for the  $\chi^2 < 2$  cut can be seen together with the trigger and the pattern recognition efficiency. Obviously a substantial decrease in the efficiency can be observed above  $10^{20}$  eV showing how the  $\chi^2$  issue becomes more and more relevant with the increasing energy.



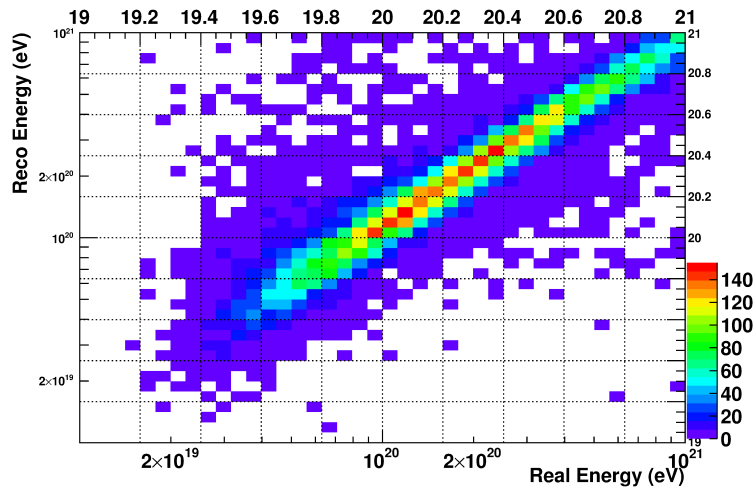


Figure 6.31: full FOV reconstruction performances. The reconstructed energy parameter can be seen as function of the real energy. The events are simulated in the  $(\pm 270, \pm 200)km$ . The zenith angle has been chosen between 0 and 90 degrees. The correction of the systematics has not been performed given the limited set of conditions analyzed in the previous chapter. The cut  $\chi^2 < 2$  is applied here. The color scale represents the number of events integrated in each bin.

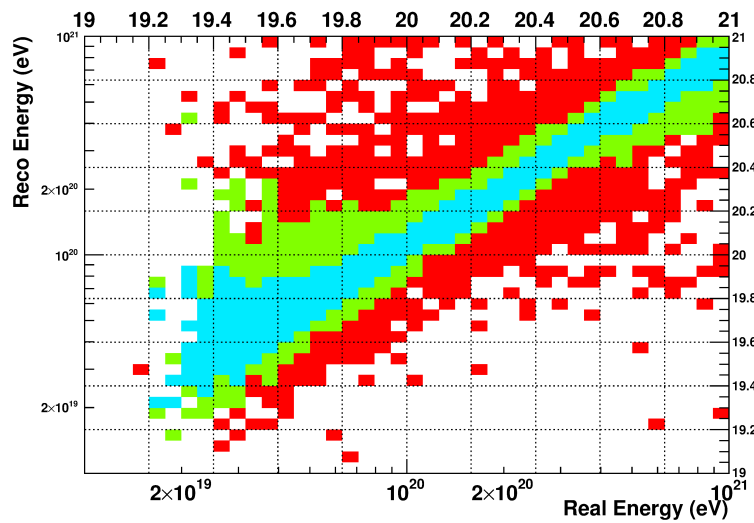


Figure 6.32: confidence intervals with respect to the median energy. In cyan green and red can be respectively identified the  $\pm 34$ ,  $45$  and  $> 45\%$  intervals. The cut  $\chi^2 < 2$  is applied here.

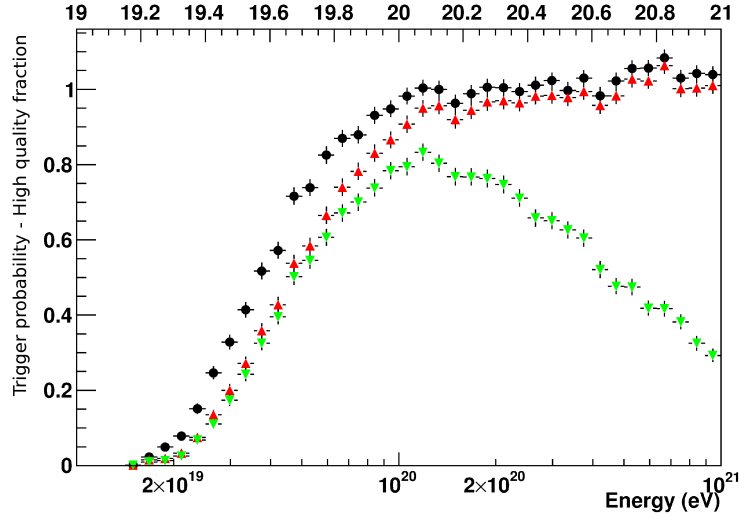


Figure 6.33: efficiency curves associated to different types of cuts. In black can be observed the trigger curve. The curve for the events identified by the pattern recognition and for the events passing the  $\chi^2 < 2$  cut can be respectively observed in red and green.

## 6.6 The $\chi^2$ at the highest energies

In this section the reason of the bad  $\chi^2$  for the fit of the electron curve of the highest energy events is investigated. In Fig. 6.34 the deviation of the reconstructed electron curve from the GIL function is shown. The residuals have been calculated according to

$$\sigma(X) = \left( \frac{N_{el}(X) - N_{el}^{GIL}}{\Delta N_{el}(X)} \right) \quad (6.2)$$

whereas  $N_{el}(X)$  is the reconstructed number of electrons,  $N_{el}^{GIL}$  the value of the GIL fit and  $\Delta N_{el}(X)$  the error on the reconstructed curve. The residuals shown here have been averaged over 8000 events of several energies and 60 degrees zenith angle.

The curve of the events with energy  $3 \cdot 10^{20}$  eV shows strong residuals both around 800–900  $g/cm^2$  and toward the end of the shower development. The GIL function will therefore overestimate the peak and underestimate the tails of the shower.

One possible source of these residuals is the appearance of non linearity effects in the PMTs at the highest luminosities. As a matter of fact, a flattening of the detector counts curve can be observed around the maximum for energies above  $2 \cdot 10^{20}$  eV. After applying the entire reconstruction procedure

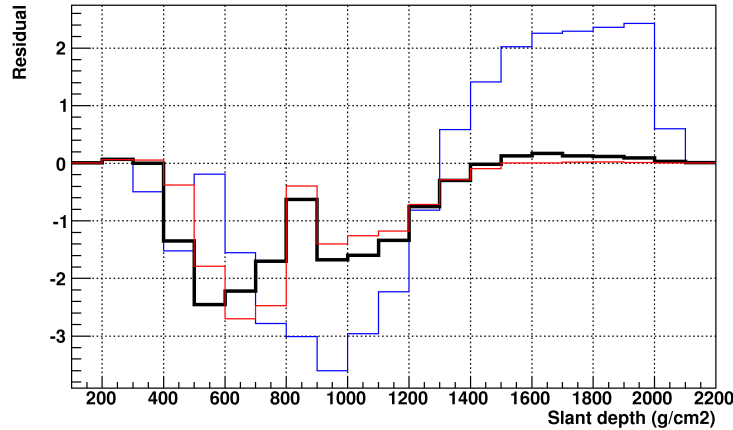


Figure 6.34: residual plot averaged over 8000 events as function of different slant depths. The zenith angle is 60 degrees.

the shower electron curve is therefore deviating from the used GIL function. However, after a careful analysis, performed by analyzing events with and without non-linear PMTs effects, it can be stated that such systematics do not affect significantly the  $\chi^2$ . The presence of such nonlinearity converts into a systematically underestimated energy but the  $\chi^2$  values will change just by some percent with respect to the linear PMTs.

The second mechanism considered was the possible presence of non linearity in the collection of the signal at the focal surface level. In some sense the broader image of the events at the highest energies might not be always properly contained in the used collection area. After several reconstruction tests with different collection areas, it can be also said that no significant variation in the  $\chi^2$  could be detected.

The effect responsible for the bad  $\chi^2$  can be probably identified in the lack of backscattered Cherenkov correction. In Fig. 6.35 the distribution of reduced  $\chi^2$  for 800 events can be seen. In this sample the events have an energy of  $3 \cdot 10^{20}$  eV, a zenith angle of 60 degrees and an impact point in the  $(\pm 20, \pm 20)$  km around the center of the FOV. The  $\chi^2$  curve of events without the simulated backscattered Cherenkov component is shown in red while in black is given the curve with the events including the simulated backscattered Cherenkov component. The removal of the backscattered Cherenkov implies a significant improvement of the  $\chi^2$  value. As a matter of fact, the average value for the  $\chi^2$  is reduced to 1.69 from the 2.62 of the events with backscattered Cherenkov.

In Fig. 6.36 the impact of the Cherenkov contamination is shown. The

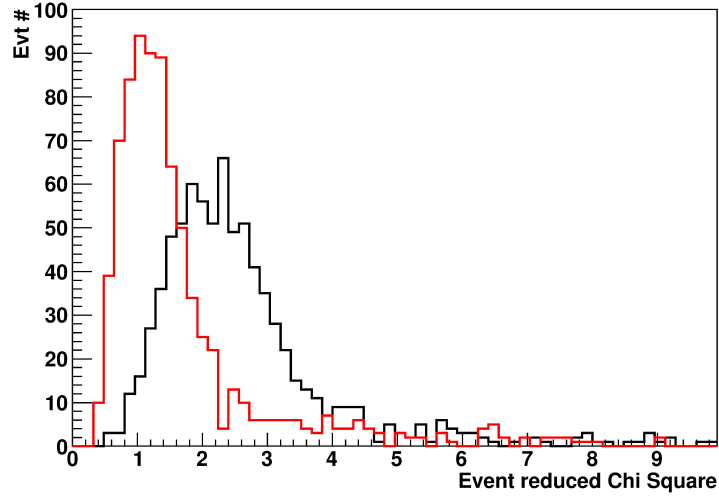


Figure 6.35:  $\chi^2$  curves for 800 events having energy equal to  $3 \cdot 10^{20}$  eV and zenith angle of 60 degrees. All the events have impact point within the  $(\pm 20, \pm 20)$  km square. In red the curve without simulated backscattered Cherenkov can be seen. In black is the curve with backscattered Cherenkov. The average  $\chi^2$  of the red curve is 1.69. The average for the black curve is 2.62.

counts curves averaged over 200 events has been produced and marked in black. The thick black curve represents the counts originated by fluorescence photons. The thin black curve, on the other hand, represents the total counts curve. The deviation of the counts curve from the fluorescence curve is represented as a thick red line. The Y axis represent the counts number (left side) and the deviation (right side—marked in red). The deviation has been expressed in  $\sigma$  units and is intended to quantify the deviation of the total counts curve from the fluorescence curve. The deviation has been expressed following

$$\Delta(GTU) = \frac{counts^{TOT} - counts^{FLUO}}{\sqrt{counts^{FLUO}}} \quad (6.3)$$

Fig. 6.36 is for  $10^{20}$  (left panel) and  $3 \cdot 10^{20}$  eV (right panel). As can be clearly observed in such plots, the  $3 \cdot 10^{20}$  eV plot is characterized by a much more statistically relevant Cherenkov component. At the maximum the events are, in fact, characterized by a deviation from the fluorescence of 0.5 and 1  $\sigma$  for the low and high energy respectively. Toward the later stages of the shower the deviation from the fluorescence grows in both cases but the largest deviation is always displayed by the highest energy events. For the  $10^{20}$  eV event the deviation becomes statistically significant ( $> 1 \cdot \sigma$ ) just  $\sim 8-9$  GTUs after the maximum.

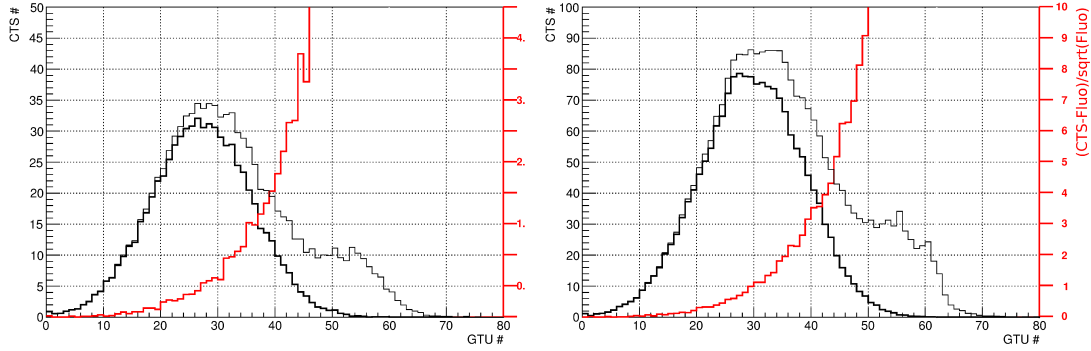


Figure 6.36: deviation of the total counts curve with respect to the curve generated by fluorescence photons (red line). The deviation value is expressed in  $\sigma$  units and can be read on the right hand red axis. Superposed with that the total counts curve and the counts from fluorescence photons can be observed respectively as thin and thick black curves. All the curves are mediated over 200 events, 60 degrees zenith angle and having impact point in the  $(\pm 20, \pm 20)$  km square. **Left Panel:**  $10^{20}$  eV. **Right Panel:**  $3 \cdot 10^{20}$  eV.

For this reason the Cherenkov will not affect the fit apart from a systematic shift of the energy value. In some sense at  $10^{20}$  eV the contamination is present and increasing the reconstructed energy value but still not statistically deviating from the GIL fit. As the signal strength increases the Cherenkov signal will exceed the statistical oscillations given the smaller statistical errors obtained in this range.

## 6.7 The reconstructed Cosmic Ray spectrum

This section of the thesis is devoted to the reconstructed spectrum. In this section the shape of the reconstructed spectrum is estimated. Here we take into account the effects of the energy reconstruction on the spectrum.

As in Chapter 4 the Pierre Auger and Telescope Array<sup>2</sup> are used. The JEM-EUSO FOV is considered to be of  $1.4 \cdot 10^5 km^2$  and the integration over the solid angle is performed over the 0–90 degrees interval. The astronomical duty cycle is assumed to be 0.2. The effects of clouds and city lights are also included and further reduce the observational duty cycle.

In Fig. 6.37, the reconstructed spectra according to the published Pierre Auger spectrum can be seen for several cuts. Superposed with the reconstructed spectra, the triggered curve has been plotted. It should be kept in mind that triggered curves are function of the real energy while reconstructed

<sup>2</sup>The detailed explanation on the mathematical shape of such functions can be found in Chapter 4.

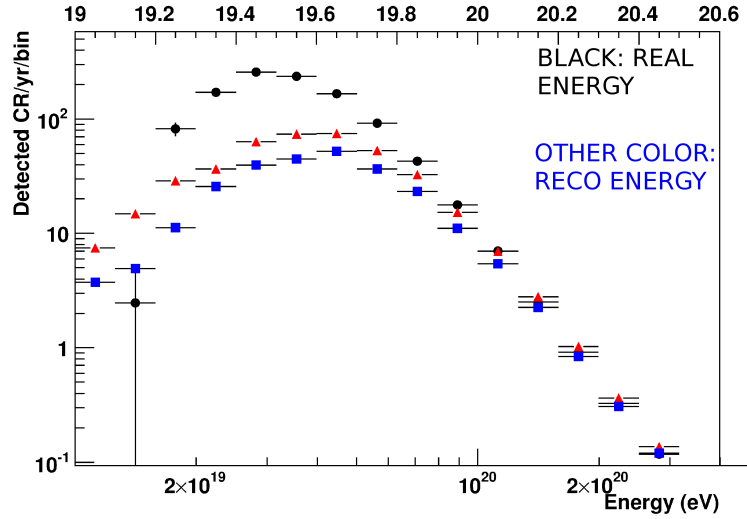


Figure 6.37: reconstructed spectrum according to the Auger flux. In black the trigger spectrum and in red the reconstructed spectrum for all the events recognized by the pattern recognition is shown. In blue the reconstruction of the events surviving the  $\text{DOF} > 5$  cut is shown.

curves of the reconstructed. More in detail the black curve represents the triggered spectrum while the red one is the spectrum of all the events recognized by the pattern recognition. The blue points show the spectrum for the cut on the number of  $\text{DOF} > 5$ . As can be seen a significant loss of events can be seen between  $2 \cdot 10^{19}$  and  $10^{20}$  eV. Such a feature is explained by the presence of a lower efficiency after the application of quality cuts. Moreover effects of spillover are present both at high and low energy. The peak at the low energies will therefore be smeared out since a lot of its events will migrate toward lower and higher energies. In fact the finite energy resolution will cause the detection of a significant number of events lower than  $2 \cdot 10^{19}$  eV in a range where a very limited number of triggering events should be expected. At the highest energies just a limited spillover can be observed given the better energy resolution at such energy. As can be seen above  $10^{20}$  eV just a very small excess of reconstructed events can be observed with respect to the triggered spectrum.

However as already discussed, an overestimation of the energy is generally present under  $10^{20}$  eV. An underestimation will set in above such a threshold. As a result, the spectrum is steeper than what would be observed after the correction. Because of this reason the spillover toward higher energies could be underestimated in the present study.

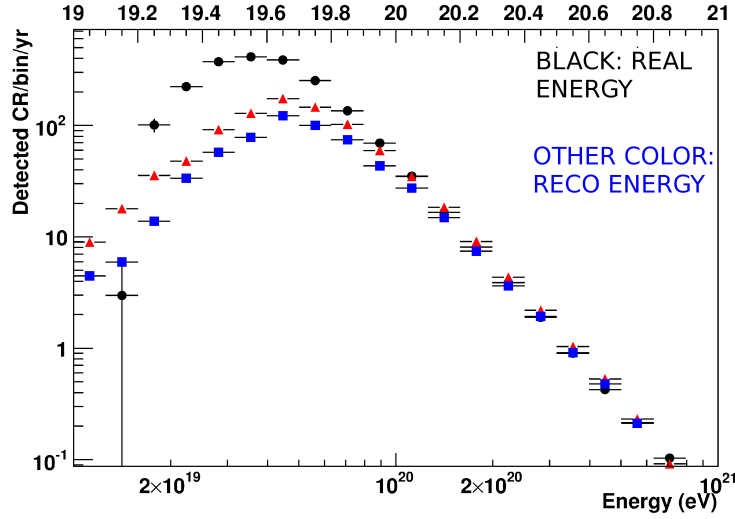


Figure 6.38: reconstructed spectrum according to the TA flux. In black the trigger spectrum is shown. In red the reconstructed spectrum is depicted for all the events recognized by the pattern recognition. In blue the reconstruction of the events surviving the  $\text{DOF} > 5$  cut is shown.

In Fig. 6.38 the reconstructed spectrum according to the Telescope Array published spectrum has been shown. The most significant difference with the previous plot is give by the much harder spectrum. As shown in the previous plot spillover is present both at higher and lower energies.

## 6.8 Parameter variation

The last topic of this chapter is devoted to an alternative reconstruction concept developed in the course of the thesis. One of the most critical points in the present reconstruction procedure is the initial assumption of the maximum altitude. Such a choice is necessary to build the shower test for the first energy and  $X_{max}$  estimation.

The present algorithm has been therefore extended to include the "backward procedure" from the shower to the detector. A similar procedure has been shown in Chapter 5 to evaluate the statistical error of the algorithms. In that context however, just energy and longitudinal maximum position have been variated.

In the present section the combination of the 3 parameters energy, longitudinal maximum position and detector–maximum distance have been variated. The test shower is therefore built based on the set of variated parameters and

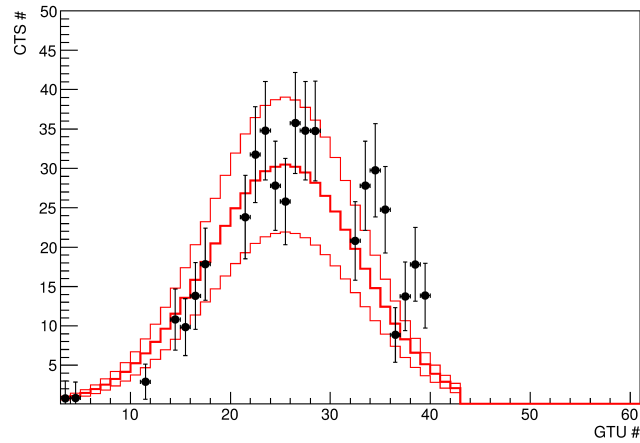


Figure 6.39: counts curve as identified by the pattern recognition (points with error bars). The test counts curve obtained with the first set of parameters is shown as thick red line. The curves obtained for a  $\pm 3 \cdot 10^{19}$  eV energy variation are shown as thin red lines.

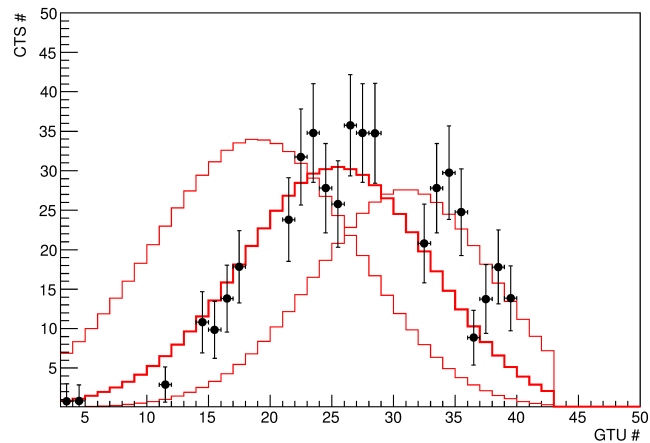


Figure 6.40: counts curve as identified by the pattern recognition (points with error bars). The test counts curve obtained with the first set of parameters is shown as thick red line. The curves obtained for a  $\pm 200 g/cm^2$  longitudinal variation are shown as thin red lines.

the entire event is followed from the shower to a test counts curve on the detector. The final step consists of the calculation of the deviation of the test curve from the originally reconstructed curve. Such a value is calculated



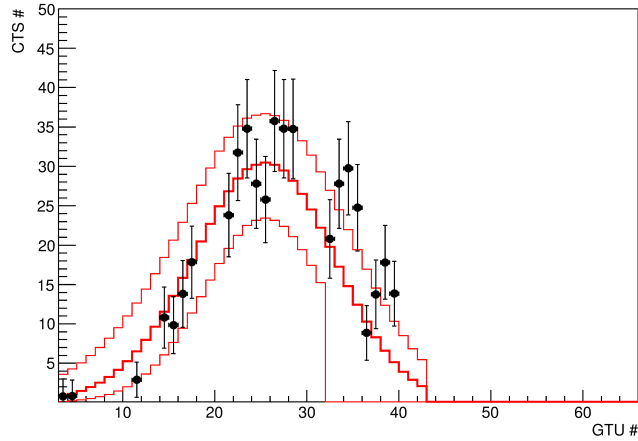


Figure 6.41: counts curve as identified by the pattern recognition (points with error bars). The test counts curve obtained with the first set of parameters is shown as thick red line. The curves obtained for a  $\pm 4\text{km}$  detector distance variation are shown as thin red lines. The previous encounter with the earth surface can be observed around GTU 32.

according to Eq. 6.4

$$\sigma(X) = \frac{N_{counts}^{reco*} - N_{counts}^{reco}}{\Delta N_{counts}^{reco}} \quad (6.4)$$

In the present equation  $N_{counts}^{reco*}$  represents the counts calculated in one of the backward tests,  $N_{counts}^{reco}$  the reconstructed counts curve as produced by the pattern recognition and  $\Delta N_{counts}^{reco}$  the error on it. The set of parameters which delivers the minimal deviation from the first reconstruction will be considered as the best set of parameters.

The procedure has been implemented and it is currently working. In Figs. 6.39, 6.40 and 6.41 the basic shower parameters have been varied. In all the plots the pattern recognition curve is depicted as points and superposed with the backward test detector response. As thick line we represent the backward test response obtained with the parameters of the first cycle. The thin red lines are representing the variation on such parameter. In Fig. 6.39 the energy is varied by  $\pm 3 \cdot 10^{19}$  eV while in Figs. 6.40 and 6.41 the  $X_{max}$  and distance from the detector are respectively varied of  $200 \text{ g/cm}^2$  and  $4 \text{ km}$ . Such plots can give an idea of how the entire procedure is established. As can be seen a higher energy implies a higher counts curve. On the other hand, a shower developing higher in the atmosphere will result in both more intense and much longer curve. Such an effect is due to the minor absorption in the atmosphere and to the smaller density at the very high altitudes. A variation on the longitudinal position of the maximum will

obviously imply a translation of the maximum. Another effect to notice is the lower maximum value for showers having deeper maximum. Again such an effect is due to the lower atmospheric transmittance for deeper showers. In Fig. 6.41 it can be seen how the deeper shower will impact the ground at a significantly earlier stage. For this reason no counts can be expected after a certain time. The algorithm will therefore look for the set of parameters which can produce the best fitting curve. The iteration for the optimization of the shower parameters is however still under development and will not be shown in the course of this thesis.

# Conclusions: the JEM–EUSO Performances

In this thesis we focused on the assessment, through simulations, of several key performances of the JEM–EUSO mission. In particular we have studied: 1) the trigger efficiencies for the nadir and tilted mode; 2) the reconstruction of the energy; and 3) the reconstruction of the maximum of the shower  $X_{max}$ .

In Chapter 4, the trigger efficiencies as a function of the energy have been estimated for different background conditions, different types of the primary particles and for different selections of the quality of the showers, that is for different cuts. The yearly exposure of the JEM–EUSO mission in nadir mode has been estimated to be  $\sim 6 \cdot 10^4 \text{ km}^2 \cdot \text{sr} \cdot \text{yr}$  or  $\sim 8\text{--}9$  times the one of the Pierre Auger Observatory at  $10^{20}$  eV. For large tilting angles and at extreme energies, where JEM–EUSO is expected to discover new science, the yearly exposure can increase up to a factor 21 with respect to the one of the Pierre Auger Observatory.

We have also shown that an increase of the maximum tolerated background, viable at extreme energies, further increases the exposure. Accepting a higher operational background increases the JEM–EUSO yearly exposure in nadir configuration up to 11 times the Pierre Auger’s exposure.

We have also presented the expected triggered spectra using the fluxes published by the Pierre Auger and TA collaborations. The number of particles triggered by JEM–EUSO is significantly increased at energies above  $10^{20}$  eV with respect to ground arrays. In fact, as can be observed in Fig. 1.14 and 1.15 both the Auger and the Telescope Array detectors can rely just on few of events above  $10^{20}$  eV in several years of operation. JEM–EUSO will instead add several tens of events each year regardless of the parameterized flux or of the composition. This confirms that JEM–EUSO can explore the extreme energies region with unprecedented capabilities. We have also shown that JEM–EUSO trigger particles even at low energies such as  $10^{19}$  eV.

The reduction of the sample to a high quality sub–selection implies, of

course, a lower efficiency threshold, however the relatively high flux at these low energies allows a meaningful overlapping of the JEM–EUSO spectrum with the ones obtained by ground detectors. We have identified in this work the range where a superposition with ground arrays can be meaningfully achieved.

The efficiency, the exposure and triggered spectra, as a function of the energy and of the arrival directions, have been calculated also for the tilt mode and for different tilt angles. The tilt configuration has been confirmed to increase the exposure above  $10^{20}$  eV. On the other hand no significant loss is found slightly above  $4\text{--}5\cdot 10^{19}$  eV especially for a mild tilting case. Our findings have confirmed the rationale and the viability of the planned operation of the mission: the mission should start observing along nadir and then, after a few years, should start operation in tilt mode. In other words after a significant overlapping with the ground arrays has been achieved, and more than one hundred events have been observed at extreme energies, the mission can be tilted to maximize the exposure at most extreme energy ranges, towards the still unexplored energy frontier.

The compliance of the JEM–EUSO telemetry capabilities with the scientific case has been also verified. More in detail, the average size of an event given the typical event distribution has been estimated. The distributions of the number of triggered PDMs, of PDMs with signal and the duration of the signal on the focal surface have been obtained. Other aspects like the persistency of the signal on single PDMs, the fraction of signal in triggering PDMs and the fraction of signal lost after a certain maximal time threshold are also key operational parameters, which have been estimated for the first time in this thesis.

We have concluded that JEM–EUSO can allow the transmission of the entire sample of triggering PDMs. The extension of the ring buffer to 256 GTUs (from 128) should however be considered by the hardware team to minimize the signal loss in non triggering PDMs. For completeness the study has been extended for a  $10^{21}$  eV sample. The constrains seem however to be smaller than in the average sample. In fact, whenever the signal is on the focal surface a trigger is issued with a very high probability clearly identifying the shower position. All these findings should be taken into account to improve the design of the trigger electronics.

In this thesis we have developed, for the first time, a detailed energy reconstruction procedure for the mission. Tables presented in Chapter 5 summarize the entire reconstruction chain. The basic idea is to reconstruct the electron profile of the shower from the observed counts taking into account all the various steps which contribute to the formation of the signal. We developed two reconstruction methods. The first uses the observed Cherenkov

---

mark, while the second relies on a parameterization of the maximum of the shower and on its direction. We have also estimated the systematic uncertainties associated to the various steps of the reconstruction procedure. Although significant in a few cases, which deserve a deeper study, in most of the cases, systematics can be taken into account through a constant factor. In fact, the rather stable nature of most of such factors makes their correction very easily implantable. With this work we have therefore posed the solid ground on which further studies can grow. A similar study, has been performed also for the reconstruction of the maximum of the shower, the  $X_{max}$  parameter. The mismatch of the single reconstruction steps with respect to the simulation has been also performed.

In Chapter 6 the energy and  $X_{max}$  reconstruction procedures have been tested and used for the study of the expected performances of the mission. The width of the event distribution and the systematic uncertainties have been obtained for different samples of events, as a function of the energy, of the arrival angle and of the position of the shower in the FOV. The developed reconstruction procedures achieve excellent performances for events in the center of the FOV. In fact, at  $10^{20}$  eV the resolution can be as good as  $\pm 10\%$ . Under such conditions the systematics have been studied in detail and a preliminary correction has been successfully performed. For obvious reasons, the reconstruction performances worsen at the lowest energies both in terms of systematics and of distribution width. This feature can be observed both for the energy and  $X_{max}$  reconstruction. The best performances seem however to be achieved around  $10^{20}$  eV while at the highest energies performances surprisingly slightly worsen, for both methods, with and without the use of the Cherenkov mark. We have understood the origin of this puzzling behavior to lie in the missing backscattered Cherenkov correction.

We have studied the quality of the modeling of the deconvoluted shower's electron profile. Furthermore possible cuts to improve the quality of the events have been introduced. At almost all energies, angles and for both methods, the  $\chi^2$  of the fit of the deconvoluted electron profile is always below 1.6. A significant exception is given by the very high energies where the reconstructed data show a statistically significant deviation from the fitting GIL function. Such a behavior, can be explained with the presence of the backscattered Cherenkov contamination. Above  $10^{20}$  eV the curve is significantly deformed and the GIL function does not model the observed profile. The introduction of the correction of the Cherenkov backscattered component is matter of further studies. Another way to evaluate the quality of the events is via the number of DOF. Such a number increases with the energy and with the inclination angle. As a matter of fact, quality cuts on this parameter tend to reject vertical and low energy events. Also the distance

of the signal from a PMT gap can be used as an estimate of the quality of the event. As explained in Chapter 6, the signal in the vicinity of a gap is potentially exposed to losses. The fraction of potentially biased signal has been therefore estimated for different classes of events. We have also estimated, the fraction of events with Cherenkov mark. At all the energies the Cherenkov recognition algorithms fail above 50 deg except at  $3 \cdot 10^{20}$  eV. This is due to the angular distribution of the Cherenkov emission, which reflects on a larger surface at the highest zenith angles worsening the signal to noise ratio.

The reconstruction performances have been also assessed in different parts of the FOV. No significant performance degradation can be observed in the inner 100 km of the FOV. On the other hand, a worsening of the performances in the external part of the FOV can be observed as consequence of the worse signal quality.

The simulation on the all–event sample has been also performed in order to give a more realistic estimate of the JEM–EUSO performances. The resolution at the lowest energies ( $3 \cdot 10^{19}$  eV) has been estimated to be  $\sim 60\text{--}70\%$ . On the other hand the resolution is reduced to  $\sim 30\%$  at  $10^{20}$  eV and  $20\%$  at  $2 \cdot 10^{20}$  eV. This study shows that the actual configuration of JEM–EUSO can meet the requirements on the energy resolution for the all event sample.

From our studies on  $X_{max}$  we have concluded that the systematics in the geometry can sensibly affect the quality of the reconstruction. An improvement of the procedure is left for further studies. However, our preliminary studies have shown that in most cases JEM–EUSO will be able to distinguish charged primary particles from neutrinos, or other exotic particles especially at the exploratory highest energies. This confirms that the current requirement of the mission on  $X_{max}$  can be achieved. Studies on an improved reconstruction procedure of the maximum can tell us in the future more on the capabilities of discriminating different types of charged primaries.

A study of cuts to improve the reconstruction performances for a selected subsample of events has been also performed. A significant improvement can be obtained with the cut on the number of DOF  $> 5$ . Such a cut improves considerably the resolution at the energies under  $10^{20}$  eV. A large number of outliers is also suppressed. No appreciable improvement is obtained at the highest energies. The cuts on  $\chi^2$  and on the gaps fraction does not bring almost any improvement in the resolution, except at the highest energies. While improving the quality of the signal, quality cuts implies a loss in efficiency. In Chapter 6 the efficiency curves for all the studied selections have been shown. As a matter of fact, the DOF  $> 5$  cut suppresses much more events than all the other cuts.

We have eventually calculated, for the first time ever, the reconstructed

---

spectrum observed by JEM–EUSO. Both the Pierre Auger and TA published fluxes have been used for all the cuts. The limit of the present estimate is however the non optimal correction of the systematics. In the low energy ranges a tendency toward the energy overestimation is present. At the highest energies the reconstruction tends to underestimate the energy. For this reason the spectrum shown in this thesis is most likely softer than it will be after the systematics correction. Nevertheless a key results is that a very small spillover is observed at the highest energies for both spectra. Further studies will reduce the systematics.

Along this line, a work in progress for an iterative optimization has been shown. The main message to the reader is how a possibility of an improvement is open in order to avoid systematics on the first geometrical reconstruction. The parameters will be changed and the deviation from the reconstructed data will be minimized. An alternative reconstruction method is therefore available and is in course of optimization.

The present work should however be seen as the first estimate ever of the JEM–EUSO performances for the energy and  $X_{max}$  reconstruction. It opened the way to further improvements of the reconstruction procedures while conducting a detailed study of the systematics and of the potential cuts. On the base of the present work, more detailed studies can be therefore carried out to assess the scientific impact of the above presented results. Assuming a particular theoretical scenario will in fact determine a particular spectral shape, composition and arrival direction at the Earth. Given such assumptions, future works should assess if the presented JEM–EUSO performances allow the discrimination between different theoretical scenarios.





# Acronyms

AGASA: Akeno Giant Air Shower Array  
AGN: Active Galactic Nuclei  
ASIC: Application Specific Integrated Circuit  
CCB: Cluster Control Board  
CORSIKA: COsmic Ray SIMulation for KAscade  
CR: Cosmic Ray  
CMB: Cosmic Microwave Background  
CPU: Central Processing Unit  
CSO: Compact Symmetric Objects  
DOF: Degrees Of Freedom  
DSP: Digital Signal Processor  
EAS: Extended Air Showers  
EC: Elementary Cell  
ESAF: Euso Simulation & Analysis Framework  
EUSO: Extreme Universe Space Observatory  
FB: FireBall  
FEE: Front End Electronics  
FOV: Field Of View  
FPGA: Field Programmable Gate Array  
FR-I: Fanaroff-Riley I  
FR-II: Fanaroff-Riley II  
GIL: Gaisser Ilina Linsley  
GRB: Gamma Ray Burst  
GTU: Gate Time Unit  
GZK: Greisen Zatsepin Kuzmin  
HiRes: High Resolution Fly's Eye  
HL – GRB: High Luminosity – GRB  
HTV: H-II Transfer Vehicle  
INFN: Istituto Nazionale di Fisica Nucleare  
IGM: InterGalactic Medium  
IR: InfraRed

ISM: InterStellar Medium  
ISS: International Space Station  
JEM: Japanese Experimental Module  
JEM–EUSO: Extreme Universe Space Observatory on the Japanese Experimental Module  
KASCADE: KARlsruhe Shower Core Array DETector  
LIDAR: Light Detection And Ranging  
LL – GRB: Low Luminosity – GRB  
LOWTRAN: LOW–resolution TRANsmittance  
LTT: Linear Tracking Trigger  
MPU: MicroProcessor Unit  
NS: Neutron Star  
OOP: Object Oriented Programming  
OWL: Orbiting Wide–angle Light–collectors  
PAO: Pierre Auger Observatory  
PDM: Photo Detection Module  
PMMA: PolyMethyl MethAcrylate  
PMT: PhotoMulTiplier  
PSF: Point Spread Function  
ROC: ReadOut and Control  
SCU: Storage and Control Unit  
SLAST: Shower Light Attenuated to the Space Telescope  
SNR: Supernova Remnant  
UHE: Ultra High Energy  
UHECR: Ultra High Energy Cosmic Ray  
UHE–Neutrino: Ultra High Energy Neutrino

# Bibliography

- [1] T. Wulf, "About the radiation of high penetration capacity contained in the atmosphere", *Physik. Zeitschr.*, no. 5, 152–157 (1909)
- [2] D. Pacini, "La radiazione penetrante alla superficie ed in seno alle acque", *Il N. Cim.*, Serie VI – Tomo III. 1912
- [3] V. F. Hess, "Penetrating Radiation in Seven Free Balloon Flights", *Physik. Zeitschr.* 13 (1912), p. 1084
- [4] M. S. Longair, "High Energy Astrophysics", vol. 1
- [5] R. A. Millikan, "High frequency rays of cosmic origin," *Proc. Natl. Acad. Sci. U.S.A.* 12, 48–55 (1926), p. 52
- [6] H. Geiger, W. Müller, "Das Elektronenzählrohr" , *Physik. Zeitschr.*, 29 p. 839–841 (1928)
- [7] E. Rutherford and H. Geiger, "An electrical method of counting the number of  $\alpha$  particles from radioactive substances," *Proc. of the Royal Society, Series A*, vol. 81, no. 546, 141–161 (1908)
- [8] L. Bonolis, "Walther Bothe and Bruno Rossi: The birth and development of coincidence methods in cosmic-ray physics", [arXiv1106.1365v2](https://arxiv.org/abs/1106.1365v2) (2011)
- [9] W. Kolhörster, "Eine neue Methode zur Richtungsbestimmung von Gamma-Strahlen" *Die Naturwiss.* 16, 10441045 (1928).
- [10] W. Bothe, W. Kolhörster, "Die Natur der Höhenstrahlung," *Die Naturwiss.* 17, 271–273 (1929), 272.
- [11] C. T. R. Wilson, "On an Expansion Apparatus for Making Visible the Tracks of Ionizing Particles in Gases and Some Results Obtained by Its Use", *Proc. R. Soc. Lond.* (1912) 87–595, 277–292
- [12] Skobelzyn, D.V.; "Über eine neue Art sehr schneller  $\beta$ -Strahlen", *Z. Phys.* 54, 686 (1929)

- [13] B. Rossi, "Method of Registering Multiple Simultaneous Impulses of Several Geiger's Counters", *Nature* 125, 636–636 (1930)
- [14] B. Rossi, "On the Magnetic Deflection of Cosmic Rays", *Phys. Rev.* 36, 606–606 (1930)
- [15] L. Alvarez, A. H. Compton, "A Positively Charged Component of Cosmic Rays", *Phys. Rev.* 43, 835–836 (1933)
- [16] B. Rossi, "Measurements on the Absorption of the Penetrating Corpuscular Rays coming from Inclined Directions", *Nature* 128, 408 (1931)
- [17] H. J. Bhabha, W. Heitler, "The passage of fast electrons and the theory of cosmic showers", *Proc. R. Soc. Lond., Ser. A* 159, 432–458 (1937)
- [18] F. Carlson, J. R. Hoppenheimer, "On Multiplicative Showers", *Phys. Rev.* 51, 220–231 (1937)
- [19] P. Auger et al., "Extensive cosmic-ray showers", *Rev. Mod. Phys.* 11, 288–291 (1939)
- [20] S. H. Neddermeyer, C. D. Anderson, "Note on the nature of cosmic-ray particles" *Phys. Rev.* 51, 884–886, (1937)
- [21] J. C. Street, E. C. Stevenson, "New evidence for the existence of a particle of mass intermediate between the proton and electron" *Phys. Rev.* 52, 1003–1004 (1937).
- [22] C. M. G. Lattes et al., "Observation of the tracks of slow Mesons in photographic emulsions", *Nature* 160 (4066), 453–456 (1947).
- [23] P. Freier et al, "Evidence for heavy nuclei in the primary cosmic radiation", *Phys. Rev.* 74, 213–217 (1948)
- [24] E. Fermi, "On the origin of cosmic radiation", *Phys. Rev.* Vol 75, Numb 8 (1949).
- [25] R. D. Blandford, J. P. Ostriker, "Particle acceleration by astrophysical shocks", *The Astrophysical Journal* 221, L29–L32 (1978)
- [26] B. Rossi, "High Energy Cosmic Rays", *Scientific American* (1959)
- [27] J. Linsley, "Evidence for a primary cosmic-ray particle with energy  $10^{20}$  eV", *Phys. Rev. Lett.* 10, 146–148 (1963)
- [28] J. Linsley, L. Scarsi, and B. Rossi, "Extremely Energetic Cosmic-Ray Event", *Phys. Rev. Lett.* 6, 485–487 (1961)

- [29] K. I. Gringauz, "Structure of the Earth's ionized gas shell according to data of direct measurements of local charged particle concentration conducted in the USSR" (1962)
- [30] A. Chudakov, 5<sup>th</sup> Inter-American Seminar on Cosmic Rays (Bolivia) (1962)
- [31] K. Greisen, Proc. Int. Cosmic Ray Conference (London) (1965)
- [32] G. W. Mason et al., "Observations of Extensive Air Showers by Air Fluorescence Description of Experimental Techniques", Proc. 15th Int. Cosmic Ray Conference (Budapest) (1977)
- [33] A. N. Bunner, "Cosmic Ray Detection by atmospheric Fluorescence", PhD Thesis (1967)
- [34] K. Greisen, "End to the cosmic-ray spectrum?", Phys. Rev. Lett. 16, 748-750 (1966)
- [35] J. Strutt, "On the light from the sky, its polarization and color," Philosoph. Mag., 4 41, 107-120, 274-279 (1871)
- [36] H.C. Van de Hulst, "Light scattering by small particles", Wiley and Sons, (1957)
- [37] S. Chapman, "On Ozone and atomic Oxygen in the Upper Atmosphere", Philosoph. Mag. (1930)
- [38] J. W. Chamberlain, "The Ultraviolet Airglow Spectrum", Astroph. Jour., 121, p. 277 (1955)
- [39] J. W. Chamberlain, "Physics of the Aurora and Airglow", AGU, Washington, (1995)
- [40] M. Füllekrug, "Sprites elves and intense lightning discharge", NATO advanced science institute (2004)
- [41] R M Tennent, " The Haverah Park extensive air shower array", Proc. Phys. Soc. 92 622 (1967)
- [42] R. Cady, "Progress report on the Utah Fly's Eye", Int. Cosmic Ray Conference, (Bangalore) (1983)
- [43] G. Taubes "Pattern Emerges in Cosmic Ray Mystery", Science, V 262, Dec 1993
- [44] W. Au, J. Boyer et al., "Description and Status of the High Resolution (HIRES) Fly's Eye Experiment", Int. Cosmic Ray Conference (Dublin) (1991)

- [45] N. Chiba et al., "Akeno Giant Air Shower Array (AGASA) Covering 100km<sup>2</sup> Area", Int. Cosmic Ray Conference (Dublin) (1991)
- [46] Pierre Auger Collaboration, "The Pierre Auger Observatory progress and first results", Int. Cosmic Ray Conference (Pune) (2005)
- [47] Pierre Auger Collaboration, "Correlation of the Highest-Energy Cosmic Rays with Nearby Extragalactic Objects", Science Vol. 318, p 938–943 (2007)
- [48] Benson, R., Linsley, J., "Satellite observation of cosmic ray air showers", Int. Cosmic Ray Conference, (Paris) (1981)
- [49] T. Ebisuzaki, "The JEM-EUSO mission", Int. Cosmic Ray Conference (Beijing) (2011)
- [50] S. P. Swordy, "The energy spectra and anisotropies of Cosmic Rays", Space Science Reviews 99: 85–94, (2001)
- [51] L. A. Fisk, "An Interpretation of the Observed Oxygen and Nitrogen Enhancements in Low-Energy Cosmic Rays", Ast. J., vol. 190, p.L35 (1974)
- [52] T. Stanev, "High Energy Cosmic Rays", Springer (2009)
- [53] G. V. Kulikov, G. B. Khristiansen, "On the size distribution of Extensive Atmospheric Showers", Zhur. Eksptl'. i Teoret. Fiz., Vol. 35
- [54] B. Peters, "Primary cosmic radiation and extensive air showers", Il Nuovo Cimento, Vol. 22, N. 4 800–819 (1961)
- [55] J.R. Hörandel, "Models of the knee in the energy spectrum of cosmic rays", Astrop. Phys., 21(3), 241–265, (2004)
- [56] M. Nagano, "Energy spectrum of primary cosmic rays above 10<sup>17</sup> eV determined from the extensive air shower experiments at Akeno", J. Phys. G 18, 423–442
- [57] D. J. Bird, "Evidence for correlated changes in the spectrum and composition of cosmic rays at extremely high energies", Phys. Rev. Lett. 71, 3401–3404 (1993)
- [58] M. A. Lawrence, "The CR energy spectrum above 4 \* 10<sup>17</sup> eV as measured by the Haverah Park array", J. Phys G, 17, 733–757
- [59] Cascade Grande Collaboration, "Knee-like Structure in the Spectrum of the Heavy Component of Cosmic Rays Observed with KASCADE-Grande", Phys. Rev. Lett. 107 (2011)

- 
- [60] J. Linsley, "Primary cosmic rays of energy  $10^{17}$  to  $10^{20}$  eV, the energy spectrum and arrival directions Proc. 8th ICRC, Jaipur, vol. 4, p. 77, (1963)
- [61] A. M. Hillas, "Can diffusive shock acceleration in supernova remnants account for high-energy galactic cosmic rays?", *J. Phys. G Nucl. Part. Phys.* 31, R95–R131 (2005)
- [62] J.R. Hörandel, "Models of the Knee in the Energy Spectrum of Cosmic Rays", *Astrop. Phys.* 21, 241–265, (2003)
- [63] T. Wibig, A. W. Wolfendale, "At what particle energy do extragalactic cosmic rays start to predominate?", *Nucl. Part. Phys.* 31, 255 (2005)
- [64] N. Globus et al., "UHE nuclei propagation and the interpretation of the ankle in the cosmic-ray spectrum", *Astr. and Astroph.*, (2005)
- [65] V. Berezhinsky, "On astrophysical solution to ultrahigh energy cosmic rays", *Phys. Rev. D* 74, (2006)
- [66] The Pierre Auger Collaboration, "Measurement of the energy spectrum of cosmic rays above  $10^{18}$  eV using the Pierre Auger Observatory", *Phys. Lett. B* 685, 239–246 (2010)
- [67] The HiRes Collaboration, "Measurement of the Flux of Ultra High Energy Cosmic Rays by the Stereo Technique", *Astr. Phys.* 32, 53–60 (2009)
- [68] R. Aloisio, "Ultra High Energy Cosmic Rays: The disappointing model", *arXiv:0907.5194v2 [astro-ph.HE]* (2011)
- [69] The Pierre Auger Collaboration, "Update on the correlation of the highest energy cosmic rays with nearby extragalactic matter", *Astrop. Phys.* 34 314 (2010)
- [70] The Telescope Array Collaboration, "Search for Anisotropy of Ultra-High Energy Cosmic Rays with the Telescope Array Experiment", *arXiv:1205.5984v1* (2012)
- [71] J. Blümer et al., "Cosmic Rays from the Knee to the Highest Energies", *arXiv:0904.0725v1* ,(2009)
- [72] S. Knurenko, "Cerenkov radiation of cosmic ray extensive air showers. Part 1. Lateral distribution in the energy region of  $10^{15}$ – $10^{17}$  eV", *Int. Cosmic Ray Conference (Hamburg)* (2001)
- [73] S. Knurenko, "Spectrum and mass composition of cosmic rays in the energy range  $10^{15}$ – $10^{17}$  eV derived from the Yakutsk array data", *Int. Cosmic Ray Conference (Beijing)* (2011)

- 
- [74] A. A. Ivanov, "Measuring extensive air showers with Cherenkov light detectors of the Yakutsk array: The energy spectrum of cosmic rays", arXiv:0902.1016v1 (2009)
- [75] L. F. Fortson et al., "Composition results at the Knee from CASA-BLANCA", Int. Cosmic Ray Conference (Salt Lake City) (1999)
- [76] M. Cassidy, "CASA-BLANCA: A Large Non-Imaging Cerenkov Detector At CASA-MIA", arXiv:astro-ph/9707038v1 (1997)
- [77] S.F. Berezhnev, "The Tunka-133 EAS Cherenkov light array: Status of 2011", Nucl. Inst. and Met. In Phys. Res. A, doi:10.1016/j.nima.2011.12.091 (2012)
- [78] KASCADE Collaboration, "Muon density measurements with the KASCADE central detector", *Astrop. Phys.* 16 373–386 (2002)
- [79] P. Sokolsky, "Comparison of UHE Composition Measurements by Flys Eye, HiRes-prototype/MIA and Stereo HiRes Experiments", Int. Cosmic Ray Conference (Pune) (2005)
- [80] The High Resolution Fly's Eye Collaboration, "Evidence for Proton-Dominated Cosmic Ray Composition above 1.6 EeV", arXiv:0910.4184.v1 (2009)
- [81] The Pierre Auger Collaboration, "The distribution of shower maxima of UHECR air showers", Int. Cosmic Ray Conference (Beijing) (2011)
- [82] The Telescope Array Collaboration, "Highlights from Telescope Array", Int. Cosmic Ray Conference (Beijing) (2011)
- [83] R. Schlickeiser, "Cosmic Ray Astrophysics"
- [84] K. Gaisser, "Cosmic Ray and Particle Physics"
- [85] L. O'C. Drury et al., "The Gamma ray visibility of supernova remnants. A test of cosmic ray origin", *Astron. and Astroph.*, 287, 959–971 (1994)
- [86] M. Ackermann et al. for the Fermi collaboration, "Detection of the Characteristic Pion-decay Signature in Supernova Remnants", *Science*, Vol. 339 no. 6121, pp. 807–811 (2013)
- [87] A. M. Hillas, "The Origin of Ultra-High-Energy Cosmic Rays", *Ann. rev. of astron. and astroph.*, Vol 22 (1984)
- [88] P. M. Bauleo, J. Rodriguez Martino, "The dawn of the particle astronomy era in ultra high energy cosmic rays", *Nature* 458, 847–851 (2009)



- [89] A. Letessier–Selvon, T. Stanev, "Ultra-high energy cosmic rays", *Rev. Mod. Phys.* 83, 907–942 (2011)
- [90] K. Kotera, A. V. Olinto, "The Astrophysics of Ultra-high–Energy Cosmic Rays", *Ann. Rev. of Astr. and Astroph.* Vol. 49 119–153 (2011)
- [91] E. Waxman, "Cosmological Origin for Cosmic Rays above  $10^{19}$  eV", *Astrop. Jour. Lett.* v.452, p.L1 (1995)
- [92] W. H. Press, P. Schechter, "Formation of Galaxies and Clusters of Galaxies by self–Similar Gravitational Condensation", *Astrophys. Journ.* 187, 425–438 (1974)
- [93] S. Gabici, P. Blasi, "Non–thermal radiation from cluster of Galaxies: the role of Merger Shocks in particle acceleration", *Astrophys. Journ.* 583, 695–705 (2003)
- [94] H. Kang et al, "Cluster accretion shocks as possible acceleration sites for Ultra–High–Energy protons below the Greisen cutoff", *Astrophys. Journ.* 456, 422–427 (1996)
- [95] H. Kang, "Contributions to the Cosmic Ray flux above the ankle: Cluster of Galaxies", *Mon. Not. R. Astron. Soc.* 286, 257–267 (1997)
- [96] M. Markevitch, A. Vikhlinin, "Shocks and cold fronts in galaxy clusters", *arXiv:astro-ph/0701821v2* (2007)
- [97] G. Vannoni et al., "Acceleration and radiation of ultra–high energy protons in galaxy clusters", *Astron. and Astroph.* (2009)
- [98] L. Feretti, "Radio observations of Galaxy Clusters: connection to cluster mergers", *arXiv:astro-ph/0612185v1* (2006)
- [99] R. Fusco et al., "Confirmation of the presence of Non–thermal Hard X–Ray excess in the Cluster A2256 from two epoch observations", *Astrophys. Journ.* 624, L69–L72 (2005)
- [100] P. Blasi, "Gamma Rays from cluster of Galaxies", *arXiv:astro-ph/0701545v1* (2007)
- [101] C. M. Urry, P. Padovani, "Unified Schemes for Radio–Loud Active Galactic Nuclei", *Publ. of the Astron. Soc. of Pac.*, vol 107, 803–845 (1995)
- [102] E. Boldt, P. Gosh, "Cosmic rays from remnants of quasars?", *Mon. Not. Roy. Astron. Soc.*, vol. 307, 491–494 (1999)
- [103] R. D. Blandford, R. L. Znajek, "Electromagnetic extraction of energy from Kerr black holes", *Mon. Not. Roy. Astron. Soc.*, vol. 179, 433–456 (1977)

- 
- [104] C. A. Norman et al., "The origin of Cosmic Rays above  $10^{18}$  eV", *Astroph. Jour.* 454, 60–68 (1995)
- [105] K. Ptitsyna, S. Troitsky, "Physical conditions in potential sources of ultra high energy Cosmic rays: Updated Hillas plot and radiation–loss constraints", arXiv:0808.0367v2 (2010)
- [106] A. Pe'er et al., "Radio quiet active galactic nuclei as possible sources of ultra–high–energy cosmic rays", *Phys. Rev. D* 80 123018 (2009)
- [107] J. Alvarez–Muñiz, P. Mszros, "High energy neutrinos from radio–quiet AGNs", arXiv:astro–ph/0409034v1 (2004)
- [108] J. P. Rachen, P. L. Biermann, "Extragalactic Ultra–High Energy Cosmic–Rays – Part One – Contribution from Hot Spots in Fr–II Radio Galaxies", *Astr. and Astrophy.*, Vol.272, P. 161 (1993)
- [109] H. Takami, S. Horiuchi, "The Production of Ultra High Energy Cosmic Rays during the Early Epochs of Radio–loud AGN", arXiv:1010.2788v2 (2011)
- [110] E. G. Berezhko, "Cosmic rays from active galactic nuclei", arXiv:0809.0734v1 (2008)
- [111] M. Kino et al., "High energy emission from AGN cocoons in clusters of galaxies", *Astr. Nachr. AN* 999, No. 789–793 (2006)
- [112] Y. Ohira et al., "Escape–limited model of cosmic–ray acceleration revisited", *Astron. and Astroph.* 513, A 17 (2010)
- [113] M. Honda, "Ultra–High Energy Cosmic–Ray acceleration in the Jet of Centaurus A", *Astroph. Journ.* 706, p 1517–1526 (2009)
- [114] R. P. Kraft et al., "Chandra observations of the X–Ray Jet in Centaurus A", *Astroph. Journ.* 569, p 54–71 (2002)
- [115] E. M. de Gouveia Dal Pino et al., "Particle Acceleration by Magnetic Reconnection in AGNs and in the IGM", arXiv:1107.2674v1 (2011)
- [116] E. G. Berezhko, G. F. Krymskii, *Soviet Astron. Lett.*, 7, 352 (1981)
- [117] F. M. Rieger, P. Duffy, "Shear acceleration in relativistic astrophysical Jets", *Astroph. Journ.* 617, 155–167 (2004)
- [118] M. Ostrowski, "Energetic Particle Acceleration in Shear Layers" *Plas. Turb. and Ener. Part. in Astroph.*, Proc. of the Int. Conf., Cracow., (1999)
- [119] V. Berezhinsky et al., "On astrophysical solution to ultra high energy cosmic rays", arXiv:hep–ph/0204357v3 (2007)

- [120] V. P. Vlasov, "The possibility of cosmic ray generation in plasma pinches", *Fizik. Plazmy*, vol. 16, p. 1457–1468 (1990)
- [121] K. Murase et al., "Blazars as Ultra-High-Energy Cosmic-Ray sources: implications for TeV Gamma-Ray observations", arXiv:1107.5576v2 (2012)
- [122] E. Waxman, "Cosmological Gamma-Ray Bursts and the Highest Energy Cosmic Rays", *Phys. Rev. Lett.* 75, 3 (1995)
- [123] M. Vietri, "On the acceleration of Ultra High Energy Cosmic Rays in Gamma Ray Bursts", *Astrop. Jour.*, 453, 883 (1995)
- [124] National Science Foundation (from [www.wikipedia.org](http://www.wikipedia.org))
- [125] K. Murase et al., "High-energy cosmic-ray nuclei from high- and low-luminosity gamma-ray bursts and implications for multi-messenger astronomy", *Phys. Rev. D* 78, 023005 (2008)
- [126] G. Sigl, "High Energy Neutrinos and Cosmic Rays", arXiv:1202.0466v1 (2012)
- [127] K. Fang et al, "Newly-born Pulsars as sources of Ultra-High Energy Cosmic Rays", arXiv:1201.5197v1 (2012)
- [128] J. Arons, "Magnetars in the metagalaxy: an origin for UltraHigh-Energy Cosmic Rays in the nearby universe." *The Astrop. Jour.* 589, p. 871892 (2003)
- [129] V. Berezhinsky et al., "Ultra-high energy cosmic rays without GZK cutoff", *Phys. Rev. Lett.* 79, 4302–4305 (1997)
- [130] P. Bhattacharjee et al., "Grand unified theories, topological defects, and ultrahigh-energy cosmic rays", *Phys. Rev. Lett.* 69, 567–570 (1992)
- [131] M. Kachelrieß, "The rise and fall of top-down models as main UHECR sources", arXiv:0810.3017v2 (2008)
- [132] E. Roulet for the Pierre Auger Collaboration, "Latest results from the Pierre Auger Observatory", arXiv:1101.1825v1 (2011)
- [133] G.T. Zatsepin, V.A. Kuz'min, "Upper limit of the spectrum of Cosmic Rays", *JETP Lett (Engl. Transl.)*, Vol 4 (1966)
- [134] F. W. Stecker, "The production of cosmic gamma-rays in interstellar and intergalactic cosmic-ray collisions", PhD thesis (1968)
- [135] H. Takami et al., "Propagation of Ultra-High-Energy Cosmic Ray Nuclei in Cosmic Magnetic Fields and Implications for Anisotropy Measurements", arXiv:1202.2874v1 (2012)

- 
- [136] J. P. Rachen, "Interaction processes and statistical properties of the propagation of cosmic-rays in photon backgrounds", PhD thesis (1996)
- [137] T. Stanev, "Ultra High Energy Cosmic Rays and the Large Scale Structure of the Galactic Magnetic Field", arXiv:astro-ph/960786v1 (1996)
- [138] P.G. Tinyakov, I.I. Tkachev, "Deflections of cosmic rays in a random component of the Galactic magnetic field", arXiv:astro-ph/0411669v2 (2005)
- [139] K. Dolag et al., "Mapping deflections of extragalactic Ultra-High Energy Cosmic Rays in magnetohydrodynamic simulations of the Local Universe", *Pisma Zh. Eksp. Teor. Fiz.* 79, 719–723 (2004)
- [140] G. Sigl et al., "Cosmic Magnetic Fields and Their Influence on Ultra-High Energy Cosmic Ray Propagation" *Nucl. Phys. B – Proc. Suppl.*, Vol. 136, P. 224–233 (2004)
- [141] The HiRes Collaboration, "Search for Correlations between HiRes Stereo Events and Active Galactic Nuclei", *Astropart. Phys.* 30, 175 (2008)
- [142] The HiRes Collaboration, "Analysis of large-scale anisotropy of ultra-high energy cosmic rays in HiRes data", arXiv:1002.1444v1 (2010)
- [143] The AGASA collaboration, "Extension of the Cosmic-Ray Energy Spectrum Beyond the Predicted Greisen-Zatsepin-Kuzmin Cutoff", arXiv:astro-ph/9807193v1 (1998)
- [144] The Pierre Auger collaboration, "Highlights from the Pierre Auger Observatory", *Int. Cosmic Ray Conference (Beijing)* (2011 – Updated in Jul 2012)
- [145] The Telescope Array collaboration, "The Cosmic Ray Energy Spectrum Observed with the Surface Detector of the Telescope Array Experiment", arXiv:1205.5067v1 (2012)
- [146] R. Alosio et al, "Disappointing model for ultrahigh-energy cosmic rays", *Nucl. Phys. in Astrop. V, Jour. of Phys.: Conf. Series* 337 (2012)
- [147] The JEM-EUSO collaboration, "Report on the phase A study 2010", *Collaboration Mission Report* (2010)
- [148] J. Matthews, "A Heitler model of extensive air showers", *Astrop. Phys.*, vol. 22, pp 387–397 (2005)
- [149] M. Nagano, "New measurement on photon yields from air and the application to the energy estimation of primary cosmic rays", arXiv:astro-ph/0406474v2 (2004)

- [150] F. Kakimoto, "A measurement of the air fluorescence yield", Nucl. Instr. and Met. in Phys. Res., vol. A 372, 527–533 (1996)
- [151] The Pierre Auger collaboration, "Properties and performance of the prototype instrument for the Pierre Auger Observatory", Nucl. Instr. and Met. in Phys. Res. A 523, 50–95 (2004)
- [152] The Telescope Array collaboration, "New air fluorescence detectors employed in the Telescope Array experiment", Nucl. Instr. and Met. in Phys. Res. A 676, 54–65 (2012)
- [153] S. Ahmad, "SPACIROC: A Front-End Readout ASIC for spatial cosmic ray observatory", proceeding of the Int. Cosmic Ray Conference (Beijing) (2011)
- [154] H. Miyamoto, "Performance of a front-end ASIC for JEM-EUSO", proceeding of the Int. Cosmic Ray Conference (Beijing) (2011)
- [155] I. Park, "The Development of Photo-Detector Module Electronics for the JEM-EUSO Experiment", proceeding of the Int. Cosmic Ray Conference (Beijing) (2011)
- [156] J. Bayer, "The Cluster Control Board of the JEM-EUSO mission", proceeding of the Int. Cosmic Ray Conference (Beijing) (2011)
- [157] M. Casolino, "Data Acquisition System of the JEM-EUSO project", proceeding of the Int. Cosmic Ray Conference (Beijing) (2011)
- [158] D. De Marco, M. Pallavicini, "EUSO Simulation and Analysis Framework", EUSO mission internal document (2002)
- [159] D. Naumov, "SLAST, Shower Light Attenuated to the Space Telescope", EUSO mission internal document (2003)
- [160] T. Pierog et al., "First Results of Fast One-dimensional Hybrid Simulation of EAS Using CONEX", arXiv:astro-ph/0411260v1 (2004)
- [161] M. Alekseeva et al., "Extensive Air Shower Simulation Program CONEX: Matching Monte Carlo and Numerical Methods", proceeding of the Int. Cosmic Ray Conference (Lodz) (2009)
- [162] D. Heck et al., "CORSIKA: A Monte Carlo Code to Simulate Extensive Air Showers", Wissenschaftliche Berichte-Forschungszentrum Karlsruhe (1998)
- [163] National Oceanic Atmospheric Administration et al., "U.S standard atmosphere, 1976", public document (1976)
- [164] Air Force Geophysics Laboratory, "Users guide to LOWTRAN 7", public document (1988)

- 
- [165] S. Bitkemerova, "Integration of ESAF and Geant4 for simulation of space based telescopes", proceeding of the Int. Cosmic Ray Conference (Lodz) (2009)
- [166] M. C. MacCarone, "Hough transform to reconstruct EUSO tracks: preliminary notes", EUSO mission internal document (2002)
- [167] M. C. MacCarone, "Cluster analysis and line fits to reconstruct EUSO tracks", EUSO mission internal document (2002)
- [168] S. Bottai, "Some algorithm for direction reconstruction in EUSO and optimization of pixel size", EUSO mission internal document (2002)
- [169] B. Rossi, "Cosmic-Ray Theory", K. Greisen, *Rev. Mod. Phys.*, 13, 240 (1941)
- [170] N. P. Ilina et al., *Sov. J. Nucl. Phys.* 55, 1540 (1992)
- [171] N. N. Kalmykov, S. S. Ostapchenko, *Sov. J. Nucl. Phys.* 50, 315 (1989)
- [172] H. H. Mielke et al., *J.Phys. G: Nucl.Part.Phys.*, V 20, P637 (1994)
- [173] M. Giller et al., "Energy spectra of electrons in the extensive air showers of ultra-high energy", *J. Phys. G: Nucl. Part. Phys.* V 30, P97-105 (2004)
- [174] C. Berat et al., "ESAF: Full Simulation of Space-Based Extensive Air Showers Detectors", *Astrop. Phys. Vol. 33*, 4, P. 221-247 (2010)
- [175] [http://www.jaxa.jp/projects/rockets/htv/index\\_e.html](http://www.jaxa.jp/projects/rockets/htv/index_e.html)
- [176] [http://iss.jaxa.jp/iss/doc04\\_e.html](http://iss.jaxa.jp/iss/doc04_e.html)
- [177] The JEM-EUSO collaboration, "An evaluation of the exposure in nadir observation of the JEM-EUSO mission", *Astrop. Phys. Vol. 44-76* (2012)
- [178] D. Gora et al., "Universal lateral distribution of energy deposit in air showers and its application to shower reconstruction", *Astrop. Phys. Vol. 24*, P. 484-494 (2006)
- [179] The Pierre Auger collaboration, "Update on the measurement of the CR energy spectrum above  $10^{18}$  eV made using the Pierre Auger Observatory", proceeding of the Int. Cosmic Ray Conference (Beijing) (2011)
- [180] P. Bobik, K. Shinozaki, private communication (2012)
- [181] Press et al., "Numerical Recipes" vol 1, (1992)

# Acknowledgements

At the end of this long experience I wish to thank all the people which made me learn a lot both from the human and professional point of view. Without their collaboration this work would not have been possible.

First of all, I wish to thank my supervisor Prof. A. Santangelo for his constant support and Prof. T. Ebisuzaki for his supervision during my stay in Japan.

A special thanks goes to K. Shinozaki and M. Bertaina. Thanks to their deep understanding of Physics and to their creativity they have been a continuous source of inspiration for all my work.

I am grateful to my Tübingen colleagues T. Mernik, A. Guzman and E. Iwotskin. Their collaboration has made possible this work and the survival of the simulation group.

I must moreover thank all the people who participated to the correction and validation of my thesis: Prof. A. Santangelo, K. Shinozaki, M. Bertaina, A. Guzman, H. Miyamoto and T. Mernik for their great help and very useful suggestions.

A great thanks goes to the first ESAF developers M. Pallavicini, A. Thea, R. Pesce, D. Naumov for their great work. Moreover I am grateful to all the active ESAF developers who contributed to the validity and completeness of the ESAF package. I thank moreover M. Bertaina for the development of the trigger chain, A. Guzman for the *PWISE* algorithm, M. Bertaina, R. Rossi and A. Gorgi for the *LTTPreclustering* module, D. Naumov, M. Gonchar and S. Bitkemerova for the *NOptics* implementation.

I owe my gratitude to all my Tübingen colleagues which I could not mention for space reasons. In many years I had plenty of occasions to learn from them both professionally and most importantly, from the personal point of view. I will have good memory of this time for many years to come.

I also want to thank all my RIKEN colleagues, Ohata-san for her wonderful support, Marco, Hiroko, Jose, Hector P., Angelica, Hector S., Tsuno-san, Takki, Yoshiya and Lech for the time we spent together. It has been a very happy and fruitful time for me in Japan.

I furthermore wish to thank the RIKEN Integrated Cluster of Clusters facility for the computer resources used for the calculations and the IPA program of RIKEN for the support during my stay in Japan.

# Lebenslauf

- 24-Januar-1982 Geboren in Villafranca di Verona (Italien)
- 1988-1993 Scuola elementare Don L. Milani,  
Sommacampagna, Verona (Italien)  
Grundschule
- 1993-1996: Scuola media inferiore Dante Alighieri  
Sommacampagna, Verona (Italien)  
Mittelschule
- 1996-2001: Liceo Scientifico Statale Galileo Galilei  
Verona (Italien)  
Gymnasium
- 2001-2005: Università degli Studi di Trento  
Trento (Italien)  
Bachelor
- 2005-2008 Eberhard Karls Universität  
Tübingen  
Diplom
- 2008-2013 Eberhard Karls Universität  
Tübingen  
Wissenschaftlicher Angestellter & Doktorand  
Anfertigung der Dissertation unter der  
Leitung von Prof. Dr. A. Santangelo